Measuring Composition and Strain in Bimetallic Catalyst Nanoparticles using Advanced Electron Microscopy



Xiaonan Luo

Corpus Christi College

University of Oxford

A thesis submitted for the degree of

Doctor of Philosophy

29 April, 2022

Abstract

Polymer electrolyte membrane fuel cells (PEMFCs) are promising energy-conversion devices due to their high efficiency and near-zero carbon emission footprint. PEMFCs still require a high mass of precious metal Pt as an electrocatalyst for oxygen reduction reaction (ORR) to ensure sufficient power output efficiency, but the sources and cost of Pt greatly limit its commercial application in fuel cells technology. The development of high-active and low-cost ORR electrocatalysts is therefore of much significance for the commercialization of fuel cells. Compared to Pt, bimetallic (Pt-Co) nanoparticles exhibit superior catalytic performance with less mass of precious metal, but the intrinsic mechanism of this catalytic enhancement has not been fully explained. Strain and composition are two fundamental effects that are highly associated with the catalytic activity of the Pt-based nanoparticles. Thus, being able to measure local composition and strain at an atomic scale within the individual nanoparticle will further our understanding of the operation of heterogeneous catalysts.

In this thesis, the strain analysis and composition quantification are precisely and simultaneously performed on the individual nanoparticle at an atomic scale for four Pt-Co nanoparticle ensembles, to relate composition and size to strain. We find that no compressive strain on the Pt-rich outer shell is imposed by the alloy core. Dilation strain is found to be distributed throughout the individual nanoparticles, with the radial dilation strain being much larger than the circumferential dilation strain at the surface. Remarkably, all the Pt-Co stoichiometries studied have a relatively invariant surface lattice parameter, which is smaller than that for pure Pt but larger than that predicted using the measured local composition, whether or not an acid de-alloying treatment is

applied. This work makes it possible to design the optimum ORR catalysts by tuning strain, composition, and structure of the Pt-based bimetallic nanoparticles.

Dedicated to my father, Yusheng Luo

Acknowledgements

It has been a long journey, and after enduring great hardship, I have finally presented this thesis here. Hopefully, my efforts could provide opportunities to establish a new understanding of this world. I would like to extend my sincere thanks to a number of people in Oxford and Johnson Matthey for their generous contributions to this work.

My deepest gratitude goes foremost to my supervisors, Peter Nellist, Sergio Lozano-Perez and Dogan Ozkaya, for their encouragement, support and knowledge. In particular, I would like to express my special appreciation to Pete. His constant mentorship, patience and unsurpassed inspiration walked me through all the stages of my Dphil study. I am very grateful to Sergio Lozano-Perez for having confidence in my abilities, and his invaluable guidance in programming and spectroscopic aspects. I am appreciative of Dogan for his constructive advice on this project.

I would like to express my huge gratitude to Aakash Varambhia. His knowledge, initial programming and analysis allow for the kick-off of this project. My thanks also go to all the members in Pete's group. In particular, I would like to thank Colum O'Leary and Alexandra Sheader for sacrificing several days to teach and supervise me on the microscope. I would like to thank Lewys Jones, Weixin Song, Zezhong Zhang, Zhao Shen, James Sode, Chen Huang and Arthur Moya for useful discussions and unbelievable helps on this project.

Last but by no means least, I am extremely grateful to my beloved family for unconditional and unwavering supports and love. Especially, my father always makes

all his efforts to support me and keeps me grounded. Also, thanks go to my girlfriend for encouraging and comforting me during difficulties. They are crucial and irreplaceable to my world.

List of outputs

Journal Articles

- **Luo, X.**, Varambhia, A., Song, W., Ozkaya, D., Lozano-Perez, S., Nellist, P.D.. High-precision atomic scale strain mapping on nanoparticles from STEM images. *In submission to Ultramicroscopy.*

- **Luo, X.**, Varambhia, A., Song, W., Shen, Z., Sheader, A., Hao B., Zhang R., Ozkaya, D., Lozano-Perez, S., Nellist, P.D.. Atomic-scale composition-strain-structure control on catalytic activity of Pt-Co nanoparticles. *In submission to Nature Chemistry.*

- Ellaby, T., Varambhia, A., **Luo, X.**, Briquet, L., Sarwar, M., Ozkaya, D., Thompsett, D., Nellist, P.D. and Skylaris, C.K. (2020). Strain effects in core–shell PtCo nanoparticles: a comparison of experimental observations and computational modelling. *Physical Chemistry Chemical Physics*, 22(42), pp.24784-24795.

- Song, W., Osorio, M., Marie, J., Liberti, E., **Luo, X.**, O'Leary, C., House, R., Bruce, P. and Nellist, P.D.. Sub-angstrom Direct Imaging of Oxygen Shifts Associated with the Oxygen Redox Process of Li-rich Layered Oxides. *In submission to Joule.*

- Shen, Z., Chen, K., Yu, H., Jenkins, B., Ren, Y., Saravanan, N., He, G., **Luo, X.**, Bagot, P.A., Moody, M.P. and Zhang, L. (2020). New insights into the oxidation mechanisms of a Ferritic-Martensitic steel in high-temperature steam. *Acta Materialia*, 194, pp.522-539.

- Shen, Z., Zhang, J., Wu, S., **Luo, X.**, Jenkins, B.M., Moody, M.P., Lozano-Perez, S. and Zeng, X., 2022. Microstructure understanding of high Cr-Ni austenitic steel corrosion in high-temperature steam. *Acta Materialia*, p.117634.

Conference proceedings

- **Luo, X.**, Nellist, P., Lozano-Perez, S., Varambhia, A., & Ozkaya, D. (2021). Quantitative STEM for Bimetallic Catalyst Nanoparticles. *Microscopy and Microanalysis*, 27(S1), 2612-2614.

- Song, W., Osorio, M., Marie, J., Liberti, E., **Luo, X.**, O'Leary, C., House, R., Bruce, P. and Nellist, P. (2021). Direct Imaging of Oxygen Sub-lattice Deformation in Li-rich Cathode Material Using Electron Ptychography. *Microscopy and Microanalysis*, 27(S1), pp.2724-2726.

Introduction 1

1.1 Overview 2

Catalysts of the Fuel Cells 4

2.1 The Hydrogen Fuel Cell 4

2.2 Catalyst design 7

2.3 Conclusions 14

2.4 References 15

Characterisation techniques 19

3.1 Optical characterisation 20

3.2 X-ray Diffraction (XRD) 21

3.3 X-ray Photoelectron Spectroscopy (XPS) 23

3.4 Atom Probe Tomography 23

3.5 Conventional transmission electron microscopy (CTEM) 24

3.5.1 CTEM diffraction 27

3.5.2 CTEM imaging 28

3.6 Scanning transmission electron microscopy (STEM) 29

3.6.1 Bright-field STEM 32

3.6.2 Annular bright-field STEM 33

3.6.3 Annular dark-field STEM 33

3.7 Energy-dispersive X-ray spectroscopy (EDS) 35

3.8 Electron energy loss spectroscopy (EELS) 37

3.9 Conclusions 40

3.10 References 42

Atomic-scale strain mapping on nanoparticles 47

4.1 Introduction.....47
4.2 Brief review of strain mapping techniques.....51
4.2.1 Convergent beam electron diffraction.....51
4.2.2 Nanobeam electron diffraction.....51
4.2.3 Dark field electron holography.....52
4.2.4 Geometric phase analysis.....53
4.2.5 Peak finding and peak pair methods.....54
4.3 Validity of projection approximation for displacements.....55
4.4 Defining and measuring strain at the atomic scale.....60
4.5 Choice of reference grid.....70
4.6 Measurements reliability on noisy images.....73
4.7 Application of the technique: de-alloyed PtCo3 bimetallic nanoparticle.....78
4.8 Conclusions.....83
4.9 References.....85
Composition determination on nanoparticles.....91
5.1 Introduction.....91
5.2 Data acquisition.....93
5.3 Estimating the number of atoms in nanoparticles.....97
5.4 EELS quantification.....98
5.4.1 Brief review of EELS quantification approaches.....98
5.4.2 Co atom counting on Pt-Co nanoparticles.....102
5.5 EDS quantification.....106
5.5.1 Brief review of EDS quantification approaches.....106
5.5.2 Pt and Co atom counting on the nanoparticle.....111
5.6 ADF quantification.....113

5.6.1 ADF scattering cross section theory 113
5.6.2 Detector calibration 115
5.6.3 Channelling effect 119
5.6.4 STEM ADF simulations 120
5.6.5 Relating spectroscopic cross sections to ADF cross section 127
5.6.6 On-axis ADF Pt-Co bimetallic nanoparticle quantification 128
5.7 Error analysis 130
5.7.1 EDS atom counting error analysis 130
5.7.2 EELS atom counting error analysis 130
5.8 Applications: Composition quantitative analysis on the Pt-Co bimetallic nanoparticles 131
5.9 Conclusions 134
5.10 References 136

Simultaneous composition and strain analyses of Pt-Co nanoparticles 141

6.1 Introduction 141
6.2 Vegard's law prediction 145
6.3 Atomic-scale simultaneous composition and strain analyses 147
6.4 Unleached Pt-Co system 150
6.5 Leached Pt-Co system 154
6.6 High ensemble number analysis 157
6.8 Conclusions 161
6.9 References 163

Summary and outlook 169

7.1 Conclusions 169

7.2 Future work.....172

Appendix A.....178

Appendix B.....185

Chapter 1

Introduction

Over the past decades, the blossoming of advanced technologies has significantly stimulated the world's energy demands. The foreseeable depletion of fossil fuels and serious environmental pollution have become the unprecedented challenges facing the world. To alleviate the global energy crisis and reduce the carbon footprints, much research has been dedicated to exploiting a clean, sustainable and high-efficient energy source. Fuel cells powered by hydrogen have emerged as an encouraging energy conversion device for applications of portable energy generation and transportation (Hass, 2004, O'hayre et al., 2016, Olabi et al., 2021). Although the production of hydrogen often releases global warming gases, hydrogen fuel cells with the only reactant product of H_2O are often regarded as a near zero-emission power source. A critical obstacle to their commercialization is the high cost and scarcity of platinum (Pt) catalysts for the oxygen reduction reaction (ORR) at the cathode (Holton and Stevenson, 2013). Tremendous research efforts, from both industry and academia, have been devoted to developing the low-cost and high-active ORR catalysts. A promising design is to alloy Pt with a secondary 3d-transition metal, including Co, Ni, Fe, Cu or Mn, to obtain Pt-based bimetallic nanoparticles (Toda et al., 1999, Stamenkovic et al., 2007). The design strategy is to limit Pt location to the nanoparticle surface while the secondary element is restricted to the nanoparticle centre. These core-shell structured bimetallic nanoparticles demonstrate a catalytic enhancement with a significantly reduced Pt loading (Wang et al., 2013, Bu et al., 2016). To understand the intrinsic mechanism behind their enhanced catalytic performance, we need to fully characterize these bimetallic catalysts at an atomic scale, especially the local strain, structure and

composition variations at the nanoparticle surface where the chemical reactions take place.

In this thesis, the Pt-Co bimetallic nanoparticles are characterized using a scanning transmission electron microscope (STEM) equipped with energy dispersive X-ray (EDS) and electron energy loss spectroscopy (EELS) detectors. An atomic site-specific strain measurement methodology based on atomic-resolution angular dark field (ADF) STEM images is further developed. Atomic-scale composition analysis is achieved by evaluating the number of atoms using spectroscopic signals (EDS and EELS signals). Finally, simultaneous composition and strain quantifications are performed on the same nanoparticles for four different Pt-Co systems.

1.1 Overview

The structure of this thesis is as follows:

- Chapter 2 contains the background on the fuel cells and the design strategies for the ORR catalysts.
- Chapter 3 presents the materials characterisation techniques which could provide crystal structure, composition, strain and size information for bi- or tri-metallic nanoparticles. The characterisation techniques can be generally classified into two categories: the bulk averaging method and precise localised method, which are discussed and compared.
- Chapter 4 builds upon our newly developed strain analysis methodology for nanoparticles. The existing deformation analysis techniques using a transmission electron microscope were first presented, their advantages and limitations are also discussed. Next, the validity of projection approximation

for displacement measurements is investigated. A mathematical description and an experimental demonstration of elastic deformation parameters defined at an atomic scale are presented. Influences from the reference lattice used and Poisson noise on strain measurements are also studied.

- Chapter 5 provides an experimental demonstration of the simultaneous ADF, EDS and EELS quantifications on the Pt-Co bimetallic nanoparticles. The background theories for the quantification techniques using ADF, EDS and EELS signals were discussed. The simulation matching technique for the ADF quantification is introduced with further details on ADF detector calibration and ADF STEM simulation. Next, the accuracy of the composition analysis methodology using the scattering cross section theory is verified by evaluating the number of atoms using different signals. Finally, the application of this composition quantification method is demonstrated by analysing the core-shell discrepancy and local crystal structure of the Pt-Co nanoparticles.
- Chapter 6 demonstrates simultaneous composition and strain quantifications at an atomic scale within the same on-axis nanoparticles for four different Pt-Co systems. Composition and size of the Pt-Co nanoparticles are related to strain.
- Chapter 7 highlights the conclusions and future work prospects of this work.

Chapter 2

Catalysts of the Fuel Cells

2.1 The Hydrogen Fuel Cell

The intensification of energy shortage and environmental pollution caused by traditional fossil fuels has become an urgent challenge to be addressed. Modern advancements such as batteries, fuel cells and solar cells have been developed to meet the world energy demand and decelerate the climate changes (Turner, 2004). Unlike batteries whose operating voltage can decline during the discharge, fuel cells or solar cells have a constant operating voltage as long as they are continuously supplied with fuel or photons, respectively, as shown in Figure 2.1. It also shows that fuel cells operate at the highest current densities compared with the other two devices (O'Hayre et al., 2016). In addition, fuel cells have been reported to have an energy conversion efficiency of 40%~60% (U.S. Department of Energy, 2011), much higher than that of the conventional internal combustion engine, which is at 12%~30% (U.S. Department of Energy, 2011). Accordingly, fuel cells have garnered considerable research interest over the recent decades (Matthey, 2013).

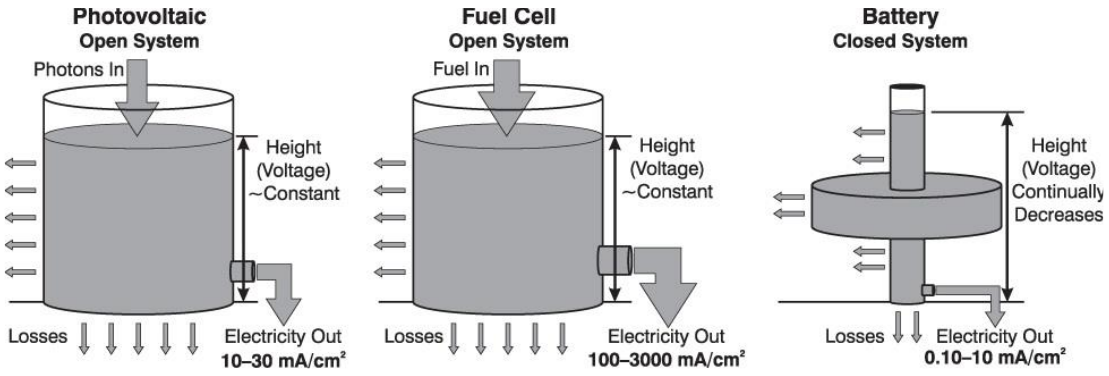

Figure 2.1 Fuel cells versus solar cells versus batteries, figure reprinted from (O'Hayre et al., 2016).

Fuel cell design concepts mainly include polymer electrolyte membrane fuel cell (PEMFC), phosphoric acid fuel cell (PAFC), alkaline fuel cell (AFC), molten carbonate fuel cell (MCFC) and solid-oxide fuel cell (SOFC) (O'hayre et al., 2016). Table 2.1 compares the key features of these five types of fuel cells. The PEMFC powered by hydrogen (H-PEMFC) is the most promising energy device for potable power generation and transportation application due to its relative low operating temperature (80°C) and the quick engine start-up time. Also, the only by-product of the reaction for the H-PEMFC is water, which makes it an encouraging option to reduce the carbon footprints. Figure 2.2 displays a simple structure of the H-PEMFC.

	PEMFC	PAFC	AFC	MCFC	SOFC
Electrolyte	Polymer membrane	Liquid H_3PO_4 (immobilized)	Liquid KOH (immobilized)	Molten carbonate	Ceramic
Charge carrier	H^+	H^+	OH^-	CO_3^{2-}	O^{2-}
Operating temperature	80°C	200°C	60-220°C	650°C	600-1000°C
Catalyst	Pt	Pt	Pt	Ni	Perovskites (ceramic)
Cell components	Carbon based	Carbon based	Carbon based	Stainless based	Ceramic based
Fuel compatibility	H_2, methanol	H_2	H_2	H_2, CH_4	H_2, CH_4, CO

Table 2.1 Description of five major types of fuel cells, figure reprinted from (O'hayre et al., 2016).

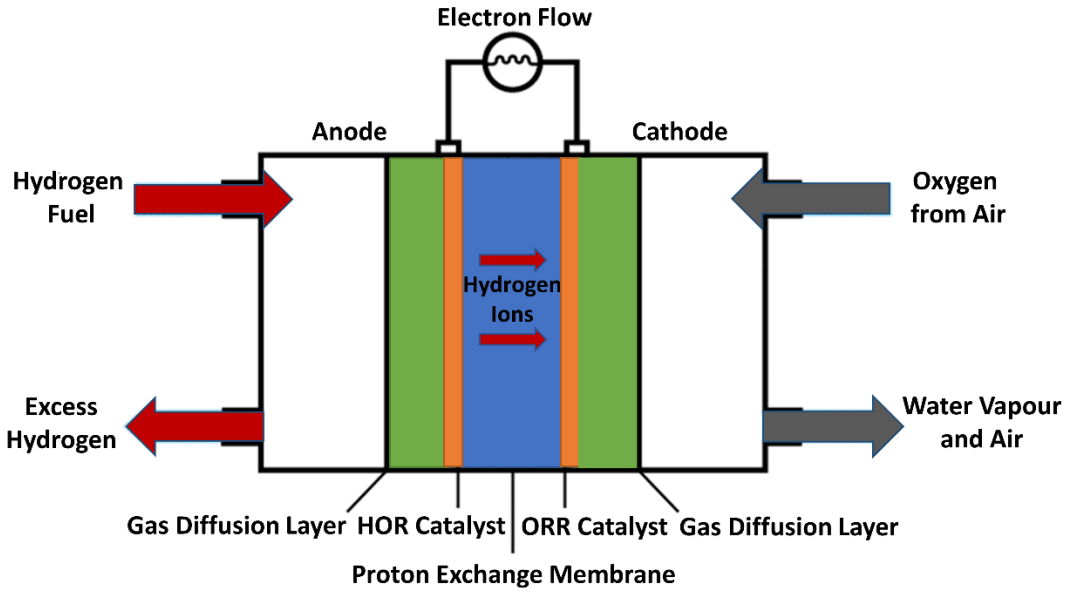

Figure 2.2 The schematic of the H-PEMFC.

In the H-PEMFC, there are two main electrochemistry reactions, which are the hydrogen oxidation reaction (HOR) on the anode and oxygen reduction reaction (ORR) on the cathode (Sheng et al., 2010). On the anode, hydrogen is adsorbed onto the surface active sites of HOR catalysts, and subsequently decomposes into hydrogen ions and electrons, which passes through the membrane and external circuit, respectively.

$$\frac{1}{2}\,H_2 + * \rightarrow H^*$$

$$H^* \rightarrow H^+ + * + e^-$$

Where * denotes the surface active site of the HOR catalysts. The active sites are defined as the optimal areas on the surface where the desired reaction takes place. On the cathode, oxygen is adsorbed onto the surface active sites of ORR catalysts, leading to the break of oxygen-oxygen bonds. A series of reactions involving the anodal products (those are, protons and electrons) and oxygen atoms could take place to produce water. This process can be explained by either the associative mechanism or dissociative mechanism, illustrated through the following equations (Jinnouchi, 2003):

(1) Associative mechanism

$$O_2 + * \rightarrow {O_2}^*$$

$$O_2 + H^+ + e^- + * \rightarrow OOH^*$$

$$OOH^* + H^+ + e^- \rightarrow {H_2O_2}^*$$

$${H_2O_2}^* \rightarrow \ H_2O_2 + *$$

(2) Dissociative mechanism

$$\frac{1}{2}O_2 + * \rightarrow O^*$$

$$O^* + H^+ + e^- \rightarrow OH^*$$

$$OH^* + H^+ + e^- \rightarrow H_2O + *$$

Where * denotes the surface active site of the ORR catalysts.

The choice of these two thermodynamic mechanisms heavily relies on the ORR catalyst type and the synthesis method (Varambhia, 2018). Compared to the efficient reaction rate of the HOR, the rate of the ORR in the H-PEMFC is relatively sluggish, resulting in the degradation of the discharge voltage of the hydrogen fuel cells (Sheng et al., 2010). The rate-limiting ORR at the cathode is the major determinant of the performance of the H-PEMFC (Rabis et al., 2012).

2.2 Catalyst design

For the heterogeneous catalysis at the cathode in the H-PEMFC, the ORR catalysts should have sufficient strength for the oxygen adsorption to break the oxygen-oxygen bonds, but the oxygen binding energy for the catalysts also needs to be weak enough to release the oxygen species for the following chemical reaction. This principle has been well described by the Sabatier principle, which is that the binding energy between the catalyst and the reactant should be neither too strong nor too weak (Medford et al., 2015).

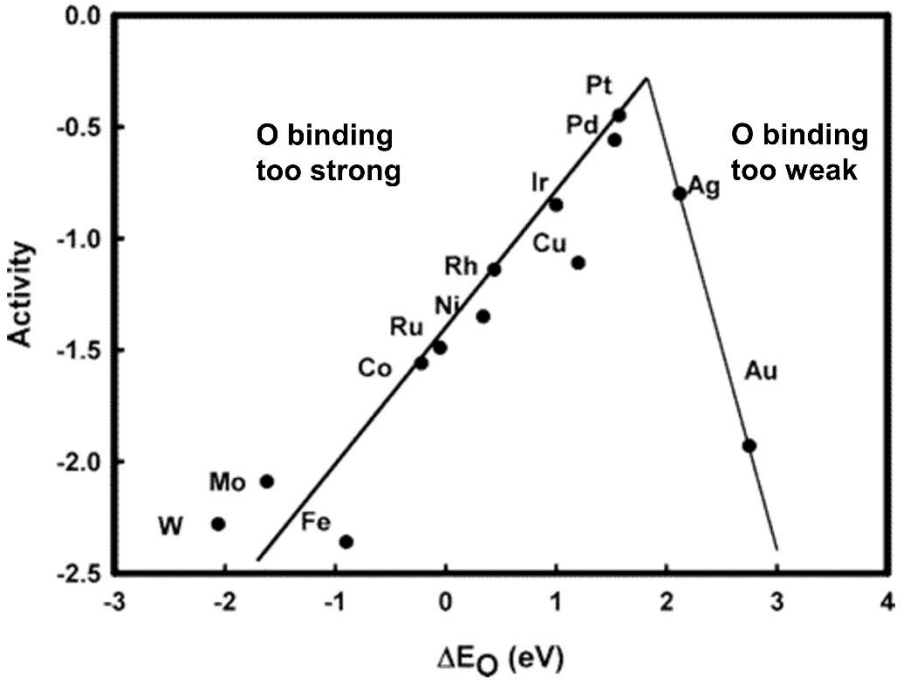

Figure 2.3 Trends in the oxygen reduction activity plotted as a function of the oxygen binding energy, figure reprinted from (Nørskov et al., 2004).

A volcano plot between the oxygen reduction activity and the oxygen binding energy for a set of transition metals is shown in Figure 2.3. It demonstrates that compared to the other pure metal species, Pt has the highest ORR catalytic activity that is closest to the optimal theoretical activity. Also, the high melting point, oxidation and corrosion resistance of Pt offer it a prominent structural stability. Thus, precious metal Pt is presently the workhorse in the ORR catalyst industry although it has limited resources with the high cost (Arblaster, 1997, Gasteiger and Marković, 2009, Holton and Stevenson, 2013). However, Figure 2.3 also illustrates that pure Pt metal still binds oxygen slightly strong by ~0.2 eV. Much research effort has been devoted to designing the ORR catalysts with enhanced catalytic performance and reduced Pt loading. There are five main strategies as follows.

(1) Crystal plane control.

It is well known that the binding energy and catalytic activity heavily rely on the surface crystal plane (Yates Jr, 1995). It has been reported that Pt concave nanotubes bounded by high-index planes exhibit enhanced catalytic activity compared to those enclosed by low-index facets (Yu et al., 2011). The reason could be that the high-index facets have a higher density of atomic ledges, kinks and steps (Nie et al., 2015). However, those Pt nanocrystals with the high-index surface planes lack stability during the fuel cells operations because of the morphological changes, leading to a consequent performance loss. For the Pt low-index surfaces, oxygen reduction was studied in 0.1 M $HClO_4$ solution by employing a hanging meniscus rotating-disk technique. It is found that the ORR activity discerned from the half-wave potential decreases in a sequence: Pt (110) > Pt (111) > Pt (100) (Marković et al., 1994). Thus, by controlling the growth of Pt crystal planes during the synthesis process, it is possible to expose the desired surface facets to air or vacuum for the ORR activity enhancement.

(2) Surface decoration with metal clusters or molecules.

Decorating Pt nanocrystals with metal clusters, molecule, ions and organics could optimize the electronic structure of Pt, further boosting their catalytic activity. For example, embellishing Pt nanoparticles with Au clusters could stabilize Pt against dissolution under the hostile working environment of the fuel cells (Zhang et al., 2007). In addition, modifying the surface of Pt catalysts with carbon or silica layers has also been proved to be efficient in suppressing the migration of Pt, offering a higher stability (Takenaka et al., 2007, Jiang et al., 2010, Takenaka et al., 2014).

(3) Supported catalysts

Carbon black is presently of widespread use as a support for Pt catalysts, but this application still faces several challenges. Numerous defects and unsaturated bonds on the carbon black significantly weaken the interaction between Pt and the support (Yu and Ye, 2007). Pt being loosely anchored to the carbon support could induce the aggregation and migration of Pt nanoparticles, resulting in the catalytic performance loss (Donthu et al., 2009, Liu and Mustain, 2011). Also, such a weak bonding between Pt and carbon is not enough to modify the electronic structure of Pt. In addition, carbon corrosion could take place in the presence of oxygen under a high electrode potential. The carbon corrosion could separate Pt from the carbon support, leading to the deterioration of the catalytic performance (Schmidt and Baurmeister, 2008, Hartnig and Schmidt, 2011, Meier et al., 2012). To tackle these issues, graphene, carbon nanotubes and nanowires have been proposed to serve as the supports for Pt catalysts (Mathias et al., 2005, Fang et al., 2009). These graphitic carbon materials have abundant π sites where Pt can be tightly anchored. This strong metal-support interaction is introduced by the electron delocalisation between the carbon π sites and Pt d-orbitals leading to the formation of the covalent bond between Pt and carbon (Coloma et al., 1995, Yu and Ye, 2007). Although Pt catalysts supported by these graphitic carbon materials demonstrate superior catalytic activity and stability, their commercial applications are still limited by the high manufacturing cost.

(4) Pt-M binary alloys.

Pt-M binary alloys with a reduced content of Pt, where M is a 3d transition metal such as Co, Ni, Fe, Cu or Cr, exhibit an enhanced ORR activity (Toda et al., 1999, Stamenkovic et al., 2006, Stamenkovic et al., 2007, Greeley et al., 2009, Chattot et al., 2018). It has been reported that the catalytic enhancement of these Pt-based alloys is

because of the near-optimal position of the Pt d-band centre of their surfaces (Gavartin et al., 2009, Chattot et al., 2018). Figure 2.4 displays a 'volcano type' behaviour between the ORR activity and the d-band centre for a set of Pt-M binary alloys.

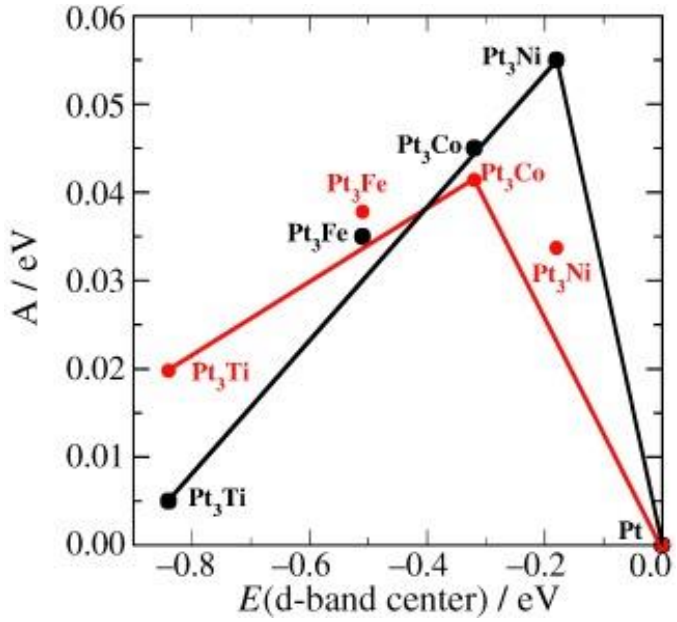

Figure 2.4 The ORR activity as a function of the Pt d-band centre (relative to pure Pt) for the Pt-based alloyed catalysts. The activity is defined as $A = K_B T ln\left(\frac{i}{i_{Pt}}\right) + A_{Pt}$, where $\frac{i}{i_{Pt}}$ is the current density relative to Pt, K_B is a rate constant and A_{Pt} is the theoretical value for the activity of Pt. Black: DFT simulations, Red: Experiments, figure reprinted from (Stamenkovic et al., 2006).

The Pt d-band centre shifts are highly associated with the ligand and strain effects (Mavrikakis et al., 1998, Kitchin et al., 2004, Strasser et al., 2010, Temmel et al., 2016). The ligand effect refers to the d-band width changes caused by the hybridization of the d orbitals between Pt and the substitute element (Bligaard and Nørskov, 2007). The strain effect is the lattice mismatch between the dissimilar metal atoms resulting in the bond length changes (Mavrikakis et al., 1998). The expansion or compression of the bond length would lead to the upward or downward shifts of the d-band centre, respectively (Kitchin et al., 2004). Also, previous work has successfully related the Pt d-band centre to the oxygen adsorption energy through the density functional theory (DFT) calculations (Stamenkovic et al., 2006), as shown in Figure 2.5. However, the

dissolution and oxidation of the secondary transition metal under the acid working environment of the fuel cells could result in the instabilities of the Pt-based alloyed catalysts (Varambhia, 2018).

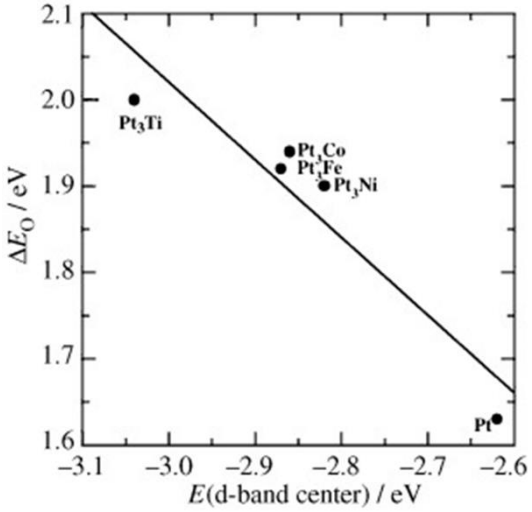

Figure 2.5 The oxygen adsorption energy as a function of the Pt d-band centre (relative to pure Pt) for the Pt-based alloyed catalysts, figure reprinted from (Stamenkovic et al., 2006).

(5) Core-shell structured nanoparticles.

To mitigate the dissolution of the secondary element from the Pt-based alloyed catalysts, a promising strategy is to layer a thin Pt shell onto the surfaces of the non-noble metal core, as shown in Figure 2.6. The obtained core-shell structured nanoparticles not only inherit the superior ORR activity of the Pt-based alloys but also feature an excellent stability due to the protection of the Pt skin (Nie et al., 2015). This design tactic has attracted considerable research interest because it fully utilises every cheaper metal atom and greatly drives down the manufacturing cost without sacrificing the catalytic performance.

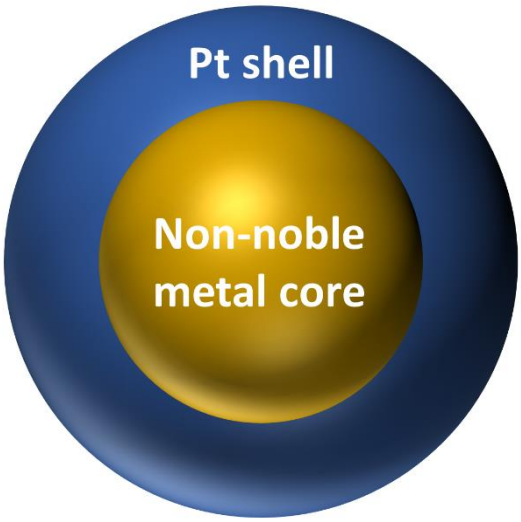

Figure 2.6 The core-shell structure of the Pt-based bimetallic nanoparticle model.

The synthesis routes for the core-shell structured Pt-based nanoparticles can be classified into three categories (Oezaslan et al., 2013, Nie et al., 2015). (1) Removing the non-Pt metal atoms from the surfaces of the uniformly alloyed precursor, such as the acid-leaching method. (2) Depositing Pt onto the preformed non-noble metal core. The deposition methods mainly include heterogeneous colloidal nucleation and underpotential deposition (UPD). (3) Inducing one metal constituent to segregate toward the surface or into the centre of the uniformly alloyed precursor, including thermal or adsorbate-induced segregation. In all the synthesis techniques, forming a pure-element shell is not always possible. Instead, we normally obtain a Pt-enriched shell and a Pt-based alloyed core. Therefore, mapping composition and strain distribution within these core-shell structured Pt-based nanoparticles is necessary for the interpretation of the intrinsic mechanism behind their superior catalytic properties.

2.3 Conclusions

The purpose of this chapter is to introduce the background for studying the ORR catalysts for the fuel cells. A brief overview of the fuel cell technology was first presented. The extremely high energy conversion efficiency, zero-emission of the greenhouse gases and continuous power generation of the fuel cells makes it an ideal alternative to traditional fossil fuels. Among the five major fuel cell types, the H-PEMFC is the most promising device due to its relatively friendly working environment and short start-up time. A summary of the H-PEMFC design and the working principle was also presented.

Currently, the wide commercial application of the H-PEMFC is limited by the expensive ORR catalysts. Here, the design strategies for the ORR catalysts were discussed and compared. The Pt-based bimetallic nanoparticles featuring a core-shell structure become the most prominent ORR catalyst due to its enhanced catalytic properties with a low content of precious metal Pt. The synthesis methods for the core-shell structured catalysts were also introduced. Their superior catalytic activity is highly associated with the Pt d-band centre, which has been further related to the composition and strain variations within the nanoparticles. Therefore, a detailed and high-throughput characterisation of size, composition, strain and structure of the core-shell structured Pt-based nanoparticles could help to directly connect their synthesis to performance.

2.4 References

Arblaster, J. (1997). "Crystallographic properties of platinum." *Platinum Metals Review* 41(1): 12-21.

Bligaard, T. and J. K. Nørskov (2007). "Ligand effects in heterogeneous catalysis and electrochemistry." *Electrochimica Acta* 52(18): 5512-5516.

Bu, L., N. Zhang, S. Guo, X. Zhang, J. Li, J. Yao, T. Wu, G. Lu, J.-Y. Ma and D. Su (2016). "Biaxially strained PtPb/Pt core/shell nanoplate boosts oxygen reduction catalysis." *Science* 354(6318): 1410-1414.

Chattot, R., O. Le Bacq, V. Beermann, S. Kühl, J. Herranz, S. Henning, L. Kühn, T. Asset, L. Guétaz and G. Renou (2018). "Surface distortion as a unifying concept and descriptor in oxygen reduction reaction electrocatalysis." *Nature Materials* 17(9): 827-833.

Coloma, F., A. Sepulvedaescribano and F. Rodriguezreinoso (1995). "Heat-treated carbon-blacks as supports for platinum catalysts." *Journal of Catalysis* 154(2): 299-305.

Donthu, S., M. Cai, M. Ruthkosky and I. Halalay (2009). "Carbon–titania composite substrates for fuel cell catalyst applications." *Chemical Communications*(28): 4203-4205.

United States Department of Energy (2011). "Comparison of Fuel Cell Technologies." from https://www.energy.gov/eere/fuelcells/comparison-fuel-cell-technologies.

United States Department of Energy (2011). "Fuel Economy: Where The Energy Goes." from https://www.fueleconomy.gov/feg/atv.shtml.

Fang, B., J. H. Kim, M. Kim and J.-S. Yu (2009). "Ordered hierarchical nanostructured carbon as a highly efficient cathode catalyst support in proton exchange membrane fuel cell." *Chemistry of Materials* 21(5): 789-796.

Gasteiger, H. A. and N. M. Marković (2009). "Just a dream—or future reality?" *Science* 324(5923): 48-49.

Gavartin, J., M. Sarwar, D. Papageorgopoulos, D. Gunn, S. Garcia, A. Perlov, A. Krzystala, D. L. Ormsby, D. Thompsett and G. Goldbeck-Wood (2009). "Exploring Fuel Cell Cathode Materials: A High Throughput Calculation Approach." *ECS Transactions* 25(1): 1335.

Greeley, J., I. Stephens, A. Bondarenko, T. P. Johansson, H. A. Hansen, T. Jaramillo, J. Rossmeisl, I. Chorkendorff and J. K. Nørskov (2009). "Alloys of platinum and early

transition metals as oxygen reduction electrocatalysts." *Nature Chemistry* 1(7): 552-556.

Hartnig, C. and T. J. Schmidt (2011). "Simulated start–stop as a rapid aging tool for polymer electrolyte fuel cell electrodes." *Journal of Power Sources* 196(13): 5564-5572.

Hass, H. (2004). "Well-to-wheels analysis of alternative fuels and powertrains in the European context; Well-to-Wheels Analyse zukuenftiger Kraftstoffe und Antriebssyteme im europaeischen Kontext."

Holton, O. T. and J. W. Stevenson (2013). "The role of platinum in proton exchange membrane fuel cells." *Platinum Metals Review* 57(4): 259-271.

Jaksic, J. M., N. M. Ristic, N. V. Krstajic and M. M. Jaksic (1998). "Electrocatalysis for hydrogen electrode reactions in the light of fermi dynamics and structural bonding FACTORS—I. individual electrocatalytic properties of transition metals." *International Journal of Hydrogen Energy* 23(12): 1121-1156.

Jiang, Z.-Z., Z.-B. Wang, D.-M. Gu and E. S. Smotkin (2010). "Carbon riveted Pt/C catalyst with high stability prepared by in situ carbonized glucose." *Chemical Communications* 46(37): 6998-7000.

Jinnouchi, R. (2003). "New insight into microscale transport phenomena in PEFC by quantum MD." *Microscale Thermophysical Engineering* 7(1): 15-31.

Kitchin, J. R., J. K. Nørskov, M. A. Barteau and J. Chen (2004). "Role of strain and ligand effects in the modification of the electronic and chemical properties of bimetallic surfaces." *Physical Review Letters* 93(15): 156801.

Liu, Y. and W. E. Mustain (2011). "Structural and electrochemical studies of Pt clusters supported on high-surface-area tungsten carbide for oxygen reduction." *Acs Catalysis* 1(3): 212-220.

Marković, N. M., R. R. Adžić, B. Cahan and E. Yeager (1994). "Structural effects in electrocatalysis: oxygen reduction on platinum low index single-crystal surfaces in perchloric acid solutions." *Journal of Electroanalytical Chemistry* 377(1-2): 249-259.

Mathias, M. F., R. Makharia, H. A. Gasteiger, J. J. Conley, T. Fuller, C. Gittleman and S. S. Kocha (2005). "Two fuel cell cars in every garage?" *The Electrochemical Society Interface* 14(3): 24.

Matthey, J. (2013). "The fuel cell industry review." *Fuel Cell Today*.

Mavrikakis, M., B. Hammer and J. K. Nørskov (1998). "Effect of strain on the reactivity of metal surfaces." *Physical Review Letters* 81(13): 2819.

Medford, A. J., A. Vojvodic, J. S. Hummelshøj, J. Voss, F. Abild-Pedersen, F. Studt, T. Bligaard, A. Nilsson and J. K. Nørskov (2015). "From the Sabatier principle to a predictive theory of transition-metal heterogeneous catalysis." *Journal of Catalysis* 328: 36-42.

Meier, J. C., C. Galeano, I. Katsounaros, A. A. Topalov, A. Kostka, F. Schüth and K. J. Mayrhofer (2012). "Degradation mechanisms of Pt/C fuel cell catalysts under simulated start–stop conditions." *Acs Catalysis* 2(5): 832-843.

Nie, Y., L. Li and Z. Wei (2015). "Recent advancements in Pt and Pt-free catalysts for oxygen reduction reaction." *Chemical Society Reviews* 44(8): 2168-2201.

Nørskov, J. K., J. Rossmeisl, A. Logadottir, L. Lindqvist, J. R. Kitchin, T. Bligaard and H. Jonsson (2004). "Origin of the overpotential for oxygen reduction at a fuel-cell cathode." *The Journal of Physical Chemistry B* 108(46): 17886-17892.

O'Hayre, R., S.-W. Cha, W. Colella and F. B. Prinz (2016). *Fuel cell fundamentals*, John Wiley & Sons.

Oezaslan, M., F. Hasche and P. Strasser (2013). "Pt-based core–shell catalyst architectures for oxygen fuel cell electrodes." *The Journal of Physical Chemistry Letters* 4(19): 3273-3291.

Olabi, A., T. Wilberforce and M. A. Abdelkareem (2021). "Fuel cell application in the automotive industry and future perspective." *Energy* 214: 118955.

Rabis, A., P. Rodriguez and T. J. Schmidt (2012). "Electrocatalysis for polymer electrolyte fuel cells: recent achievements and future challenges." *Acs Catalysis* 2(5): 864-890.

Schmidt, T. J. and J. Baurmeister (2008). "Properties of high-temperature PEFC Celtec®-P 1000 MEAs in start/stop operation mode." *Journal of Power Sources* 176(2): 428-434.

Sheng, W., H. A. Gasteiger and Y. Shao-Horn (2010). "Hydrogen oxidation and evolution reaction kinetics on platinum: acid vs alkaline electrolytes." *Journal of The Electrochemical Society* 157(11): B1529.

Stamenkovic, V., B. S. Mun, K. J. Mayrhofer, P. N. Ross, N. M. Markovic, J. Rossmeisl, J. Greeley and J. K. Nørskov (2006). "Changing the activity of electrocatalysts for oxygen reduction by tuning the surface electronic structure." *Angewandte Chemie* 118(18): 2963-2967.

Stamenkovic, V. R., B. S. Mun, M. Arenz, K. J. Mayrhofer, C. A. Lucas, G. Wang, P. N. Ross and N. M. Markovic (2007). "Trends in electrocatalysis on extended and nanoscale Pt-bimetallic alloy surfaces." *Nature Materials* 6(3): 241-247.

Strasser, P., S. Koh, T. Anniyev, J. Greeley, K. More, C. Yu, Z. Liu, S. Kaya, D. Nordlund and H. Ogasawara (2010). "Lattice-strain control of the activity in dealloyed core–shell fuel cell catalysts." *Nature Chemistry* 2(6): 454-460.

Takenaka, S., H. Matsumori, K. Nakagawa, H. Matsune, E. Tanabe and M. Kishida (2007). "Improvement in the durability of Pt electrocatalysts by coverage with silica layers." *The Journal of Physical Chemistry C* 111(42): 15133-15136.

Takenaka, S., H. Miyamoto, Y. Utsunomiya, H. Matsune and M. Kishida (2014). "Catalytic activity of highly durable Pt/CNT catalysts covered with hydrophobic silica layers for the oxygen reduction reaction in PEFCs." *The Journal of Physical Chemistry C* 118(2): 774-783.

Temmel, S. E., E. Fabbri, D. Pergolesi, T. Lippert and T. J. Schmidt (2016). "Investigating the role of strain toward the oxygen reduction activity on model thin film Pt catalysts." *ACS Catalysis* 6(11): 7566-7576.

Toda, T., H. Igarashi, H. Uchida and M. Watanabe (1999). "Enhancement of the electroreduction of oxygen on Pt alloys with Fe, Ni, and Co." *Journal of the Electrochemical Society* 146(10): 3750.

Turner, J. A. (2004). "Sustainable hydrogen production." *Science* 305(5686): 972-974.

Varambhia, A. M. (2018). *Quantitative structural and compositional studies of catalyst nanoparticles using imaging and spectroscopy in STEM*, University of Oxford.

Wang, D., H. L. Xin, R. Hovden, H. Wang, Y. Yu, D. A. Muller, F. J. DiSalvo and H. D. Abruña (2013). "Structurally ordered intermetallic platinum–cobalt core–shell nanoparticles with enhanced activity and stability as oxygen reduction electrocatalysts." *Nature Materials* 12(1): 81-87.

Yates Jr, J. T. (1995). "Surface chemistry at metallic step defect sites." *Journal of Vacuum Science & Technology A: Vacuum, Surfaces, and Films* 13(3): 1359-1367.

Yu, T., D. Y. Kim, H. Zhang and Y. Xia (2011). "Platinum concave nanocubes with high - index facets and their enhanced activity for oxygen reduction reaction." *Angewandte Chemie* 123(12): 2825-2829.

Yu, X. and S. Ye (2007). "Recent advances in activity and durability enhancement of Pt/C catalytic cathode in PEMFC: Part II: Degradation mechanism and durability enhancement of carbon supported platinum catalyst." *Journal of Power Sources* 172(1): 145-154.

Zhang, J., K. Sasaki, E. Sutter and R. Adzic (2007). "Stabilization of platinum oxygen-reduction electrocatalysts using gold clusters." *Science* 315(5809): 220-222.

Chapter 3

Characterisation techniques

Characterising ORR catalysts such as the Pt-based bimetallic nanoparticles is crucial for the interpretation of their physicochemical properties. The available characterisation techniques can be classified into two main categories.

(1) Bulk averaging techniques, including optical characterisation, X-ray diffraction (XRD), X-ray photon spectroscopy (XPS). The key feature of these techniques is to provide an averaged information of the whole ensemble at a low spatial resolution (for optical characterisation, 1-20 μm; for XPS, ~3 μm; for XRD, ~20 nm). These techniques are normally performed at a fast speed with the analysis time from minutes to hours.

(2) Precise localised techniques, including atom probe tomography (APT), conventional transmission electron microscopy (CTEM), scanning transmission electron microscopy (STEM), energy-dispersive X-ray spectroscopy (EDS) and electron energy loss spectroscopy (EELS). These techniques give much more detailed information of a single or a few nanoparticles at a high spatial resolution of (~1 nm). However, these techniques are quite time-consuming and normally require hours or days to collect the data.

To fully characterise the ORR catalysts, both the statistically averaged information of a whole ensemble and high-resolution localised information of a single nanoparticle are required. In this chapter, the typical characterisation techniques commonly used for the catalysts will be presented, and their advantages and limitations will be compared and discussed.

3.1 Optical characterisation

Optical characterisation techniques mainly make use of inelastic or elastic scattering of light with a particular wavelength, including infrared (IR), Ultraviolet–visible (UV-vis) and Raman spectroscopy. These techniques are on the basis of the interaction between radiation and matter.

Infrared light has a longer wavelength and a lower frequency than visible light. When the incident infrared light with the continuous wavelength irradiates matter, the molecule would absorb the infrared light having a specific frequency if the frequency of the absorbed infrared light matches the vibrational frequency of the molecule. The adsorption is a chemically unique resonant frequency, a molecular fingerprint can be obtained accordingly. This technique has been widely used for the identification of the chemical bonding and functional group in the fields of both organic and inorganic chemistry (Eischens et al., 1954, Mapes and Eischens, 1954, Wachs, 1996).

The UV-vis spectroscopy is an analytical technique that measures the absorption or reflectance ability of matter when irradiated by ultraviolet and visible light. Compared to the infrared light, shorter wavelengths of the ultraviolet and visible light always feature higher energy. The light with a specific amount of energy could be absorbed to

promote electrons from the ground state to the excited state. This excitation energy is highly sensitive to electrons in different bonding environments. Thus, this technique can provide composition and structure information of chemical compounds (Weber, 1995, Ross-Medgaarden and Wachs, 2007).

For the Raman spectroscopy, when a sample is illuminated by a laser beam (monochromatic light), the incident laser photons excite electrons from the vibrational states to virtual states. Subsequently, the excited electrons jump back to the vibrational states and release scattered photons. Rayleigh radiation refers to the radiation where the scattered photons have the same energy as the incident photons. Stokes radiation occurs at lower energy than the Rayleigh radiation, where anti-Stokes radiation has greater energy. The energy shifts of the photons are highly associated with the vibrational state of the molecule. The Raman spectroscopy is a distinct chemical fingerprint for a particular molecule or material (Colthup, 2012, Kumar et al., 2015, Butler et al., 2016).

3.2 X-ray Diffraction (XRD)

X-ray powder diffraction (XRD) is a most popular and non-destructive x-ray characterisation technique. The X-ray is normally generated by the sudden deceleration of fast moving electrons or the synchrotron radiation. Most X-rays have high energy with a wavelength ranging from 0.01 nm to 10 nm. When a powder sample that contains numerous crystals with different orientations is illuminated by the monochromatic X-rays, those incident X-rays are diffracted by regular arrays of atoms into many specific directions, as shown in Figure 3.1. The diffracted X-ray waves add constructively if the diffraction follows the Bragg's law (Bragg, 1929).

$$2d \sin\theta = n\lambda \qquad \textit{Eq. 3.1}$$

Where θ is the incident angle, d indicates the spacing between diffracting planes, n is an integer, and λ represents the wavelength of the incident X-ray. Here, since the distance between atom planes have the same order of magnitude as the X-ray wavelength, XRD could easily provide information about the atomic arrangement of materials. By measuring the diffracted angles and intensities, it is possible to identify crystalline phases and determine structural properties, including lattice parameters, strain and grain size (Patterson, 1939, Thamaphat et al., 2008, Monshi et al., 2012).

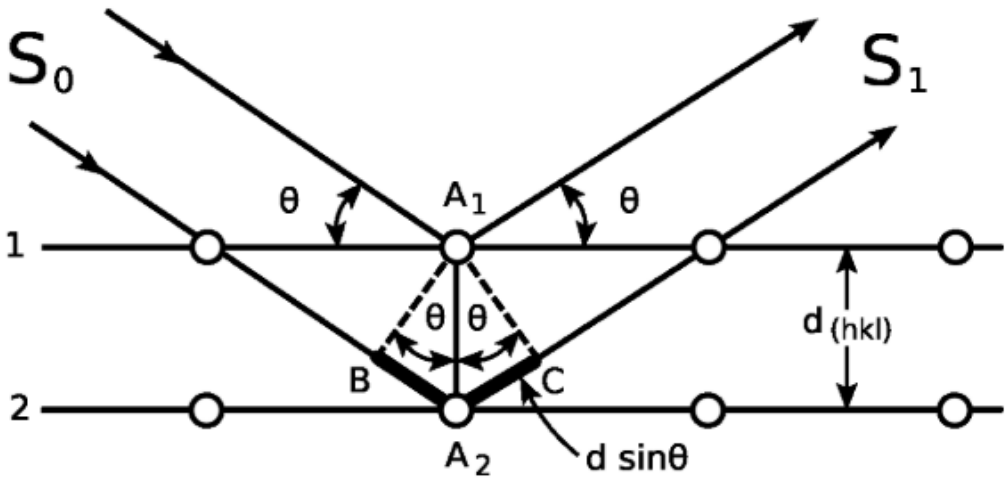

Figure 3.1 Bragg diffraction in a crystal with a d-spaced plane, figure adapted from (https://commons.wikimedia.org).

However, this technique only gives average information about the overall crystallography of the powder sample, and cannot characterise any amorphous materials. Additionally, the relatively large incident X-ray probe size of ~20 nm limits its application in the characterisation of the ORR bimetallic nanoparticles (typically, 3 nm -10 nm).

3.3 X-ray Photoelectron Spectroscopy (XPS)

X-ray Photoelectron Spectroscopy (XPS) is a surface-sensitive technique for analyses of the elemental composition, bonding state and chemical state in the 1 nm – 10 nm depth into the sample surface (Dupin et al., 2000, Yamashita and Hayes, 2008, Biesinger et al., 2011, Ray and Shard, 2011). The XPS technique uses an X-ray beam with high energy (usually Al Kα X-rays with a photon energy of 1468.7 eV) to irradiate a sample. The incident high-energy X-rays would excite and eject electrons out of the sample surface. The XPS spectra can be obtained by measuring the kinetic energy and number of the emitted electrons. The binding energy of each emitted electron which can be determined by subtracting the kinetic energy from the energy of the X-ray photon, relies on the atomic number. Unfortunately, the low spatial resolution (3 μm) of this technique limits its application in the single-nanoparticle analysis.

3.4 Atom Probe Tomography

Atom probe tomography (APT) is an atomic-resolution three-dimensional analytical technique which can also offer chemical composition measurements. The APT technique imposes a high electrostatic field on the sample mounted onto a sharp tip. A pulsed laser is used to induce the evaporation of one or more ions. The evaporated ions then arrive at a Position Sensitive Detector (PSD) to create interpretable patterns. The flight time of the ions can be measured and converted to a mass to charge ratio for chemical composition analysis. The APT technique gains its popularity due to simultaneously obtaining composition and 3D structure information. It has been successfully applied to 3D atomic mapping of ligands on Pd nanoparticles (Kim et al., 2018). However, deposition of the nanoparticles on the sharp tip is difficult and time-consuming (Yang et al., 2015, Kim et al., 2018, Jang et al., 2021).

3.5 Conventional transmission electron microscopy (CTEM)

Direct imaging is always the first choice for looking into the structure, size, shape and even the composition of the catalysts. Transmission electron microscopy (TEM) has been widely used for the high-resolution and localised characterisation of the catalysts, especially the nanoparticles. In TEM, either a broad parallel or a convergent electron beam can be obtained by tuning the strength of a condenser lens system. The sample is illuminated by the incident electrons with an ultra-small wavelength. The electron wavelength (λ) can be calculated using the relativistic equation:

$$\lambda = \frac{h}{\sqrt{2m_0 eV\left(1 + \frac{eV}{2m_0 c^2}\right)}} \qquad \textit{Eq. 3.2}$$

Where h is the Planck's constant, m_0 and e indicate the rest mass and charge of the electron, respectively. V represents the accelerating voltage in the electron microscope, and c is the speed of light in vacuum. For an accelerating voltage of 200 kV, λ = 2.51 pm. Such a small wavelength of the incident electrons enables TEM to easily achieve a resolution below the nanoparticle length scale. TEM techniques can be grouped into three categories, which are conventional transmission electron microscopy (CTEM), scanning transmission electron microscopy (STEM) and analytical electron microscopy (AEM) which further includes energy-dispersive X-ray spectroscopy (EDS) and electron energy loss spectroscopy (EELS).

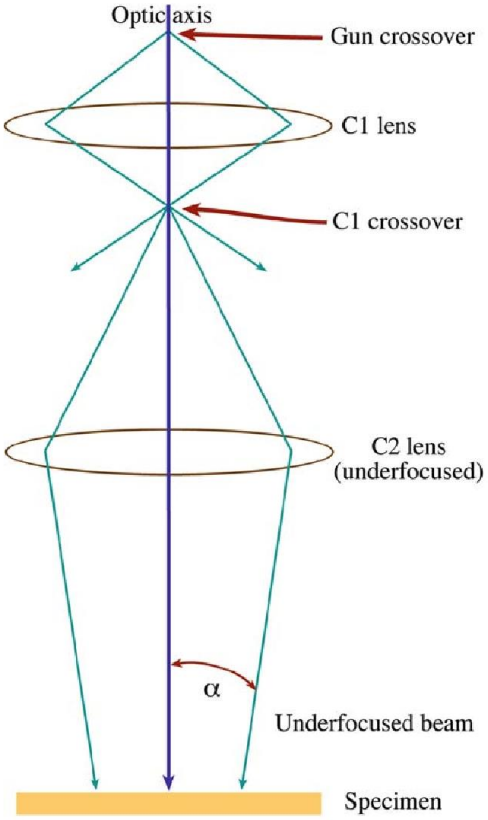

Figure 3.2 The basic principle of parallel-beam operation in the CTEM, using the C1 and underfocused C2 lenses. Figure reprinted from (Williams and Carter, 1996).

CTEM is often operated at the parallel beam mode where condenser lens 1 images the gun crossover in the front-focal plane of condenser lens 2, which then produces a broad parallel beam on the specimen, as shown in Figure 3.2. After the electron beam is transmitted through the specimen, the objective lens disperses the transmitted electrons to create diffraction spots in the back-focal plane, and recombines them to form an image in the image plane. There are two common primary modes central to CTEM operation, which are diffraction mode and imaging mode. Figure 3.3 displays the simplified electron paths and lens settings for the diffraction and imaging mode in CTEM.

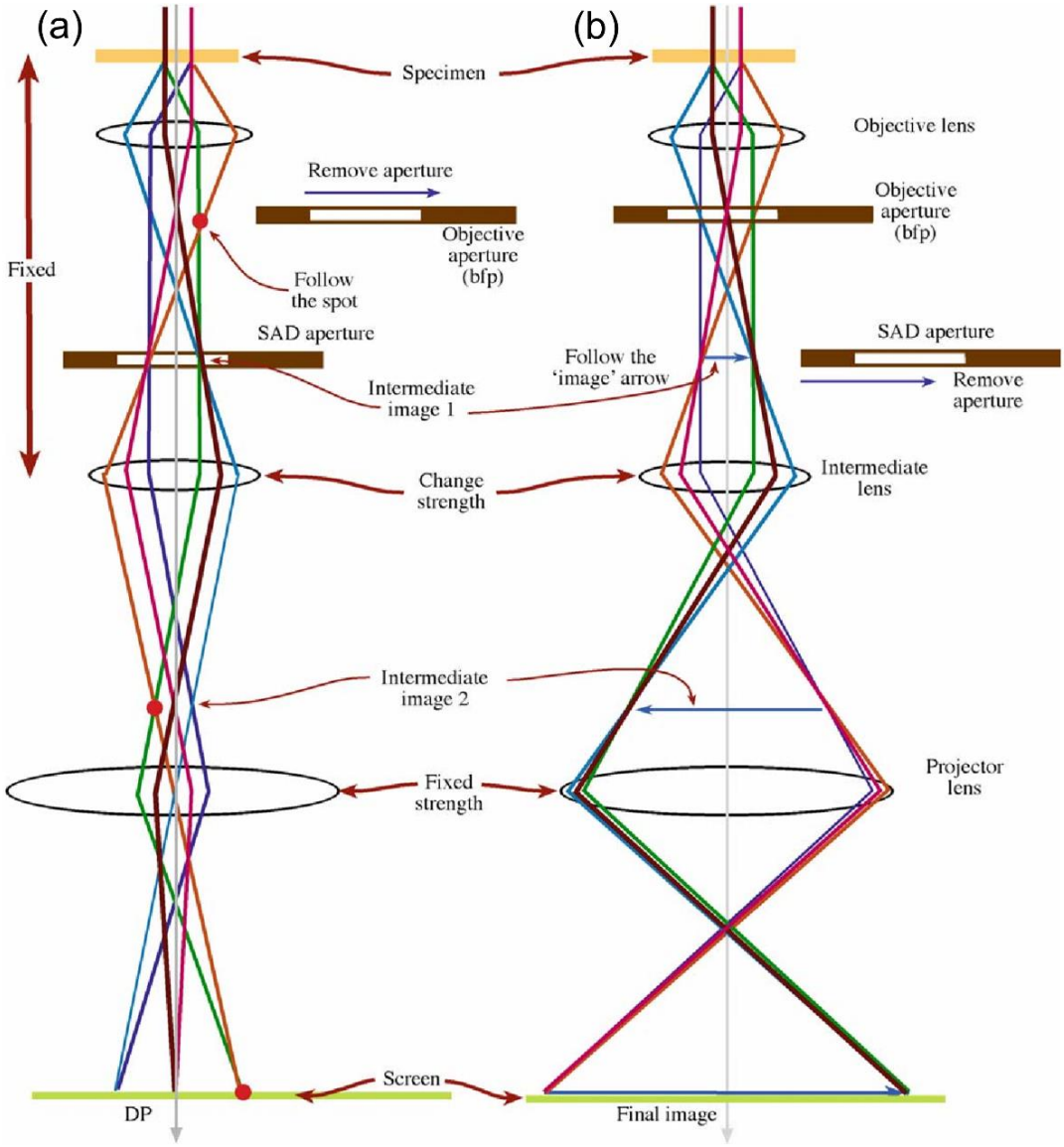

Figure 3.3 The two basic schematics of the CTEM imaging system. A broad parallel electron beam travels through the specimen where most electrons in brown and pink transmission paths are not scattered but others are scattered. The transmitted electrons are then focused in the back-focal plane of an objective lens. The following path involves two operation settings: (a) The diffraction mode. The intermediate lens system projects the diffraction pattern in the back-focal plane of the objective lens onto a viewing screen or a CCD. Here, a SAD aperture can be inserted in the image plane of the objective lens to select a specific specimen region where to obtain the diffraction pattern. (b) The imaging mode. The strength of the intermediate lens system is changed to magnify and project the image plane of the objective lens onto the viewing screen or CCD. Here, the objective aperture can be inserted to select the electrons that contribute to image formation. Figure reprinted from (Williams and Carter, 1996).

3.5.1 CTEM diffraction

In the diffraction mode, the strength of the intermediate lens can be adjusted so that its object plane is the back-focal plane of the objective lens. Subsequently, the projector lens projects the diffraction spots to a charge-coupled device (CCD) camera or a viewing screen. Here, the first thing to note is that the intense direct transmitted beam could saturate and damage the CCD camera. To solve this issue, a needle is often used to block part of the direct beam to reduce the intensity. Additionally, the diffraction pattern that contains the transmitted electrons from the whole illuminated area of the sample is not always useful, especially when analysing a minuscule sub-region of the sample. Fortunately, two strategies can be used to reduce the region of the sample that contributes to the diffraction pattern. (1) Making the electron beam smaller by adjusting the condenser lenses to converge the beam. However, converging the electron beam would destroy the parallelism and broaden the sharply defined diffraction spots into discs in the back-focal plane, forming a convergent beam electron diffraction (CBED) pattern. The CBED pattern contains a wealth of crystallographic information about the specimen since it contains useful contrast effects such as higher-order Laue-zone spots (HOLZ) and lines (Tanaka, 1994). Therefore, CBED is a versatile technique that has been used to determine crystal symmetry, analyse phase transition and measure sample thickness and lattice strain (Yonemura et al., 1998, Hashimoto et al., 2000, Delille et al., 2001, Klinger et al., 2015). (2) Inserting a selected-area aperture. This straightforward method is popular because the incident electron beam still remains parallel. The selected-area aperture is located at the real-space image plane of the objective lens, which is a plane conjugate with the specimen. This operation is generally called selected-area diffraction (SAD) and has been commonly used to

analyse the crystal structure and orientation of a specific sample region (Phillips, 1960, Drits et al., 1997).

3.5.2 CTEM imaging

Switching to the imaging mode is achieved by readjusting the strength of the intermediate lens so that its object plane acts as the image plane of the objective lens. A real image of the object is then projected onto the CCD camera or viewing screen by the projector lens. An objective aperture at the back-focal plane of the objective lens is often used to control the transmitted electrons that contribute to image formation. The diffraction pattern normally consists of a bright central spot and some diffracted spots (or rings). If the direct-beam electrons (the central spot) are chosen by the aperture, the resultant image is called a bright-field (BF) image. If instead the scattered electrons (the specific diffracted spot) are chosen, the corresponding image is called a dark-field (DF) image. Both BF and DF images can be viewed at any magnification by simply adjusting the strength of the intermediate and projector lenses. The objective aperture is crucial to the performance of the CTEM imaging mode. If the objective aperture selects one spot in the diffraction pattern, the resultant image mainly makes use of diffraction contrast. The diffraction and imaging modes of CTEM can provide information about the crystal structure, defects, dislocations and grain size (Williams and Carter, 1996, De Graef, 2003). In particular, DF CTEM can form an image of a particular crystallographic feature.

CTEM at high resolution (HRTEM) has become a powerful tool for characterising the catalysts because it can provide precise positions of atomic columns. HRTEM makes use of the phase contrast by using spherical aberration to cause coherent interference

between transmitted and scattered electron beams. Thus, HRTEM mode often operates without the objective aperture inserted. The coherent nature of HRTEM makes it difficult to derive quantitative information from the image with the phase contrast. However, HRTEM has the ability to analyse the atomic structure, size and shape of an isolated single nanoparticle although it is of low throughput (Snoeck et al., 1998, Hsiung et al., 2011, House et al., 2016).

3.6 Scanning transmission electron microscopy (STEM)

The STEM configuration is formed by adjusting the strength of the condenser lens 2 (in practice, upper objective lens) to focus an electron beam on a sample, as shown in Figure 3.4. In the scanning mode, the convergent electron beam (a probe) parallel to the optical axis is scanned in a raster across the sample using a set of scan coils. A CBED pattern formed in the back-focal plane of the lower objective lens (detector plane in STEM) is then obtained at every scanned point where the probe interacts with the specimen. A set of single channel detectors are imposed on the detector plane to collect the scattered electrons, forming an image for each scanned point. The magnification for all STEM imaging is controlled by the scan dimensions on the specimen. Unlike CTEM, STEM uses detectors to integrate various signals produced by local interaction between the probe and specimen for image formation. To achieve atomic resolution, a probe diameter of ~0.1 nm is commonly used to ensure sufficient sampling. In addition, only the probe aberration needs to be corrected because no post-specimen lenses (intermediate and projector lenses) are required for image formation (Krivanek et al., 2008).

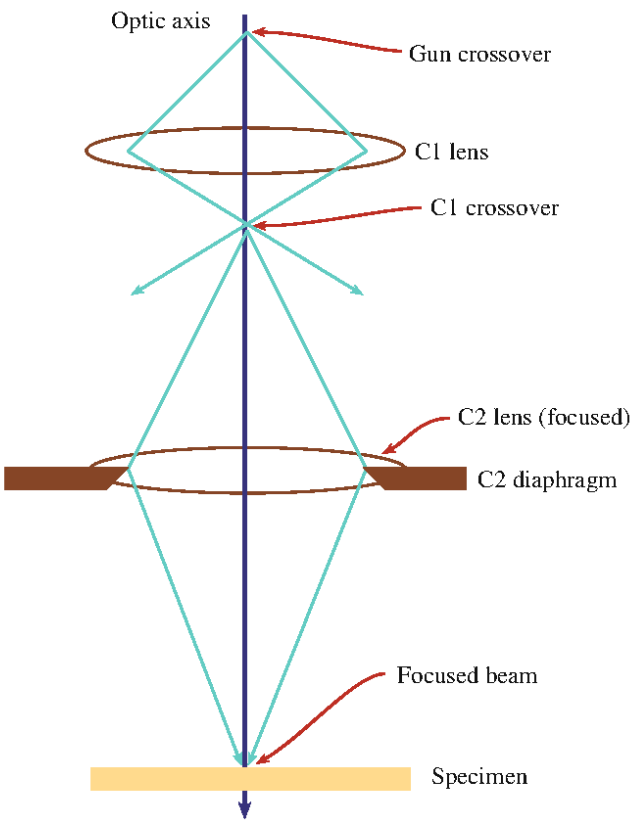

Figure 3.4 The basic principle of convergent-beam operation in the STEM, using the C1 and focused C2 lenses. Figure reprinted from (Williams and Carter, 1996).

A ronchigram is often used for the determination and examination of optical aberrations during STEM experiments (Sawada et al., 2008, Lupini, 2011). When the electron beam is stopped from scanning, the ronchigram can be observed by focusing the convergent probe closely onto an amorphous specimen. Ideally, the ronchigram has an infinite magnification and a uniform intensity as the convergence point of the incident probe is exactly focused onto the specimen. Accordingly, the angular range of the incident probe with no aberrations can be determined by measuring the angular range of the area having a uniform intensity in the ronchigram.

Depending on the signal types measured by the detectors, STEM imaging can be grouped into three categories, bright-field (BF) STEM, annular bright-field (ABF)

STEM and annular dark-field (ADF) STEM. Figure 3.5 shows a simplified diagram of STEM image formation using the different angular range of scattering electrons.

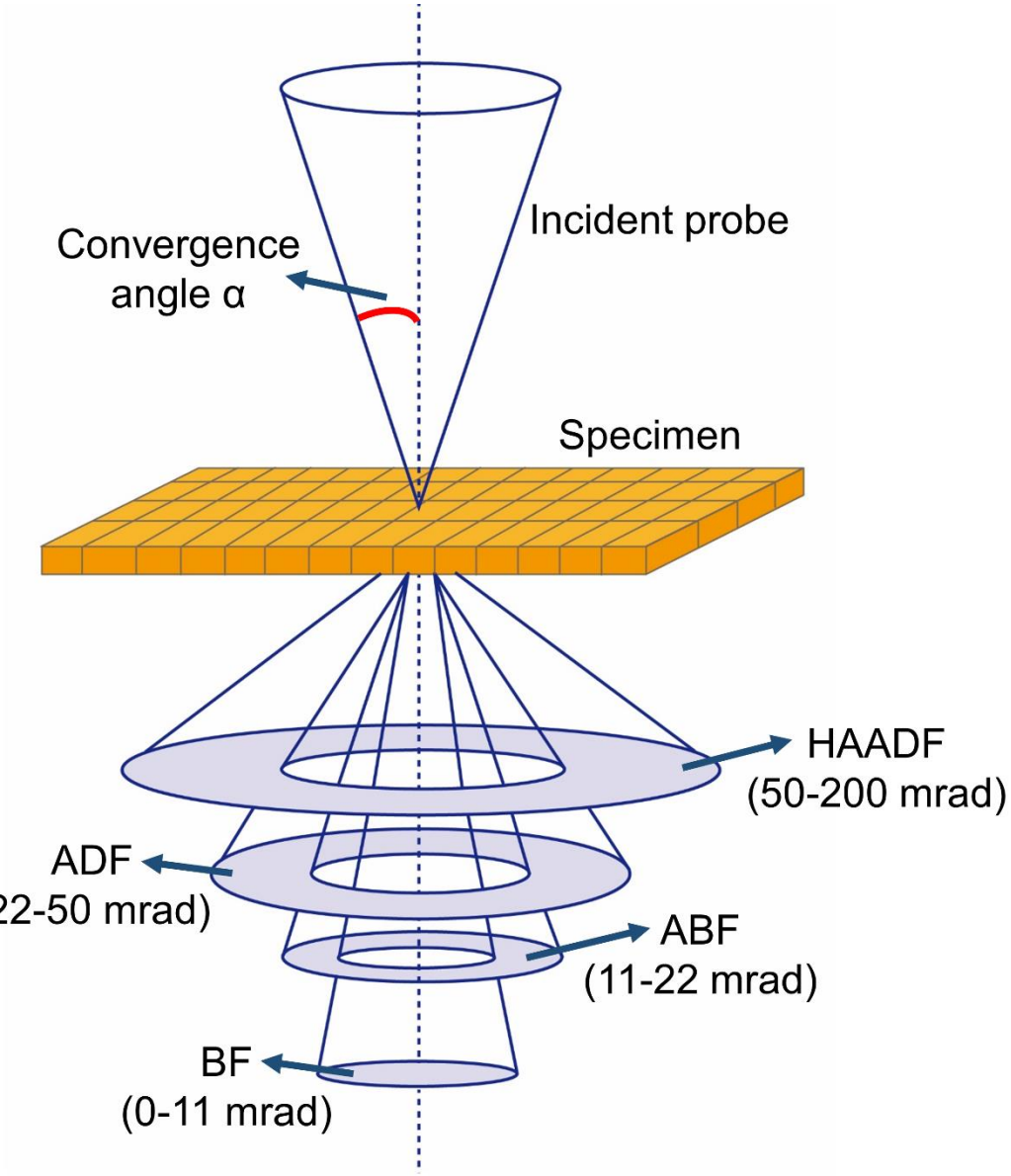

Figure 3.5 The basic schematic of the STEM imaging system. A convergent electron probe is scanned in a raster across the specimen by using a set of scan coils. The incident electrons interact with the specimen at every scanning point. A BF detector intercept the direct beam with the most coherent electrons, while an ABF detector makes use of partially coherent electrons. Incoherent electrons that are normally scattered into high angles are collected by an ADF detector.

3.6.1 Bright-field STEM

In the BF STEM mode, electrons from the central CBED disc are integrated using a small on-axis detector. The reciprocity theorem states that a reverse of beam direction together with a switch between the electron source and detector in the microscope does not affect the electron intensities and beam paths (Pogany and Turner, 1968). Figure 3.6 demonstrates that the geometry of the electron paths for BF STEM appear identical to that for BF CTEM except for the beam direction, which implies that BF STEM is analogous to BF CTEM (Cowley, 1969, Engel, 1974). Therefore, BF STEM also inherits the coherent nature of BF CTEM, which results in difficulties in the quantitative image interpretation.

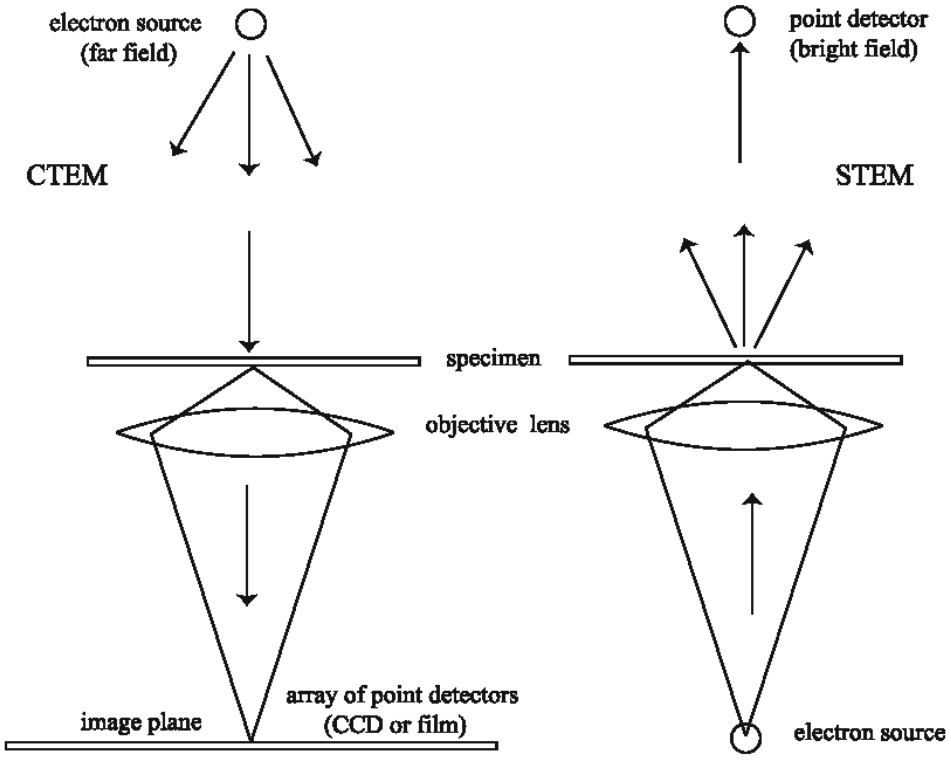

Figure 3.6 The diagram of reciprocity applied to CTEM and STEM. The arrows indicate the direction of electron path, where the electrons travel downward in CTEM (left) and upward in STEM (right). Figure reprinted from (Kirkland, 1998).

3.6.2 Annular bright-field STEM

In the ABF STEM configuration, an annular detector is used to collect both coherent and incoherent signals because it has an inner angle inside the central bright disc and an outer angle equal to the beam convergence angle (Humphreys, 1981). The resultant partially coherent BF image is commonly applied to imaging light elements such as lithium and oxygen amongst heavier elements (Findlay et al., 2009, Findlay et al., 2010). The origin of ABF image formation could come from both the phase contrast and channelling contrast, but is still not fully explained. Although quantitative ABF image interpretations based on image simulations are feasible, determining defocus, sample thickness and aberration conditions significantly complicates the modelling of image formation (Lee et al., 2013).

3.6.3 Annular dark-field STEM

ADF STEM is the most promising and powerful technique for quantitative imaging. Electrons scattered to higher angles, typically larger than the radius of the bright-field disc, are collected by an annular detector to avoid the coherent signals, forming a mostly incoherent dark-field image. Depending on the inner collection angle of the detector, ADF STEM can further be classified into high-angle ADF (HAADF) and low-angle ADF (LAADF). HAADF makes use of the fully incoherent electrons whose scattering angle is three times larger than that of the bright-field disc. HAADF image formation shows Z-contrast where the resultant intensity is highly sensitive to the atomic number and thickness of the sample. The measured scattered intensity of each probe scanning position is Z^n dependent where Z is the atomic number and n is between 1.2 and 1.7 (Nellist and Pennycook, 2000). It is ideal to map heavier elements amongst light elements because of this power law relationship (Z^n). LAADF imaging

collects partially coherent electrons since the inner collection angle of the LAADF detector is slightly larger than the bright-field disc. The image formation relies on not only the Z-contrast but also the diffraction contrast. However, it is possible to have incoherent imaging from coherently scattered electrons through the integration over the detector (Nellist and Pennycook, 2000). Thus, LAADF is often used as a complementary technique to HAADF, for light elements observation (Gonnissen et al., 2014).

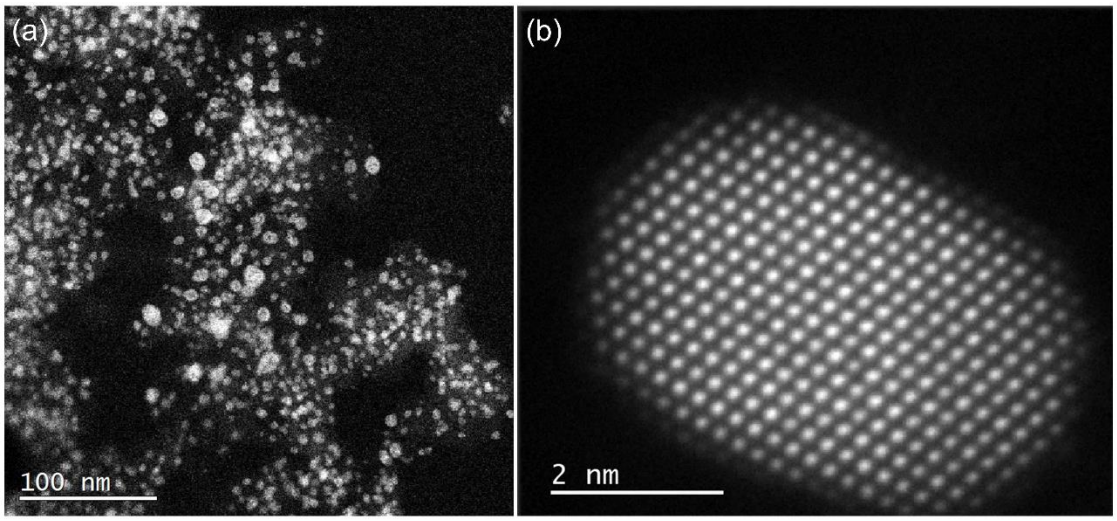

Figure 3.7 (a) A HAADF STEM image of dispersed Pt-Co nanoparticles on the carbon-black support. (b) An atomic resolution HAADF STEM image of an on-zone axis Pt-Co nanoparticle.

In the application of imaging Pt-based catalytic nanoparticles supported by carbon, HAADF STEM is the most prominent characterisation technique (Nellist and Pennycook, 1996), as shown in Figure 3.7. The spatial resolution for STEM imaging is predominately determined by the probe diameter, and can be easily pushed up to sub-angstrom with aberration correctors. STEM imaging can now routinely map atomic columns of the nanoparticles, where the 2D x-y coordinate information of each column can be obtained. Also, the intensities of the HAADF image have been successfully quantified to calculate the number of atoms (atom counting) in each atomic column for pure-element samples (Varambhia et al., 2016, Aarons et al., 2017). Given that the z-

height information of atomic columns can be obtained via tomography or energy minimization (Bals et al., 2011, Jones et al., 2014), it is possible to reconstruct 3D structure of pure-element nanoparticles (Jones et al., 2014). However, for the Pt-based bimetallic nanoparticles, atom counting cannot be achieved by using the HAADF signals alone because the image intensity will rely on both the atomic number and thickness of the sample. To decouple the composition and thickness effects, spectroscopic signals need to be collected together with the HAADF signals. The basic principles of spectroscopic techniques are now discussed.

3.7 Energy-dispersive X-ray spectroscopy (EDS)

EDS spectrometers have been equipped in both CTEM and STEM instruments in order to obtain composition information of the sample during imaging. Whereas, EDS in CTEM can only produce an overall spectrum of a field of view (Tumolva et al., 2010), while EDS in STEM generates a spectrum at each probe scanning position. In other words, EDS in STEM is able to provide localised composition information but EDS in CTEM gives average information (Williams and Carter, 1996). EDS signals arise from inelastic scattering and excitation during the interactions between the probe and sample. When the incident electrons interact with an atom, the incident electron with more than a critical amount of energy ejects an inner-shell electron out of the atom. Consequently, this atom with a void left in the inner shell is promoted into an excited state. An electron from an outer shell of the atom then fills the void and the atom relaxes back to its ground state. During this process, the energy difference between the outer and inner shells is released in the form of an X-ray, as shown in Figure 3.8. These X-rays are collected by EDS detectors surrounding the sample to obtain a spectrum.

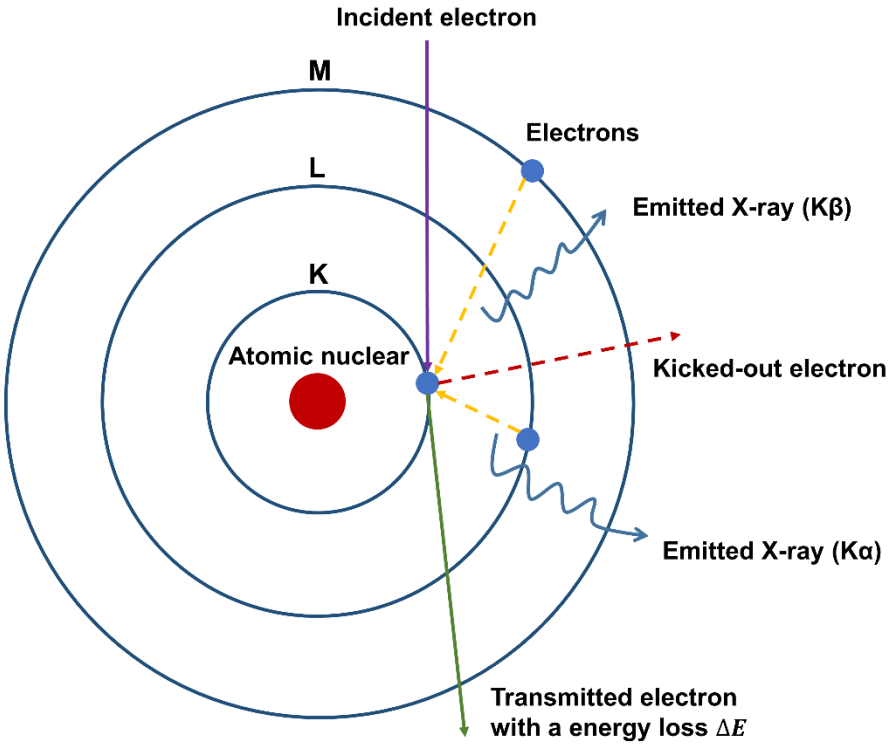

Figure 3.8 Principles of EDS and EELS. An incident electron interacts with the atom, where an ionised electron in the K-shell is emitted. An electron in an outer shell such as L or M shell fills the hole in the K-shell and an X-ray (Kα or Kβ X-ray, respectively) is released. The characteristic X-ray energy or the energy loss (ΔE) of the transmitted electron are measured by the EDS and EELS spectrometers, respectively.

For the signals collection system, either Si or Ge semiconductor is used as an X-ray detector which generates charged pulses proportional to the X-ray energy. The charged pulse is then amplified and identified as a signal which will be assigned to a specific channel in a computer display. Here, only one incoming X-ray photon can be processed by the detector at one time. Each peak intensity in the spectrum is expressed by the number of X-ray photons in a specific energy channel.

The main limitation for EDS is the low X-ray ionisation probability and insufficient collection efficiency of the detector, leading to poor counting statistics when characterising thin specimens such as nanoparticles (MacArthur et al., 2016). However, this can be improved by installing more EDS detectors or increasing beam dwell time.

Increasing beam dwell time could cause irreversible sample damage, such as atom displacements, this will be discussed in detail on Chapter 5. The key advantages for EDS are (1) The spectrum covers almost all elements (carbon and above are detectable). (2) Straightforward and easy data process because of relatively low noise background (compared to EELS). Therefore, EDS in STEM has gained massive popularity in analysing the localised composition variations such as estimating the element ratio and the number of atoms (Shindo and Oikawa, 2013, MacArthur et al., 2016).

3.8 Electron energy loss spectroscopy (EELS)

EELS involves the detection of the energy difference between inelastically scattered and incident electrons. During the interactions of the probe with the sample, an incident electron would lose energy (ΔE) and excite an atom to an excited state, as shown in Figure 3.8. The transmitted electrons then travel through a magnetic prism, and be dispersed as a function of the energy loss (ΔE) in the detection system (Gubbens et al., 2010).

The EELS spectrum is composed of a low-loss region and a core-loss region. The low-loss region covers the energy loss from 0 eV to 50 eV, where the ionization edges normally don't appear. The zero loss peak (ZLP) located at the energy loss of ~ 0 eV contains all the elastically scattered electrons which normally contribute to more than 90% (depends on sample thickness) of the EELS signals. Accordingly, the ZLP can describe the energy spread of the electron source. After the ZLP, the next major peak is the plasmon peak which is basically a longitudinal wave-like oscillation of the free electrons. The low-loss region is dominated by beam interactions with loosely bound valence and conduction bands. Thus, the low-loss region is often used to estimate the

sample thickness, the free-electron density, the band gap and observe interband transitions (Williams and Carter, 1996).

The core-loss portion of the EELS spectrum defined at the energy loss starting from 50 eV consists primarily of ionization edges, which reflects beam interactions with the inner shells of the atom. An ionization edge appears as a sharp jump in intensity superimposed on a uniformly decreasing background intensity (Liu and Brown, 1987). The decaying background intensity is contributed by the plasmon tail (the gradually decaying intensity from the plasmon peak), low energy electron excitations, instrument noise and plural scattering (Fung et al., 2020). Some ionization edges could show strong fine structure oscillations within 30 eV-50 eV of the ionization threshold due to bonding effects, which is called energy-loss near-edge structure (ELNES). The weaker intensity oscillations could also occur within several hundred eV after the edge, which is called extended energy-loss fine structure (EXELFS). EXELFS is introduced by diffraction effects from the surrounding atoms of the ionized atom. Both ELNES and EXELFS have a wealth of detailed information about the sample, such as the elemental oxidation state and bonding environment (Ni et al., 2011, Tan et al., 2012).

Another application for the ionization edges is to give quantitative composition information. The main issue that hampers the quantitative elemental analyses is the removal of the background from the core-loss spectrum. For thin specimens such as nanoparticles, the decaying background exhibits inverse power-law behaviour. Thus, the background can be easily subtracted using a power law fitting algorithm. However, for thicker specimens with a thickness larger than one mean free path (typically 50 nm), the plural scattering needs to be considered when subtracting the background. The

plural scattering also adds some intensities to the ionization edges. To address this issue, three methods for deconvolution and background subtraction are generally used, including the Fourier-Log method, the Fourier-Ratio method and the multiple least-squares fitting (Williams and Carter, 1996, Egerton, 2011).

Apart from obtaining EELS spectra, an energy-filtered image can also be formed by choosing a specific energy range of electrons, which is called energy-filtered TEM (EFTEM) (Leapman, 2017). For example, if all electrons are filtered out except for those from ZLP, the obtained image or diffraction pattern generally exhibit higher resolution and enhanced contrast than the unfiltered one. This is because chromatic aberration and inelastic scattering effects are eliminated.

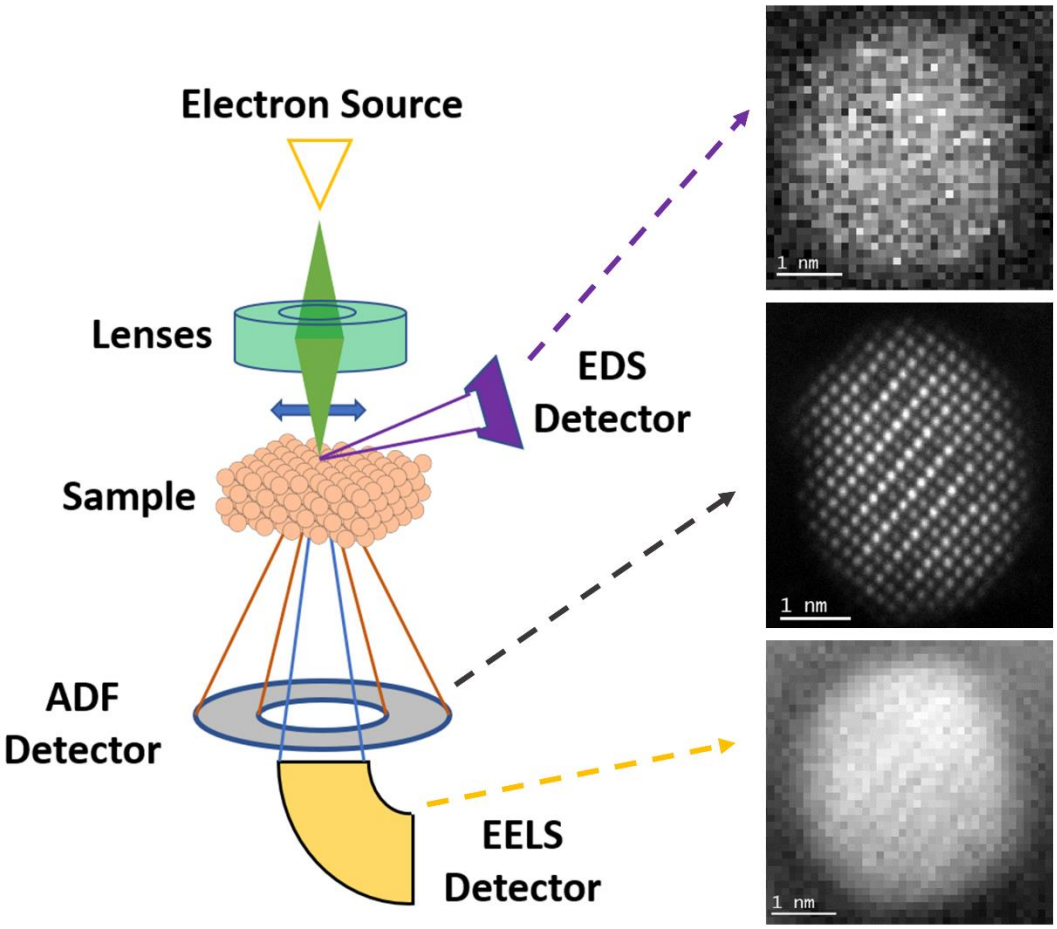

Figure 3.9 (a) The simplified schematic of STEM equipped with spectroscopic detectors. Multiple EDS detectors can be inclined at an angle above the specimen to collect emitted X-rays, while an EELS spectrometer is installed beneath the camera system to collect transmitted electrons. Reprinted from (Varambhia, 2018). (b) The simultaneous ADF, EDS and EELS images acquisition at an atomic scale for a Pt-Co nanoparticle.

Compared to EDS, EELS has a small effective electron-mass interaction volume because the entrance aperture blocks electrons scattered to high angles. Accordingly, EELS is able to provide higher spatial resolution (Williams and Carter, 1996). Furthermore, EELS also features a better energy resolution (~ 1 eV) than EDS (~ 120 eV). However, the ionization edges intensity for EELS decreases to the background level at the energy loss of ~ 2 keV, which makes it difficult to analyse heavier elements. Also, the EELS quantitative analyses are sensitive to sample oxidation, contamination and equipment condition. Therefore, for estimating the number of atoms in the catalytic Pt-based bimetallic nanoparticles, EDS is the preferred characterisation technique, and simultaneous EELS can serve as a complementary technique to verify the accuracy of EDS quantification, as shown in Figure 3.9.

3.9 Conclusions

In this chapter, the typical characterisation techniques for the catalysts which can be grouped into the bulk averaging and precise localised methods are reviewed. The optical characterisation, XRD and XPS generally give average chemical and structural information of the whole ensemble of a sample, while TEM-based techniques are often applied to analysing a precisely localised minuscule region of the sample. A brief comparison between these techniques has been presented. The TEM-based techniques are the most promising method to realize simultaneous structure and composition determination on the bimetallic nanoparticles at atomic resolution.

The basic principles of the TEM-based techniques have been discussed in detail. Both CTEM and STEM could offer structure information of a single nanoparticle at atomic resolution, but quantitatively interpreting CTEM images is much harder than quantifying STEM images. Also, although the spectroscopic signals (EDS and EELS) can be used for composition analyses, EDS and EELS incorporated into CTEM can only give overall composition information of a field of view in the sample. With the advanced hardware and software for the microscope, STEM equipped with EDS and/or EELS where multivariate signals can be collected allows for simultaneous composition and structure analyses at an atomic scale for the nanoparticles.

3.10 References

Aarons, J., L. Jones, A. Varambhia, K. E. MacArthur, D. Ozkaya, M. Sarwar, C.-K. Skylaris and P. D. Nellist (2017). "Predicting the oxygen-binding properties of platinum nanoparticle ensembles by combining high-precision electron microscopy and density functional theory." *Nano Letters* 17(7): 4003-4012.

Bals, S., M. Casavola, M. A. van Huis, S. Van Aert, K. J. Batenburg, G. Van Tendeloo and D. Vanmaekelbergh (2011). "Three-dimensional atomic imaging of colloidal core–shell nanocrystals." *Nano Letters* 11(8): 3420-3424.

Biesinger, M. C., B. P. Payne, A. P. Grosvenor, L. W. Lau, A. R. Gerson and R. S. C. Smart (2011). "Resolving surface chemical states in XPS analysis of first row transition metals, oxides and hydroxides: Cr, Mn, Fe, Co and Ni." *Applied Surface Science* 257(7): 2717-2730.

Bragg, W. L. (1929). "The diffraction of short electromagnetic waves by a crystal." *Scientia* 23(45).

Butler, H. J., L. Ashton, B. Bird, G. Cinque, K. Curtis, J. Dorney, K. Esmonde-White, N. J. Fullwood, B. Gardner and P. L. Martin-Hirsch (2016). "Using Raman spectroscopy to characterize biological materials." *Nature Protocols* 11(4): 664-687.

Colthup, N. (2012). *Introduction to infrared and Raman spectroscopy*, Elsevier.

Cowley, J. M. (1969). "Image contrast in a transmission scanning electron microscope." *Applied Physics Letters* 15(2): 58-59.

De Graef, M. (2003). *Introduction to conventional transmission electron microscopy*, Cambridge University Press.

Delille, D., R. Pantel and E. Van Cappellen (2001). "Crystal thickness and extinction distance determination using energy filtered CBED pattern intensity measurement and dynamical diffraction theory fitting." *Ultramicroscopy* 87(1-2): 5-18.

Drits, V. A., E. Silvester, A. I. Gorshkov and A. Manceau (1997). "Structure of synthetic monoclinic Na-rich birnessite and hexagonal birnessite: I. Results from X-ray diffraction and selected-area electron diffraction." *American Mineralogist* 82(9-10): 946-961.

Dupin, J.-C., D. Gonbeau, P. Vinatier and A. Levasseur (2000). "Systematic XPS studies of metal oxides, hydroxides and peroxides." *Physical Chemistry Chemical Physics* 2(6): 1319-1324.

Egerton, R. F. (2011). *Electron energy-loss spectroscopy in the electron microscope*, Springer Science & Business Media.

Eischens, R., W. Pliskin and S. Francis (1954). "Infrared spectra of chemisorbed carbon monoxide." *The Journal of Chemical Physics* 22(10): 1786-1787.

Engel, A. (1974). "THE PRINCIPLE OF RECIPROCITY AND ITS APPLICATION TO CONVENTIONAL AND SCANNING DARK FIELD ELECTRON MICROSCOPY."

Findlay, S., N. Shibata, H. Sawada, E. Okunishi, Y. Kondo and Y. Ikuhara (2010). "Dynamics of annular bright field imaging in scanning transmission electron microscopy." *Ultramicroscopy* 110(7): 903-923.

Findlay, S., N. Shibata, H. Sawada, E. Okunishi, Y. Kondo, T. Yamamoto and Y. Ikuhara (2009). "Robust atomic resolution imaging of light elements using scanning transmission electron microscopy." *Applied Physics Letters* 95(19): 191913.

Fung, K. L., M. W. Fay, S. M. Collins, D. M. Kepaptsoglou, S. T. Skowron, Q. M. Ramasse and A. N. Khlobystov (2020). "Accurate EELS background subtraction–an adaptable method in MATLAB." *Ultramicroscopy*.

Gonnissen, J., A. De Backer, A. Den Dekker, G. Martinez, A. Rosenauer, J. Sijbers and S. Van Aert (2014). "Optimal experimental design for the detection of light atoms from high-resolution scanning transmission electron microscopy images." *Applied Physics Letters* 105(6): 063116.

Gubbens, A., M. Barfels, C. Trevor, R. Twesten, P. Mooney, P. Thomas, N. Menon, B. Kraus, C. Mao and B. McGinn (2010). "The GIF Quantum, a next generation post-column imaging energy filter." *Ultramicroscopy* 110(8): 962-970.

Hashimoto, T., N. Tsuzuki, A. Kishi, K. Takagi, K. Tsuda, M. Tanaka, K. Oikawa, T. Kamiyama, K. Yoshida and H. Tagawa (2000). "Analysis of crystal structure and phase transition of LaCrO3 by various diffraction measurements." *Solid State Ionics* 132(3-4): 181-188.

House, S. D., C. S. Bonifacio, R. V. Grieshaber, L. Li, Z. Zhang, J. Ciston, E. A. Stach and J. C. Yang (2016). "Statistical analysis of support thickness and particle size effects in HRTEM imaging of metal nanoparticles." *Ultramicroscopy* 169: 22-29.

Hsiung, L., M. Fluss, S. Tumey, J. Kuntz, B. El-Dasher, M. Wall, B. Choi, A. Kimura, F. Willaime and Y. Serruys (2011). "HRTEM study of oxide nanoparticles in K3-ODS ferritic steel developed for radiation tolerance." *Journal of Nuclear Materials* 409(2): 72-79.

Humphreys, C. (1981). "Fundamental concepts of STEM imaging." *Ultramicroscopy* 7(1): 7-12.

Jang, K., S.-H. Kim, H. Jun, C. Jung, J. Yu, S. Lee and P.-P. Choi (2021). "Three-dimensional atomic mapping of ligands on palladium nanoparticles by atom probe tomography." Nature Communications 12(1): 1-10.

Jones, L., K. E. MacArthur, V. T. Fauske, A. T. van Helvoort and P. D. Nellist (2014). "Rapid estimation of catalyst nanoparticle morphology and atomic-coordination by high-resolution Z-contrast electron microscopy." *Nano Letters* 14(11): 6336-6341.

Kirkland, E. J. (1998). *Advanced computing in electron microscopy*, Springer.

Kim, S.-H., P. W. Kang, O. O. Park, J.-B. Seol, J.-P. Ahn, J. Y. Lee and P.-P. Choi (2018). "A new method for mapping the three-dimensional atomic distribution within nanoparticles by atom probe tomography (APT)." Ultramicroscopy 190: 30-38.

Klinger, M., M. Němec, L. Polívka, V. Gärtnerová and A. Jäger (2015). "Automated CBED processing: Sample thickness estimation based on analysis of zone-axis CBED pattern." *Ultramicroscopy* 150: 88-95.

Krivanek, O., G. Corbin, N. Dellby, B. Elston, R. Keyse, M. Murfitt, C. Own, Z. Szilagyi and J. Woodruff (2008). "An electron microscope for the aberration-corrected era." *Ultramicroscopy* 108(3): 179-195.

Kumar, N., B. Stephanidis, R. Zenobi, A. J. Wain and D. Roy (2015). "Nanoscale mapping of catalytic activity using tip-enhanced Raman spectroscopy." *Nanoscale* 7(16): 7133-7137.

Leapman, R. D. (2017). "Application of EELS and EFTEM to the life sciences enabled by the contributions of Ondrej Krivanek." *Ultramicroscopy* 180: 180-187.

Lee, S., Y. Oshima, E. Hosono, H. Zhou and K. Takayanagi (2013). "Reversible contrast in focus series of annular bright field images of a crystalline LiMn2O4 nanowire." *Ultramicroscopy* 125: 43-48.

Liu, D. R. and L. Brown (1987). "Influence of some practical factors on background extrapolation in EELS quantification." *Journal of Microscopy* 147(1): 37-49.

Lupini, A. R. (2011). "The electron ronchigram." *Scanning Transmission Electron Microscopy*: 117-161.

MacArthur, K. E., T. J. Slater, S. J. Haigh, D. Ozkaya, P. D. Nellist and S. Lozano-Perez (2016). "Quantitative energy-dispersive X-ray analysis of catalyst nanoparticles using a partial cross section approach." *Microscopy and Microanalysis* 22(1): 71.

Mapes, J. and R. Eischens (1954). "The infrared spectra of ammonia chemisorbed on cracking catalysts." *The Journal of Physical Chemistry* 58(12): 1059-1062.

Monshi, A., M. R. Foroughi and M. R. Monshi (2012). "Modified Scherrer equation to estimate more accurately nano-crystallite size using XRD." *World Journal of Nano Science and Engineering* 2(3): 154-160.

Nellist, P. and S. Pennycook (2000). "The principles and interpretation of annular dark-field Z-contrast imaging." *Advances in Imaging and Electron Physics* 113: 147-203.

Nellist, P. D. and S. J. Pennycook (1996). "Direct imaging of the atomic configuration of ultradispersed catalysts." *Science* 274(5286): 413-415.

Ni, N., S. Lozano-Perez, J. Sykes and C. Grovenor (2011). "Quantitative EELS analysis of zirconium alloy metal/oxide interfaces." *Ultramicroscopy* 111(2): 123-130.

Patterson, A. (1939). "The Scherrer formula for X-ray particle size determination." *Physical Review* 56(10): 978.

Phillips, R. (1960). "Selected-area diffraction in the electron microscope." *British Journal of Applied Physics* 11(11): 504.

Pogany, A. and P. Turner (1968). "Reciprocity in electron diffraction and microscopy." *Acta Crystallographica Section A: Crystal Physics, Diffraction, Theoretical and General Crystallography* 24(1): 103-109.

Ray, S. and A. G. Shard (2011). "Quantitative analysis of adsorbed proteins by X-ray photoelectron spectroscopy." *Analytical Chemistry* 83(22): 8659-8666.

Ross-Medgaarden, E. I. and I. E. Wachs (2007). "Structural determination of bulk and surface tungsten oxides with UV− vis diffuse reflectance spectroscopy and raman spectroscopy." *The Journal of Physical Chemistry C* 111(41): 15089-15099.

Sawada, H., T. Sannomiya, F. Hosokawa, T. Nakamichi, T. Kaneyama, T. Tomita, Y. Kondo, T. Tanaka, Y. Oshima and Y. Tanishiro (2008). "Measurement method of aberration from Ronchigram by autocorrelation function." *Ultramicroscopy* 108(11): 1467-1475.

Shindo, D. and T. Oikawa (2013). *Analytical electron microscopy for materials science*, Springer Science & Business Media.

Snoeck, E., B. Warot, H. Ardhuin, A. Rocher, M.-J. Casanove, R. Kilaas and M. Hytch (1998). "Quantitative analysis of strain field in thin films from HRTEM micrographs." *Thin Solid Films* 319(1-2): 157-162.

Tan, H., J. Verbeeck, A. Abakumov and G. Van Tendeloo (2012). "Oxidation state and chemical shift investigation in transition metal oxides by EELS." *Ultramicroscopy* 116: 24-33.

Tanaka, M. (1994). "Convergent-beam electron diffraction." *Acta Crystallographica Section A: Foundations of Crystallography* 50(3): 261-286.

Thamaphat, K., P. Limsuwan and B. Ngotawornchai (2008). "Phase characterization of TiO2 powder by XRD and TEM." *Agriculture and Natural Resources* 42(5): 357-361.

Tumolva, L., J.-Y. Park, J.-s. Kim, A. L. Miller, J. C. Chow, J. G. Watson and K. Park (2010). "Morphological and elemental classification of freshly emitted soot particles and atmospheric ultrafine particles using the TEM/EDS." *Aerosol Science and Technology* 44(3): 202-215.

Varambhia, A. M. (2018). *Quantitative structural and compositional studies of catalyst nanoparticles using imaging and spectroscopy in STEM*, University of Oxford.

Varambhia, A. M., L. Jones, A. De Backer, V. T. Fauske, S. Van Aert, D. Ozkaya and P. D. Nellist (2016). "Quantifying a heterogeneous Ru catalyst on carbon black using ADF STEM." *Particle & Particle Systems Characterization* 33(7): 438-444.

Wachs, I. E. (1996). "Raman and IR studies of surface metal oxide species on oxide supports: Supported metal oxide catalysts." *Catalysis Today* 27(3-4): 437-455.

Weber, R. S. (1995). "Effect of local structure on the UV-visible absorption edges of molybdenum oxide clusters and supported molybdenum oxides." *Journal of Catalysis* 151(2): 470-474.

Williams, D. B. and C. B. Carter (1996). *Transmission electron microscopy*, Springer.

Yamashita, T. and P. Hayes (2008). "Analysis of XPS spectra of Fe^{2+} and Fe^{3+} ions in oxide materials." *Applied Surface Science* 254(8): 2441-2449.

Yang, Q., D. Joyce, S. Saranu, G. Hughes, A. Varambhia, M. Moody and P. Bagot (2015). "A combined approach for deposition and characterization of atomically engineered catalyst nanoparticles." *Catalysis, Structure & Reactivity* 1(3): 125-131.

Yonemura, M., K. Sueoka and K. Kamei (1998). "Analysis of local lattice strain around oxygen precipitates in silicon crystals using CBED technique." *Applied Surface Science* 130: 208-213.

Chapter 4

Atomic-scale strain mapping on nanoparticles

Strain is a crucial factor that influences the physicochemical properties of nanoparticles. Being able to precisely measure strain is important in understanding the intrinsic mechanism of the enhanced performance of nanoparticles. Techniques that have been developed for strain analysis using scanning transmission electron microscopy (STEM) images can be categorized into diffraction-based method and imaging-based method. Here, image simulations are used to investigate to what extent the measured two-dimensional (2D) displacements from ADF STEM images can be interpreted as a projection of the actual three-dimensional (3D) displacements. A methodology for deformation analysis is presented which is based on the detection of atomic columns from atomic-resolution STEM images in real space. Elastic deformation parameters such as strain are usually defined on the basis of a continuum of deformation. The appropriateness of various deformation parameters for atomic-scale investigation is explored and a method for determining these is presented. The influence of the choice of reference lattice on strain mapping is studied. Finally, this approach is applied to a $PtCo_3$ bimetallic nanoparticle to quantify its deformation behaviour.

4.1 Introduction

Nanoparticles have been widely used as catalysts in applications including clean energy systems and gaseous pollutant purification due to excellent physicochemical properties compared to their bulk counterparts (Toda et al., 1999, Gasteiger and Marković, 2009,

Heck et al., 2016). Previous work has shown that the enhanced performance of nanoparticles is dependent on structure, morphology, composition, and size (Stamenkovic et al., 2006, Wang et al., 2009, Gan et al., 2013). The finite size, morphology, and lattice mismatch between different elements can induce strain that results in modification of the electronic structure (Solliard and Flueli, 1985, Strasser et al., 2010, Wu et al., 2012, Zhang et al., 2014, Bu et al., 2016, Temmel et al., 2016, Aarons et al., 2017, Pingel et al., 2018). The strain has also been shown to be related to the catalytic activity of nanoparticles through density functional theory (DFT) calculations (Gavartin et al., 2009). As strain is believed to play a significant role in understanding the intrinsic mechanism behind the improved catalytic activity, it needs to be measured precisely (Ellaby et al., 2020).

A number of methods have been developed for deformation mapping with a transmission electron microscope. The methodologies can be classified into two categories: diffraction-based and imaging-based methods. The former method is based on measuring displacements from diffraction patterns in reciprocal space, including convergent-beam electron diffraction (CBED) and nano-beam electron diffraction (NBED). The imaging-based methods quantify the displacement of atomic columns or lattice fringes from high-resolution images in real space. Imaging-based techniques can further be categorized into four different approaches, Geometric Phase Analysis (GPA), Dark Field Electron Holography (DFEH), Peak Pair (PP), and Peak Finding (PF).

The diffraction-based techniques often feature a relatively low spatial resolution (Hÿtch and Minor, 2014), and are presently of widespread use in the semiconductor industry (Cooper et al., 2016). The imaging-based techniques are more promising for atomic

site-specific strain measurements on nanoparticles due to the high spatial resolution (Galindo et al., 2007, Yankovich et al., 2014). However, imaging aberrations and the projection approximation need to be carefully considered when applying the imaging-based techniques. The imaging aberrations refer to imperfect lenses in the electron microscope (Williams and Carter, 1996). The aberration in lenses may lead to precision loss when detecting atomic column positions. For the projection approximation, strain mapping on the STEM images is 2D, but the actual strain distribution within the specimen is 3D and not always uniform along the viewing direction. Because of this limitation any local strain measured via imaging techniques cannot always fully express the real 3D distortion behaviour of the sample (Hÿtch and Minor, 2014). Here, we investigate, to what extent the measured displacements from the ADF STEM images match the in-plane components of the displacement averaged through the thickness.

While characterising the distortion behaviour of materials is of great importance, the deformation parameters quantified within the literature are inconsistent. Material deformation parameters such as strain have usually been defined on a continuum basis (Jones et al., 1977, Hanszen, 1986, Hÿtch et al., 1998, Hÿtch et al., 2003, Naito et al., 2004, Usuda et al., 2005, Galindo et al., 2007, Hÿtch et al., 2008, Toda et al., 2008, Cooper et al., 2011, Diercks et al., 2011, Hÿtch and Minor, 2014, Zuo et al., 2014, Cooper et al., 2016). However, for atomic-resolution images of nanoparticles, material deformation should be defined on the discrete atomic columns. Material distortions have been described using the following deformation parameters: the displacement vector (Bierwolf et al., 1993, Pingel et al., 2018), the local lattice parameter (Goris et al., 2015, Ellaby et al., 2020), some or all of the strain components (Galindo et al., 2007,

Zuo et al., 2014) and occasionally also including the lattice rotation (Hÿtch et al., 1998). The two-dimensional strain tensor consists of two normal strain components and one shear strain component. Rotation of the coordinate axes on which these are defined, for example by applying the Mohr's circle construction, can change the strain components with normal strains converting into shear strains and vice-versa. Rarely in previous work has the full strain tensor been presented. Here, the relevance and usefulness of various elastic displacement parameters is considered in the context of atomic resolution with the aim of identifying a physically meaningful parameter that can be related to other measurements and modelling.

In this chapter, the existing strain analysis techniques using a transmission electron microscope are first reviewed. The validity of the projection approximation is then studied using ADF STEM imaging simulation. To precisely measure the strain field, an algorithm based on locating atomic columns in real space is presented. Our methodology is robust enough to be applied to strain mapping on both nanoparticles and bulk materials with defects, dislocations and interfaces. Next, the materials deformation parameters defined on a 2D primitive cell are compared and the relationship between them is investigated. Differences of strain mapping using different reference lattices are then discussed. In addition, the influence from Poisson noise on strain measurements is studied. Finally, the application of this methodology in the experimental nanoparticles is demonstrated by quantifying the displacement fields, the local lattice parameters, and the strain fields on a $PtCo_3$ bimetallic nanoparticle.

4.2 Brief review of strain mapping techniques

4.2.1 Convergent beam electron diffraction

High order Laue zone (HOLZ) diffraction effects in CBED patterns were first used to determine the lattice parameter (Jones et al., 1977). The CBED pattern on the back focal plane of the objective lens is often in form of a series of large discs. Because of the incident electron probe having a convergence angle of α, the Ewald sphere will intercept a number of reciprocal lattice points in HOLZ. As the result, some dark HOLZ lines are formed in those bright diffracted discs. The CBED approach provides strain profiles by measuring the position shifts of the dark HOLZ lines (Jones et al., 1977, Diercks et al., 2011). As the HOLZ lines usually occur at high scattering angles, this technique is highly sensitive to strain with a measurement precision of 2×10^{-4} (Diercks et al., 2011, Hÿtch and Minor, 2014). However, because of its extreme strain sensitivity, the relaxation of the thin film could result in the splitting of HOLZ lines. This technique also has a spatial resolution of $0.5 - 2$ nm since the convergence angle needs to be sufficiently small to prevent diffracted disc overlap (Hÿtch and Minor, 2014). The application of the CBED technique to nanoparticles for the deformation analysis is still difficult, because HOLZ lines are not detectable in the diffraction patterns on thin samples such as nanoparticles (Hÿtch and Minor, 2014). Also, it fails to provide atomic site-specific strain information.

4.2.2 Nanobeam electron diffraction

The NBED approach makes use of a near-parallel nanometre-sized beam with a convergence angle of less than 0.5 mrad (Toda et al., 2008, Hÿtch and Minor, 2014). The incident narrow beam is scanned across the specimen while a diffraction pattern is recorded at each scanning point. The deformation field at each scanning position can

be determined by comparing the diffraction pattern of each probe position with a reference pattern (Naito et al., 2004, Kim et al., 2014). The spatial resolution of this technique is not high and mainly depends on the size of the electron beam, typically at $5 - 10$ nm, but the better spatial resolution can be achieved by combining higher brightness guns and smaller condenser apertures (Cooper et al., 2016).

Both the CBED and NBED techniques broaden the diffraction spots into discs. Each diffraction disc results from a combination of both single scattering electrons and multiple scattering electrons. Dynamical electron scattering can change the intensity distribution within the diffraction discs (Lubk et al., 2014). The resultant non-uniform intensity in the discs affects the determination of scattering angles. In other words, the scattering angles measured from the diffraction discs do not always correspond to the atom planes that we want to measure (Hÿtch and Minor, 2014). Accordingly, the larger convergence angle used to improve the spatial resolution, the lower precision for strain measurements. Additionally, the precision of this technique ($\sim 10^{-3}$) is also determined by the size of the detector (Armigliato et al., 2008, Hÿtch and Minor, 2014). Overall, its application to nanoparticles is highly limited by its relatively low spatial resolution.

4.2.3 Dark field electron holography

The technique of DFEH was first applied to the deformation analysis on semiconductors by Hÿtch in 2008s (Hÿtch et al., 2008). The DFEH approach tries to overcome the precision limitation by using an electron biprism to interfere the diffracted beams from the region of interest and a reference area (Hÿtch et al., 2008). Particularly, the strained region should be in a similar orientation, thickness and

diffraction conditions as the reference region. The deformation tensor can be calculated by measuring the phase difference from holographic fringes (Hüe et al., 2009, Béché et al., 2011). The spatial resolution of this technique mainly relies on the fringe spacing in the interference pattern, and can reach 1 nm in principle (Cooper et al., 2011). Strain can be measured at a high precision of 2×10^{-4} if lateral averaging is applied (Hüe et al., 2009). DFEH also gains its popularity due to the large field of view, at about 1500 × 500 nm (Hÿtch and Minor, 2014). However, a specimen with both a non-strained and a strained area is required, which is impossible for nanoparticles.

4.2.4 Geometric phase analysis

The GPA method was first proposed and used to map lattice changes across a domain wall (Hÿtch et al., 1998). The idea of this technique is to demodulate the lattice fringes associated with a selected Bragg spot giving a phase map that describes the deformation. The Fourier transform is first performed on a high-resolution electron microscope (HREM) image, after which a strong Bragg reflection is selected by placing a mask. Then, an inverse Fourier transform is performed to obtain a Bragg filtered image (complex image). The Bragg filtered image is the key point of the GPA method and can be described using the following equation:

$$B_g(\boldsymbol{r}) = 2A_g(\boldsymbol{r})\cos\{2\pi \boldsymbol{g}\cdot\boldsymbol{r} + P_g(\boldsymbol{r})\} \qquad \textit{Eq. 4.1}$$

Where $\boldsymbol{r}$ is the position in the real-space image, and $\boldsymbol{g}$ is the periodicity corresponding to the Bragg reflection in the reciprocal space. $A_g(\boldsymbol{r})$ and $P_g(\boldsymbol{r})$ indicate the amplitude and phase of the sets of lattice fringes in the complex image. The phase ($P_g(\boldsymbol{r})$) can describe the regularity of lattice fringes across the complex image, including the spacing and positions (Hÿch and Potez, 1997). For ideal lattice fringes, the phase should have a constant value and is independent of position. A phase image is then

derived from the Bragg filtered image to give a component of the displacement field in the direction of the reciprocal lattice vector ($\boldsymbol{g}$). To describe the two-dimensional displacement field, two Bragg reflections corresponding to a pair of non-collinear reciprocal vectors are masked to produce the phase images, respectively. The strain tensor can be further calculated from the obtained two-dimensional displacement field. Compared to the diffraction methods, the GPA method features a fast processing speed and a good spatial resolution (~ 1 nm) (Hÿtch et al., 1998). This technique has been extensively used in the deformation analysis of materials that contain grain boundaries or defects (Hÿtch et al., 2003, Hÿtch et al., 2006, Sennour et al., 2007), but it fails to give atomic site-specific strain maps.

4.2.5 Peak finding and peak pair methods

To measure strain at atomic resolution, the most promising approaches are PF and PP. Both the PF and PP approaches are based on detecting the intensity maxima of each atomic column directly in real space from the experimental images (Bierwolf et al., 1993, Bayle et al., 1994, Galindo et al., 2007, Galindo et al., 2009). The PF method was first demonstrated to analyse the displacement distribution across material interfaces by Bierwolf in 1993 (Bierwolf et al., 1993). In the PF methodology, a reference grid is extrapolated from what is assumed to be a non-strained area of the sample and cast over the deformed region. The discrete displacement field at each atomic column is calculated to obtain the strain field. Based on the PF method, Galindo proposed the PP method to study the materials interface and dislocations in 2006 (Galindo et al., 2007). In the PP approach, two non-collinear basis vectors are defined using a reference lattice. A pair of peaks at each atomic column are located along the

two basis vector directions. The local strain field is determined by comparing pairs of peaks with reference atom-to-atom bond lengths.

Both the PF and PP approaches gain popularity due to their extremely high spatial resolution down to atomic level and less demanding memory during computation (Bayle et al., 1994, Galindo et al., 2007). The precision of these two methods is determined by the accuracy of peak detection, which further relies on the noise level of the image. In practice, either a Wiener filter or Bragg filter is often used to improve the SNR of the raw experimental image (Galindo et al., 2009). However, both techniques require a non-strained reference area in the field of view, which is not available for nanoparticles. Unlike bulk materials, the deformation can be distributed throughout the whole nanoparticle due to the finite size and domain structure. Also, both methods are sensitive to errors in the formation of a reference lattice and fail to determine the deformation in the edge of nanoparticles.

In this work, strain mapping on nanoparticles is based on detecting the atom column positions in real space from the atomic-resolution STEM images. An algorithm is developed to study the projection approximation for displacements and quantify various deformation parameters on nanoparticles in the following sections.

4.3 Validity of projection approximation for displacements

For atomic-resolution imaging, nanoparticles are viewed along a low-order zone axis in the microscope. The obtained STEM image is generally interpreted as the 2D projection of the 3D sample. The distortion distribution of the nanoparticle is always 3D and is never uniform along the viewing direction. The question then arises of

whether the displacements of atomic columns measured in a 2D image can be interpreted as the components (perpendicular to the beam) of the 3D atomic displacements averaged along the column. The effects of dynamical electron scattering and the resultant channelling of the beam may preclude such a simple interpretation. Here, the influence from the 2D projection approximation on the displacement measurements from the ADF STEM images is investigated.

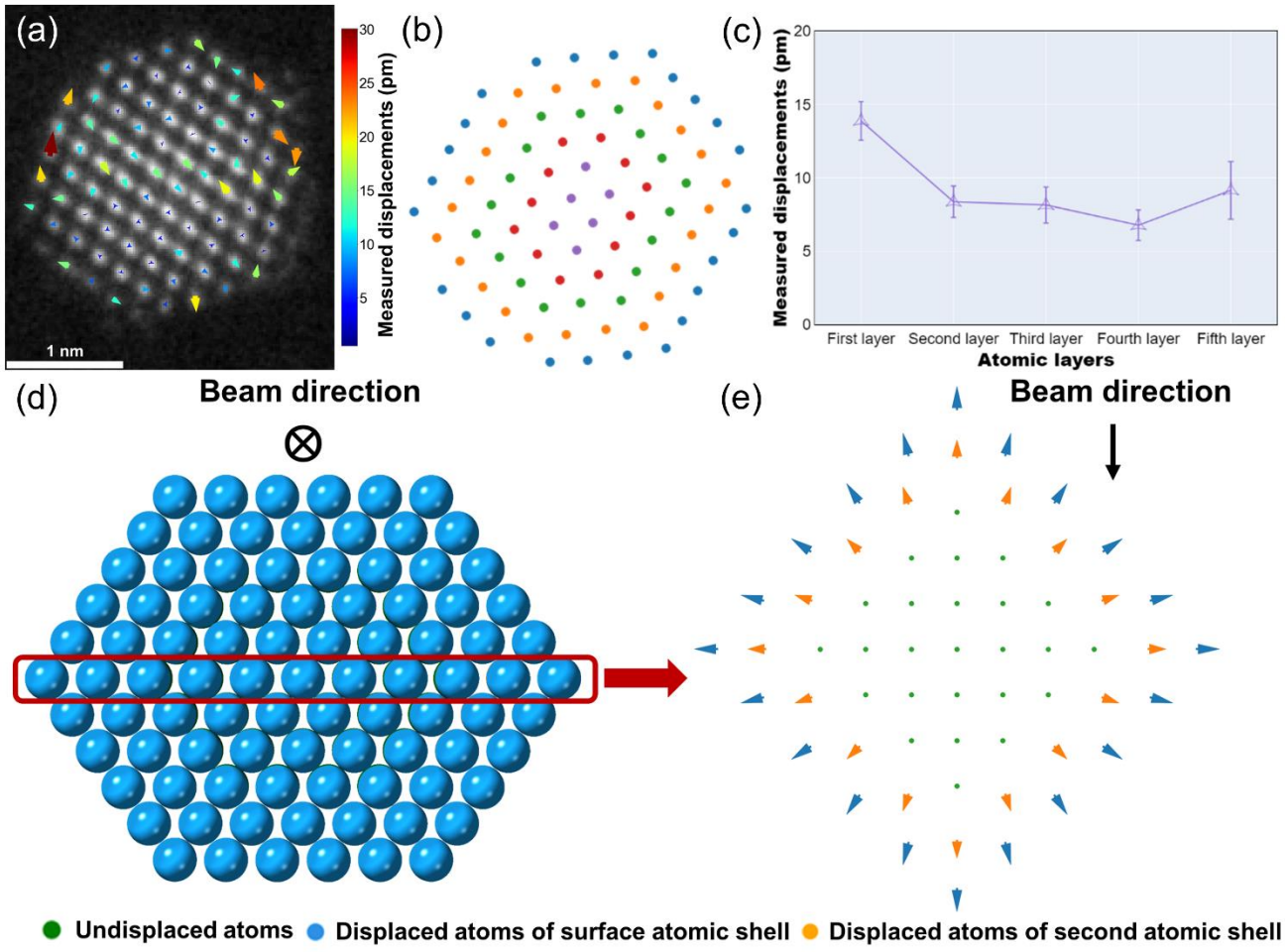

Figure 4.1. (a) The displacement map from an experimental Pt nanoparticle. (b) Atomic columns colour coded with each 2D projected atomic layer. The outermost layer (blue) is the first atomic layer and the core (purple) is the fifth atomic layer. (c) Plot of the average magnitude of the measured displacements as a function of each atomic layer from the experimental image. (d) The perfect cuboctahedra Pt 3D model with the outermost atomic shell coloured blue. This nanoparticle model is aligned along the [110] direction (beam direction). Note that this model is modified from the experimental nanoparticle, and therefore has six layers. (e) The middle atom plane from the nanoparticle model in (d), where atoms in two outer atomic shells are displaced (shown as arrows).

To create a nanoparticle model containing strain, we used a perfect zero-strain cuboctahedron Pt 3D model with a diameter of 2.5 nm and bulk lattice parameter of

0.39231 nm at 280 K (Arblaster, 1997), as shown in Figure 4.1d, and displacements with similar magnitudes to those measured experimentally were artificially added to the perfect 3D model. The experimental displacement measurements were measured from an ADF image of an experimental Pt nanoparticle with a diameter of ~2.5 nm, which is similar to the model, using our proposed methodology described in section 4.4, as shown in Figure 4.1a. The experimental ADF image comes from the previously published work by Aarons, et al.(Aarons et al., 2017). For the 3D nanoparticle model, the atomic shells are defined as a series of one-atom-thick 3D hollow shells, moving from the nanoparticle surface to its centre. The outermost atomic shell is composed of all surface atoms in the 3D nanoparticle model. Each atomic column in Figure 4.1d, which is a projection, could have atoms from different atomic shells of the model. We use the term "atomic layers" as rings of atomic columns in the 2D image of the nanoparticle model projected along the beam direction in Figure 4.1d, starting from the surface and moving in towards the centre. Thus, there are six atomic layers in Figure 4.1d, where the sixth atomic layer only has a centre atomic column. Figure 4.1c displays the measured displacement as a function of the atomic layer of the experimental nanoparticle defined in Figure 4.1b, where the average displacement of atoms in the surface layer is measured to be ~13 pm. To create the strained Pt 3D model, the atoms in the outermost atomic shell of the perfect Pt 3D model are radially displaced relative to their original positions by the same amount (13 pm), while the second outer atomic shell displacement is calculated by linearly scaling the added surface displacement with respect to the shell radius to give a displacement of 10.5 pm. Figure 4.1e shows the middle atom plane of the Pt nanoparticle model along the beam direction. In the selected atom plane, the atoms in the two outer atomic shells have been

displaced (shown as arrows). As the result, atomic columns along the beam direction have a curved shape.

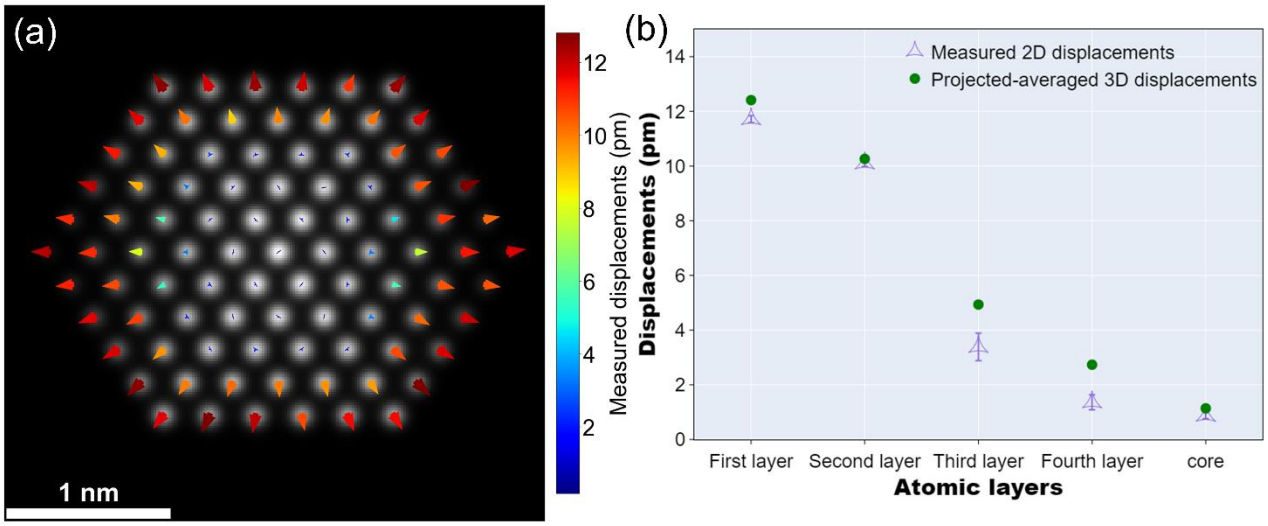

Figure 4.2. (a) The displacement map of the strained Pt model. (b) The average magnitude of the measured displacements as a function of the atomic layer, the error bar is displayed as the standard error of each atomic layer.

The high-resolution ADF STEM images of both the perfect and strained Pt 3D models along [110] direction were simulated using the MULTEM software (Lobato and Van Dyck, 2015). The simulation voltage was set to 200 kV with a source size broadening value of 0.8Å. The probe convergence angle was set as 22.48 mrad whereas the ADF detector collection angles spanned from 72.8 to 271 mrad. The multislice frozen phonon calculation was performed using the Einstein model with 50 phonon configurations and a root mean square (RMS) displacement of 0.06917 Å derived from the Debye-Waller factor of the Pt bulk materials (Gao and Peng, 1999).

A 2D Gaussian function was then fitted to each atomic column in the simulated image of the strained Pt model using the ATOMAP software (Nord et al., 2017), yielding the 2D coordinates. The 3D coordinates of the perfect model without strain are projected along the [110] direction, yielding a 2D reference grid. The displacement map extracted from the strained model was calculated by measuring the distances between the

observed positions of atomic columns and the corresponding reference point positions, as shown in Figure 4.2a. It is clear that the measured displacements are symmetrically distributed and the atoms of the outer two atomic layers are displaced outward from the nanoparticle. The measured 2D displacements from the simulated image were then compared with the averaged-projected real 3D displacements calculated using the coordinates of the 3D strained model, as shown in Figure 4.2b. Here, the atomic core is defined as all the atomic columns in the fifth and sixth atomic layers. Overall, the measured 2D displacements follow the projected-averaged 3D displacements well. For the outer two atomic layers, there is minimal difference between the measured and real 2D displacements. However, for the inner atomic layers, some discrepancies are detected. The maximum difference between the measured and real 2D displacement is within 1.5 pm. This inconsistency comes from the so-called 'channelling effect' (Van Dyck and De Beeck, 1996) where the atoms that are close to being aligned have a disproportionately stronger scattering effect. The well-aligned middle undisplaced atoms (green atoms in Figure 4.1e) have more influence on the atomic column position detection compared to the mis-aligned displaced atoms in the two outer atomic shells. The influence from the 'channelling effect' are reduced as the atomic column gets thicker because the averaged-projected displacement vectors will be smaller as the undisplaced core atoms dominate. We can therefore expect the smaller nanoparticle to have more columns in an image that suffer from the 'channelling effect' than the larger one in terms of the discrepancy between the measured 2D and projected actual 3D displacements, hence the use in the simulation is the nanoparticle with a diameter of 2.5 nm.

In general, the projection approximation for displacement measurements on ADF images is found to be reasonable for nanoparticles. For the nanoparticle simulated here, the maximum error in displacement measurements is found to be 1.5 pm. This is sufficiently small to allow the application of this approach to understand the actual 3D distortion behaviour of the nanoparticle from its 2D strain map.

4.4 Defining and measuring strain at the atomic scale

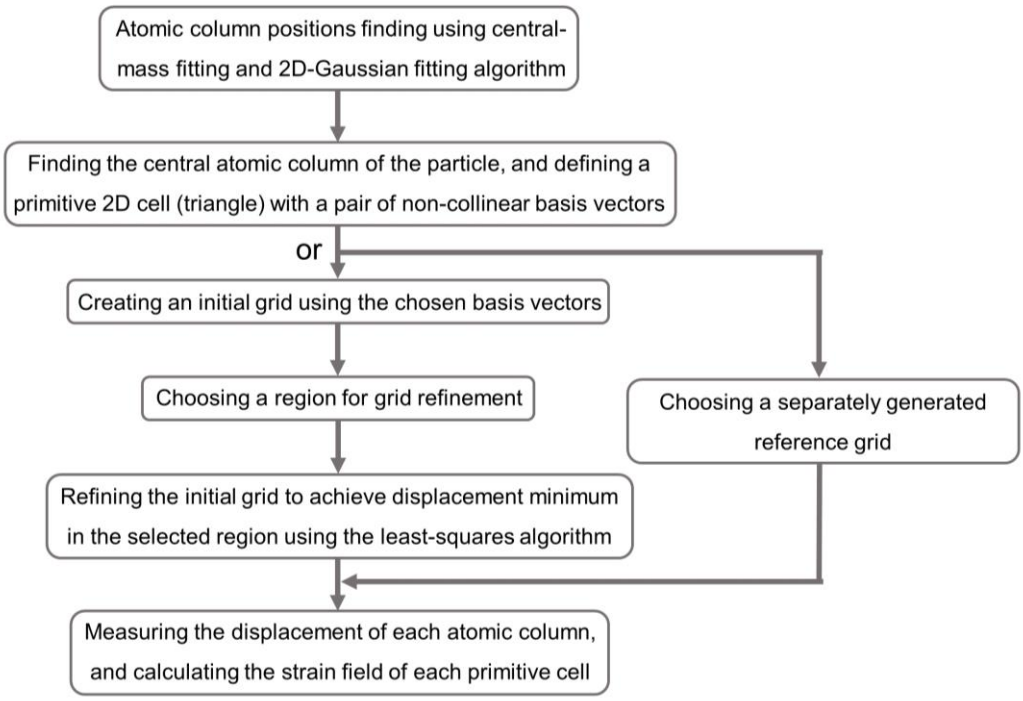

Figure 4.3. Flow diagram of the deformation analysis algorithm.

The overall proposed methodology for nanoparticle strain analysis is based on the detection of atomic columns in the atomic-resolution images, similar to the PF and PP approaches. Figure 4.3 shows an outline of the methodology used in this work. For STEM image acquisitions, the multi-frame imaging technique is used to reduce the influence of scan instabilities and drift (Jones et al., 2017). The acquired experimental atomic-resolution ADF image frames of an on-axis nanoparticle are aligned using non-

rigid registration method and averaged to obtain a zero-drift ADF image (Jones et al., 2015). The following step is to locate the positions of all the atomic columns that are of interest in the aligned ADF image. The initial positions are detected using the peak finding algorithm implemented in the ATOMAP Python library, where the relative intensity threshold and the smallest peak separation are taken as inputs. The initial positions are further refined first by finding the centre of mass and then by fitting 2D Gaussian peaks to atomic columns. This allows us to precisely determine the 2D coordinates of the atomic column positions.

Next, the centre atomic column and its nearest neighbouring columns are found to determine a primitive 2D cell (a parallelogram) defined by two non-collinear basis vectors (a and b). Let us consider FCC crystal structure down a [110] projection, as shown in Figure 4.4b The centre atomic column and its six neighbouring columns form six triangles, and each of them can be used to define the two basis vectors.

The following step is the selection of a reference grid. The reference grid can be a separately generated reference grid such as from a bulk material with known lattice constants, or generated from a region of the nanoparticle. The differences of using the different reference grids for strain mapping will be compared and discussed in the following section. To create a reference grid from the nanoparticle, an initial reference grid is first generated using the initial basis vectors. The next step is to choose a region to refine the initial reference grid. The selected region can be either the whole particle or a part of the particle. Then, the initial grid is contracted, expanded, rotated, and offset to achieve the displacement minimum in the selected region using a least-squares fitting

algorithm. The reference basis vectors and the reference triangles are extracted from the refined reference grid.

On the basis of having the atomic column positions and the reference grid, all the observed triangles and the reference triangles in the region of interest are searched. Subsequently, the displacement vector of each atomic column is measured. The local differential displacement and the strain tensor of each triangle unit are extracted from the displacement field.

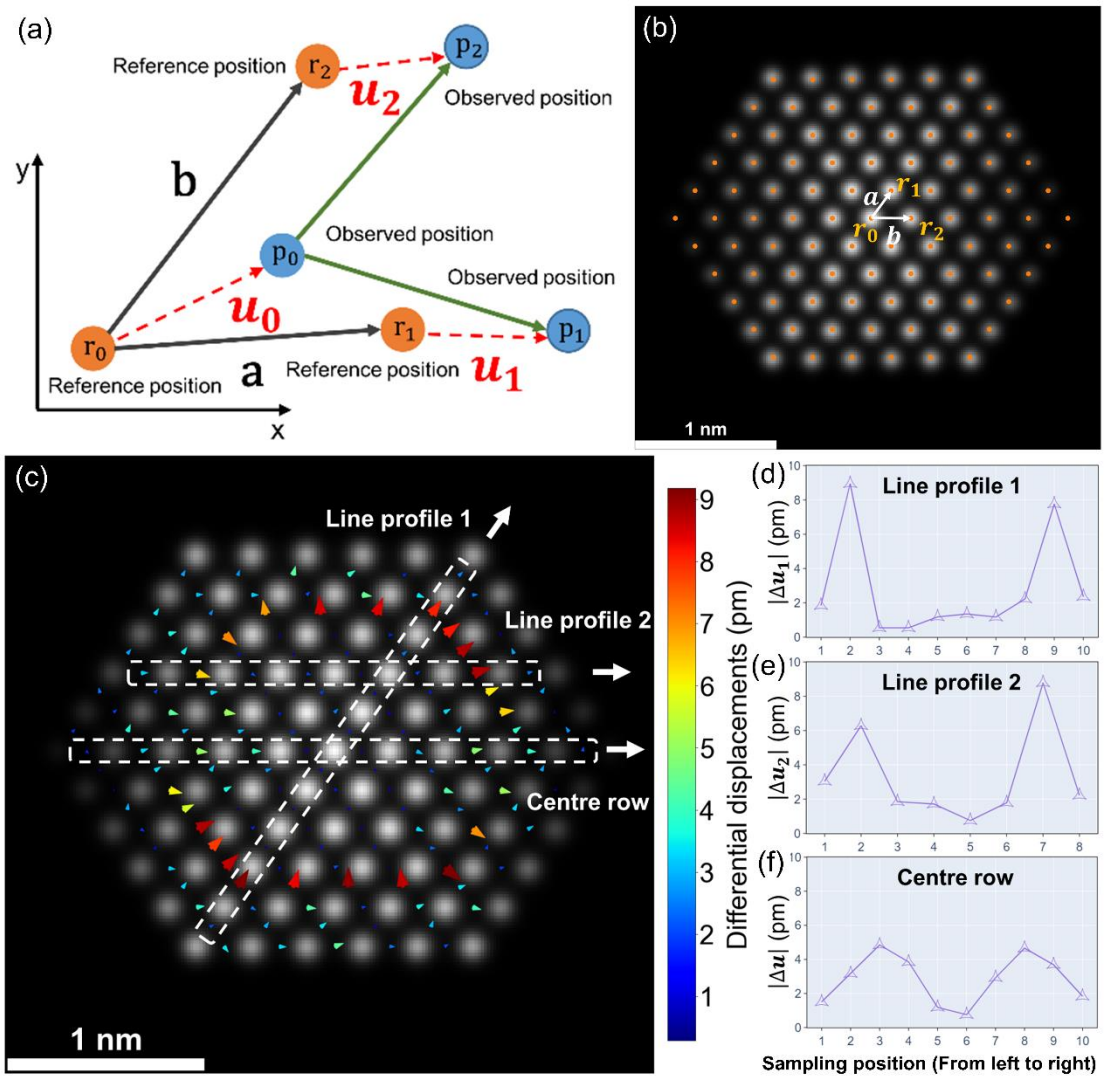

Figure 4.4. (a) Diagram of the definition of the local displacement vectors. (b) The reference primitive unit of the strained Pt model. (c) The differential displacement map of the strained Pt model. (d-f) The selected line profiles in (c) of the differential displacements $|\Delta \boldsymbol{u_1}|$, $|\Delta \boldsymbol{u_2}|$ and $|\Delta \boldsymbol{u}|$ (pm).

Materials deformation parameters such as elastic strain are often associated with continuum elasticity. When dealing with nanoparticles where the discrete atomic nature becomes important, it is important to consider which deformation parameters are appropriate. In order to investigate this, the following deformation descriptors were calculated on the simulated image of the strained Pt model. The reference grid is still the projection along the [110] direction of the perfect Pt model without strain. We start with the local displacement vector u_i that is associated with each atomic column in the image. The displacement vector is defined by the position offset of each observed atomic column with respect to the closest reference point, as shown in Figure 4.4a. If we consider a triangle formed from the primitive basis vectors in the projected 2D lattice, we can define the differential displacement field, the strain field, the fractional area expansion and the local lattice parameter. The non-collinear basis vectors ($a = (a_x, a_y)$ and $b = (b_x, b_y)$) and the 2D primitive triangle ($r_0 r_1 r_2$) of the reference grid are defined in Figure 4.4b.

The differential displacement field Δu is first introduced by the following equations:

$$\Delta u_1 = u_1 - u_0$$
$$\Delta u_2 = u_2 - u_0 \qquad \textit{Eq. 4.2}$$

Where u_0, u_1 and u_2 are the displacement vectors of the atomic columns in each triangle and can be calculated using the position offsets between the observed and reference atomic columns. The differential displacement field is composed of vectors calculated between two nearest neighbour atomic columns along the two basis vectors. The two measured differential displacement vectors can be shown at the centre of each of the two basis vectors, respectively, as shown in Figure 4.4c. Unlike the displacement measurements where a zero-displacement region is required to fix the reference grid,

the differential displacement measurements are robust to rigid-body shifts of the reference grid (the reference grid does not deform or change shape during the shifting). Previous work has used the differential displacement maps to study atomic-scale deformation associated with dislocations (Vitek et al., 1970, Clouet, 2020). If the measured differential displacement vectors (Δu_1 and Δu_2) are parallel to the basis vectors (a and b), this indicates tensile strain. If the differential displacement vectors are antiparallel to the basis vectors, it indicates compressive strain. Shear strain exists when a differential displacement vector is perpendicular to its associated basis vector. Figure 4.4d and e display the selected line profiles of the magnitude of the two differential displacement vectors. The selected atomic rows are along the directions of two basis vectors, respectively. Here, it can be seen that unlike the displacement distribution in Figure 4.2a where the outermost layer has the largest displacement, the measured differential displacements peak between the second and third atomic layer. The main reason is that although the atoms in the surface atomic layer are displaced by 13 pm, the distance between the surface and second atomic layer only increases by 2.55 pm since the second atomic layer also moves outward the nanoparticle by 10.45 pm. However, in the centre row, the largest measured differential displacements are located between the third and fourth atomic layer, as shown in Figure 4.4f. This is because the atomic column in the third atomic layer of the centre row only has 5 atoms, and four of them are the displaced atoms belonging to the two outer atomic shells due to the projection effect, as shown in Figure 4.1e. As the result, this atomic column itself has a larger displacement compared to the other atomic column in the third atomic layer.

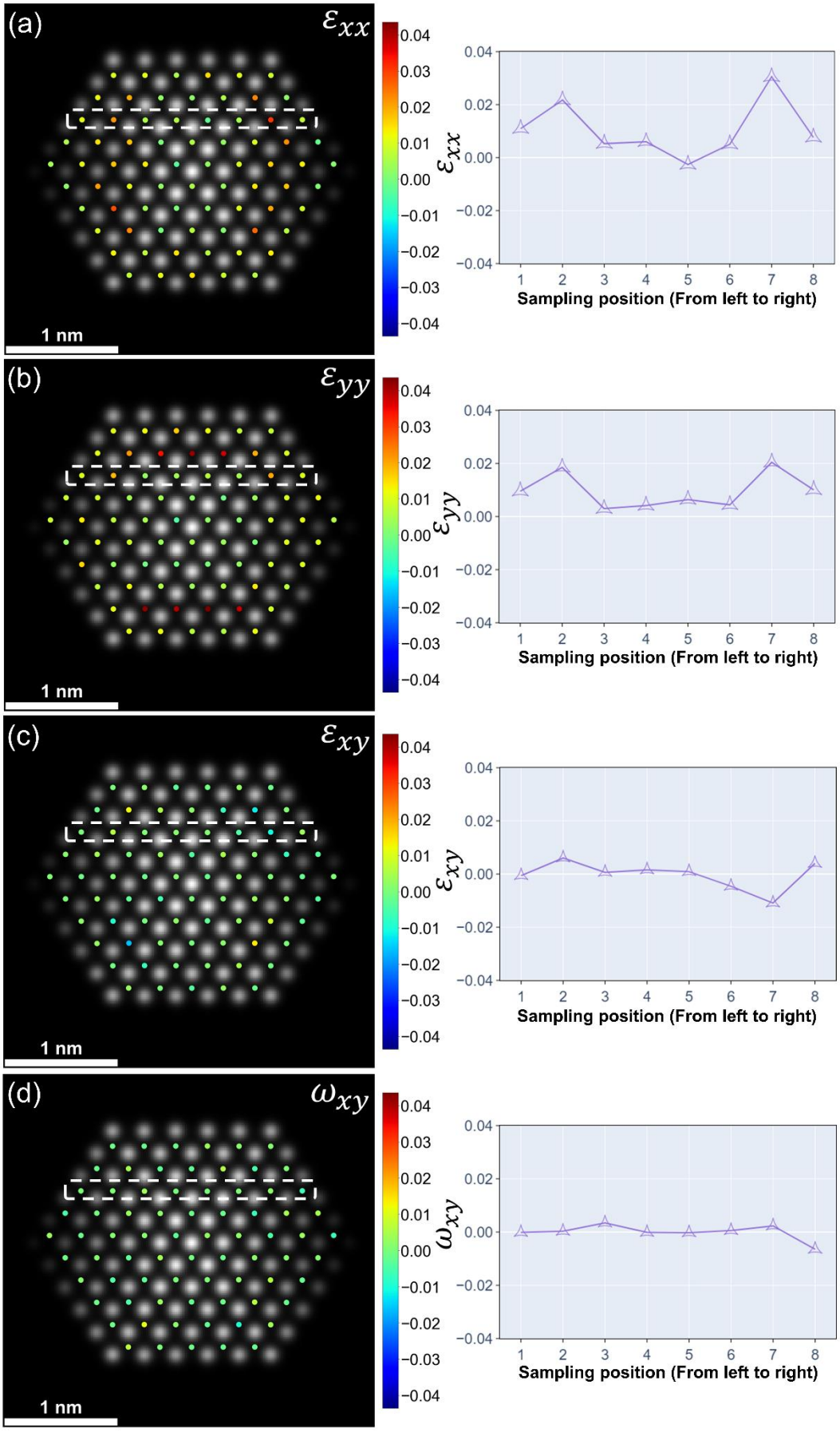
(a)
ε_{xx}
1 nm
0.04
0.03
0.02
0.01
0.00
−0.01
−0.02
−0.03
−0.04
ε_{xx}
Sampling position (From left to right)
(b)
ε_{yy}
1 nm
ε_{yy}
Sampling position (From left to right)
(c)
ε_{xy}
1 nm
ε_{xy}
Sampling position (From left to right)
(d)
ω_{xy}
1 nm
ω_{xy}
Sampling position (From left to right)

Figure 4.5. The ε_{xx}, ε_{yy}, ε_{xy}, ω_{xy} maps and the corresponding line profiles of the strained Pt model.

Based on the displacement field of the primitive triangle, we can have (Galindo et al., 2007):

$$\begin{aligned} \Delta u_{1x} &= a_x \varepsilon_{xx} + a_y \mathrm{e_{xy}} \\ \Delta u_{1y} &= a_y \varepsilon_{yy} + a_x \mathrm{e_{yx}} \\ \Delta u_{2x} &= b_x \varepsilon_{xx} + b_y \mathrm{e_{xy}} \\ \Delta u_{2y} &= b_y \varepsilon_{yy} + b_x \mathrm{e_{yx}} \end{aligned} \qquad \textit{Eq. 4.3}$$

Where ε_{xx} and ε_{yy} are normal strains; $\mathrm{e_{xy}}$ and $\mathrm{e_{yx}}$ are intermediate variables; a_x, a_y, b_x and b_y are the *x* and *y* components of the basis vectors a and b respectively. Shear strain (ε_{xy}) and lattice rotation (ω_{xy}) are defined as follows:

$$\begin{aligned} \varepsilon_{xy} &= \frac{1}{2}\left(\mathrm{e_{xy}} + \mathrm{e_{yx}}\right) \\ \omega_{xy} &= \frac{1}{2}\left(\mathrm{e_{xy}} - \mathrm{e_{yx}}\right) \end{aligned} \qquad \textit{Eq. 4.4}$$

Because the differential displacement field in Eq. 4.3 can be written as a matrix multiplication, the expression can be inverted to give:

$$\begin{bmatrix} \varepsilon_{xx} & \mathrm{e_{xy}} \\ \mathrm{e_{yx}} & \varepsilon_{yy} \end{bmatrix} = \begin{bmatrix} \Delta u_{1x} & \Delta u_{2x} \\ \Delta u_{1y} & \Delta u_{2y} \end{bmatrix} \begin{bmatrix} a_x & b_x \\ a_y & b_y \end{bmatrix}^{-1} \qquad \textit{Eq. 4.5}$$

Thus, the strain tensor for each primitive triangle is calculated using the differential displacement field and the reference basis vectors. Figure 4.5 shows the measured strain maps alongside the selected line profiles of the strained Pt model. The first thing we can find is that the measured normal strains (ε_{xx} and ε_{yy}) peak between the second and third atomic layer. The reason has been explained in the differential displacement analysis. It indicates that unlike the displacement map in Figure 4.2, strain mapping and differential displacement mapping provide the local distortion information of the materials. The shear strain (ε_{xy}) and rotation (ω_{xy}) are smaller than the two normal

strains, as might be expected from this simple dilation model. It can also be seen that the line profiles of the strain components are not perfectly symmetric. This is because unlike the radial displacements whose symmetric centre is the centre atom of the nanoparticle, use of the consistent basis vectors used for the strain calculation means that the two basis vectors do not represent symmetrically equivalent sides of the symmetrically related primitive triangles. Importantly, it can be seen that ε_{xx} mainly exists at the left and right sides of the strained nanoparticle, while ε_{yy} is mainly located at the top and bottom of the strained nanoparticle. This indicates that the two normal strain maps (ε_{xx} and ε_{yy}) can visualize the distortion behaviour of the materials along *x* and *y* directions but do not provide an overall measure of local deformation.

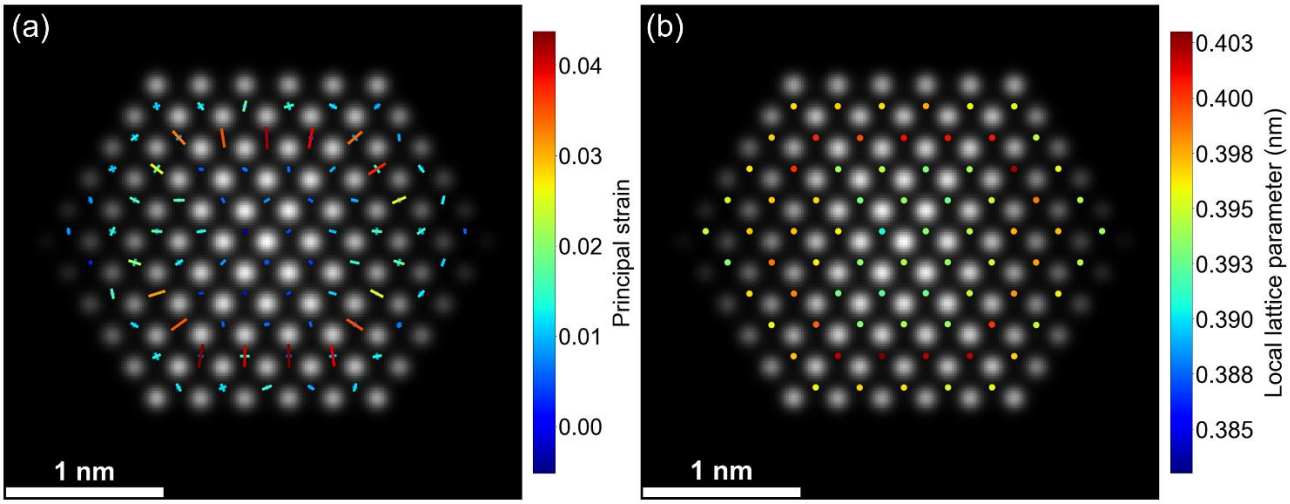

Figure 4.6. The principle strain and local lattice parameter maps of the strained Pt model

The principal strains (ε_{max} and ε_{min}) are the maximum and minimum normal strains using a specific axis orientation where the shear strain is zero. They can be calculated for each of the primitive triangles using the strain tensor components (ε_{xx}, ε_{yy} and ε_{xy}) using the following equations:

$$\varepsilon_{max} = \frac{1}{2}(\varepsilon_{xx} + \varepsilon_{yy}) + \sqrt{[\frac{1}{2}(\varepsilon_{xx} - \varepsilon_{yy})]^2 + \varepsilon_{xy}^2} \qquad \textit{Eq. 4.6}$$

$$\varepsilon_{min} = \frac{1}{2}(\varepsilon_{xx} + \varepsilon_{yy}) - \sqrt{[\frac{1}{2}(\varepsilon_{xx} - \varepsilon_{yy})]^2 + \varepsilon_{xy}^2} \qquad \textit{Eq. 4.7}$$

The orientation of the principal strain can be calculated by:

$$\tan 2\theta_p = \frac{2\varepsilon_{xy}}{\varepsilon_{xx} - \varepsilon_{yy}} \qquad \textit{Eq. 4.8}$$

Where θ_p is the angle between the maximum principal strain and x axis. This equation gives two values of θ_p which are 90˚ apart, indicating that the two principal strain components are perpendicular to each other. Figure 4.6a displays the principal strain map extracted from the normal and shear strain maps. The measured principal strains not only well-express the magnitude and orientation of the local strain configuration, but also are robust to both rigid-body shifts and rotations of the reference grid. In Figure 4.6a it demonstrates that the largest maximum principal strain is located between the second and third outer atomic layers, and is oriented outward the nanoparticle. The principle strain map carries the same information as that expressed by the conventional strain tensor components seen in Figure 4.5, but provides a more intuitive view of the strain in the nanoparticle. Note is that the measured principal strain between the first and second outer atomic layer is randomly oriented. This is because the measured ε_{xx} and ε_{yy} which are used for the orientation (θ_p) calculation in this region are small and close to each other, and therefore the orientation calculation is easily influenced by random displacements from the frozen phonon model used in the simulation.

In addition, the area change of each observed triangle with respect to the reference standard triangle can also be used to describe the distortion behaviour. The area of the reference triangle (S) can be computed by the following equation:

$$S = \frac{1}{2} \times a \times b \times \sin(\theta) \qquad \textit{Eq. 4.9}$$

Where a and b are the length of two sides of the triangle, θ is the included angle. Assuming that the reference and observed triangles have the same θ because the shear strain (ε_{xy}) is negligible, a differential can be applied to Eq. 4.9, to arrive at:

$$\frac{dS}{S} = \frac{da}{a} + \frac{db}{b} = \varepsilon_{xx} + \varepsilon_{yy} \qquad \textit{Eq. 4.10}$$

It can be clearly seen that the fractional area expansion ($\frac{dS}{S}$) and $\varepsilon_{xx} + \varepsilon_{yy}$ are equivalent. Similarly, the average fractional local lattice parameter change ($\frac{dl}{l}$) can be defined as:

$$\frac{dl}{l} = \frac{1}{2}\left(\frac{da}{a} + \frac{db}{b}\right) \qquad \textit{Eq. 4.11}$$

where l is the reference lattice parameter. Combining Eq. 4.10 and Eq. 4.11, this gives:

$$\frac{dl}{l} = \frac{1}{2}(\varepsilon_{xx} + \varepsilon_{yy}) \qquad \textit{Eq. 4.12}$$

We now can write the local lattice parameter (l_{loc}) of each observed triangle as:

$$l_{loc} = l \times \left(\frac{1}{2}\left(\varepsilon_{xx} + \varepsilon_{yy}\right) + 1\right) \qquad \textit{Eq. 4.13}$$

At this point, the distortion descriptors based on either the atomic column or the distortion triangle are successfully defined. The differential displacement components (Δu_1 and Δu_2) are the differential of the distortion along the two pre-defined basis vectors. The normal strains (ε_{xx} and ε_{yy}) can tell us about local compressive or tensile strain, along with the shear strain (ε_{xy}) and local lattice rotation (ω_{xy}), but are more intuitively expressed through the principal strains. The fractional area expansion, the

sum of two normal strain components ($\varepsilon_{xx} + \varepsilon_{yy}$), the local lattice parameter (l_{loc}) and the average fractional local lattice parameter change ($\frac{dl}{l}$) tell us equivalent information for the distortion analysis on materials. It is important to note that the absolute values of the strain tensor components depend on the reference grid and its orientation. Rotation of the basis vectors can transform normal strains into shear strains and vice-versa. The principal strain is, however, independent of the rotation of the reference axes. It also describes the maximum normal strain that the local object can experience and the deformation direction. The determination of the local lattice parameter does not rely on the reference grid, as shown in Figure 4.6b. How the rotation, scaling and shearing of the reference grid influence the strain components will be explored next.

4.5 Choice of reference grid

In an experimental nanoparticle, the strain can be distributed throughout the particle due to its finite size and domain structure. It is almost impossible to have a non-strained region in the particle to generate the reference grid. In section 4.4, it can be seen that the choice of the reference grid is crucial for the strain measurements. To investigate how the reference grid influences the strain analysis, three different reference grids were used for the strain mapping on the simulated image of the strained Pt model. The three different reference grids are the projected pure bulk Pt crystal lattice with a lattice constant of 0.39231 nm at 280 K (Arblaster, 1997), the grids refined from the whole particle and also the centre region of the particle. The centre region is defined as the centre atom and its six closest neighbouring atoms, as shown in Figure 4.7a. There are two reasons why the pure bulk Pt crystal lattice is not always used as the reference grid but that two other two grids derived from the nanoparticle are used: (1) During the

experiments, the magnification of the electron microscope may not be well-calibrated, leading to the inaccurate pixel size of the experimental images. It is meaningless to compare the inaccurate experimental lattice parameters with the accurate pure bulk Pt lattice parameter. (2) A non-strained area in the experimental nanoparticle cannot be found to fix the pure bulk Pt crystal lattice. Rotation of pure Pt reference grid could affect displacement measurements and convert normal strains into shear strains. Here, the measured strain components using the three different reference grids were compared.

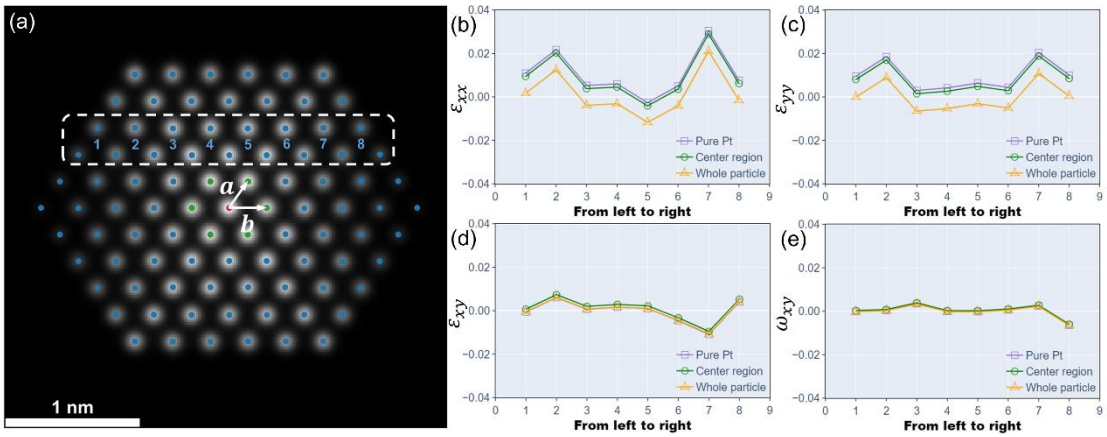

Figure 4.7. (a) An initial triangle and a pair of basis vectors of the centre atom. Red: the centre atom; Green: the six neighbouring atoms; Blue: the observed atoms. (b-e) The line profiles of ε_{xx}, ε_{yy}, ε_{xy}, ω_{xy} in the selected region in (a) using the pure Pt crystal, centre region and whole particle to generate reference grids, respectively.

Figure 4.7b-e display the line profiles of each strain component from the same region of the nanoparticle. The line profile has eight primitive triangles (Labelled from 1 to 8 in Figure 4.7a, which are composed of the atoms in the outer four atomic layers. The distortion triangles 1 and 8 are from the first triangle layer, while the second triangle layer has the triangles 2 and 7. The rest of the triangles belong to the third triangle layer. The same variation can be observed in the strain maps using the three different reference grids, but the difference arising from using different reference grids for the

strain measurements is a series of uniform offsets added to the measured strain components.

As mentioned before, the reference grid is created by periodically growing two reference basis vectors. Here, two different reference grids are described as a & b and a' & b' where the vectors denoted with primes are those that have some errors relative to correct unstrained basis vectors. The modified vectors can be defined by:

$$a' = T \cdot a$$
$$b' = T \cdot b \qquad \textit{Eq. 4.14}$$

Where T is a linear transformation matrix (scaling, shearing, rotation, etc.) to the reference grid. The differential displacement field in the a' & b' reference grid can be written as:

$$\Delta u_1{}' = \Delta u_1 + a - a' = \Delta u_1 + (I - T) \cdot a$$
$$\Delta u_2{}' = \Delta u_2 + b - b' = \Delta u_2 + (I - T) \cdot b \qquad \textit{Eq. 4.15}$$

Where I is the identity matrix. The strain component, ε_{xx} and ε_{yy} are found using Eq. 4.3. Because Eq. 4.15 shows that the effect of an error in the reference grid adds a constant to the differential displacement vector, it can be seen from Eq. 4.3 that it will also add a constant to each of the components of the strain tensor. Thus, we arrive at:

$$\varepsilon_{xx}{}' = \varepsilon_{xx} + constant$$
$$\varepsilon_{yy}{}' = \varepsilon_{yy} + constant \qquad \textit{Eq. 4.16}$$

This mathematic treatment can also be applied to the other strain components.

The scaling, shearing and rotation of the reference grid introduce additional erroneous apparent displacements that build up linearly with respect to the distance from the chosen origin of the reference lattice. However, the strain components are calculated

by the derivative of the displacements (Eq. 4.3). Thus, the change of the strain component equals the slope of the linear variation of the introduced extra displacement, which is a constant. To conclude, using different reference grids influences the absolute values of the measured strain components, but it only adds a series of uniform offsets to the results. The variation of the strain distribution is robust to the selection of the reference grid.

4.6 Measurements reliability on noisy images

In previous sections, the strain measurements methodology has been introduced and its reliability on the simulated ADF image has been verified. The reliability of the strain measurements depends on the accuracy and precision of the atomic column position detection in the image. Thus, it is crucial to precisely determine atomic column positions, which is affected by the Poisson noise and scan instability. However, the multi-frame technique could be used to record multiple ADF frames with a shorted pixel dwell-time, to minimize the sample drift within each frame. By comparing the image frames, it is also possible to determine whether atom mobility introduced by the electron beam has influenced the precision of the atomic column position detection (De Backer et al., 2020). Those atomic columns where the atoms are moving would be excluded for the strain measurements. The obtained image stacks are aligned using the non-rigid registration technique to reduce the scan distortions and the resulting strain measurements have previously been compared and validated against the GPA approach, (Jones and Nellist, 2013, Jones et al., 2015, Jones et al., 2017).It has been reported that an uncertainty of 0.5 pm for the position detection on the averaged non-rigid registered ADF image can be achieved (Yankovich et al., 2014, Nord et al., 2017).

Here, we attempt to investigate the accuracy of our strain measurements on the simulated Poisson-distributed ADF images under different electron doses.

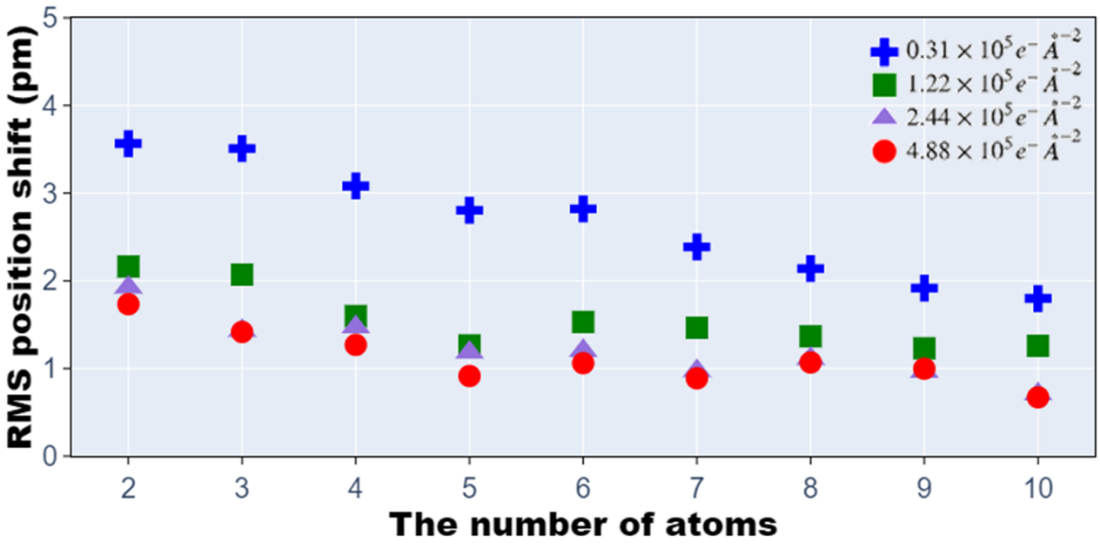

Figure 4.8. The detected root mean square (RMS) position shift as a function of number of atoms in an atomic column in the simulated Poisson-distributed images of the perfect Pt model under the different electron doses.

During a typical experimental data acquisition (De Backer et al., 2015, Jones et al., 2017), around 16 ADF image frames with a total electron dose of $\sim 4.88 \times 10^5 e^- \text{Å}^{-2}$ are obtained for the non-rigid alignment. In order to better understand the effect of the noise, Poisson noise under typically single-frame ($0.31 \times 10^5 e^- \text{Å}^{-2}$), low ($1.22 \times 10^5 e^- \text{Å}^{-2}$), medium ($2.44 \times 10^5 e^- \text{Å}^{-2}$) and high ($4.88 \times 10^5 e^- \text{Å}^{-2}$) electron doses, was added to the simulated ADF images of the perfect (zero-strain) and strained Pt models, respectively. The Poisson noise is added by replacing each pixel with a value selected randomly from a Poisson distribution with a mean given by the simulated number of electron counts. The determined atomic column positions in the simulated Poisson-distributed images of the perfect Pt model were compared with the real atom positions of the model averaged along a column, the distances between them are defined as the position shifts. Figure 4.8 shows the measured RMS position shift as a function of number of atoms in an atomic column under the multiple noise realisations.

For those atomic columns having more than 4 atoms, the accuracy of the atomic column position finding reaches 1 pm under the medium or high electron dose. The accuracy could be improved as the scattered intensity of the atomic column increases (higher electron dose or more atoms). The error of the length of the differential displacement vector can be calculated from the error of atomic column position detection using the error propagation theory(Lyons and Louis, 1991), expressed as:

$$\Delta d = \sqrt{(\Delta d_1)^2 + (\Delta d_2)^2} = \sqrt{2}\, pm \qquad \textit{Eq. 4.17}$$

Where Δd_1 and Δd_2 indicate the errors in the determination of the two atomic columns that constitute a differential displacement vector, and are ~1 pm. Similarly, the error of strain calculation is mainly introduced by the error of the differential displacement measurement. Thus, the precision of strain measurements can be estimated by the equation:

$$\frac{\Delta \varepsilon}{\varepsilon} = \frac{\Delta d}{d} \qquad \textit{Eq. 4.18}$$

Where d is the length of the differential displacement vector. For the differential displacement vectors chosen here, the precision of the strain measurements on STEM images is about 5×10^{-3}. It has been reported that the precision of strain mapping using the high-resolution transmission electron microscopy (HRTEM) images also could approach 10^{-3} (Hÿtch and Minor, 2014). However, compared to the TEM mode, STEM mode equipped with spectrometers allows for simultaneous local strain and composition analyses at an atomic scale.

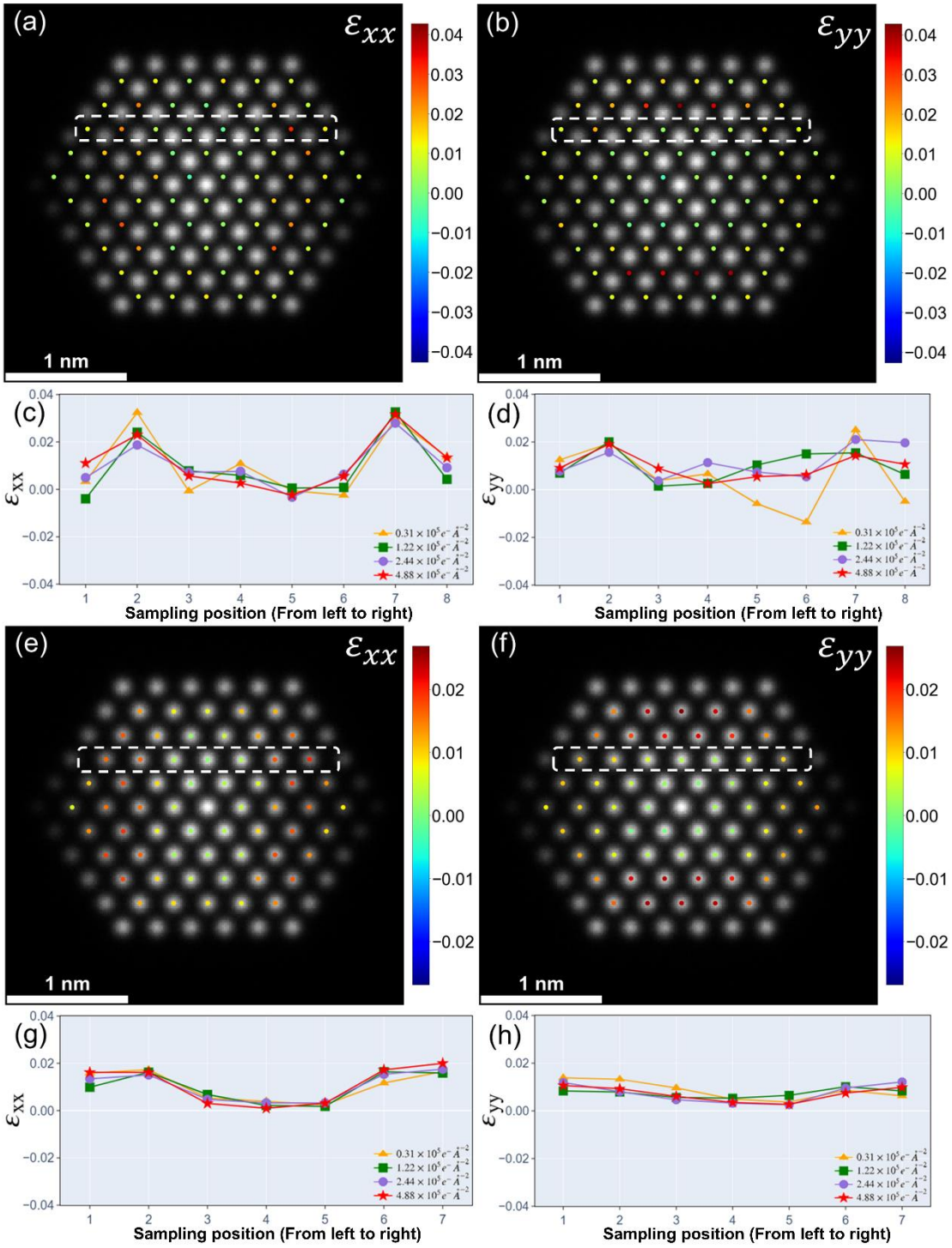

Figure 4.9. The ε_{xx} and ε_{yy} maps from the simulated image of the strained Pt model with Poisson noise under the high electron dose, (a-b) measured using one neighbouring triangle, and (e-f) measured using six neighbouring triangles. The line profiles of ε_{xx} and ε_{yy} in the selected regions under different electron doses, (c-d) measured using one neighbouring triangle, and (g-h) measured using six neighbouring triangles.

To investigate the electron dose influence on the strain analysis, the strain measurements were performed on the simulated images of the strained Pt model with

different electron doses (and therefore, noise levels). The simulated images in Figure 4.9a, b, e and f are under the high electron dose and purely used to illustrate the positions of the measured strains relative to the nanoparticle lattice. Figure 4.9c and d shows how the measured normal strains can fluctuate from the actual ones under the different electron doses. For these plots, only one neighbouring triangle (as shown in Figure 4.7) around each atomic column is used as the primitive unit for the measurements. The influence from the electron dose can be further reduced by sacrificing the spatial resolution of the strain analysis. All the neighbouring triangles of each atomic column (which are six triangles for the Pt model along the [110] projection) can be combined for the strain measurements. The measured strain components from the six neighbouring triangles are then averaged and plotted at the atomic column, as shown in Figure 4.9g and h. It can be clearly seen that the averaged normal strains using six primitive triangles are more robust to the electron dose.

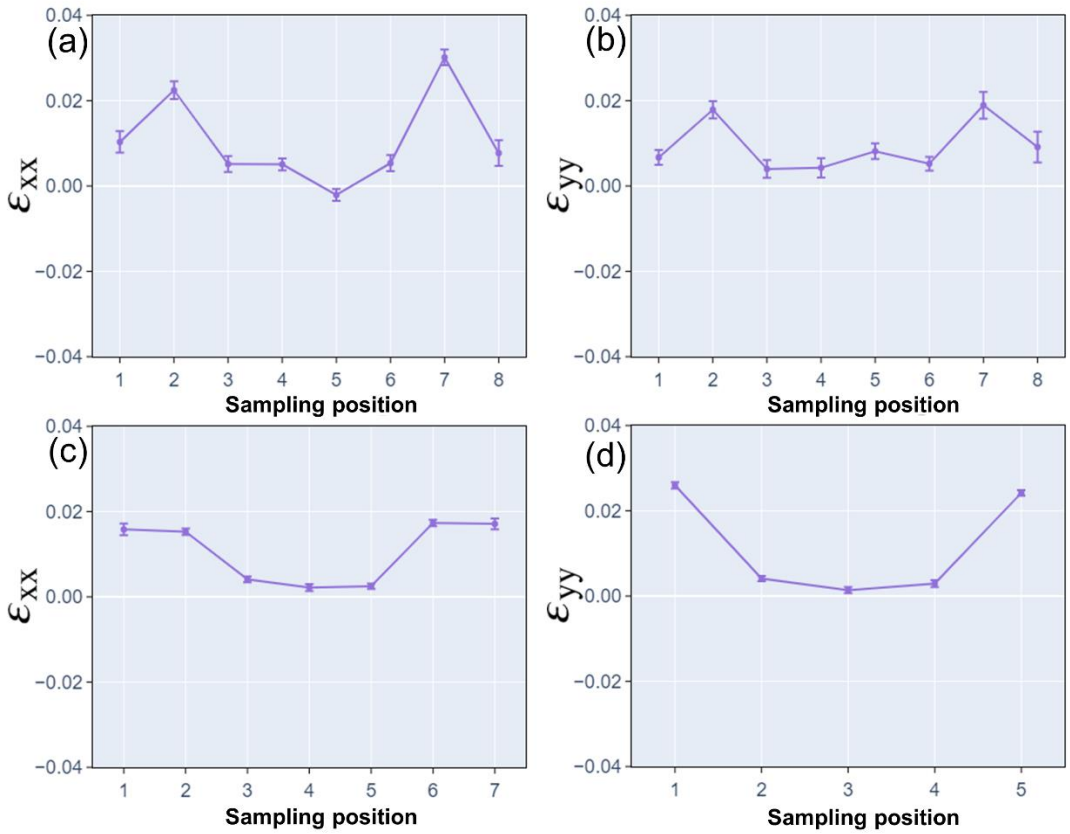

Figure 4.10. Strain measurements on 10 simulated Poisson-distributed images under the high electron dose ($4.88 \times 10^5 e^- Å^{-2}$). The line profiles of averaged ε_{xx} and ε_{yy} in the selected regions in Figure 9, (a-b) measured using one neighbouring triangle, (c-d) measured using six neighbouring triangles.

To study the Poisson noise influence on the strain analysis under the high electron dose, the process of Poisson-distributed image simulation with the dose of $4.88 \times 10^5 e^- Å^{-2}$ was repeated 10 times. The strain measurements using one or six neighbouring triangles were then performed on these 10 simulated images, respectively. The line profiles of two averaged normal strain components with the standard deviations plotted as the error bars are compared in Figure 4.10. Here, the standard deviation is calculated using the measured strain component of each atomic column from ten simulated Poisson-distributed images. A considerable reduction in the uncertainty is observed when averaging six neighbouring triangles for the strain measurements.

To conclude, a precision of 5×10^{-3} for strain analysis and an accuracy of 1 pm for displacement measurements can be achieved on the simulated Poisson-distributed images under the high electron dose used in this work. The electron dose and associated Poisson noise have a slight influence on the strain analysis. To improve the uncertainty of our measurements, an average over primitive cells can be taken, but the spatial resolution of the strain map will be reduced.

4.7 Application of the technique: de-alloyed $PtCo_3$ bimetallic nanoparticle

To demonstrate the potential of our proposed method, we applied the strain analysis method on a carbon supported de-alloyed $PtCo_3$ nanoparticle provided by Johnson Matthey plc. The $PtCo_3$ nanoparticles have been widely used as a catalyst for oxygen

reduction reaction (ORR) in fuel cells due to the enhanced catalytic activity compared to the pure Pt. Precisely measuring the strain distribution at an atomic scale within the $PtCo_3$ nanoparticles could help a better understanding of the intrinsic mechanism behind their catalytic enhancement. The TEM specimen was prepared by drop-casting the nanoparticles on a holey carbon grid and baked in vacuum for 8 hours at 80 °C for hydrocarbon decontamination before imaging in the electron microscope. The specimen was imaged using the STEM mode on a JEOL ARM 200F electron microscope fitted with a probe-forming aberration corrector. An operation voltage of 200 kV and a condenser lens aperture yielding a probe-convergence angle of 22.48 mrad were selected. The HAADF detector collection angles range from 72.8 to 271 mrad. The magnification of the microscope was calibrated using a UO_2 standard. To reduce scan distortion and minimise sample damage, 20 atomic-resolution ADF image frames with a short pixel dwell time of 4 µs and a pixel size of 0.0164 nm were recorded successively. Each image frame having 512×512 pixels was recorded under the beam current of 23.2 pA, yielding a total electron dose of about $4.3 \times 10^5 e^- Å^{-2}$. The frames with good quality in the image stack were non-rigid aligned and averaged to improve SNR using the smart alignment software (Jones et al., 2015). The strain analysis was performed on this nanoparticle using the reference grid refined from the whole particle using in-house developed code.

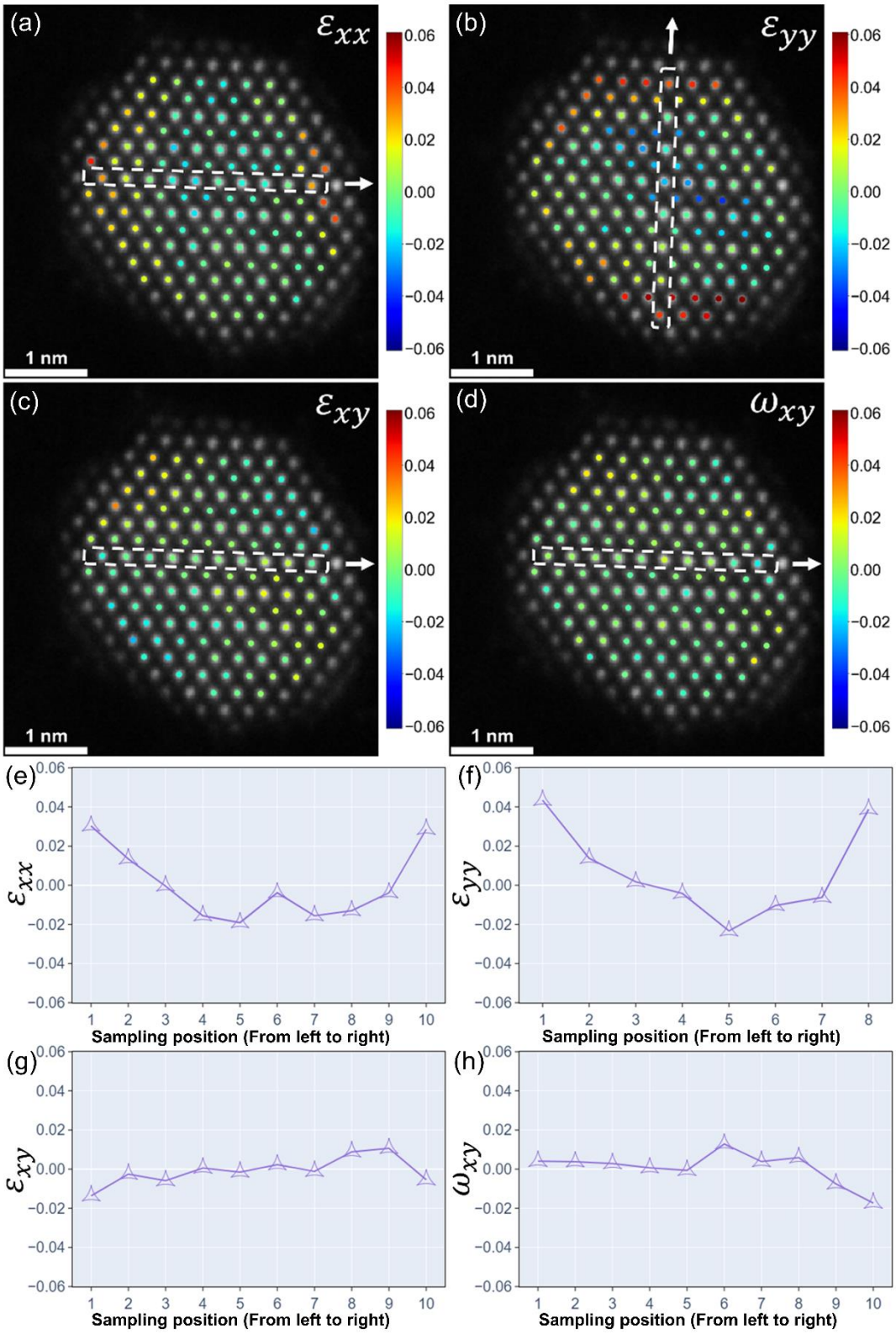

Figure 4.11. The strain maps (a-d) of a $PtCo_3$ nanoparticle and corresponding line profiles (e-h).

To extract local distortion information, the measured strain components were averaged using six neighbouring triangles around each atomic column and are shown in Figure

4.11a-d. In the ε_{xx} map, the atoms on the left and right surfaces of the nanoparticle have the largest strain. In contrast, the largest ε_{yy} components mainly exist in top and bottom layers. It indicates that the atoms in outer atomic layers show larger interatomic distances than the average of the nanoparticle, but the appearance of large strain values is associated with the arbitrary choice of the *x* and *y* axes. The selected line profiles are plotted in Figure 4.11e-h. Unlike the normal strains, the ε_{xy} and ω_{xy} components are quite small. The detected shear strain and lattice rotation on the surface layer may be introduced by the surface atom mobility.

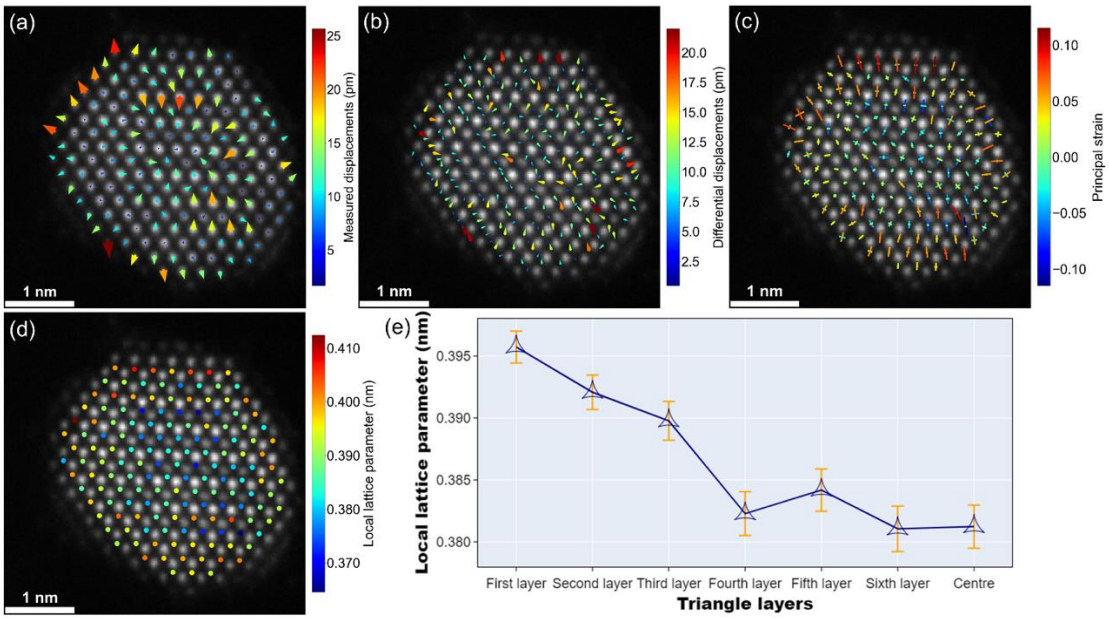

Figure 4.12. (a) The measured displacement map, (b) the differential displacement map, (c) the principal strain map and (d) the local lattice parameter map of an experimental $PtCo_3$ nanoparticle. (e) The measured local lattice parameters vs triangle layers.

Directly interpreting the distortion behaviour of the $PtCo_3$ nanoparticle from its displacement map in Figure 4.12a is difficult because the displacement measurements are highly sensitive to the shift, rotation, shearing and scaling of the reference grid. Here, to improve the spatial resolution of the distortion analysis, only one triangle around each atomic column is used as a distortion unit. The results are therefore plotted at the centre of the triangles instead of the atomic columns. The differential

displacement map in Figure 4.12b shows that along the predefined basis vectors, tensile strain relative to the reference lattice is observed in the near-surface region while compressive strain dominates the centre region of the nanoparticle. The absolute values and directions of these differential displacements are independent of the rigid-body shift but affected by the rotation, shearing and scaling of the reference grid. The principal strain map of the nanoparticle (Figure 4.12c) exhibits a similar distribution symmetry as that of the simulated strained Pt nanoparticle mode in Figure 4.6a. It indicates that atoms in the near-surface regions are dilated outwards relative to the reference lattice. Although the measured principal strain is robust to both the rigid-body shift and rotation, its absolute value still relies on the shearing and scaling of the reference grid. However, the measured local lattice parameters are absolute values that are independent of the reference grid, as long as the image magnification is accurate, as shown in Figure 4.12d. Thus, the local lattice parameter can be directly compared between different Pt-Co species, and further used as a meaningful parameter to modelling for relating strain to catalytic activity.

To investigate the distortion variations from the surface to core of this nanoparticle, the measured local lattice parameter is plotted as a function of the triangle layer, as shown in Figure 4.12e. Similar to the definition of the atomic layer, the triangle layers are defined as rings of primitive triangles moving from the surface to core of the nanoparticle, where the surface triangle layer is composed of those primitive triangles between the outermost and second atomic layers. Note is that the error bar of each triangle layer is demonstrated by the standard error. The first layer has more primitive triangles than the other layers, therefore it has the smallest standard error of the measured lattice parameter among the others. The local lattice parameter can be seen

to increase approaching the particle surface. However, the local lattice parameters are uniformly distributed in the inner four triangle layers. One of the reasons might be that the finite size of the nanoparticle leads to surface lattice relaxations. In addition, the $PtCo_3$ nanoparticles have been reported to have a 'core-shell' effect on the composition distribution (Ellaby et al., 2020). Thus, the composition variations across the nanoparticle are also considered as a contributor to its distortion behaviour. A detailed study correlating composition changes to strain is beyond the scope of this chapter, but will be reported in the following chapters.

4.8 Conclusions

In this chapter, first, it has been shown that the difference between the measured 2D displacements and the real projected 3D displacements of the strained layers for nanoparticles is sufficiently small to allow for the strain analysis from atomic-resolution ADF STEM images. A technique for the atomic site-specific deformation analysis on nanoparticles is then proposed. The variables defining the deformation of materials at an atomic scale are presented and compared. The displacement vector on each atomic site is not effective for the local deformation analysis of nanoparticles because the measurements heavily rely on the shift, rotation, shearing and scaling of the reference grid. The differential displacement and strain tensor are robust to the rigid-body shift of the reference grid. Rotation of the reference grid can transform the normal strains to the shear strains (ε_{xy} and ω_{xy}), and vice-versa. Thus, measuring the strain tensor is not straightforwardly applied for the visualization of the local deformation behaviour of materials. The differential displacement (Δu_1 and Δu_2) can directly express the differential of the local distortion with both magnitude and direction. However, the principal strain (ε_{max} and ε_{min}) is robust to both the rigid-body

shift and rotation of the reference grid. It provides information about the local maximum normal strain and the deformation direction. Unlike the other deformation parameters, the local lattice parameter that is independent of the reference grid, as long as the image magnification is accurate, is the absolute value of the local distortion, but it cannot give information about the distortion direction. Thus, measuring local lattice parameter together with either differential displacement or principal strain mapping enables us to comprehensively understand the distortion behaviour of nanoparticles.

Next, to understand how the rotation, shearing and scaling of the reference grid influence the strain tensor measurements, strain mapping on the simulated strained Pt nanoparticle using three different reference grids is compared. It has been found that although the absolute values of the strain components rely on the reference grid, the different reference grids only add a series of uniform offsets to the strain variations. Also, the reliability of the proposed strain analysis approach on the simulated Poisson-distributed ADF images under the different electron doses is studied. The Poisson noise under the high electron dose has a negligible impact on atomic column position detection. A precision of 5×10^{-3} for strain analysis and an accuracy of 1 pm for displacement measurements can be achieved under the commonly-used experimental conditions. This methodology is able to provide a robust strain analysis on the non-rigid aligned experimental ADF STEM images.

Finally, quantitative results of the strain analysis on an experimental $PtCo_3$ nanoparticle are reported. Compared with the centre of the nanoparticle, the presence of the expansion strain is mainly detected at the near-surface regions. This deformation behaviour is likely introduced by the finite size and composition variations of the

nanoparticle. The precise measurements of the local lattice parameter will significantly improve the comprehensive understandings in terms of the catalytic performance. In future works, the measured strain distribution will be related to local composition variations and catalytic activity of the Pt-Co nanoparticles.

4.9 References

Aarons, J., L. Jones, A. Varambhia, K. E. MacArthur, D. Ozkaya, M. Sarwar, C.-K. Skylaris and P. D. Nellist (2017). "Predicting the oxygen-binding properties of platinum nanoparticle ensembles by combining high-precision electron microscopy and density functional theory." *Nano Letters* 17(7): 4003-4012.

Arblaster, J. (1997). "Crystallographic properties of platinum." *Platinum Metals Review* 41(1): 12-21.

Armigliato, A., S. Frabboni and G. Gazzadi (2008). "Electron diffraction with ten nanometer beam size for strain analysis of nanodevices." *Applied Physics Letters* 93(16): 161906.

Bayle, P., T. Deutsch, B. Gilles, F. Lançon, A. Marty and J. Thibault (1994). "Quantitative analysis of the deformation and chemical profiles of strained multilayers." *Ultramicroscopy* 56(1-3): 94-107.

Béché, A., J. Rouvière, J. Barnes and D. Cooper (2011). "Dark field electron holography for strain measurement." *Ultramicroscopy* 111(3): 227-238.

Bierwolf, R., M. Hohenstein, F. Phillipp, O. Brandt, G. Crook and K. Ploog (1993). "Direct measurement of local lattice distortions in strained layer structures by HREM." *Ultramicroscopy* 49(1-4): 273-285.

Bu, L., N. Zhang, S. Guo, X. Zhang, J. Li, J. Yao, T. Wu, G. Lu, J.-Y. Ma and D. Su (2016). "Biaxially strained PtPb/Pt core/shell nanoplate boosts oxygen reduction catalysis." *Science* 354(6318): 1410-1414.

Clouet, E. (2020). "Ab initio models of dislocations." *Handbook of Materials Modeling: Methods: Theory and Modeling*: 1503-1524.

Cooper, D., T. Denneulin, N. Bernier, A. Béché and J.-L. Rouvière (2016). "Strain mapping of semiconductor specimens with nm-scale resolution in a transmission electron microscope." *Micron* 80: 145-165.

Cooper, D., J.-L. Rouviere, A. Béché, S. Kadkhodazadeh, E. S. Semenova, K. Yvind and R. Dunin-Borkowski (2011). "Quantitative strain mapping of InAs/InP quantum dots with 1 nm spatial resolution using dark field electron holography." *Applied Physics Letters* 99(26): 261911.

De Backer, A., L. Jones, A. Varambhia, P. D. Nellist and S. Van Aert (2020). "Measuring dynamic structural changes of nanoparticles at the atomic scale using scanning transmission electron microscopy." *Physical Review Letters* 124(10): 106105.

De Backer, A., G. Martinez, K. MacArthur, L. Jones, A. Béché, P. Nellist and S. Van Aert (2015). "Dose limited reliability of quantitative annular dark field scanning transmission electron microscopy for nano-particle atom-counting." *Ultramicroscopy* 151: 56-61.

Diercks, D., G. Lian, J. Chung and M. Kaufman (2011). "Comparison of convergent beam electron diffraction and geometric phase analysis for strain measurement in a strained silicon device." *Journal of Microscopy* 241(2): 195-199.

Ellaby, T., A. Varambhia, X. Luo, L. Briquet, M. Sarwar, D. Ozkaya, D. Thompsett, P. D. Nellist and C.-K. Skylaris (2020). "Strain effects in core–shell PtCo nanoparticles: a comparison of experimental observations and computational modelling." *Physical Chemistry Chemical Physics* 22(42): 24784-24795.

Galindo, P., J. Pizarro, S. Molina and K. Ishizuka (2009). "High resolution peak measurement and strain mapping using peak pairs analysis." *Microscopy and Analysis-UK*(130): 23.

Galindo, P. L., S. Kret, A. M. Sanchez, J.-Y. Laval, A. Yanez, J. Pizarro, E. Guerrero, T. Ben and S. I. Molina (2007). "The Peak Pairs algorithm for strain mapping from HRTEM images." *Ultramicroscopy* 107(12): 1186-1193.

Gan, L., M. Heggen, R. O'Malley, B. Theobald and P. Strasser (2013). "Understanding and controlling nanoporosity formation for improving the stability of bimetallic fuel cell catalysts." *Nano Letters* 13(3): 1131-1138.

Gao, H. and L.-M. Peng (1999). "Parameterization of the temperature dependence of the Debye–Waller factors." *Acta Crystallographica Section A: Foundations of Crystallography* 55(5): 926-932.

Gasteiger, H. A. and N. M. Marković (2009). "Just a dream—or future reality?" *Science* 324(5923): 48-49.

Gavartin, J., M. Sarwar, D. Papageorgopoulos, D. Gunn, S. Garcia, A. Perlov, A. Krzystala, D. L. Ormsby, D. Thompsett and G. Goldbeck-Wood (2009). "Exploring Fuel Cell Cathode Materials: A High Throughput Calculation Approach." *ECS Transactions* 25(1): 1335.

Goris, B., J. De Beenhouwer, A. De Backer, D. Zanaga, K. J. Batenburg, A. Sánchez-Iglesias, L. M. Liz-Marzán, S. Van Aert, S. Bals, J. Sijbers and G. Van Tendeloo (2015). "Measuring Lattice Strain in Three Dimensions through Electron Microscopy." *Nano Letters* 15(10): 6996-7001.

Hÿch, M. and L. Potez (1997). "Geometric phase analysis of high-resolution electron microscopy images of antiphase domains: example Cu3Au." *Philosophical Magazine A* 76(6): 1119-1138.

Hÿtch, M., F. Houdellier, F. Hüe and E. Snoeck (2008). "Nanoscale holographic interferometry for strain measurements in electronic devices." *Nature* 453(7198): 1086-1089.

Hÿtch, M., J.-L. Putaux and J. Thibault (2006). "Stress and strain around grain-boundary dislocations measured by high-resolution electron microscopy." *Philosophical Magazine* 86(29-31): 4641-4656.

Hÿtch, M., E. Snoeck and R. Kilaas (1998). "Quantitative measurement of displacement and strain fields from HREM micrographs." *Ultramicroscopy* 74(3): 131-146.

Hÿtch, M. J. and A. M. Minor (2014). "Observing and measuring strain in nanostructures and devices with transmission electron microscopy." *MRS Bulletin* 39(2): 138.

Hÿtch, M. J., J.-L. Putaux and J.-M. Pénisson (2003). "Measurement of the displacement field of dislocations to 0.03 Å by electron microscopy." *Nature* 423(6937): 270-273.

Hanszen, K.-J. (1986). "Method of off-axis electron holography and investigations of the phase structure in crystals." *Journal of Physics D: Applied Physics* 19(3): 373.

Heck, R. M., R. J. Farrauto and S. T. Gulati (2016). *Catalytic air pollution control: commercial technology*, John Wiley & Sons.

Hüe, F., M. Hÿtch, F. Houdellier, H. Bender and A. Claverie (2009). "Strain mapping of tensiley strained silicon transistors with embedded Si 1− y C y source and drain by dark-field holography." *Applied Physics Letters* 95(7): 073103.

Jones, L. and P. D. Nellist (2013). "Identifying and correcting scan noise and drift in the scanning transmission electron microscope." *Microscopy and Microanalysis* 19(4): 1050.

Jones, L., S. Wenner, M. Nord, P. H. Ninive, O. M. Løvvik, R. Holmestad and P. D. Nellist (2017). "Optimising multi-frame ADF-STEM for high-precision atomic-resolution strain mapping." *Ultramicroscopy* 179: 57-62.

Jones, L., H. Yang, T. J. Pennycook, M. S. Marshall, S. Van Aert, N. D. Browning, M. R. Castell and P. D. Nellist (2015). "Smart Align—a new tool for robust non-rigid registration of scanning microscope data." *Advanced Structural and Chemical Imaging* 1(1): 1-16.

Jones, P., G. Rackham and J. W. Steeds (1977). "Higher order Laue zone effects in electron diffraction and their use in lattice parameter determination." *Proceedings of the Royal Society of London. A. Mathematical and Physical Sciences* 354(1677): 197-222.

Kim, S.-W., D.-S. Byeon, H. Jang, S.-M. Koo, H.-J. Lee and D.-H. Ko (2014). "Strain characterization of fin-shaped field effect transistors with SiGe stressors using nanobeam electron diffraction." *Applied Physics Letters* 105(8): 083104.

Lobato, I. and D. Van Dyck (2015). "MULTEM: A new multislice program to perform accurate and fast electron diffraction and imaging simulations using Graphics Processing Units with CUDA." *Ultramicroscopy* 156: 9-17.

Lubk, A., E. Javon, N. Cherkashin, S. Reboh, C. Gatel and M. Hÿtch (2014). "Dynamic scattering theory for dark-field electron holography of 3D strain fields." *Ultramicroscopy* 136: 42-49.

Lyons, L. and L. Louis (1991). *A practical guide to data analysis for physical science students*, Cambridge University Press.

Naito, M., M. Ishimaru, Y. Hirotsu and M. Takashima (2004). "Local structure analysis of Ge-Sb-Te phase change materials using high-resolution electron microscopy and nanobeam diffraction." *Journal of Applied Physics* 95(12): 8130-8135.

Nord, M., P. E. Vullum, I. MacLaren, T. Tybell and R. Holmestad (2017). "Atomap: a new software tool for the automated analysis of atomic resolution images using two-dimensional Gaussian fitting." *Advanced Structural and Chemical Imaging* 3(1): 1-12.

Pingel, T. N., M. Jørgensen, A. B. Yankovich, H. Grönbeck and E. Olsson (2018). "Influence of atomic site-specific strain on catalytic activity of supported nanoparticles." *Nature Communications* 9(1): 1-9.

Sennour, M., S. Lartigue-Korinek, Y. Champion and M. Hÿtch (2007). "HRTEM study of defects in twin boundaries of ultra-fine grained copper." *Philosophical Magazine* 87(10): 1465-1486.

Solliard, C. and M. Flueli (1985). "Surface stress and size effect on the lattice parameter in small particles of gold and platinum." *Surface Science* 156: 487-494.

Stamenkovic, V., B. S. Mun, K. J. Mayrhofer, P. N. Ross, N. M. Markovic, J. Rossmeisl, J. Greeley and J. K. Nørskov (2006). "Changing the activity of electrocatalysts for

oxygen reduction by tuning the surface electronic structure." *Angewandte Chemie* 118(18): 2963-2967.

Strasser, P., S. Koh, T. Anniyev, J. Greeley, K. More, C. Yu, Z. Liu, S. Kaya, D. Nordlund and H. Ogasawara (2010). "Lattice-strain control of the activity in dealloyed core–shell fuel cell catalysts." *Nature Chemistry* 2(6): 454-460.

Temmel, S. E., E. Fabbri, D. Pergolesi, T. Lippert and T. J. Schmidt (2016). "Investigating the role of strain toward the oxygen reduction activity on model thin film Pt catalysts." *ACS Catalysis* 6(11): 7566-7576.

Toda, A., H. Nakamura, T. Fukai and N. Ikarashi (2008). "Channel strain in advanced complementary metal–oxide–semiconductor field effect transistors measured using nano-beam electron diffraction." *Japanese Journal of Applied Physics* 47(4S): 2496.

Toda, T., H. Igarashi, H. Uchida and M. Watanabe (1999). "Enhancement of the electroreduction of oxygen on Pt alloys with Fe, Ni, and Co." *Journal of the Electrochemical Society* 146(10): 3750.

Usuda, K., T. Numata, T. Irisawa, N. Hirashita and S. Takagi (2005). "Strain characterization in SOI and strained-Si on SGOI MOSFET channel using nano-beam electron diffraction (NBD)." *Materials Science and Engineering: B* 124: 143-147.

Van Dyck, D. and M. O. De Beeck (1996). "A simple intuitive theory for electron diffraction." *Ultramicroscopy* 64(1-4): 99-107.

Vitek, V., R. Perrin and D. Bowen (1970). "The core structure of ½ (111) screw dislocations in bcc crystals." *Philosophical Magazine* 21(173): 1049-1073.

Wang, J. X., H. Inada, L. Wu, Y. Zhu, Y. Choi, P. Liu, W.-P. Zhou and R. R. Adzic (2009). "Oxygen reduction on well-defined core− shell nanocatalysts: particle size, facet, and Pt shell thickness effects." *Journal of the American Chemical Society* 131(47): 17298-17302.

Williams, D. B. and C. B. Carter (1996). *Transmission electron microscopy*, Springer.

Wu, J., P. Li, Y.-T. F. Pan, S. Warren, X. Yin and H. Yang (2012). "Surface lattice-engineered bimetallic nanoparticles and their catalytic properties." *Chemical Society Reviews* 41(24): 8066-8074.

Yankovich, A. B., B. Berkels, W. Dahmen, P. Binev, S. I. Sanchez, S. A. Bradley, A. Li, I. Szlufarska and P. M. Voyles (2014). "Picometre-precision analysis of scanning transmission electron microscopy images of platinum nanocatalysts." *Nature Communications* 5(1): 1-7.

Zhang, S., X. Zhang, G. Jiang, H. Zhu, S. Guo, D. Su, G. Lu and S. Sun (2014). "Tuning nanoparticle structure and surface strain for catalysis optimization." *Journal of the American Chemical Society* 136(21): 7734-7739.

Zuo, J.-M., A. B. Shah, H. Kim, Y. Meng, W. Gao and J.-L. Rouviére (2014). "Lattice and strain analysis of atomic resolution Z-contrast images based on template matching." *Ultramicroscopy* 136: 50-60.

Chapter 5

Composition determination on nanoparticles

This chapter aims to precisely determine the composition distributions within the individual Pt-Co bimetallic nanoparticles. Currently, measuring composition variations on multi-element samples is not possible by solely interpreting ADF signals. To decouple composition and mass-thickness effects for the bimetallic nanoparticles, the spectroscopic signals (EELS and EDS) are used to evaluate the number of Pt and Co atoms on the nanoparticles. In this chapter, the spectroscopic signals were quantified into the number of atoms using the partial scattering cross sections theory. Here, ADF, EELS and EDS signals emitted from the nanoparticles were simultaneously collected at high speed. The accuracy of our composition quantification method was examined by Co atom counting on a $PtCo_3$ nanoparticle using the EELS and EDS signals respectively. Then, the quantified ADF, EELS and EDS scattering cross sections were also unified and related to each other. Finally, this approach was applied to the $PtCo_3$ nanoparticle to analyse its composition distribution at an atomic scale.

5.1 Introduction

A thorough composition characterisation of the bimetallic nanoparticles is crucial to the interpretation of the operation of the catalysts (Bligaard and Nørskov, 2007). The catalytic activities have been successfully related to the electronic structure of the nanoparticle surfaces (Kitchin et al., 2004, Stamenkovic et al., 2006, Gavartin et al., 2009). It has also been found that the surface electronic structure depends on the localised composition of the bimetallic nanoparticles (Kitchin et al., 2004, Bligaard and

Nørskov, 2007). Uniform composition distribution is rarely observed within the individual heterogeneous nanoparticle, such as Pt-Co systems which have been reported to have a core-shell effect in composition variations (Wang et al., 2009, Zhang et al., 2014, MacArthur et al., 2016, Temmel et al., 2016, Chen et al., 2020, Ellaby et al., 2020). Thus, it is necessary to quantify the composition variations within the single bimetallic nanoparticle at an atomic scale. Currently, STEM equipped with EDS or EELS detectors is of widespread use for high-resolution and localised composition determination (MacArthur et al., 2016, Varambhia, 2018). It is well established that ADF STEM imaging can provide the size, shape and composition information from pure-element nanoparticles (Varambhia et al., 2016, Aarons et al., 2017). However, for the bimetallic nanoparticles, composition information cannot be visible by solely interpreting the ADF signals (Varambhia et al., 2018). The reason is that the ADF intensities scattered from the sample depend on not only the atomic number (Z) but also the sample thickness (Williams and Carter, 1996). To decouple composition and thickness combination of the multi-element samples, the spectroscopic signals (EDS or EELS) are also required.

The partial scattering cross section theory (described later in this chapter) can be used to quantify both EDS and EELS signals (Varambhia et al., 2018). The current commercial software often uses a theoretical model for the partial scattering cross section determination. Although the theoretical calculation is fast and easy with an advanced computer, it may produce systematic errors of ±15~20% because it is hard to precisely quantify the microscope geometry factors (Maher et al., 1981, Newbury et al., 1984, Watanabe et al., 2003). To obtain reliable quantification results, the partial scattering cross section needs to be experimentally measured. Varambhia determined

the spectroscopic partial cross sections for both Pt and Co elements by using the pure-element needle and nanoparticle standards (Varambhia et al., 2018). Here, those experimentally measured partial cross sections will be used for both EDS and EELS quantification performed on the same electron microscope with the same detector setting. In addition, ADF intensities can also be interpreted in terms of the scattering cross sections (MacArthur et al., 2013). With careful detector calibration, the measured ADF cross section can be an absolute value and does not vary with the different microscopes (MacArthur et al., 2014, Jones, 2016, Jones et al., 2018). ADF quantification has become a well-established technique and been successfully applied to atom counting on pure-element samples (Jones et al., 2014, Varambhia et al., 2016, Aarons et al., 2017).

This chapter briefly reviews the composition quantification techniques using ADF, EDS and EELS signals. Then, to investigate the accuracy and reliability of our quantification methodology, atom counting using ADF, EDS and EELS signals respectively was performed on the same $PtCo_3$ nanoparticle. Also, an attempt was made at studying the crystal structure of the on-axis Pt-Co bimetallic nanoparticle solely using the ADF quantification technique. Finally, the composition variations from the surface to centre of a $PtCo_3$ bimetallic nanoparticle were analysed.

5.2 Data acquisition

The imaging conditions used in this section and the following section are exactly the same as that for the EDS and EELS cross sections calibration in our previous work (Varambhia et al., 2018). To obtain a dispersed range of isolated particles, the Pt-Co bimetallic nanoparticles were dissolved in ethanol, followed by dropping the obtained

solution on a holey carbon grid. The prepared sample grids were then baked in vacuum for at least 8 hours at 80 ℃ for hydrocarbon decontamination before being mounted onto a JEOL Be double-tilt holder. Experimental data were acquired on a JEOL ARM 200CF electron microscope equipped with a probe-forming aberration corrector, featuring 100mm^2 Centurion EDX detector and Gatan GIF Quantum 965 ER with Dual EELS and EFTEM capabilities. The microscope was operated under a voltage of 200 kV with a probe size of ~0.8-1 Å. The probe convergence angle was 22.48 mrad. The camera length was set as 4 cm to ensure that more than enough transmitted electrons enter the EELS drift tube. Under this cameral length, the collection angles for the ADF detector range from 72.8 to 271 mrad. The double-tilt holder was tilted towards the EDS detector by 20˚in the +x direction for optimal X-ray collection. An EELS entrance aperture of 5mm was selected to yield a collection angle of 37.94 mrad. The energy dispersions for EELS and EDS spectra were set as 0.25 eV and 0.01 keV.

The SNR of the obtained spectrum images plays a key role in the accuracy of the quantification results (De Backer et al., 2015, Jones et al., 2018, Varambhia et al., 2018). To obtain a high SNR spectra, we can either increase the collection angle (or detector solid angle for EDX, e.g. by using more spectrometers) or increase the electron beam dose. However, installing more detectors is often not practical due to the high cost of the detector and the lack of space in the microscope. Thus, a proper electron beam dose is crucial to the spectra data acquisition on the small nanoparticles. A lower beam dose leads to the poor SNR of the spectra while a higher beam dose could lead to irreversible structure damage or rotation. A balance between the SNR and sample damage is required. Additionally, two main experimental parameters that can be used to tune the electron beam dose are the pixel exposure time and beam current. Increasing the pixel

exposure time would introduce stage drifts or scan distortions (Jones and Nellist, 2013). Strengthening beam current could cause severe nanoparticle damage and carbon contamination. To tackle this problem, the Multi-Frame Spectrum-Imaging (MFSI) technique is used in this work (Jones et al., 2018). When collecting spectroscopic signals at a fixed beam dose, instead of acquiring only one spectrum image, multiple spectroscopic frames are acquired alongside the ADF images. Because the total beam dose is fixed, each frame is recorded at a fast scan speed with a fractionated beam dose. The resulting averaged spectroscopic image shows reduced sample damage and drifts (Jones et al., 2018). Here, the isolated Pt-Co nanoparticles overhanging over a vacuum region from the carbon support were chosen for imaging. The reason is that the C-edge caused by the carbon grid could worsen the SNR of the EELS spectra. It has been reported that imaging at a pixel exposure time of 0.005s and a pixel size less than 1 Å would not introduce severe structure damage to the nanoparticles with size above 3 nm (Varambhia, 2018). Therefore, 40 ADF, EDS and EELS frames of the off-axis nanoparticles were simultaneously acquired with a pixel exposure time of 0.005s and a pixel size of ~1 Å, as shown in Figure 5.1. The beam current was set as ~23pA, yielding a $\sim 7.5 \times 10^5$ electron/Å beam dose of each frame.

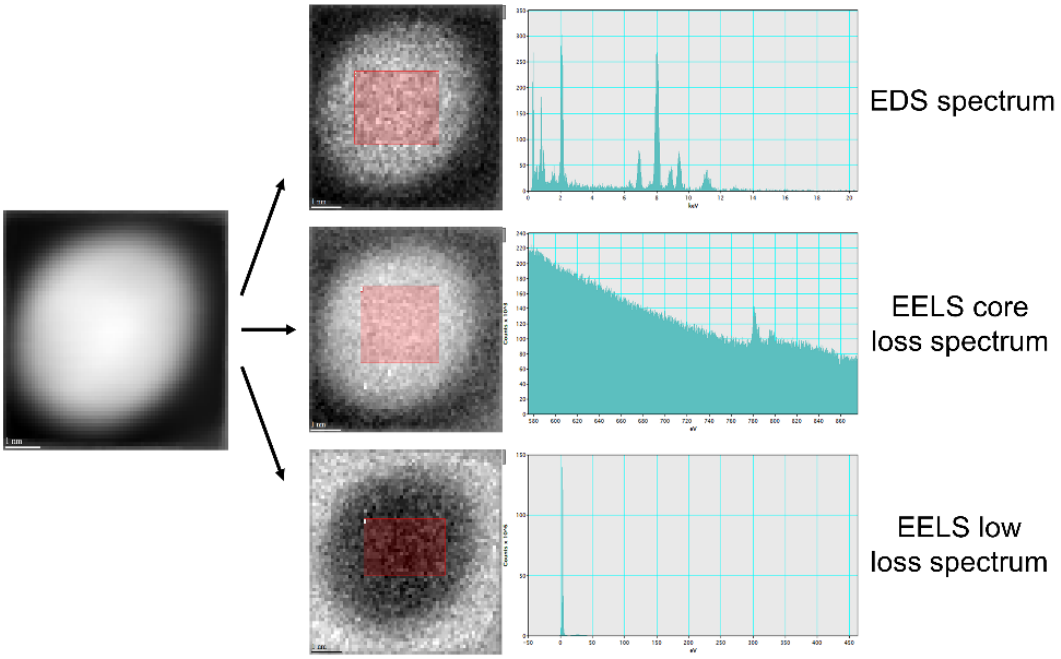

Figure 5.1 Simultaneous ADF, EDS and EELS dataset for an unleached $PtCo_3$ bimetallic nanoparticle.

The obtained ADF image frames were first aligned using the non-rigid registration method implemented in the Digital Micrograph software. Next, the acquired spectrum frames (EDS and EELS) were registered using the aligned ADF frames as the references. These near-zero drift aligned spectrum images were then summed, yielding a higher beam dose of $\sim 3 \times 10^7$ electron/Å in total. Applying the MFSI technique to the data acquisition on the Pt-Co nanoparticles significantly improves the SNR of the spectra without introducing the sample damage and stage drifts, paving the way for precise composition quantification. The whole data acquisition and pre-processing were achieved in a previously-developed interactive graphical script writing in Digital Micrograph (Jones et al., 2018), as shown in Figure 5.2.

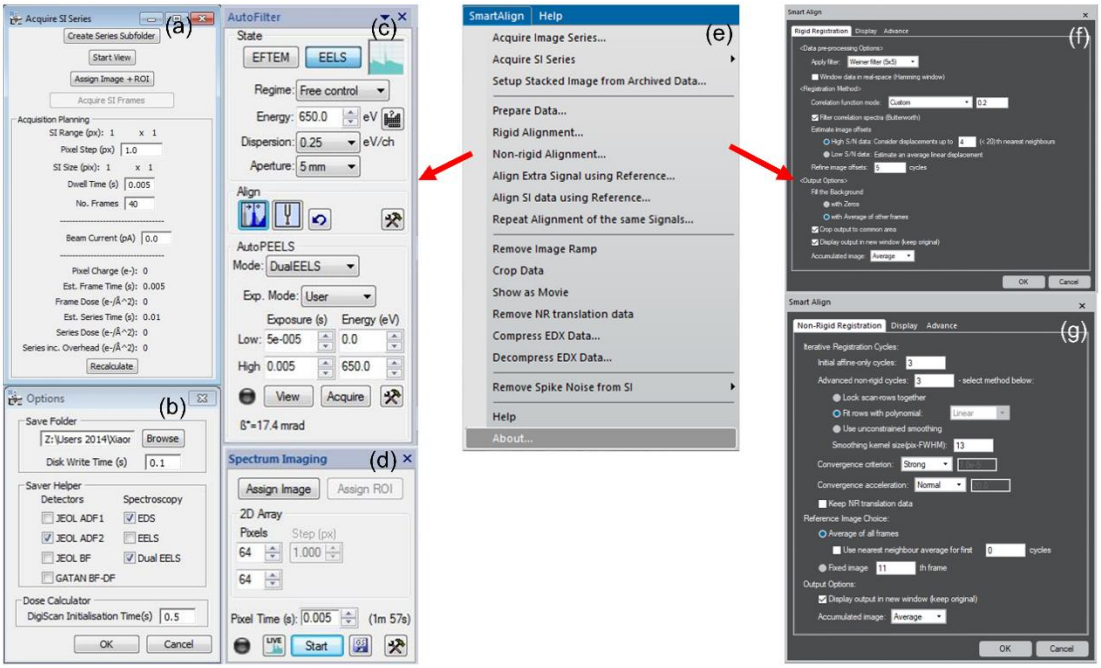

Figure 5.2. The interactive graphical user interface for the MFSI technique. (a-d) Experimental multi-frame data acquisitions. (f-g) Multi-frame images alignment. (a) Multi-frame images control panel. (b) Data saving panel. (c) EELS parameters setting. (d) SI parameters setting. (e) Smart alignment general manual. (f) Rigid alignment and (g) Non-rigid alignment for multi-frame images.

5.3 Estimating the number of atoms in nanoparticles

When dealing with both ordered Pt_3Co and $PtCo_3$ alloys as the $L1_2$ type structure, each unit cell has 4 atoms. The number density of each unit cell (ρ_{atom}) is given by:

$$\rho_{atom} = \frac{Atoms\ per\ unit\ cell}{unit\ cell\ volume} = \frac{4}{a^3} \qquad Eq.\ 5.1$$

Where a is the lattice parameter. Assuming the shape of nanoparticles as spherical, then we can have:

$$\text{Number of atoms} = \frac{4}{3}\pi r^3 \cdot \frac{4}{a^3} \qquad Eq.\ 5.2$$

Where r is the radius of the nanoparticle. These expressions cannot provide an accurate number of atoms if the nanoparticle has an irregular shape or randomly ordered crystal structure.

5.4 EELS quantification

5.4.1 Brief review of EELS quantification approaches

To quantify the EELS signals, both the low loss (0~50 eV) and core loss (>50 eV) spectra need to be acquired simultaneously in a single dataset, which is termed DualEELS. Assuming that an L-edge in the core loss spectrum is quantified, then the L-edge integrated intensity above background (I_L) can be expressed as (Williams and Carter, 1996, Egerton, 2011):

$$I_L = P_L \cdot I_T \qquad \textit{Eq. 5.3}$$

Where P_L is the probability of ionization, and I_T is the total transmitted electron intensities measured over the whole angular range. For the thin samples such as the Pt-Co nanoparticles with a size range between 3 nm and 6 nm, the transmitted electrons can be regarded to only undergo single scattering events. We can have:

$$P_L = N_\rho \cdot \sigma_L \cdot \exp(-\frac{t}{\lambda_L}) \qquad \textit{Eq. 5.4}$$

Where N_ρ is the number of atoms per unit area that contribute to the L-edge (the areal density of the corresponding element). σ_L is the EELS partial scattering cross section of a single atom. t and λ_L indicate the sample thickness and the mean free path, respectively. Given the fact that $t \ll \lambda_L$, then we arrive at:

$$N_\rho = \frac{I_L}{\sigma_L \cdot I_T} \qquad \textit{Eq. 5.5}$$

In this work, EELS signals were not used for Pt element quantification on the bimetallic nanoparticles due to the poor SNR of the Pt M4, M5 edges at 2202 and 2122 eV (Varambhia, 2018). In practice, the collected EELS intensities at energy losses above 2000 eV fall below the system noise level due to the short dwell times used. Co atom

counting was achieved by quantifying Co L3, L2 edges at 779eV, 794eV respectively. The Co L3, L2 scattering cross section of a single atom (σ_L), which is 1.43 kb, was measured by Dr. Varambhia using a pure Co needle standard (Varambhia et al., 2018). In order to calculate I_L, an integration window (Δ) is required. The reason is that the intensities in the edge fall below the background level within ~100 eV after the ionization threshold, risking the accuracy of background subtraction. Here, to stay consistent between the previous work on the Co cross section measurements and our composition analysis, an integration window (Δ) of 30 eV from 774 eV to 804 eV over the Co core-edges was used for Co quantification. The Eq. 5.5 can be re-written as:

$$N_\rho = \frac{I_L(\Delta)}{\sigma_L(\Delta) \cdot I_T} \qquad \textit{Eq. 5.6}$$

At this point, I_T is the last variable needed to be calculated. There are three different conventional definitions of I_T:

(1) The intensity of the zero loss peak (ZLP) in vacuum.

(2) The intensity of the ZLP in the low loss spectrum.

$$N_\rho = \frac{I_L^l(\Delta)}{\sigma_L(\Delta) \cdot I_0} \qquad \textit{Eq. 5.7}$$

Where I_0 is the integrated intensity of the ZLP, $I_L^l(\Delta)$ is the integrated intensity of the ionization edges after deconvolution, as shown in Figure 5.3.

(3) The intensity of the ZLP and low loss electrons over an integration window of equal width to the edge integration window (Δ).

$$N_\rho = \frac{I_L(\Delta)}{\sigma_L(\Delta) \cdot I_T(\Delta)} \qquad \textit{Eq. 5.8}$$

The first approach is not accurate because the angle-limiting EELS aperture could cut off a certain fraction of electrons scattered by the elastic scattering. Also, this approach does not consider the electron backscattering and absorption effects. The third method

is often applied to the spectra where the plural scattering happens. Because of the plural scattering of the transmitted electrons, a fraction of intensities will be redistributed toward the higher energy loss, which is away from the ZLP in the low loss spectrum or the threshold of the ionization edge in the core loss spectrum. The edge integration window (Δ) in the low loss spectrum can only include a certain fraction of the redistributed intensities. However, the fraction included will be the same as the fraction that falls within the ZLP integration window of equal width to the edge integration window (Δ). If the plural scattering is removed by deconvolving the spectra, the second approach could be used for quantification.

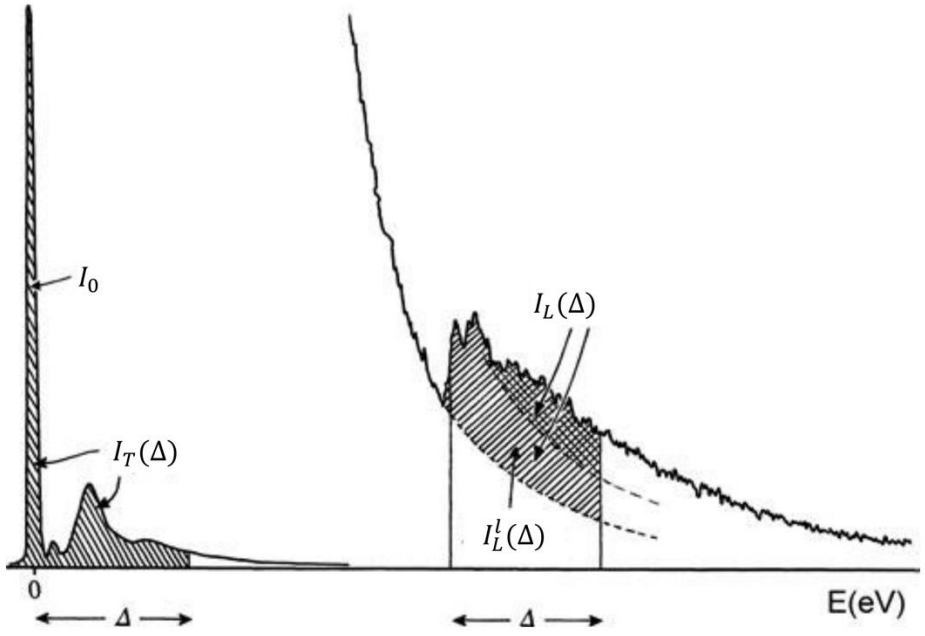

Figure 5.3. Energy-loss spectrum showing the low-loss region and (with change in intensity scale) a single ionization edge. The cross-hatched area represents electrons that have undergone multiple scattering. Reprinted from (Egerton, R.F., 2011.).

Previous work has normalized the integrated intensities of Co L edges ($I_L(\Delta)$) using the I_T calculated by these three different approaches, and plotted it as a function of the number of Co atoms (N) (Varambhia et al., 2018), as shown in Figure 5.4. Theoretically, a linear relationship should be observed between $I_L(\Delta)/I_T(\Delta)$ and the number of atoms (N) since $\sigma_L(\Delta)$ is a constant. It can be seen that for the sample thickness below 10 nm,

all three methods give sensible and consistent results. However, as the sample gets thicker, only the fractional intensity calculated using the 30eV ZLP window remains linear. This is because more transmitted electrons are intercepted by the EELS entrance aperture. In this work, the intensity of the ZLP and low loss electrons over a 30 eV energy window was used for the Co quantification.

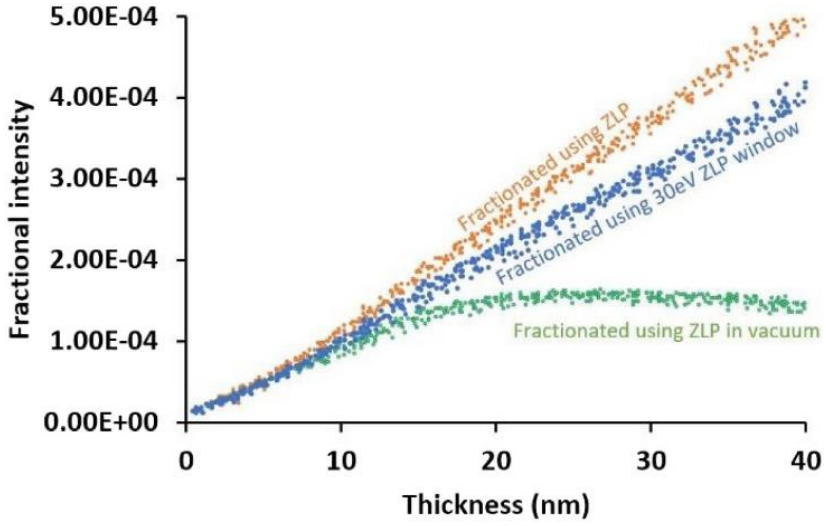

Figure 5.4. Fractional intensity ($I_L(\Delta)/I_T$) from Co L2 and L3 edges plotted as a function of thickness with different definitions of I_T that can be used in Eq. 3. Reprinted from (Varambhia, Aakash, et al., 2018.).

When collecting the DualEELS signals, the low loss spectra were recorded at a pixel dwell time of 5×10^{-5} s to avoid the CCD saturation, whereas, the pixel dwell time for the core loss spectra was 0.005 s. Therefore, the final expression for the areal density of atoms can be written as:

$$N = \frac{I_L(\Delta)/t_{cl}}{\sigma_L(\Delta) \cdot I_T(\Delta)/t_{ll}} \times S \qquad \textit{Eq. 5.9}$$

Where N is the number of atoms in each pixel and S is the area of each pixel, t_{cl} and t_{ll} indicate the pixel dwell time for the core loss and low loss spectra, respectively. The experimental acquisition parameters, background subtraction and integration windows used for the Co EELS quantification are listed in Table 5.1.

Pixel exposure time	EELS aperture	Energy dispersion (eV)	Number of frames
Core loss spectrum: 0.005s Low loss spectrum: $5*10^{-5}$s	5 mm	0.25	40
EELS edge	Background removal Windows (eV)	Integration windows (eV)	Partial cross-section (barns)
Co L2+L3	[714, 774]	Low loss: [-5, 25] Core loss: [774, 804]	1430

Table 5.1. Summary of data acquisition and processing parameters for the EELS quantification.

5.4.2 Co atom counting on Pt-Co nanoparticles

Although much more EELS signal can be collected compared to EDS, quantifying the ionization edges is still difficult due to the noisy background in the spectra. In Figure 5.5, the Co L2 and L3 edges can barely be observed in the core loss spectrum from a single pixel in the Pt-Co nanoparticle due to the poor SNR. Whereas, increasing the EELS signals by integrating the spectra over all pixels in the nanoparticle could significantly improve the SNR, which is termed whole-particle spectrum, as shown in Figure 5.5c. Principle Component Analysis (PCA) was also used to denoise the core loss spectrum, as shown in Figure 5.5b and c. The decision on how many components should be included in the denoised data is not straight-forward due to the high noise levels in the individual spectra. Here, six PCA components were used to denoise the core loss spectrum image of the nanoparticle. Although it can be clearly seen that after the PCA denoising, the sharp Co L2 and L3 edges appear and background noise is remarkably reduced in the single-pixel spectrum, some artefacts are introduced in the whole-particle spectrum where the denoised intensities are increased. These artefacts disappear until nearly all PCA components were chosen for denoising, indicating that the original dataset noise levels are too high to see a real improvement. As a consequence, PCA denoising is only recommended if a clear threshold between the components containing information and noise is observed in the scree test. The scree test often displays the eigenvalues of the principal components in a downward curve,

the ‘elbow’ of the curve where the eigenvalues seem to level off is found and components to the left of this point should be retained to obtain the denoised data.

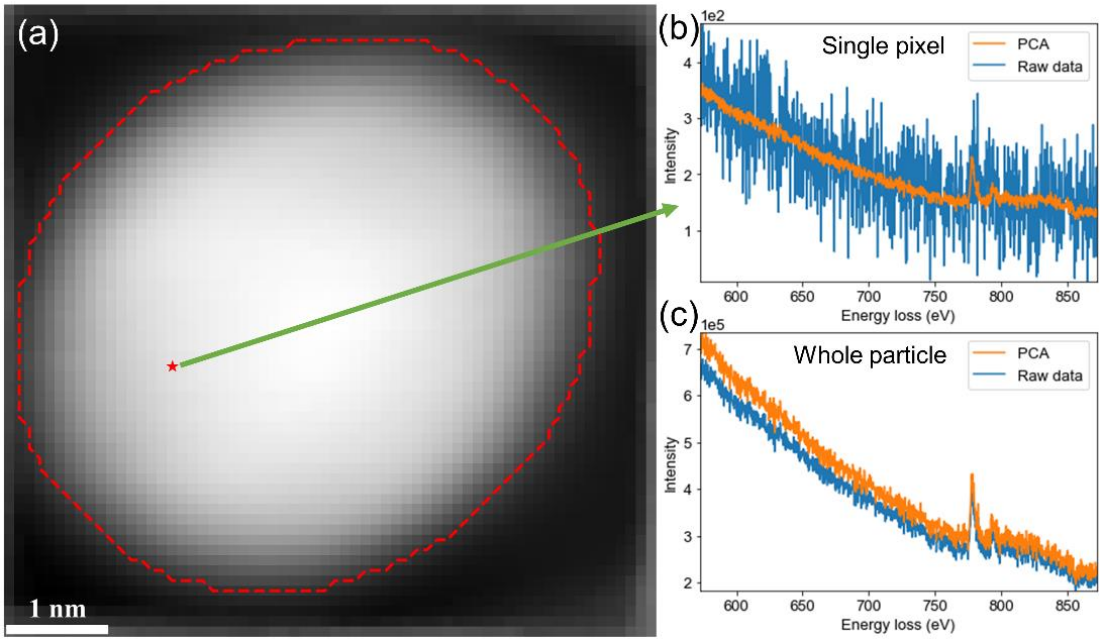

Figure 5.5. (a) Average-aligned ADF image of an unleached $PtCo_3$ nanoparticle. (b) The core loss spectrum from a single pixel before and after PCA denoising. (c) The core loss spectrum integrated over the whole particle (red circle in (a)) before and after PCA denoising using six components.

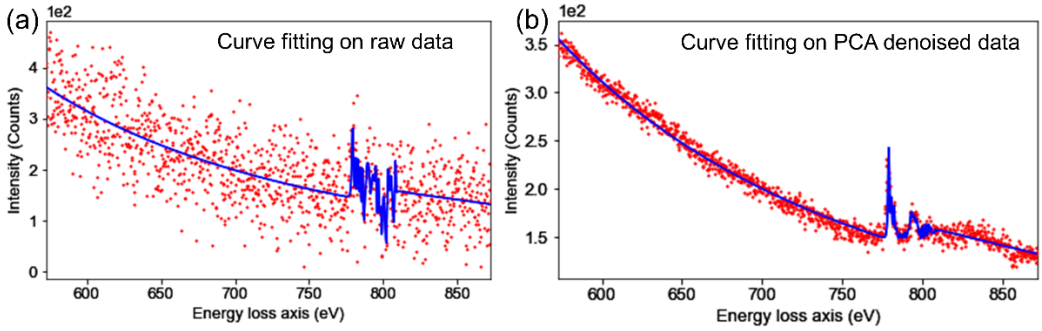

Figure 5.6. Curving fitting on the spectra of a single pixel before (a) and after (b) PCA denoising.

To investigate how the PCA denoising affects the ionization edges quantification, the integration method and curve fitting method were used to count Co atoms on the core loss spectra before and after the PCA denoising, respectively. In the integration method, deconvolution to remove the multiple scattering is not necessary since the nanoparticles with a size range between 3 nm and 6 nm are thin enough. An inverse power-law fitting

was used to subtract the EELS background. Curve fitting on the core loss spectra was performed using the Hyperspy Python library. Figure 5.6 compares curve fitting on the single-pixel core loss spectra before and after the PCA denoising. The curve fitting method does not work on the raw single-pixel spectrum, but provides a promising result on the denoised data. The spectrum of every pixel in the Pt-Co nanoparticle was then quantified to count Co atoms using these four different approaches. The obtained areal density maps are shown in Figure 5.7. Although both the integration method and curve fitting method give a similar total number of atoms, the quantification results at pixel level are different. Compared with the raw spectra quantification, the total number of Co atoms calculated on the denoised spectra are slightly smaller. This is because the PCA denoising increases the intensities before the ionization edge threshold more than the post-threshold intensities, as shown in Figure 5.5c. When removing the background using the power law fitting, more intensities are subtracted from the ionization edges. In addition, the total number of Co atoms was also calculated directly from the whole-particle spectra, and compared with the single-pixel spectra quantification, as shown in Figure 5.8. The first thing to note is that the quantification on the whole-particle spectra gives a larger number of atoms compared to the quantification on the single-pixel spectra. This reveals that the SNR in each EELS spectrum is influenced by the sample contamination and the equipment noise, and varies with the pixel. The total number of atoms calculated by applying the integration method and curve fitting method to the raw whole-particle spectra are ~2185 and ~3272, respectively. It is worth mentioning that the curve fitting method uses the theoretically calculated Hartree Slater partial scattering cross section (0.88 kb) for the quantification, but the integration method uses the experimentally measured scattering cross section (1.43 kb). The atom ratio between these two methods is ~1.5, close to the ratio of the measured partial cross section used

in the integration method to the theoretical Hartree Slater partial cross section used in the curve fitting method, which is ~1.62.

In conclusions, the PCA denoising does improve the SNR of the single-pixel core loss spectrum but also introduces some artefacts, and is therefore not trustful for the EELS quantification in these type of "noisy" datasets. Increasing the EELS signals by integrating the spectra over multiple pixels could also improve the SNR, leading to an accurate atom counting. Both the integration method and curve fitting method give the sensible and consistent quantification results. However, attention needs to be paid to the discrepancy of the atom counts between these two methods. In the following chapters, these quantification results will be compared to the EDS quantification to investigate which method is more accurate and suitable for the composition analysis on the Pt-Co nanoparticles.

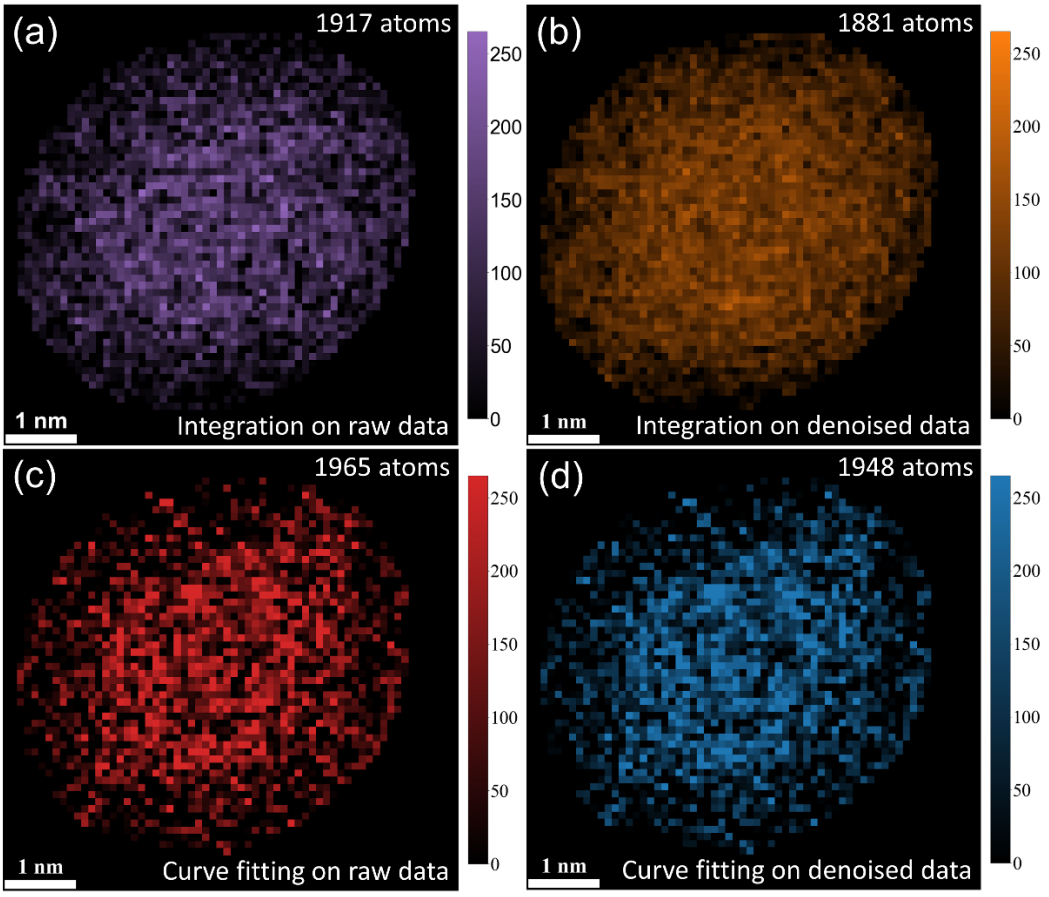

Figure 5.7. The Co EELS areal density maps of the leached $PtCo_3$ nanoparticle calculated using both the (a-b) integration method and (c-d) curve fitting method, on both raw data and PCA denoised data, respectively. Note that the colorbar unit is atoms/nm^2.

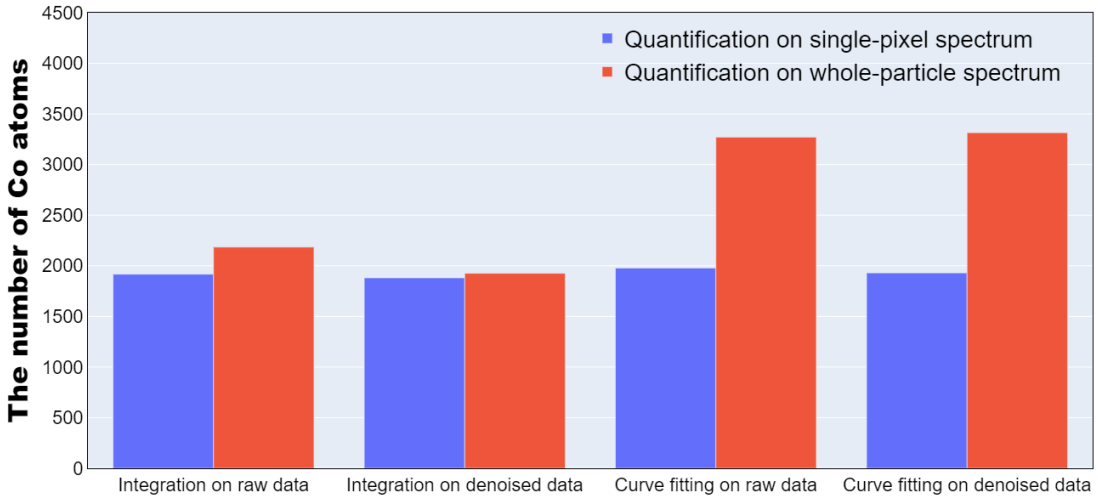

Figure 5.8. The histogram of the number of Co atoms in the leached $PtCo_3$ nanoparticle calculated using various methods.

5.5 EDS quantification

5.5.1 Brief review of EDS quantification approaches

K-factor approach

Historically, Castaing first built the X-ray spectrometer which is used to give quantitative composition information from bulk specimens in 1951 (Castaing, 1951). He successfully related the element concentration to the intensity of the corresponding characteristic X-ray by a simple expression:

$$\frac{I_i}{I_0} = K\frac{C_i}{C_0} \qquad \textit{Eq. 5.10}$$

Where I_0 and I_i are the measured X-ray intensity emerging from the specimen and the standard with the known composition, respectively. C_0 and C_i represent the element concentration in the standard and the specimen, respectively. K is a sensitivity factor and mainly depends on the atomic number (Z), the absorption (A) and of the

fluorescence (F) of X-rays. However, keeping changing samples to measure the standards is cumbersome and could reduce the quantification accuracy. The reason is that while changing samples, the probe current would change due to instrument instabilities and contamination build-up (Williams and Carter, 1996). To address this problem, the Cliff-Lorimer ratio technique was first proposed in 1972 (Cliff and Lorimer, 1975). For thin specimens where the X-rays adsorption and fluorescence can be neglected, the ratio of the X-ray intensities collected simultaneously from different elements in a binary specimen can be related to their concentration ratio by the following equations:

$$\frac{I_A}{I_B} = K_{AB}\frac{C_A}{C_B} \qquad \textit{Eq. 5.11}$$

$$C_A + C_B = 1$$

Where I_A and I_B are the measured X-ray intensities of the element A and B after background subtraction. C_A and C_B indicate the concentration of each element. K_{AB} is a Cliff-Lorimer factor and varies with the instrument and the accelerating voltage. K_{AB} can be either experimentally measured using standards with known compositions or theoretically calculated from first principles. This method can also be easily extended to ternary and higher order element systems. Compared with the first method, the Cliff-Lorimer ratio technique cancels out variations in the probe current, and has been widely applied to quantifying the composition of thin samples, such as nanoparticles (Liu et al., 2012, Esparza et al., 2017). However, the determination of an accurate enough K_{AB} using the theoretical calculation is hampered by difficulties in quantifying the geometry of the detection system. Also, the experimental measurement of K_{AB} requires careful multi-element sample preparation, which is challenging and time-consuming (Williams and Carter, 1996). Therefore, a more advanced technique, called ζ (zeta)-factor method, was developed.

ζ (zeta)-factor approach

Applications of the K-factor techniques are limited by difficulties in the fabrication of multi-element thin standards used for the K-factor experimental determination. The composition of the multi-element standards might also change during thinning. To tackle the problems, the ζ (zeta)-factor method which makes use of pure-element standards was developed by Watanabe and Williams in 2006 (Watanabe and Williams, 2006). In a thin binary specimen, the measured characteristic X-ray intensity (I_A) of a specific element (A) is proportional to its composition (C_A) and the sample mass-thickness (ρt) with the assumption of no absorption and fluorescence of X-rays, which can be described by the following equations:

$$\rho t = \zeta_A \frac{I_A}{C_A D_e} \qquad \textit{Eq. 5.12}$$

$$D_e = N_e I_p \tau$$

Where D_e is the total electron dose during the acquisition. N_e represents the electron counts, I_p is the incident probe current and τ is the acquisition time. ζ_A is a proportional factor that is independent of the acquisition time and probe current. Then Eq. 5.12 can also be applied to the second element (B) in the binary specimen, then we can have:

$$\rho t = \zeta_B \frac{I_B}{C_B D_e} \qquad \textit{Eq. 5.13}$$

$$C_A + C_B = 1$$

Rewriting the Eq. 5.12 and Eq. 5.13, C_A, C_B and ρt can be further expressed as:

$$C_A = \frac{\zeta_A I_A}{\zeta_A I_A + \zeta_B I_B}$$

$$C_B = \frac{\zeta_B I_B}{\zeta_A I_A + \zeta_B I_B} \qquad \textit{Eq. 5.14}$$

$$\rho t = \frac{\zeta_A I_A + \zeta_B I_B}{D_e}$$

Here, to improve the quantification precision, an absorption-correction term for a single X-ray line can be incorporated into a quantification iteration process to reduce the impact of the X-ray absorption(Goldstein, 1977, Watanabe et al., 1996).

Similarly, the ζ-factor can be determined by both the experimental measurement and theoretical calculation. For the theoretical determination, the ζ-factor can be calculated by:

$$\zeta = \frac{M}{N_A Q \omega a [\Omega/(4\pi)] \varepsilon} \qquad \textit{Eq. 5.15}$$

Where M represents the atomic weight and N_A is the Avogadro's number. Q is the ionization cross-section, ω indicates the fluorescence yield, a is the relative transition probability, Ω is the collection angle and ε represents the detector efficiency. Clearly, the ζ-factor only relies on the atomic number and the accelerating voltage.

Unlike the experimental measurement of the K-factor where a multi-element standard with the known composition is required, determining the ζ-factor makes use of a pure-element, thin standard. Fabricating the pure-element, thin standard is easy and cheap, and do not change the composition during thinning. Two methods including pure-element standards method and universal standards method are often used to experimentally determine the ζ-factor. In the former method, sample preparation techniques such as evaporation, electron deposition and focused ion-beam can be used

to synthesize a thin standard of a specific element. The thickness of the pure-element thin standard can be measured by the transmission electron microscopy. Its ζ-factor can be easily calculated by measuring the characteristic X-ray intensity of the element. In the universal standards method, the ζ-factors of only a few elements are experimental measured and the ζ-factors of the other elements are obtained by inter/extrapolation from those measured ζ-factors (Watanabe and Williams, 2006).

Scattering cross section approach

Quantifying EDS signals into partial scattering cross sections is much more straightforward compared to the EELS quantification. For thin samples such as nanoparticles, the X-ray absorption and fluorescence can be neglected. In the same way that the EELS scattering cross section is defined, the number of atoms per unit area of a given element, *x*, should be linearly proportional to the corresponding X-ray counts (MacArthur et al., 2016). Thus, we have:

$$N_\rho = \frac{I_x}{D \cdot \sigma_x} \qquad \textit{Eq. 5.16}$$

Here, N_ρ is the number of atoms per unit area (the areal density), I_x is the X-ray intensities above background of the element *x*. σ_x indicates the EDS partial scattering cross section of a single atom for the corresponding element. D is the total number of incident electrons and can be expressed as:

$$D = \frac{i\tau}{e} \qquad \textit{Eq. 5.17}$$

Where i and τ indicate the beam current and the exposure time, respectively, and e is the electronic charge. Then, the areal density of atoms quantified using the EDS signals can be calculated by:

$$N = \frac{I_x e}{\sigma_x i \tau} \cdot S \qquad \textit{Eq. 5.18}$$

Where N is the number of atoms in the pixel, and *S* is the pixel area. Here, the beam current is calibrated using the EELS drift tube under the different emission currents. The experimental acquisition parameters, background subtraction and integration windows used for both the Pt and Co EDS quantifications are listed in Table 5.2.

Pixel exposure time	Holder title angle	Energy dispersion (keV)	Number of frames
0.005s	+X 20 °	0.01	40
EDS peak	Background removal Windows (keV)	Integration windows (keV)	Partial cross-section (barns)
Co: Kα Pt: Mα+Mβ+Lα+Lβ1	Co Kα: [6.512, 6.651], [7.209, 7.349] Pt Mα: [1.768, 1.854], [2.400, 2.486] Pt Mβ: [1.768, 1.854], [2.400, 2.486] Pt Lα: [9.084, 9.154], [9.651, 9.722] Pt Lβ1: [10.642, 10.714], [11.427, 11.498]	Co Kα: [6.651, 7.209] Pt Mα: [1.854, 2.236] Pt Mβ: [1.854, 2.236] Pt Lα: [9.155, 9.651] Pt Lβ1: [10.7135, 11.4265]	Co Kα: 5.88 Pt L+M: 20.60

Table 5.2 Summary of data acquisition and processing parameters for the EDS quantification.

5.5.2 Pt and Co atom counting on the nanoparticle

The EDS spectrum covers an energy loss range from 0 to 20.48 keV with an energy dispersion of 0.01 keV. Both Pt and Co peaks are included within a single EDS spectrum and can be quantified simultaneously. In order to ensure the consistency between atom counting and the single-atom EDS partial cross sections calibration, the three window approach (two background windows and one integration window) was used for the EDS quantification. Given that the Bremsstrahlung is negligible and neighbouring peaks are not overlaid, the subtracted background was estimated by averaging the intensities in the two background windows on each side of the corresponding X-ray peak. However, counting statistics is the major factor that hampers the EDS quantification accuracy. To achieve a high enough number of X-ray counts for atom counting, multiple EDS peaks with good SNR (for Pt, L+M peaks; for Co, Kα peak) were used in this work. Figure 5.9 displays the quantified Co and Pt areal density maps of the same nanoparticle. The total number of Co and Pt atoms in this

nanoparticle quantified using the EDS signals are 2182 and 3240, respectively. Atom counting was also performed on the whole-particle spectrum, providing the same total number of Co and Pt atoms. Another important finding is that Co atom counts from the EDS quantification (2182) agree well with the number calculated using the integration method in the EELS quantification (2185). It reveals that for the EELS quantification, the integration method using the calibrated partial cross section is more accurate than the curve fitting method with the theoretical partial cross section. Additionally, the measured total number of atoms is within 7% agreement with the estimated total number of atoms if the nanoparticle is assumed to have a spherical shape. This again confirms the reliability of atom counting using the EDS or EELS signals.

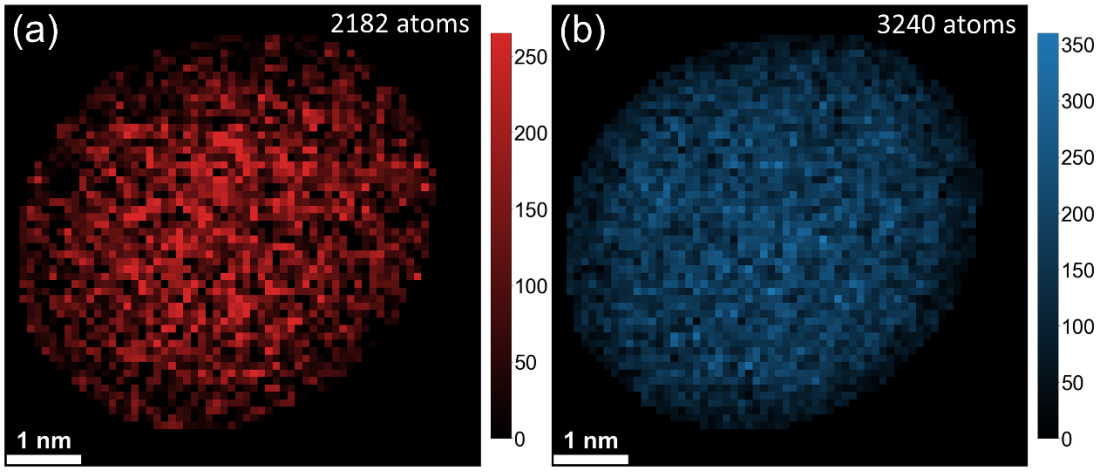

Figure 5.9. The EDS areal density maps of the leached $PtCo_3$ nanoparticle for Co (a) and Pt (b). The unit is atoms/nm^2.

To conclude, a high accuracy composition quantification using experimentally calibrated partial scattering cross sections for both EELS and EDS signals has been achieved. In the "noisy" datasets generated by the nanoparticles studied, the background subtraction in the EELS quantification can be influenced by equipment noise, sample contamination and oxidation (Tenailleau and Martin, 1992, Williams and Carter, 1996). Whereas, the EDS quantification is less impacted by the equipment and

sample condition, and can be a robust tool to precisely measure the composition variations of the Pt-Co nanoparticles at an atomic scale.

5.6 ADF quantification

ADF signals which originate from the incoherent electrons only rely on the atomic number and sample thickness. It is possible to extract structure and composition information from ADF images, simultaneously. Considerable research has been conducted in quantifying ADF intensity into the number of atoms (Jones et al., 2014, Varambhia et al., 2016, Aarons et al., 2017). Techniques for ADF quantification includes simulation matching method (Aarons et al., 2017), statistical decomposition methods (Van Aert et al., 2011, De Backer et al., 2013), hybrid statistics-simulations method (De Backer et al., 2017) and newly developed hidden Markov model method (De Backer et al., 2020, De Backer and Van Aert, 2020). The simulation matching method is much more straightforward and can be related to spectroscopic signals (EDS and EELS) quantification. In this work, the simulation matching method was used for ADF quantification, and its related techniques and principles will be described here.

5.6.1 ADF scattering cross section theory

The value of each pixel in a simulated STEM image is often in the form of a fraction of the incident electrons. In order to directly compare experimental ADF image intensities to the simulated ones, the experimental images should be normalised with respect to the incoming electron beam, to an absolute scale (LeBeau et al., 2010, Wang et al., 2011). Additionally, the ADF detector response has been found to be both inhomogeneous and asymmetric and varies between different electron microscopes (Martinez et al., 2015). Thus, it needs to be carefully considered to improve the quality

of quantitative analyses. Incorporating a detector map in simulations for every experiment carried out is very time-consuming and wastes lots of computing power. Alternatively, the detector response can also be incorporated into the experimental image normalisation. Then, we can have:

$$I_{normalised} = \frac{I_{experiment} - I_{vacuum_experiment}}{I_{detector} - I_{vacuum_detector}} \left(\frac{i_{detector}}{i_{experiment}}\right) \qquad \textit{Eq. 5.19}$$

Where $I_{experiment}$ is the measured intensity of the experimental ADF image. $I_{detector}$ represents the measured intensity of the detector in vacuum. $I_{vacuum_experiment}$ and $I_{vacuum_detector}$ indicate the vacuum intensity in the ADF image and detector map, respectively. The vacuum intensity is often non-zero because of the amplifier offset. $\frac{i_{detector}}{i_{experiment}}$ is the incident probe current ratio between the detector mapping and experimental imaging. The scattering cross section describes the effective area corresponding to the probability of electron scattering, and it can be mathematically calculated by multiplying the normalised intensity by the area of pixels.

In ADF STEM imaging, the annular geometry of a sufficiently large detector can impose incoherence, making the resulting image free from contrast reversal (Nellist and Pennycook, 2000). This means that the vacuum is always dark and atoms are bright in an ADF image. Accordingly, the measured incoherent ADF intensity can be described as a convolution between the probe intensity profile $p(\boldsymbol{r_p} - \boldsymbol{r})$and the object function $o(\boldsymbol{r})$ (Nellist and Pennycook, 2000, MacArthur et al., 2013), Eq. 5.20.

$$I(\boldsymbol{r_p}) = \int p(\boldsymbol{r_p} - \boldsymbol{r}) o(\boldsymbol{r}) d\boldsymbol{r} \qquad \textit{Eq. 5.20}$$

Where $\boldsymbol{r}$ is a 2D position vector in sample plane, where the probe is located at $\boldsymbol{r_p}$. Regarding the scattering cross sections we integrate over an area of pixels, we can have:

$$\int_{area} I(\boldsymbol{r_p})d\boldsymbol{r_p} = \int o(\boldsymbol{r}) \int_{area} p(\boldsymbol{r_p} - \boldsymbol{r})d\boldsymbol{r_p}d\boldsymbol{r} \qquad \textit{Eq. 5.21}$$

However, the detector calibration method has normalised the experimental ADF image intensity as a fraction of the incident beam. Thus, the integration of the normalised probe function over the area is unity (MacArthur et al., 2013). The integrated normalised intensity of the area can be expressed as:

$$\int_{area} I(\boldsymbol{r_p})d\boldsymbol{r_p} = \int o(\boldsymbol{r})d\boldsymbol{r} \qquad \textit{Eq. 5.22}$$

The real image is often in the form of discrete pixels, where each pixel has an intensity I_i and the same area A. Then, the scattering cross section of the area can be written as:

$$\Theta = A\sum_i I_i = \int o(\boldsymbol{r})d\boldsymbol{r} \qquad \textit{Eq. 5.23}$$

It can be seen that the resulting scattering cross section only relies on the object function rather than the probe function. The ADF scattering cross section is robust to many imaging parameters, including defocus, astigmatism, magnification, probe size, convergence angle and source coherence (MacArthur et al., 2013). With the appropriate calibration of the ADF detector, the calculated scattering cross sections are absolute value and can be directly compared to the simulation library for atom counting.

5.6.2 Detector calibration

In practice, the detector response towards electrons at small scattering angles is often different from that at large scattering angles. It has been shown that the detector sensitivity at low angles is only one third that at high angles (MacArthur et al., 2014). Moreover, the inner and outer collection angles of the detector do not always correspond to the shadow of the detector projected on the CCD. Usually, the inner hole

of the detector is surrounded by a dead region, which is not sensitive to electrons. For the outer collection angle, some electrons scattered to high angles might be cut off by the post-specimen optics. The collection angles of the detector also rely on the camera-length used (Martinez et al., 2015, Varambhia, 2018). It has been reported that measuring the collection angles from the detector shadow could lead to an overestimation of the ADF scattering cross sections (Martinez et al., 2015). In addition, the electron flux which describes the amount and distribution of the scattered electrons at the detector plane (diffraction plane) also could influence the ADF quantification (Martinez et al., 2015). Due to the inhomogeneity and asymmetry of the detector response, it is important to know what proportion of the scattered electrons reaches each region of the detector. Then, Eq. 5.19 can be re-written as:

$$I_{normalised} = \frac{I_{experiment} - I_{vacuum_experiment}}{\xi \cdot \overline{D}} \left(\frac{i_{detector}}{i_{experiment}}\right) \qquad \textit{Eq. 5.24}$$

Where $\xi \cdot \overline{D}$ is the normalization factor. ξ is a proportionality factor, $\overline{D}$ represents the average detector response. Considering the scattered electron flux distribution, the normalization factor is given by:

$$\xi \cdot \overline{D} = \int \frac{F(\boldsymbol{k}) \cdot d_{DSP}(\boldsymbol{k}) d^2\boldsymbol{k}}{F(\boldsymbol{k}) \cdot d_{HDP}(\boldsymbol{k}) d^2\boldsymbol{k}} \cdot \overline{D} = \int \frac{F(\boldsymbol{k}) \cdot D(\boldsymbol{k}) d^2\boldsymbol{k}}{F(\boldsymbol{k})\, d\boldsymbol{k}} \qquad \textit{Eq. 5.25}$$

Where $\boldsymbol{k}$ is the vector in reciprocal space. $d_{DSP}(\boldsymbol{k})$ and $d_{HDP}(\boldsymbol{k})$ indicate the actual detector sensitivity profile and homogeneous detector sensitivity profile, respectively. $D(\boldsymbol{k})$ corresponds to the recorded detector intensity map subtracting the vacuum intensity ($I_{detector} - I_{vacuum_detector}$). $F(\boldsymbol{k})$ represents the electron flux distribution on the diffraction plane, which can be obtained by either simulation or experiment. $F(\boldsymbol{k})$ can be further approximated as a power-law function by rotationally averaging the CBED patterns, then we can have:

$$F(\boldsymbol{k}) = A \cdot \rho^{-\boldsymbol{b}} \qquad \textit{Eq. 5.26}$$

Where A represents a scaling factor and ρ is the scattering angle. b is a fitting variable that is robust to composition and thickness. At this point, all three factors including the collection angles, the detector inhomogeneous response and the electron flux distribution are taken into consideration in the measurement of $\xi \cdot \overline{D}$.

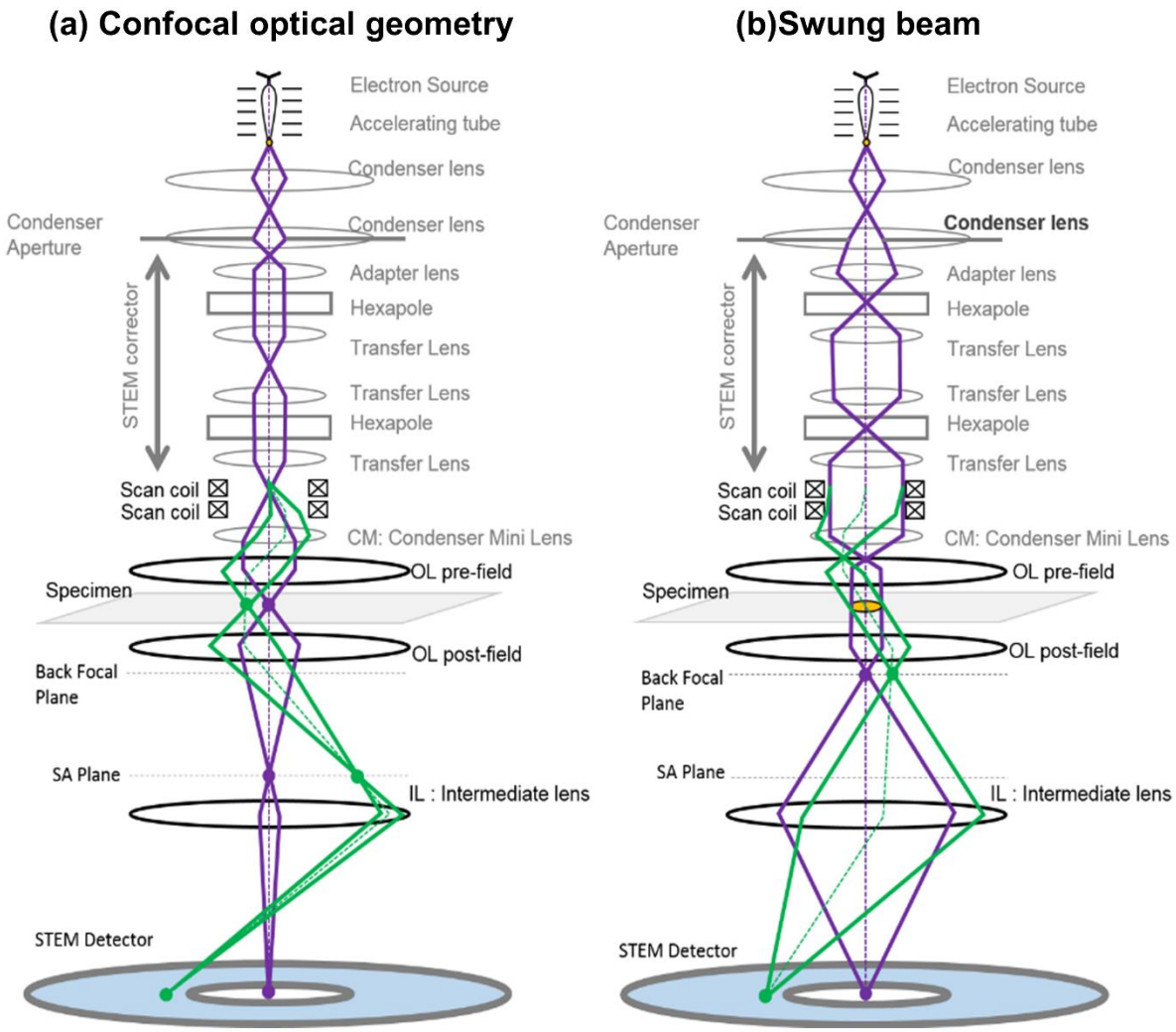

Figure 5.10 Diagrams of optical ray for (a) the confocal optical geometry, (b) the swung beam method. Figure reprinted from (Jones et al., 2018)

Two approaches for detector mapping have been developed, which are confocal optical geometry (LeBeau et al., 2008, Fritz et al., 2011, Findlay and LeBeau, 2013) and swung beam methods (Jones et al., 2018), Figure 5.10. In the former method, the pre-specimen

lenses are configured as in the STEM probe mode while the post-specimen lenses are configured as in the TEM-imaging mode, where the probe scanned at the sample plane is reimaged in the detector plane. In the latter method, a parallel pencil beam is formed and scanned at the sample plane, while the post-specimen lenses are configured to be in the TEM-diffraction mode to map the detector in angular space.

The confocal optical geometry method is appealing because its optical configuration can be easily selected by a press of button in most microscopes. However, the configuration of its post-specimen lenses is different from that in the STEM imaging experiments. As a result, the disparity in the electron flux distribution and cut-off could be introduced. The swung beam approach overcomes this problem and allows for a more accurate measurement of the collection angles. This method can also be extended to determining the inner-angles of EELS acceptance apertures. In this work, the swung beam method was used for the determination of the ADF detector collection angles. Figure 5.11 shows the ADF detector map recorded at a pixel dwell time of 4 us using the swung beam method.

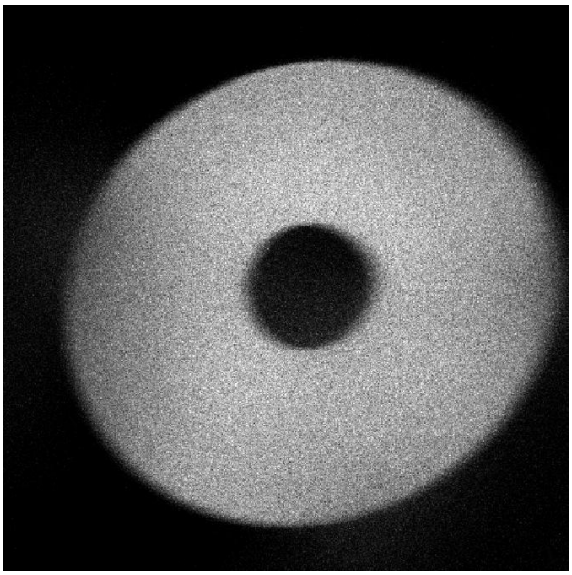

Figure 5.11. The ADF detector efficiency scan.

5.6.3 Channelling effect

Usually, viewing the specimen along a low order zone-axis is necessary for atomic-resolution STEM ADF imaging. Quantitative interpretation of the atomic-resolution images is difficult because the ADF scattering cross section of a column is not linearly proportional to the number of atoms. When atoms are aligned parallel to the incident probe, a small lensing (focus) effect will be introduced on the beam, as shown in Figure 5.12. The subsequent atoms in the atomic column experience a more focused probe, leading to a stronger electron scattering than the first atom (Van Dyck and De Beeck, 1996). As the result, the subsequent atoms contribute more to the integrated intensity of the column than the first atom and so on. Such a non-linear relationship between the scattering cross section and the number of atoms is referred to channelling effect.

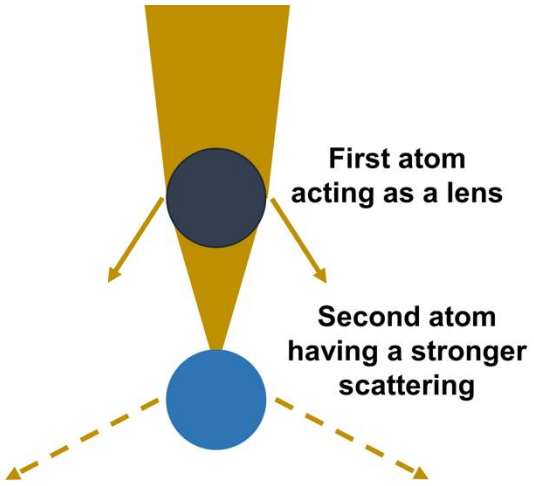

Figure 5.12 Schematic of electron channelling effect. A column of atoms would produce a higher intensity than the atoms would produce individually.

Heavier atoms normally have a stronger channelling effect than light atoms. In the case of the Pt-Co bimetallic nanoparticles where an atomic column could have a mixture of Pt and Co atoms, the specific sequence of atoms in the column will influence the

integrated intensity. Thus, the spectroscopic signals (EDS and EELS) are often required for the quantification of the bimetallic nanoparticles (Varambhia et al., 2018).

5.6.4 STEM ADF simulations

5.6.4.1 Multislice theory

STEM simulation is on the basis of the multislice approach, where the specimen is divided into many thin slices perpendicular to the optical axis (Kirkland, 1998), as shown in Figure 5.13. Because of the fast speed and high energy of the incident electrons, the transmission time of these electrons is very short compared to the vibration time of the crystal lattice, which is known as the frozen phonon approximation. The crystal lattice vibrations arise from the thermal effect.

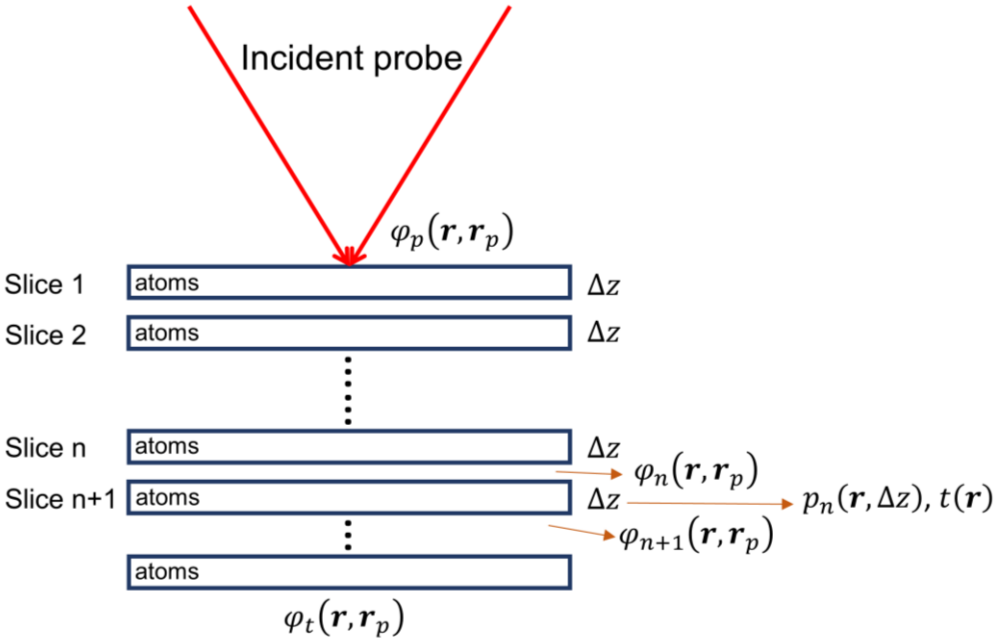

Figure 5.13 Multislice decomposition of a thick specimen.

Each sample slice is thin enough to be regarded as the weak phase object, where the incident electrons only experience small deviations in their paths when passing through.

Thus, the effect of the thin slice can be modeled as a simple transmission function, given by:

$$t(\boldsymbol{r}) = \exp[i\sigma_e v_z(\boldsymbol{r})] \approx 1 + i\sigma_e v_z(\boldsymbol{r}) \qquad \textit{Eq. 5.27}$$

Where $\boldsymbol{r}$ is a 2D position vector in real space. σ_e is a scaling factor and $v_z(\boldsymbol{r})$ represents the projected atomic potential of the thin slice. In the STEM mode, a probe is focused on the sample plane by the objective lens. An aberration wave function of the objective lens over the objective aperture can be expressed as:

$$H(\boldsymbol{k}) = A(\boldsymbol{k})\exp[-i\chi(\boldsymbol{k})] \qquad \textit{Eq. 5.28}$$

Where $\boldsymbol{k}$ is a 2D vector in reciprocal space. $A(\boldsymbol{k})$ and $\chi(\boldsymbol{k})$ indicate the aperture shape function and the aberration function, respectively. $A(\boldsymbol{k})$ can be described by:

$$\begin{aligned} A(\boldsymbol{k}) &= 1; \lambda|\boldsymbol{k}| = \alpha < \alpha_{\boldsymbol{max}} \\ A(\boldsymbol{k}) &= 0; \qquad \text{otherwise} \end{aligned} \qquad \textit{Eq. 5.29}$$

Where $\alpha_{\boldsymbol{max}}$ indicates the maximum semiangle allowed by the objective aperture and λ is the electron wavelength. In most electron microscopes, $\chi(\boldsymbol{k})$ is mainly dominated by the spherical aberration (C_s) and defocus (Δf), and can be calculated by:

$$\chi(\boldsymbol{k}) \approx \frac{2\pi}{\lambda}\left(\frac{1}{4}C_s\lambda^4k^4 - \frac{1}{2}\Delta f\lambda^2k^2\right) \qquad \textit{Eq. 5.30}$$

Where k is the spatial frequency. The aberrated electron probe wave function at position $\boldsymbol{r}_p$ in the sample plane can be obtained by integrating the aberration wave function over the objective aperture. Then, we can have:

$$\varphi_p(\boldsymbol{r}, \boldsymbol{r}_p) = A_p \int_0^{\alpha_{max}/\lambda} \exp[-i\chi(\boldsymbol{k}) - 2\pi i\boldsymbol{k}\cdot(\boldsymbol{r} - \boldsymbol{r}_p)]d^2\boldsymbol{k} \qquad \textit{Eq. 5.31}$$

Where A_p is a normalization constant chosen to yield:

$$\int \left|\varphi_p(\boldsymbol{r},\boldsymbol{r}_p)\right|^2 d^2\boldsymbol{r} = 1 \qquad \textit{Eq. 5.32}$$

The electron probe wave function after passing through the slice n^{th} with a thickness of Δz is:

$$\varphi_{n+1}(\boldsymbol{r},\boldsymbol{r}_p) = p_n(\boldsymbol{r},\Delta z)\otimes[t(\boldsymbol{r})\cdot\varphi_n(\boldsymbol{r},\boldsymbol{r}_p)] \qquad \textit{Eq. 5.33}$$

Where $p_n(\boldsymbol{r},\Delta z)$ is the propagator function of the electron wave, which can be associated with the Fresnel diffraction within the slice.

After passing through all the slices, the exit wave function ($\varphi_t(\boldsymbol{r},\boldsymbol{r}_p)$) is diffracted onto the detector plane, which can be calculated by a Fourier transform:

$$\Psi_t(\boldsymbol{k},\boldsymbol{r}_p) = FT\left[\varphi_t(\boldsymbol{r},\boldsymbol{r}_p)\right] = \int \exp(2\pi i\boldsymbol{k}\cdot\boldsymbol{r})\cdot\varphi_t(\boldsymbol{r},\boldsymbol{r}_p)\,d^2\boldsymbol{r} \qquad \textit{Eq. 5.34}$$

Here, the intensity of $\left|\Psi_t(\boldsymbol{k},\boldsymbol{r}_p)\right|^2$ is in the form of the CBED pattern, which can be incoherently integrated over the ADF detector to produce an 'image' of the scanned point. The final ADF signal for one probe position ($\boldsymbol{r}$) can be calculated using the following equation:

$$g(\boldsymbol{r}_p) = \int_{k_{Dmin}}^{k_{Dmax}} \left|\Psi_t(\boldsymbol{k},\boldsymbol{r}_p)\right|^2 d^2\,\boldsymbol{k} \qquad \textit{Eq. 5.35}$$

Where λk_{Dmax} and λk_{Dmin} indicate the inner and outer collection angles of the ADF detector. By repeating the above calculation process over phonons at each probe position, an ADF STEM image of the specimen can be simulated. The multislice approach has its advantages in the fast computation speed and high precision (Kirkland et al., 1987). The algorithm has been implemented in the Multem software which was used for simulations in this project (Lobato and Van Dyck, 2015).

5.6.4.2 ADF simulations on Pt-Co crystals

For off-axis non-channelling Pt-Co nanoparticles, the total ADF scattering cross section is linearly proportional to the number of atoms. Thus, we only need to simulate the ADF cross sections of a single Pt or Co atom for quantifying the off-axis nanoparticles. Here, a 6×6 Pt super cell and a 6×6 Co super cell were simulated along the <100> zone axis, with a 1024×1024 reciprocal mesh. The Debye-Waller factors (DMFs) for Pt and Co were calculated using the parametrization at 295.15 K temperature (Gao and Peng, 1999). The root mean square (rms) displacements derived from DMF are 0.06917 Å for Pt and 0.06244 for Co. The simulation parameters are summarized in Table 5.3. The ADF scattering cross sections of atomic columns were calculated by integrating the intensities over the columns within the simulated images using the Voronoi cells. The simulated ADF scattering cross sections are presented in Table 5.4 and compared to the experimentally measured EDS and EELS partial scattering cross sections (Varambhia et al., 2018). The simulated ADF cross sections are three orders of magnitude larger than the EELS cross sections and six orders of magnitude larger than the EDS ones. This is as expected since when the incident electrons interact with the atoms, an elastic scattering event occurring has a much higher probability than the occurring of an inelastic scattering event or an ionisation event that releases an X-ray photon.

Accelerating voltage	200 kV
Convergence angle	22.48 mrad
ADF detector collection angles	72.8 – 271 mrad
Phonon configuration	50
Potential parameterization	Lobato et al.
Potential sampling in reciprocal space	1024×1024
Potential slicing	Slice by plane
Scanning grid in real space	100×100 pixels
Root mean square displacement of Pt	0.06917
Root mean square displacement of Co	0.06244

Table 5.3 Summary of the parameters for the multislice simulation

Scattering cross section (**σ**)	Pt	Co
ADF	1.09 Mb	0.18 Mb
EELS	1.02 Kb	1.43 Kb
EDS	20.6 b	5.88 b

Table 5.4 Summary of single atom partial cross sections (in barns) for both ADF, EDS and EELS signals. Note that ADF cross sections are from simulation, EELS and EDS cross sections are experimentally measured values using needle standards. Note that Mb = 10^3 Kb = 10^6 b.

However, when quantifying the on-zone axis Pt-Co nanoparticles, the channelling effect needs to be considered. The ADF simulations have to be performed at different atomic column thicknesses. It has been reported that both ordered $PtCo_3$ and Pt_3Co have a crystal structure of $L1_2$ type with the lattice parameters of 0.36636 nm and 0.38540 nm, respectively (Kootte et al., 1991), as shown in Figure 5.14. As mentioned before, the ADF scattering cross section heavily relies on the atomic number (Z) and the sample thickness. Quantifying the number of atoms in a multi-elements column cannot be achieved by using the ADF cross section alone. Therefore, atom counting on the bimetallic nanoparticles using the ADF signals can only be achieved on the ordered Pt-Co crystals aligned along <001> zone axis where each atomic column consists of

pure Pt or Co atoms. Here, the $PtCo_3$ and Pt_3Co crystals were simulated along <001> direction using the multislice method implemented in the MULTEM software. The microscope settings used in the STEM simulations are the same as the experimental parameters and summarized in Table 5.3.

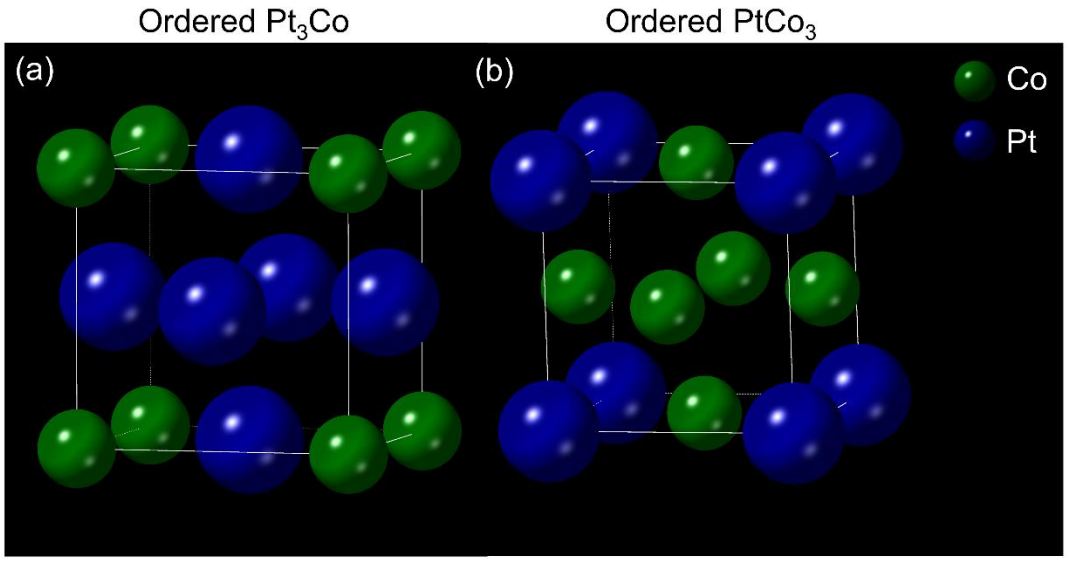

Figure 5.14. The unit cells of ordered Pt_3Co (a) and $PtCo_3$ (b), produced by the Crystal Maker™ software.

For the ordered $PtCo_3$ phase, a <001> projected super cell size of 2.1982 nm × 2.1982 nm was used. The crystal was simulated by thickness with a step thickness of 0.36636 nm. The sample thickness was set up to 7.3272 nm, consistently with the maximum nanoparticle size. A numerical real space grid of 100 × 100 scan positions was chosen as the scanning area, yielding a sampling resolution of 0.0146 nm/pixel. For the ordered Pt_3Co phase, a 6×6 super cell with the size of 2.3124 nm × 2.3124 nm was sampled along the <001> zone axis. The crystal thickness was gradually increased to 7.7080 nm by a step thickness of 0.38540 nm. For the scanned region in real space, a pixel size of 0.0154 nm was achieved by using a numerical grid of 100 × 100 scan positions. In all calculations, the Einstein model with 50 phonon configurations was used for the multislice frozen phonon calculation. The potential sampling in reciprocal space was

1024 × 1024 pixels, while the potential slicing was chosen as slicing by planes. Figure 5.15 displays the simulated image of the ordered $L1_2$ structured $PtCo_3$ and Pt_3Co crystals with 20 unit cells along the beam direction. Both Pt and Co atomic columns have two different sites in the simulated ADF images of $PtCo_3$ and Pt_3Co, respectively. Centre Site is on the upper layer with respect to side site. It can be seen that for the atomic columns having the same number of atoms, the simulated ADF cross sections on the side site are slightly larger than those on the centre site. The reason is that during the simulation, the incident electrons first interact with the atoms on the centre site in the upper layer and then propagate to the atoms on the side site. The atoms in the upper layer could contribute some intensities to the atoms on the side site, leading to the slight overestimate cross sections on the side site. However, these small discrepancies are negligible compared to the differences of the ADF scattering cross sections between Pt and Co elements.

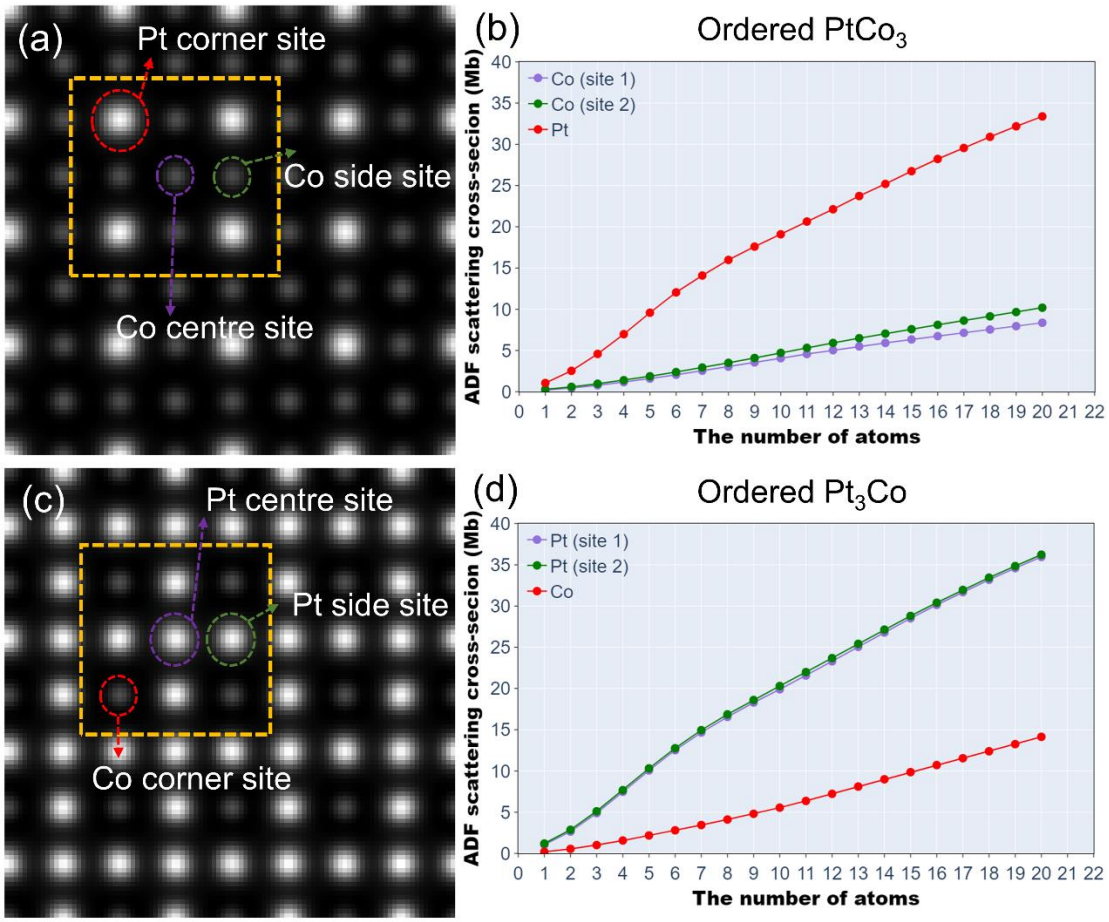

Figure 5.15. (a)(c) The simulated ADF images of ordered $PtCo_3$ and Pt_3Co crystals. (b)(d) The simulated cross sections for different atomic sites as a function of atomic column thickness.

5.6.5 Relating spectroscopic cross sections to ADF cross section

With the simulated reference libraries for the scattering cross sections (Table 5.4) and the properly calibrated detector map (Figure 5.11), the ADF quantification was then performed on the same unleached $PtCo_3$ nanoparticle, as shown in Figure 5.16. The integrated total scattering cross section in this nanoparticle is about 3841 Mb. Solely using the ADF scattering cross section is not enough to quantify the number of Pt and Co atoms in this nanoparticle. However, in previous chapters, the numbers of Pt and Co atoms have been successfully measured from the spectroscopic signals, which are 3240 and 2182 atoms, respectively. Given the fact that this nanoparticle is off-axis, its

ADF cross section can also be calculated by multiplying the simulated single-atom cross sections by the number of atoms quantified from the spectroscopic signals. As the result, the ADF cross section of this nanoparticle derived from the spectroscopic quantification is about 3924 Mb. The calculated ADF cross sections between the two quantification techniques are within ~2% agreement with one another. Here, the EELS and EDS quantification has been successfully related to the ADF quantification via representing these signals as the scattering cross sections. Such a great agreement between these quantification techniques confirms the high accuracy of the composition measurements used in this work.

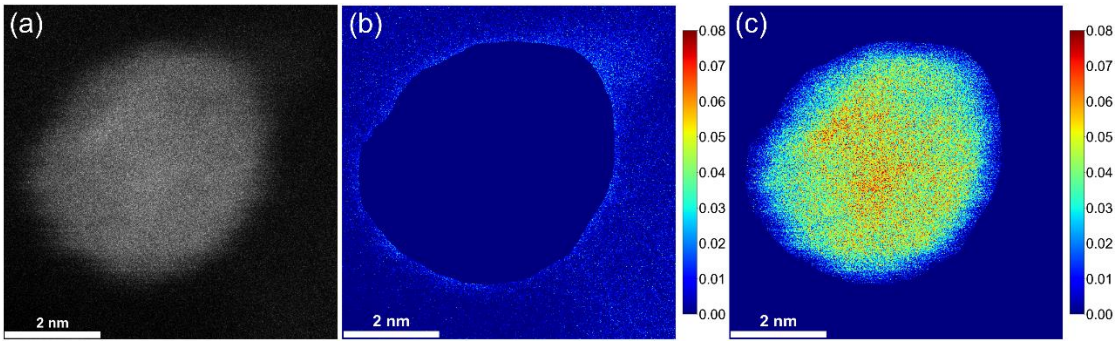

Figure 5.16. (a) The experimental single-frame ADF image of the PtCo nanoparticle. (b) The normalised background intensities of the nanoparticle. (c) The ADF scattering cross sections of the particle. Note that the colorbar unit is Mb.

5.6.6 On-axis ADF Pt-Co bimetallic nanoparticle quantification

Quantifying the intensities of atomic columns on the atomic-resolution ADF images into the scattering cross sections could allow us to interpret the crystal structure of the sample. In this application, when the $L1_2$ type structured $PtCo_3$ or Pt_3Co crystals are viewed along <001> direction, the imaged atomic columns are composed of the pure element (Pt or Co). Following the ADF simulations we carried out before, a huge discrepancy between the scattering cross sections of pure Pt and pure Co atomic columns can be observed, as shown in Figure 5.15. To investigate the crystal structure

of the Pt-Co bimetallic nanoparticles, the ADF quantification was performed on an atomic-resolution image of an on <001> zone axis unleached Pt_3Co nanoparticle, as shown in Figure 5.17. The selected region is likely to have three projected unit cells with the $L1_2$ type structure, where Co atoms occupy the corner sites and Pt atoms are at the centre and side sites. The atomic columns at the corner sites of each unit cell have a scattering cross section of ~ 8.3 Mb, much smaller than the atomic columns at the other sites (~13.3 Mb). Comparing the measured cross sections with the Pt and Co simulation libraries in Figure 5.15, there should be 13 Co atoms in every atomic column at the corner sites and 6 Pt atoms in every atomic column at the other sites. However, assuming that the thickness of the selected region equals the nanoparticle's diameter, which is about 3.54 nm, there would be 9-10 atoms along the viewing direction. Therefore, the atomic columns at the different sites appear to have mixed atoms instead of pure atoms. It reveals that the crystal structure might be well-ordered as $L1_2$ type in the nanoparticle core, but randomly ordered in the near-surface regions of the $PtCo_3$ nanoparticle.

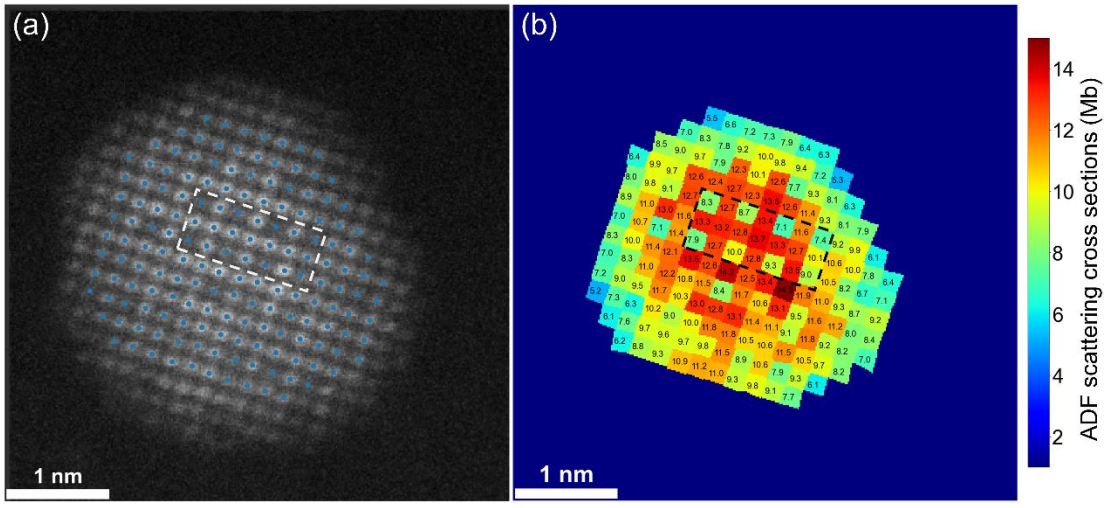

Figure 5.17. (a) The experimental non-rigid aligned ADF image of an unleached Pt_3Co nanoparticle. (b) The measured ADF scattering cross sections of atomic columns in the nanoparticle.

5.7 Error analysis

5.7.1 EDS atom counting error analysis

For a single measurement, the error of an individual quantification can be regarded as the propagation of a series of uncorrelated errors (Lyons and Louis, 1991, Watanabe and Williams, 2006). Generally, the error (d_f) of a function $f = f(x_1, x_2, \dots, x_n)$ can be expressed from the standard deviations (d_i) of uncorrelated variables (x_i) as:

$$d_f^2 = \sum_{i=1}^{n} (\frac{\partial f}{\partial x_i} d_i)^2 \qquad \textit{Eq. 5.36}$$

For an individual EDS atom counting, the uncorrelated variables contributing to the error (Δn) are the scattering cross section of a single atom (σ_{single}), the measured X-ray counts (I), the probe current (i) and the pixel exposure time (τ). The contributions from the probe current and the pixel exposure time can be considered negligible (MacArthur et al., 2016). Accordingly, the error of EDS atom counting can be expressed as:

$$\Delta n = n \sqrt{\left[(\frac{\Delta \sigma_{single}}{\sigma_{single}})^2 + (\frac{\Delta I}{I})^2 \right]} \qquad \textit{Eq. 10}$$

Where n is the calculated number of atoms. $\Delta\sigma_{single}$ and ΔI indicate the standard deviation in σ_{single} and I. respectively. The ΔI term can be $\sqrt{I}$ assuming the EDS signals follow the Poisson distribution.

5.7.2 EELS atom counting error analysis

The error analysis for the EELS atom counting is more complicated. In addition to the counting statistics and single-atom cross section errors, contributions from the equipment and the samples which are harder to quantify are expected. The errors

arising from the equipment mainly include the CCD gain and dark reference which rely on the exposure time and experiment mode used (Jones et al., 2016, Varambhia et al., 2018). Regarding the error from the samples, the nanoparticle oxidation and carbon contamination could add extra noise to the spectrum or shift the core-edges, which also impact the background subtraction (Craven et al., 2016). However, this can be minimised by sample baking. Here, we only considered the major errors from the counting statistics and single-atom cross section calibration for the error analysis on the single EELS measurement. The error of an individual EELS atom counting is given by:

$$\Delta n = n\sqrt{\left[(\frac{\Delta\sigma_{single}}{\sigma_{single}})^2 + (\frac{\Delta I_T}{I_T})^2 + (\frac{\Delta I_L}{I_L})^2\right]} \qquad \textit{Eq. 5.38}$$

Where I_T and I_L indicate the integrated intensity of the ZLP and core loss edge over a same energy loss window, respectively. The ΔI_T and ΔI_L terms are regarded as $\sqrt{I_T}$ and $\sqrt{I_L}$, respectively.

5.8 Applications: Composition quantitative analysis on the Pt-Co bimetallic nanoparticles

The accuracy and reliability of the spectroscopic quantification using the scattering cross sections have been successfully verified by atom counting on the unleached $PtCo_3$ nanoparticle in the previous chapters. It has been reported that the Pt-Co bimetallic nanoparticles feature a core-shell structure with Pt enriched surface. To investigate this, we eroded the nanoparticle from its surface to the centre to obtain five hollow shells and a core. These hollow shells have a width of 0.4 nm, which is close to the width of two or three (depending on the viewing direction) projected 2D atomic planes. Both

the EELS and EDS signals of each shell were integrated and quantified to obtain the number of atoms in each atomic shell. Figure 5.18 displays the quantification procedure used for the atom counting of each shell with the general workflows for both EELS and EDS techniques. The whole procedure was achieved by using Python programming language with more advanced libraries such as Hyperspy, Scikit-image and OpenCV.

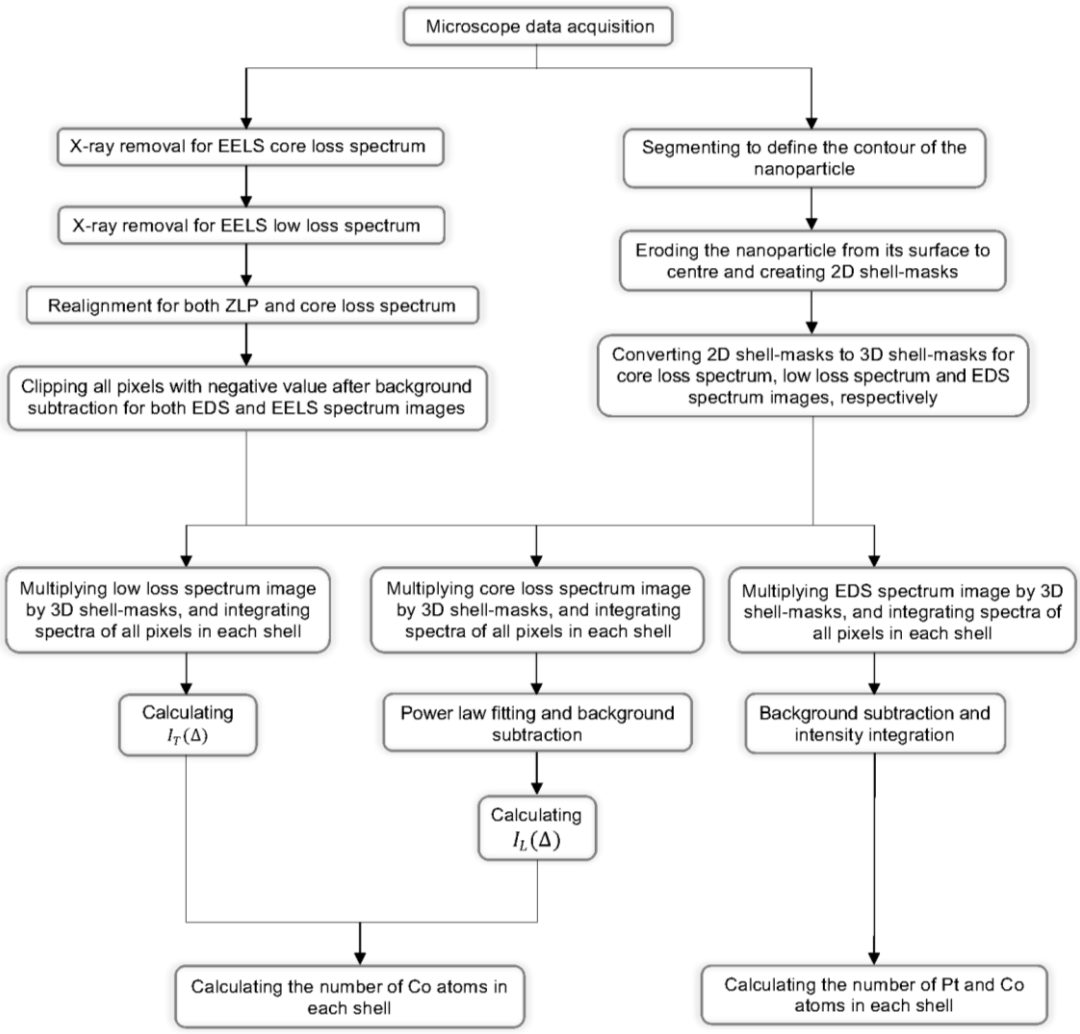

Figure 5.18. The spectroscopic data acquisition, processing and analysis workflow.

The number of Co atoms of each atomic shell was calculated using both the EDS and EELS signals, as shown in Figure 5.19b. It can be seen that the Co atom counts of each shell quantified using these two spectroscopic techniques agree well with each other. The maximum discrepancy between the quantification results is ~12% at the surface shell. The reason is that the contamination and Co oxidation on the surface shell impact the EELS quantification. Both EDS and EELS atom counts will be more accurate as the number of atoms increases where the SNR of the spectrum is also improved. Figure 5.19d shows the numbers of Pt and Co atoms in each atomic shell quantified using the EDS signals. From the quantification results, the atomic ratio between Pt and Co is

(1.5±0.2):1, which is different from the nominal stoichiometry (1:3) of this nanoparticle. As shown in Figure 5.19c, this nanoparticle exhibits a clear core-shell structure, where Pt atoms dominate the outer three shells compared to the other shells and core.

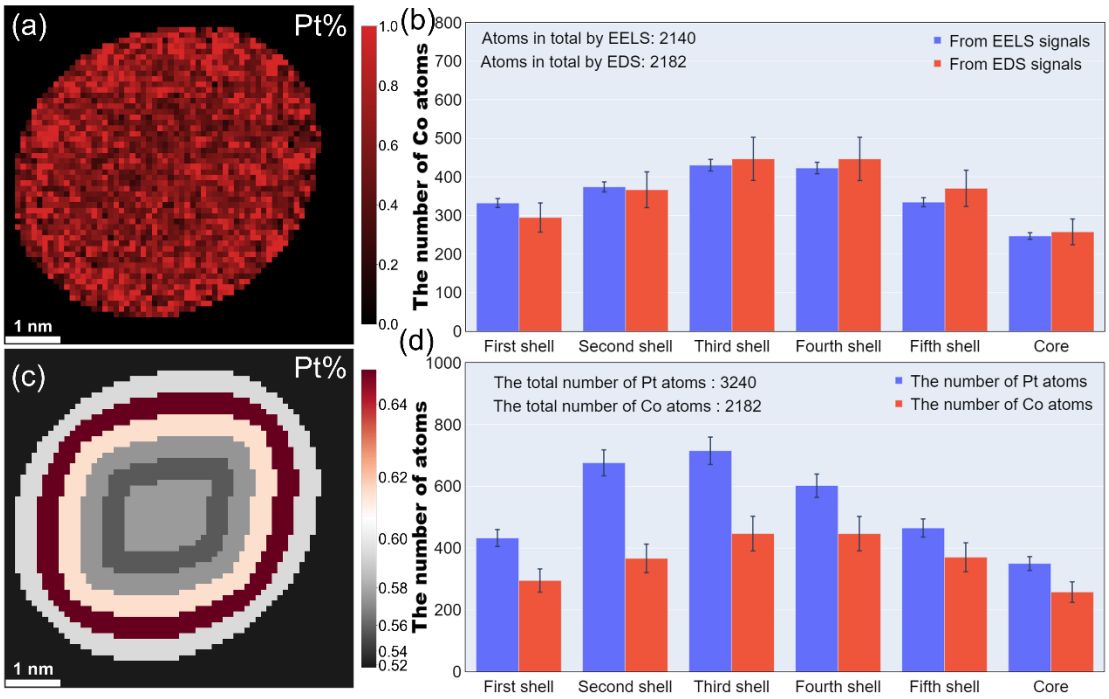

Figure 5.19. (a) A map of the fractional composition of Pt from the EDS signals for the unleached $PtCo_3$ nanoparticle. (b) The number of Co atoms in each shell of the nanoparticle calculated using both the EELS and EDS signals. (c) A compositional core-shell map of the nanoparticle derived from (a). (d) The number of Pt and Co atoms in each shell of the nanoparticle calculated using EDS signals.

5.9 Conclusions

To decouple the composition and mass-thickness effects of the Pt-Co bimetallic nanoparticles, the spectroscopic signals such as EDS and EELS are used to obtain the composition information. The spectroscopic signals are acquired simultaneously with the ADF signals when the sample is illuminated by the incident electron beam. These ADF, EDS and EELS signals can be linked to each other by representing their intensities into the scattering cross sections in ‘barns’. These scattering cross sections are robust to mis-tilt, defocus, source size and astigmatism but heavily relies on the

spectrum integration window, collection angle and detector efficiency. To obtain reliable quantification results, we used the experimentally determined scattering cross section to quantify the EDS and EELS signals.

Regarding the error analysis for the spectroscopic quantification, the experimental measurement of the scattering cross sections for both Pt and Co, with the experimental conditions used, contributes to the 85% error of the atom counting. The errors arising from the determined cross section in the previous work can be significantly reduced by collecting more spectroscopic signals when measuring these scattering cross sections. The EELS quantification is also sensitive to the background subtraction which could be influenced by sample contamination and equipment noise. As a comparison, the EDS quantification is less impacted by the equipment and sample condition but limited by the counting statistics.

Here, the high accuracy of the spectroscopic quantification using the experimentally determined scattering cross sections has been successfully verified by counting atoms in an unleached $PtCo_3$ nanoparticle from three aspects:

(1) A great agreement is achieved between the Co atom counting using the EELS signals (2185 Co atoms) and using the EDS signals (2182 Co atoms).

(2) The ADF scattering cross section measured from the ADF image is within 2% agreement with the value calculated using the numbers of Pt and Co atoms quantified from the spectroscopic signals.

(3) The total number of atoms (Pt and Co atoms) in the nanoparticle calculated using the spectroscopic signals agrees well with the theoretical number of atoms if the nanoparticle is assumed to have a spherical shape.

Such high-accurate composition quantification allows us to analyse the composition distribution within the nanoparticle at an atomic scale. A clear composition discrepancy between the outer shells and inner shells of the nanoparticle is observed, where the proportion of Pt increases in the outer shells.

5.10 References

Aarons, J., L. Jones, A. Varambhia, K. E. MacArthur, D. Ozkaya, M. Sarwar, C.-K. Skylaris and P. D. Nellist (2017). "Predicting the oxygen-binding properties of platinum nanoparticle ensembles by combining high-precision electron microscopy and density functional theory." *Nano Letters* 17(7): 4003-4012.

Bligaard, T. and J. K. Nørskov (2007). "Ligand effects in heterogeneous catalysis and electrochemistry." *Electrochimica Acta* 52(18): 5512-5516.

Castaing, R. (1951). *Application of electron probes to local chemical and crystallographic analysis*, University of Paris.

Chen, S., M. Li, M. Gao, J. Jin, M. A. van Spronsen, M. B. Salmeron and P. Yang (2020). "High-performance Pt–Co nanoframes for fuel-cell electrocatalysis." *Nano Letters* 20(3): 1974-1979.

Cliff, G. and G. W. Lorimer (1975). "The quantitative analysis of thin specimens." *Journal of Microscopy* 103(2): 203-207.

Craven, A. J., J. Bobynko, B. Sala and I. MacLaren (2016). "Accurate measurement of absolute experimental inelastic mean free paths and EELS differential cross-sections." *Ultramicroscopy* 170: 113-127.

De Backer, A., L. Jones, P. D. Nellist and S. Van Aert (2017). "Hybrid statistics-simulations based method for atom-counting from ADF STEM images." *Ultramicroscopy* 177: 69-77.

De Backer, A., L. Jones, A. Varambhia, P. D. Nellist and S. Van Aert (2020). "Measuring dynamic structural changes of nanoparticles at the atomic scale using scanning transmission electron microscopy." *Physical Review Letters* 124(10): 106105.

De Backer, A., G. Martinez, K. MacArthur, L. Jones, A. Béché, P. Nellist and S. Van Aert (2015). "Dose limited reliability of quantitative annular dark field scanning transmission electron microscopy for nano-particle atom-counting." *Ultramicroscopy* 151: 56-61.

De Backer, A., G. T. Martinez, A. Rosenauer and S. Van Aert (2013). "Atom counting in HAADF STEM using a statistical model-based approach: methodology, possibilities, and inherent limitations." *Ultramicroscopy* 134: 23-33.

De Backer, A. and S. Van Aert (2020). "Hidden Markov model for atom-counting from sequential ADF STEM images: Methodology, possibilities and limitations." *Ultramicroscopy* 219: 113131.

Egerton, R. F. (2011). *Electron energy-loss spectroscopy in the electron microscope*, Springer Science & Business Media.

Ellaby, T., A. Varambhia, X. Luo, L. Briquet, M. Sarwar, D. Ozkaya, D. Thompsett, P. D. Nellist and C.-K. Skylaris (2020). "Strain effects in core–shell PtCo nanoparticles: a comparison of experimental observations and computational modelling." *Physical Chemistry Chemical Physics* 22(42): 24784-24795.

Esparza, R., A. Santoveña, A. Ruíz-Baltazar, A. Angeles-Pascual, D. Bahena, J. Maya-Cornejo, J. Ledesma-García and R. Pérez (2017). "Study of PtPd bimetallic nanoparticles for fuel cell applications." *Materials Research* 20: 1193-1200.

Findlay, S. and J. LeBeau (2013). "Detector non-uniformity in scanning transmission electron microscopy." *Ultramicroscopy* 124: 52-60.

Fritz, R., A. Beyer, W. Stolz, K. Müller, M. Schowalter, A. Rosenauer, I. Häusler, H. Kirmse, A. Mogilatenko and W. Neumann (2011). "Quantitative analysis of chemical composition using HAADF-STEM in a JEOL 2200FS." *Microscopy and Microanalysis* 17(S2): 1410-1411.

Gao, H. and L.-M. Peng (1999). "Parameterization of the temperature dependence of the Debye–Waller factors." *Acta Crystallographica Section A: Foundations of Crystallography* 55(5): 926-932.

Gavartin, J., M. Sarwar, D. Papageorgopoulos, D. Gunn, S. Garcia, A. Perlov, A. Krzystala, D. L. Ormsby, D. Thompsett and G. Goldbeck-Wood (2009). "Exploring Fuel Cell Cathode Materials: A High Throughput Calculation Approach." *ECS Transactions* 25(1): 1335.

Goldstein, J. I. (1977). "Quantitative X-ray analysis in the electron microscope." *Scanning Electron Microscopy 1977*: 315-324.

Jones, L. (2016). *Quantitative ADF STEM: acquisition, analysis and interpretation*. IOP Conf. Ser. Mater. Sci. Eng.

Jones, L., K. E. MacArthur, V. T. Fauske, A. T. van Helvoort and P. D. Nellist (2014). "Rapid estimation of catalyst nanoparticle morphology and atomic-coordination by high-resolution Z-contrast electron microscopy." *Nano Letters* 14(11): 6336-6341.

Jones, L. and P. D. Nellist (2013). "Identifying and correcting scan noise and drift in the scanning transmission electron microscope." *Microscopy and Microanalysis* 19(4): 1050.

Jones, L., A. Varambhia, R. Beanland, D. Kepaptsoglou, I. Griffiths, A. Ishizuka, F. Azough, R. Freer, K. Ishizuka and D. Cherns (2018). "Managing dose-, damage-and data-rates in multi-frame spectrum-imaging." *Microscopy* 67(suppl_1): i98-i113.

Jones, L., A. Varambhia, D. Kepaptsoglou, Q. Ramasse, R. Freer, F. Azough, S. Lozano-Perez, R. Beanland and P. Nellist (2016). *New Opportunities in multi-frame STEM Spectroscopy & Fractional Beam-current EELS*. European Microscopy Congress 2016: Proceedings, Wiley Online Library.

Jones, L., A. Varambhia, H. Sawada and P. Nellist (2018). "An optical configuration for fastidious STEM detector calibration and the effect of the objective-lens pre-field." *Journal of Microscopy* 270(2): 176-187.

Kirkland, E. J. (1998). *Advanced computing in electron microscopy*, Springer.

Kirkland, E. J., R. F. Loane and J. Silcox (1987). "Simulation of annular dark field STEM images using a modified multislice method." *Ultramicroscopy* 23(1): 77-96.

Kitchin, J. R., J. K. Nørskov, M. A. Barteau and J. Chen (2004). "Role of strain and ligand effects in the modification of the electronic and chemical properties of bimetallic surfaces." *Physical Review Letters* 93(15): 156801.

Kootte, A., C. Haas and R. De Groot (1991). "The electronic structure of ordered binary Co-Pt compounds." *Journal of Physics: Condensed Matter* 3(9): 1133.

LeBeau, J. M., S. D. Findlay, L. J. Allen and S. Stemmer (2008). "Quantitative atomic resolution scanning transmission electron microscopy." *Physical Review Letters* 100(20): 206101.

LeBeau, J. M., S. D. Findlay, L. J. Allen and S. Stemmer (2010). "Standardless atom counting in scanning transmission electron microscopy." *Nano Letters* 10(11): 4405-4408.

Liu, J.-f., S.-j. Yu, Y.-g. Yin and J.-b. Chao (2012). "Methods for separation, identification, characterization and quantification of silver nanoparticles." *TrAC Trends in Analytical Chemistry* 33: 95-106.

Lobato, I. and D. Van Dyck (2015). "MULTEM: A new multislice program to perform accurate and fast electron diffraction and imaging simulations using Graphics Processing Units with CUDA." *Ultramicroscopy* 156: 9-17.

Lyons, L. and L. Louis (1991). *A practical guide to data analysis for physical science students*, Cambridge University Press.

MacArthur, K., L. Jones and P. Nellist (2014). *How flat is your detector? Non-uniform annular detector sensitivity in STEM quantification*. Journal of Physics: Conference Series.

MacArthur, K., T. Pennycook, E. Okunishi, A. D'Alfonso, N. Lugg, L. Allen and P. Nellist (2013). "Probe integrated scattering cross sections in the analysis of atomic resolution HAADF STEM images." *Ultramicroscopy* 133: 109-119.

MacArthur, K., T. Slater, S. Haigh, D. Ozkaya, P. Nellist and S. Lozano-Perez (2016). "Compositional quantification of PtCo acid-leached fuel cell catalysts using EDX partial cross sections." *Materials Science and Technology* 32(3): 248-253.

MacArthur, K. E., T. J. Slater, S. J. Haigh, D. Ozkaya, P. D. Nellist and S. Lozano-Perez (2016). "Quantitative energy-dispersive X-ray analysis of catalyst nanoparticles using a partial cross section approach." *Microscopy and Microanalysis* 22(1): 71.

Maher, D., D. Joy, M. Ellington, N. Zaluzec and P. Mochel (1981). "Relative accuracy of k-factor calculations for thin-film X-ray analysis." *Analytical Electron Microscopy*: 33-38.

Martinez, G., L. Jones, A. De Backer, A. Béché, J. Verbeeck, S. Van Aert and P. Nellist (2015). "Quantitative STEM normalisation: the importance of the electron flux." *Ultramicroscopy* 159: 46-58.

Nellist, P. and S. Pennycook (2000). "The principles and interpretation of annular dark-field Z-contrast imaging." *Advances in Imaging and Electron Physics* 113: 147-203.

Newbury, D., D. Williams, J. Goldstein and C. Fiori (1984). "Observation on the calculation of kAB factors for analytical electron microscopy." *Anal Electron Microsc* 2: 276-278.

Stamenkovic, V., B. S. Mun, K. J. Mayrhofer, P. N. Ross, N. M. Markovic, J. Rossmeisl, J. Greeley and J. K. Nørskov (2006). "Changing the activity of electrocatalysts for oxygen reduction by tuning the surface electronic structure." *Angewandte Chemie* 118(18): 2963-2967.

Temmel, S. E., E. Fabbri, D. Pergolesi, T. Lippert and T. J. Schmidt (2016). "Investigating the role of strain toward the oxygen reduction activity on model thin film Pt catalysts." *ACS Catalysis* 6(11): 7566-7576.

Tenailleau, H. and J. Martin (1992). "A new background subtraction for low-energy EELS core edges." *Journal of Microscopy* 166(3): 297-306.

Van Aert, S., K. J. Batenburg, M. D. Rossell, R. Erni and G. Van Tendeloo (2011). "Three-dimensional atomic imaging of crystalline nanoparticles." *Nature* 470(7334): 374-377.

Van Dyck, D. and M. O. De Beeck (1996). "A simple intuitive theory for electron diffraction." *Ultramicroscopy* 64(1-4): 99-107.

Varambhia, A., L. Jones, A. London, D. Ozkaya, P. D. Nellist and S. Lozano-Perez (2018). "Determining EDS and EELS partial cross-sections from multiple calibration standards to accurately quantify bi-metallic nanoparticles using STEM." *Micron* 113: 69-82.

Varambhia, A. M. (2018). *Quantitative structural and compositional studies of catalyst nanoparticles using imaging and spectroscopy in STEM*, University of Oxford.

Varambhia, A. M., L. Jones, A. De Backer, V. T. Fauske, S. Van Aert, D. Ozkaya and P. D. Nellist (2016). "Quantifying a heterogeneous Ru catalyst on carbon black using ADF STEM." *Particle & Particle Systems Characterization* 33(7): 438-444.

Wang, J. X., H. Inada, L. Wu, Y. Zhu, Y. Choi, P. Liu, W.-P. Zhou and R. R. Adzic (2009). "Oxygen reduction on well-defined core− shell nanocatalysts: particle size, facet, and Pt shell thickness effects." *Journal of the American Chemical Society* 131(47): 17298-17302.

Wang, Z., Z. Li, S. Park, A. Abdela, D. Tang and R. Palmer (2011). "Quantitative Z-contrast imaging in the scanning transmission electron microscope with size-selected clusters." *Physical Review B* 84(7): 073408.

Watanabe, M., Z. Horita and M. Nemoto (1996). "Absorption correction and thickness determination using the ζ factor in quantitative X-ray microanalysis." *Ultramicroscopy* 65(3-4): 187-198.

Watanabe, M. and D. Williams (2006). "The quantitative analysis of thin specimens: a review of progress from the Cliff-Lorimer to the new ζ-factor methods." *Journal of Microscopy* 221(2): 89-109.

Watanabe, M., D. B. Williams and Y. Tomokiyo (2003). "Comparison of detectability limits for elemental mapping by EF-TEM and STEM-XEDS." *Micron* 34(3-5): 173-183.

Williams, D. B. and C. B. Carter (1996). *Transmission electron microscopy*, Springer.

Zhang, S., X. Zhang, G. Jiang, H. Zhu, S. Guo, D. Su, G. Lu and S. Sun (2014). "Tuning nanoparticle structure and surface strain for catalysis optimization." *Journal of the American Chemical Society* 136(21): 7734-7739.

Chapter 6

Simultaneous composition and strain analyses of Pt-Co nanoparticles

Strain and composition are two fundamental effects that have been proposed to explain the mechanistic origin of catalytic enhancement of the Pt-Co bimetallic nanoparticles. Herein, we precisely and simultaneously quantify composition and strain variations at an atomic scale within the individual alloyed and dealloyed Pt-Co nanoparticles. Unlike the previously assumed effects of dealloying, we find that no compressive strain on the Pt-rich outer shell is imposed by the alloy core. Dilation strain is found to be distributed throughout the individual nanoparticles, with the radial dilation strain being much larger than the circumferential dilation strain at the surface. Remarkably, all the Pt-Co stoichiometries studied have a relatively invariant surface lattice parameter, which is smaller than that for pure Pt but larger than that predicted using the measured local composition, whether or not an acid de-alloying treatment is applied. These findings provide a new understanding of the origins of enhanced catalytic performance.

6.1 Introduction

In the applications of ORR catalysts in the H-PEMFC, alloying Pt with a secondary 3d-transition element such as Co, Ni, Fe, Ti or Fe is a promising strategy to reduce the mass of Pt required without sacrificing catalytic performance (Toda et al., 1999, Stamenkovic et al., 2006, Stamenkovic et al., 2007, Greeley et al., 2009). Previous

work has found that the ORR activity enhancement of these Pt-based bimetallic catalysts is due to the near-optimal position of the Pt d-band centre of surfaces (Gavartin et al., 2009, Chattot et al., 2018). Ligand and strain effects have been proposed to explain the shift of the Pt d-band centre at the surfaces (Mavrikakis et al., 1998, Kitchin et al., 2004, Strasser et al., 2010, Temmel et al., 2016, Chattot et al., 2018, Li et al., 2019). The ligand effect is the hybridization of the d orbitals between Pt and the secondary metal atoms inducing d-band width changes, resulting in modification of the surface electronic structure (Bligaard and Nørskov, 2007, Strasser et al., 2010). The strain effect refers to the compressed or expanded bond lengths caused by lattice mismatch between dissimilar metal atoms (Kitchin et al., 2004, Strasser et al., 2010, Luo and Guo, 2017). Compressive strain narrows the interatomic spacing between atoms, resulting in the d-band broadening. Given the fact that the d band filling remains constant, the average energy of the d-band decreases and the d-band centre moves downward (Kitchin et al., 2004, Stamenkovic et al., 2006, Khorshidi et al., 2018). A downward shift of the Pt d-band centre leads to an increase in the oxygen adsorption energy (Stamenkovic et al., 2006). A volcano-type dependence of the ORR activity on the Pt d-band centre negative shifts has been predicted by density function theory (DFT) calculation and verified by experiments (Stamenkovic et al., 2006). To realize the potential of Pt-based bimetallic catalysts, the surface d-band centre position, which is affected by both ligand and strain effects, needs to be optimized. However, ligand and strain effects are always both associated with composition variations, domain structure and morphology of the bimetallic catalysts (Kitchin et al., 2004, Strasser et al., 2010). It has also been reported that voids and surface defects are beneficial to the ORR kinetics (Gan et al., 2013, Chattot et al., 2018). To elucidate the intrinsic mechanisms that underlie the enhanced reactivity, local strain, composition, size and structure of the

nanoparticles must be fully quantified (Solliard and Flueli, 1985, Wang et al., 2009, Fujita et al., 2012, Cleve et al., 2017, Chen et al., 2020).

The most practical Pt-based alloy catalyst is the core-shell structured bimetallic nanoparticles, which exhibit superior catalytic performance compared with pure Pt catalysts (Toda et al., 1999, Lima et al., 2009, Schulenburg et al., 2009, Oezaslan and Strasser, 2011, Saquib and Halder, 2018). With regard to the effect of strain, it is argued that the alloy core imposes a compressive strain on the near-surface shell of the bimetallic nanoparticles, with the assumption that the shell consists of pure Pt (Gavartin et al., 2009, Strasser et al., 2010). As the result, the surface lattice parameter of the nanoparticles is smaller than that of pure bulk Pt (Gavartin et al., 2009, Strasser et al., 2010). The local structure and composition of the surface could, however, also contribute to its smaller lattice parameter. This has not been studied due to the lack of simultaneous local composition and strain measurements within the nanoparticle at atomic resolution. Here, we investigate core-shell structured Pt-Co bimetallic nanoparticles, with a Pt-rich shell over an alloy core, as candidate ORR electrocatalysts. The Pt-Co nanoparticles were also dealloyed by acid-leaching Co from the nanoparticle surfaces, increasing the surface Pt content or producing porous nanoparticles. Some initial studies reported that the Pt-Co nanoparticles have a larger lattice parameter at the surfaces compared to the centre (Ellaby et al., 2020). The reasons causing the core-shell difference in the lattice parameter could be the finite size (Solliard and Flueli, 1985), structure (Walsh et al., 2012) or composition variations of the nanoparticle (Wu et al., 2012), but it has not previously been directly determined whether any elastic compressive strain is actually present in these nanoparticles, as has previously been

assumed (Strasser et al., 2010) or whether changes in lattice parameter are simply associated with composition changes.

As mentioned before, atomic-resolution STEM with EDS or EELS detectors can be used for characterising these Pt-Co nanoparticles (Wang et al., 2013, Aarons et al., 2017, Xiong et al., 2020). Strain, size and structure information are visible in high-resolution HAADF imaging, while composition information of the bimetallic nanoparticles can be routinely obtained from the EELS or EDS spectrum images. Although several attempts have been made at quantifying composition distribution within the nanoparticles using the ratio of either EDS or EELS intensities (Ferrer et al., 2007, An and Somorjai, 2015), precise composition measurements such as evaluating the number of atoms (termed atom counting) within bimetallic nanoparticles has been more rarely attempted (Goris et al., 2013, MacArthur et al., 2016). Limited studies of truly atomic site-specific deformation analysis on an entire nanoparticle have been published (Pingel et al., 2018, Ellaby et al., 2020) due to the difficulties of imaging such easily damaged small nanoparticles along a low-order zone axis at atomic resolution. In particular, to date, simultaneous strain, structure and composition characterisations at atomic resolution on an individual nanoparticle has never been achieved.

The present work simultaneously quantifies local composition, structure and strain at an atomic scale within 12 individual nanoparticles for unleached and acid-leached, Pt_3Co and $PtCo_3$ nanoparticle species. Experimentally calibrated scattering cross-sections (Varambhia et al., 2018) for the spectroscopic signals were used for Co and Pt atom counting within each nanoparticle to ensure the high accuracy of our composition

quantification methodology. Atomic site-specific strain measurements were made from high-resolution HAADF images of the on-axis nanoparticles. Strain and composition analyses were also separately applied to large ensembles of Pt-Co nanoparticles with a size range between 2 nm and 10 nm where it was not possible to record both composition and strain because of the nanoparticle rotating under the electron beam. The large ensemble data analyses are important to get an understanding of the strain-composition-structure-size dependence of Pt-Co nanoparticles.

6.2 Vegard's law prediction

The theoretical lattice parameters were computed from the composition fractions by using the Vegard's law. The lattice parameter of a binary solid solution can be calculated by weighted-averaging the lattice parameters of its two constituents. Here, the lattice parameters of ordered $L1_2$ structured $PtCo_3$ and Pt_3Co alloys (Kootte et al., 1991), pure Pt and Co bulk materials (Arblaster, 1997, LaBrosse et al., 2010) were presented by the scatter plot and fitted with a red line using a linear function, as shown in Figure 6.1. For Pt-Co system, the theoretical lattice parameter can be then easily calculated from the given Pt content using the fitted curve.

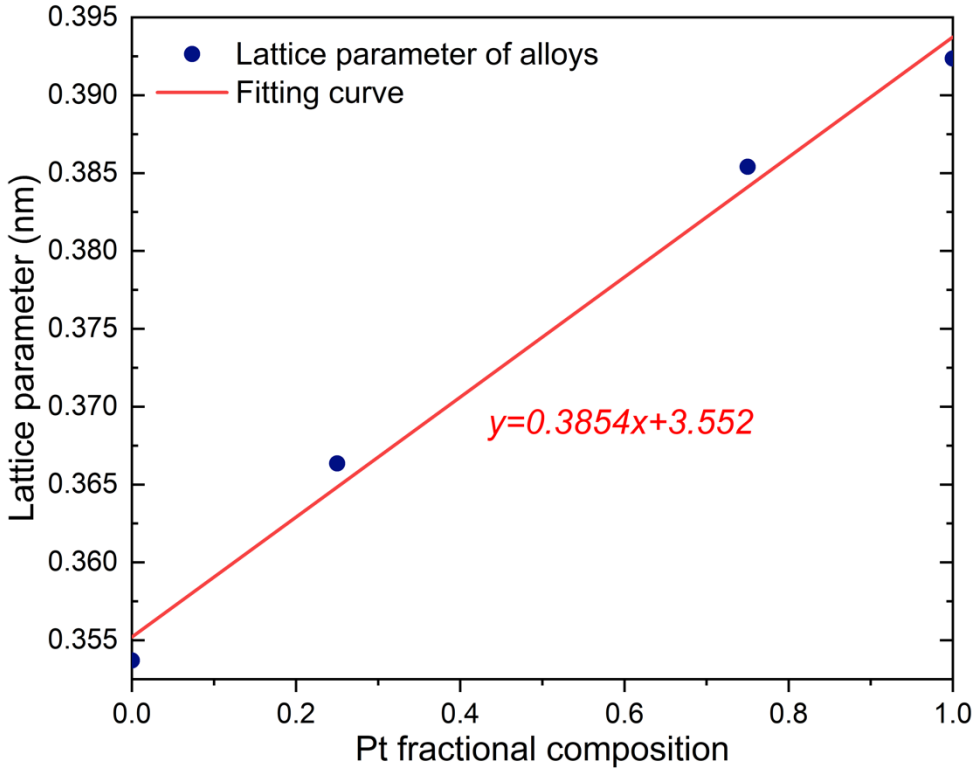

Figure 6.1 Experimentally measured lattice parameters of Pt-Co alloys and the corresponding fitting curve

6.3 Atomic-scale simultaneous composition and strain analyses

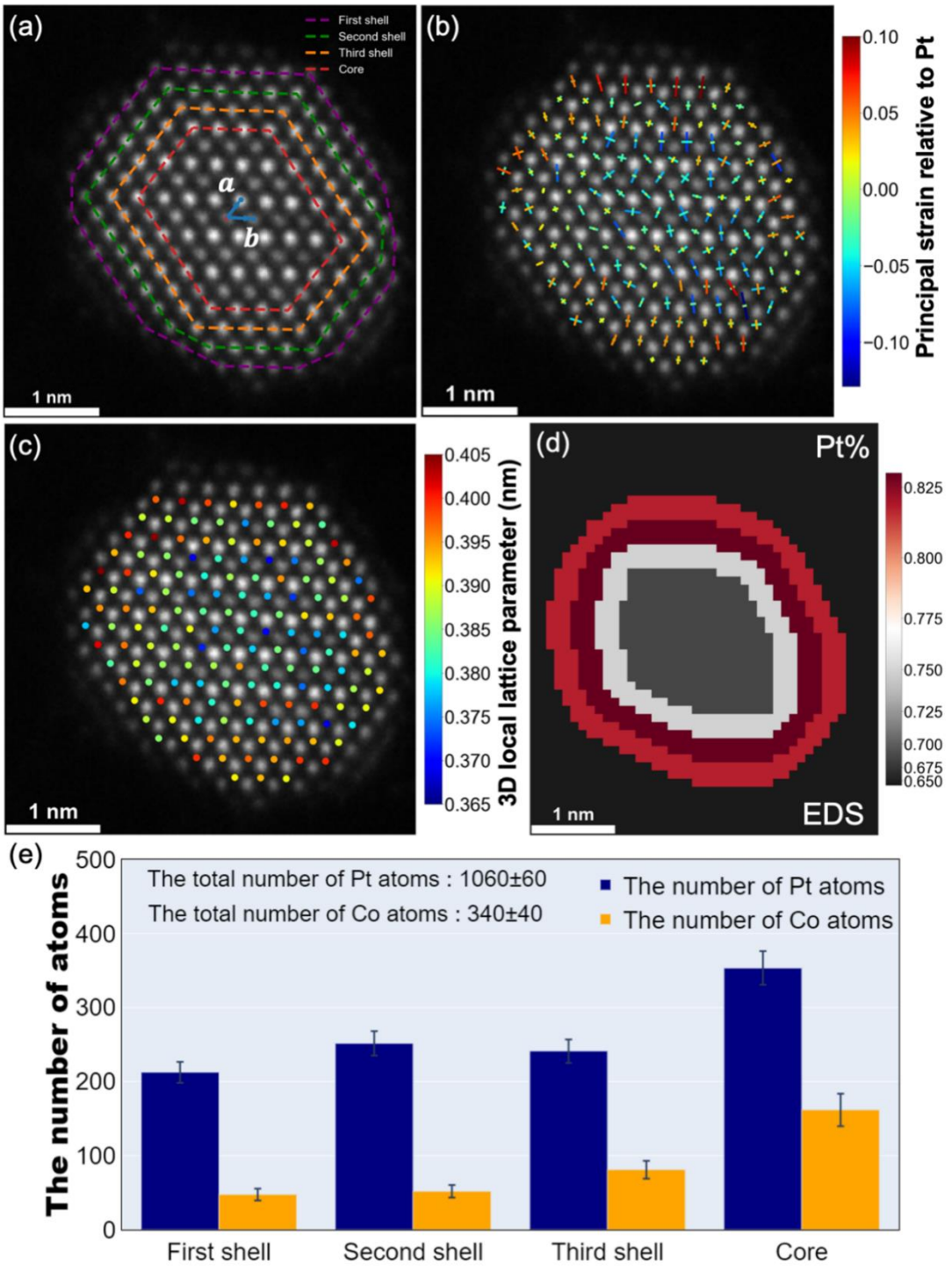

Figure 6.2 Simultaneous composition and strain quantifications of an experimental dealloyed $PtCo_3$ nanoparticle at an atomic scale. (a) The atomic-resolution HAADF STEM image of the dealloyed $PtCo_3$ nanoparticle with the defined atomic shells and primitive unit cell. (b) The measured principal strain map and (c) the 3D local lattice parameter map of the nanoparticle. (d) The nanoparticle core-shell map for Pt fractional composition quantified using the EDS spectrum images. (e) The number of Pt and Co atoms in each shell of the nanoparticle quantified from the EDS signals.

To demonstrate how local composition can be correlated with strain, here we show atomic-resolution strain analysis and atom counting simultaneously performed on an individual Pt-Co nanoparticle. Figure 6.2a shows the high-resolution HAADF STEM image of an experimental dealloyed $PtCo_3$ nanoparticle. This nanoparticle was well-aligned along the low order zone axis [110] so that atomic columns can be clearly observed. Atomic site-specific strain measurements were performed on the nanoparticle using our previously developed methodology, which is based on atomic column detection in atomic-resolution STEM images. Here, the reference grid used for strain measurements is the projected crystal lattice of the pure Pt bulk material with the lattice constant of 0.3923 nm at 293 K (Arblaster, 1997). Measurements of the three independent strain components require two, non-collinear interatomic vectors ($\boldsymbol{a}$ and $\boldsymbol{b}$ in Figure 6.2a), which bound a triangle. The measured deformation parameters are therefore shown at the centre of each local triangle. The principal strains are the maximum and minimum normal strains along a specific axis orientation where the shear strain is zero (Sadd, 2009). They well-express the magnitude and orientation of the local deformation configuration, as displayed in Figure 6.2b. Based on the two principal strains, the 2D local lattice parameter can be calculated using Eq. 6.1.

$$l_{2D} = l \times \left(\frac{1}{2}\left(\varepsilon_{xx} + \varepsilon_{yy}\right) + 1\right) = l \times \left(\frac{1}{2}\left(\varepsilon_{rr} + \varepsilon_{\theta\theta}\right) + 1\right) \qquad \textit{Eq. 6.1}$$

Because the image is a projection, the calculations of the 2D lattice parameter in previous studies (Zuo et al., 2014, Kwon et al., 2016, Ellaby et al., 2020) also only use local deformation along the x and y directions, but ignore the deformation along the z direction (parallel to the incident beam direction). To address this, the strain tensors were converted from the 2D Cartesian coordinate system (ε_{xx} and ε_{yy}) to the 2D circular-polar coordinate basis (ε_{rr} and $\varepsilon_{\theta\theta}$) using Eq. 6.2.

$$\begin{bmatrix} \varepsilon_{rr} & \varepsilon_{r\theta} \\ \varepsilon_{\theta r} & \varepsilon_{\theta\theta} \end{bmatrix} = \begin{bmatrix} \cos\theta & \sin\theta \\ -\sin\theta & \cos\theta \end{bmatrix} \cdot \begin{bmatrix} \varepsilon_{xx} & \varepsilon_{xy} \\ \varepsilon_{yx} & \varepsilon_{yy} \end{bmatrix} \cdot \begin{bmatrix} \cos\theta & -\sin\theta \\ \sin\theta & \cos\theta \end{bmatrix} \qquad \textit{Eq. 6.2}$$

In the case that the nanoparticle has a near-spherical shape with symmetrical strain distribution, the other circumferential strain ($\varepsilon_{\phi\phi}$) in the 3D spherical-polar coordinate system can be assumed as being equal to $\varepsilon_{\theta\theta}$. Accordingly, the 3D local lattice parameters were computed using *Eq. 6.3*, as shown in Figure 6.2c.

$$l_{3D} = l \times \left(\frac{1}{3}\left(\varepsilon_{rr} + \varepsilon_{\theta\theta} + \varepsilon_{\phi\phi}\right) + 1\right) \qquad \textit{Eq. 6.3}$$

The principal strain map (Figure 6.2b) demonstrates that the core region of the nanoparticle has a compressive strain relative to pure bulk Pt, while the outer atomic shells are radially expanded. This is within our expectation because the lattice ordering being clearly present in the core region indicates that the core is well alloyed. Regarding the local lattice parameters in Figure 6.2c, the near-surface region of the nanoparticle has a measured 3D local lattice parameter larger than that of the centre, as might be expected for a dealloyed particle (Strasser et al., 2010). This nanoparticle exhibits a clear core-shell discrepancy in terms of the deformation behaviour.

Composition analysis was achieved using spectroscopic quantification techniques. By atom counting for the same element using the EDS and EELS signals respectively, our quantification methodology has been shown to have high accuracy and reliability (in Chapter 5). To study the origin of the variation in the measured 3D lattice parameters in Figure 6.2c, the same nanoparticle was analysed for composition using the EDS signals. Here, the experimentally calibrated EDS partial scattering cross sections for both Pt and Co elements were used for the quantifications (Varambhia et al., 2018). The EDS signals in each atomic shell and the core region (defined in Figure 6.2a) were then integrated and quantified to evaluate the number of atoms and the Pt content of

each shell, as shown in Figure 6.2d and e. It is demonstrated that the near-surface region of this nanoparticle has a higher Pt content, but is not Co-free, and therefore the question remains of whether the measured strain is caused by the local composition. To answer this, the simultaneous quantification methodology described here is applied to a wider ensemble of unleached and acid leached nanoparticles.

6.4 Unleached Pt-Co system

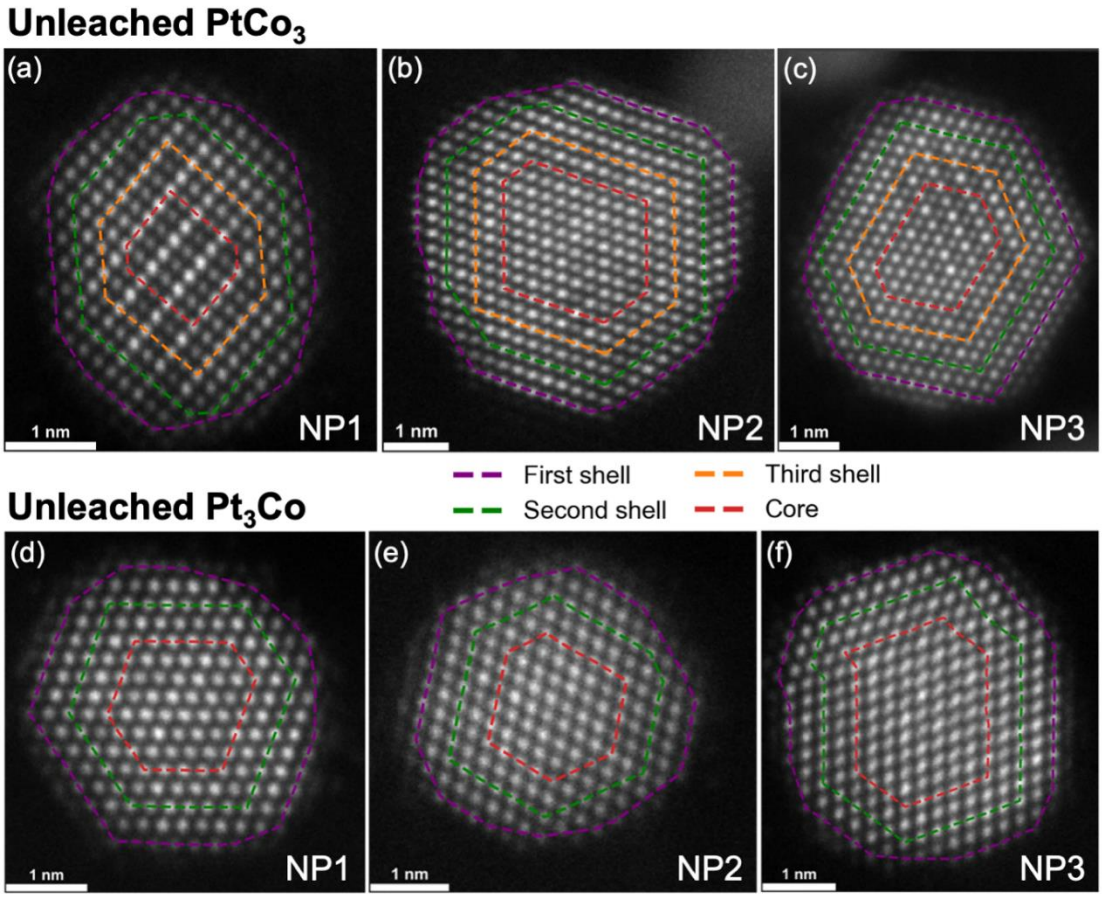

Figure 6.3 The experimental high-resolution HAADF STEM images for the unleached nanoparticle system. (a-c) The unleached $PtCo_3$ nanoparticles and (d-e) the unleached Pt_3Co nanoparticles with the defined areas. For the unleached $PtCo_3$ species, NP1 is aligned along the [100] zone axis, while NP2 and NP3 are viewed along the [110] direction. For the unleached Pt_3Co species, all three nanoparticles are viewed along the [110] zone axis.

To compare the composition and strain variations between the different Pt-Co species, the simultaneous analyses were applied to the unleached $PtCo_3$ and Pt_3Co nanoparticles.

Here, three different experimental on-axis nanoparticles for each unleached Pt-Co species were imaged to evidence the reproducibility of the results. Figure 6.3a-c display the atomic-resolution HAADF STEM images of three on-axis unleached $PtCo_3$ nanoparticles with analysis areas defined. From the quantification results (see **Figure S1, S2** and **S3** in **Appendix A**), the measured atom ratios of Pt to Co for the unleached NP1, NP2 and NP3 are $(1.0 \pm 0.1): 1.0$, $(0.7 \pm 0.1): 1.0$ and $(0.9 \pm 0.1): 1.0$, respectively, which differ from the nominal stoichiometry $(1: 3)$. The reasons will be explored later. The first thing to note is that in the core region of the unleached NP1 and NP3, lattice ordering is observed. It indicates that the alloyed Pt-Co core with the element ratio close to 1:1 has an $L1_0$ ordered crystal structure, in line with previous studies (Liang et al., 2019). The atomic-resolution HAADF images for the unleached Pt_3Co species are shown in Figure 6.3d-e. The overall stoichiometry for the unleached Pt_3Co NP1, NP2 and NP3 was quantified to be $(5.0 \pm 0.7): 1.0$, $(2.1 \pm 0.3): 1.0$ and $(4.9 \pm 0.7): 1.0$ (see **Figure S4, S5** and **S6** in **Appendix A**), respectively, fluctuating around the nominal stoichiometry $(3: 1)$.

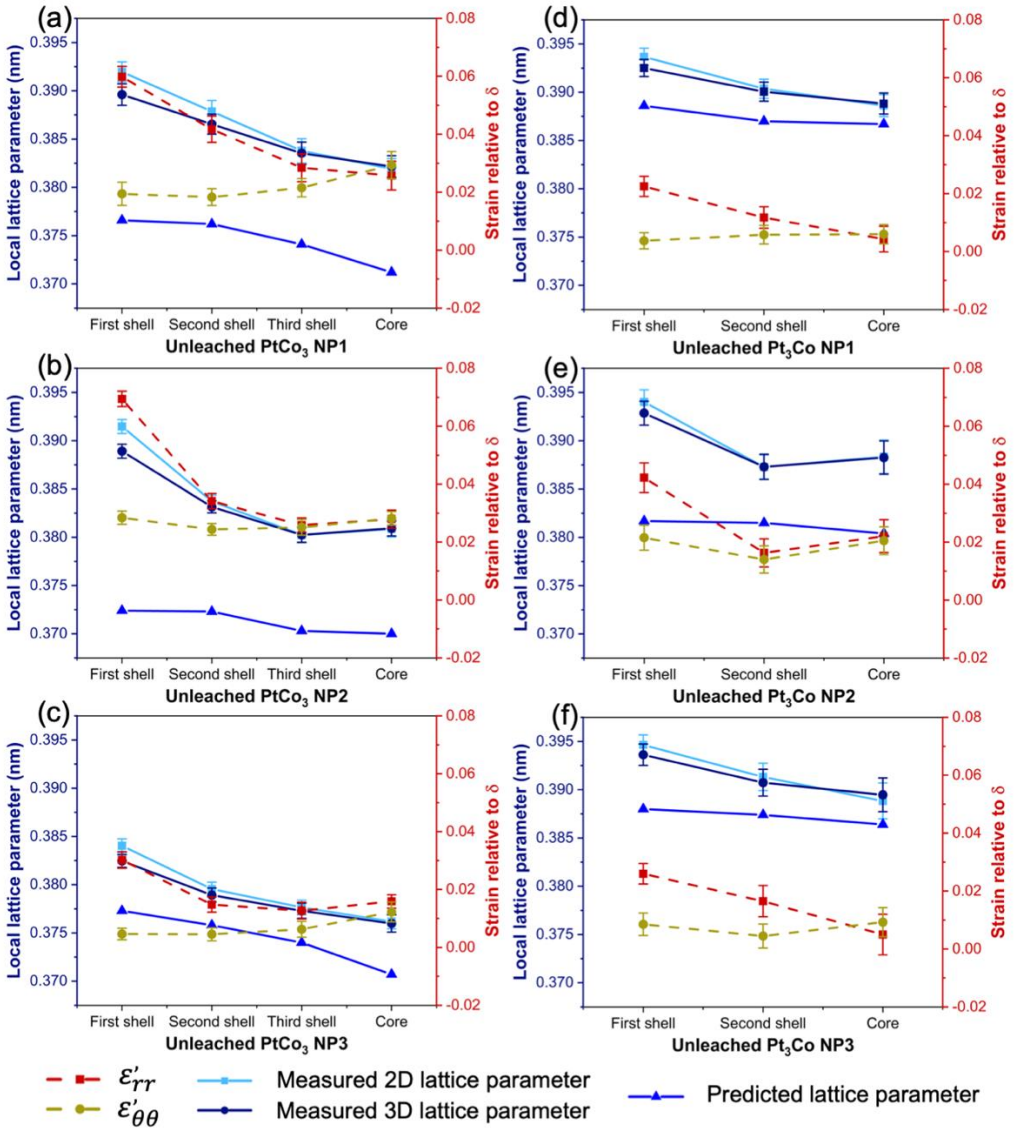

Figure 6.4 Polar strain, predicted, 2D and 3D local lattice parameters measurements for the unleached both $PtCo_3$ and Pt_3Co nanoparticle systems. The nanoparticles and corresponding shells are displayed and defined in Figure 6.3. Note that the calculated elastic polar strain is relative to the theoretical local lattice parameter predicted by Vegard's law. The predicted lattice parameters are calculated from the local composition using Vegard's law.

The Pt fractional composition of each defined area for these six nanoparticles was also quantified (see **Figure S1-S6** in **Appendix A**) to predict the theoretical lattice parameter using Vegard's law which states that the lattice parameter of a solid solution linearly depends on its composition. Figure 6.4 compares the measured local lattice parameters with the predicted ones from the nanoparticle surface to centre. All six unleached nanoparticles exhibit a core-shell structure with Pt enrichment and a larger

3D lattice parameter at the near-surface region. The unleached $PtCo_3$ nanoparticles have a larger core-shell discrepancy in both composition and strain compared to the Pt_3Co counterparts. Remarkably, the enlargement of all the measured lattice parameters relative to the corresponding predicted ones is observed in every nanoparticle. To determine whether the alloy core is applying any compressive elastic strain to the Pt-rich shell, the radial and circumferential strains (ε_{rr} and $\varepsilon_{\theta\theta}$) relative to pure Pt were compared to a parameter (δ) expressing the fraction by which the alloy lattice parameter (calculated using Vegard's law) is reduced relative to pure Pt:

$$\delta = \frac{\left(l_{Vegard} - l_{Pt}\right)}{l_{Pt}} \qquad \textit{Eq. 6.4}$$

Where l_{Vegard} is the predicted lattice parameter, and l_{Pt} is the lattice parameter of pure bulk Pt. The resultant relative radial and circumferential strains ($\varepsilon'_{rr} = \varepsilon_{rr} - \delta$ and $\varepsilon'_{\theta\theta} = \varepsilon_{\theta\theta} - \delta$), which indicate the potential presence of elastic deformation, are computed each analysis area and shown in Figure 6.4. The relative circumferential strain ($\varepsilon'_{\theta\theta}$) stays small, dilated and constant from the nanoparticle surface to core, and no evidence of circumferential compression is observed. The relative radial dilation strain (ε'_{rr}) is much larger than $\varepsilon'_{\theta\theta}$ at outer shells, and is responsible for the core-shell discrepancy and the enlargement in the local lattice parameter. A situation where the two perpendicular normal strains are very different can be described as having large shear strain through the Mohr's circle construction (Sadd, 2009). In the nanoparticle core, $\varepsilon'_{rr} = \varepsilon'_{\theta\theta}$, which well-explains why the 3D and 2D lattice parameters are equivalent in the core. Although the measured lattice parameter in the outer shell region agrees well with previous studies (Lima et al., 2006) and is smaller than pure Pt, our study shows that the reduction in the outer shell lattice parameter is due to the presence of Co, and the largest elastic effect seen is a radial dilation.

6.5 Leached Pt-Co system

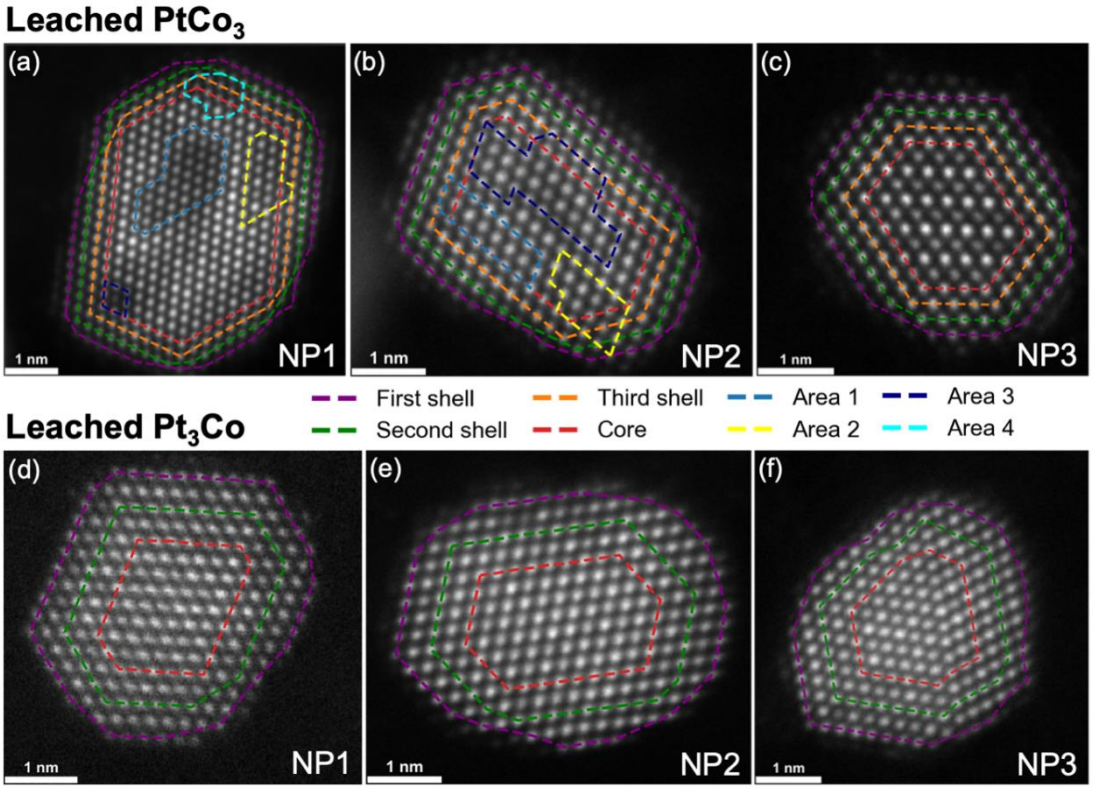

Figure 6.5 The experimental high-resolution HAADF STEM images for the leached nanoparticle system. (a-c) The leached $PtCo_3$ nanoparticles and (d-e) the leached Pt_3Co nanoparticles with the defined areas. All the six leached nanoparticles are viewed along the [110] zone axis.

To investigate the effect of the dealloying process, the same simultaneous quantification analyses were applied to the dealloyed Pt-Co system. To obtain dealloyed nanoparticles, the Pt-Co alloys were exposed to perchloric acid to 'leach' Co off the nanoparticle surface. Figure 6.5a-c shows the atomic-resolution HAADF images of three on-axis leached $PtCo_3$ nanoparticles with defined areas. The Pt fractional composition of the leached $PtCo_3$ NP1, NP2 and NP3 increases dramatically compared to the unleached counterparts, resulting in the nominal stoichiometry changes from 1: 3 to (2.7 ± 0.3): 1.0, (3.0 ± 0.4): 1.0 and (3.1 ± 0.4): 1.0, respectively (see **Figure S7, S8** and **S9** in **Appendix A**). This is within our expectation because a great number of Co atoms are aggressively leached off the $PtCo_3$ nanoparticles. Atomic-resolution

HAADF images for the leached Pt_3Co species are shown in Figure 6.5d-f. The acid-leaching process slightly increases the Pt content of the leached Pt_3Co NP1, NP2 and NP3, raising the nominal stoichiometry from $3:1$ to$(3.4 \pm 0.5):1.0$, $(3.6 \pm 0.5):1.0$ and $(3.3 \pm 0.5):1.0$, respectively (see **Figure S10, S11** and **S12** in **Appendix A**).

In the HAADF images of the leached $PtCo_3$ NP1 and NP2, some dark patches are observed. Compared to the other regions, both the Pt content and measured local lattice parameters dramatically decrease in these dark patches (See **Figure S15**). the area 1 in the leached $PtCo_3$ NP1 was used to study the formation mechanism of the dark patches by Pt and Co atom counting. The total number of atoms (Pt and Co) in the area 1 was measured to be 357 (see **Figure S7**), and there are 27 atomic columns in this region. Each atomic column therefore has about 13 atoms on average. The $PtCo_3$ alloy has an $L1_2$ ordered structure, as previously suggested (Kootte et al., 1991), and the measured local lattice parameter in this area is about 0.383 nm. Given that the nanoparticle is viewed along [110] direction, the distance between the neighbouring atoms in an atomic column is about 0.284 nm. Thus, the thickness of the atomic column having 13 atoms is 3.692 nm, which is much smaller than the mean nanoparticle diameter (5.640 nm). This indicates that the acid-leaching process has created some pores, voids or divots in these dark patches. It has been reported that the surface defectiveness of bimetallic catalysts improves the catalytic performance (Gan et al., 2013, Chattot et al., 2018). These defects in the dark patches could be one of the contributors to the ORR activity enhancement of the leached $PtCo_3$ species.

In addition, the $L1_0$ type lattice ordering is also observed in the core of the leached $PtCo_3$ NP3, which indicates that its core is well-alloyed. This finding is consistent with

the preceding observation on the unleached $PtCo_3$ nanoparticles. Interestingly, the lattice ordering is only observed in the relatively small $PtCo_3$ nanoparticles. The reason might be (1) the relatively small nanoparticle was less affected by the acid-leaching process. (2) the small nanoparticle has a thinner Pt-rich surface shell that does not contribute much to the scattered electron intensity in the alloy core region of the nanoparticle in the HAADF image.

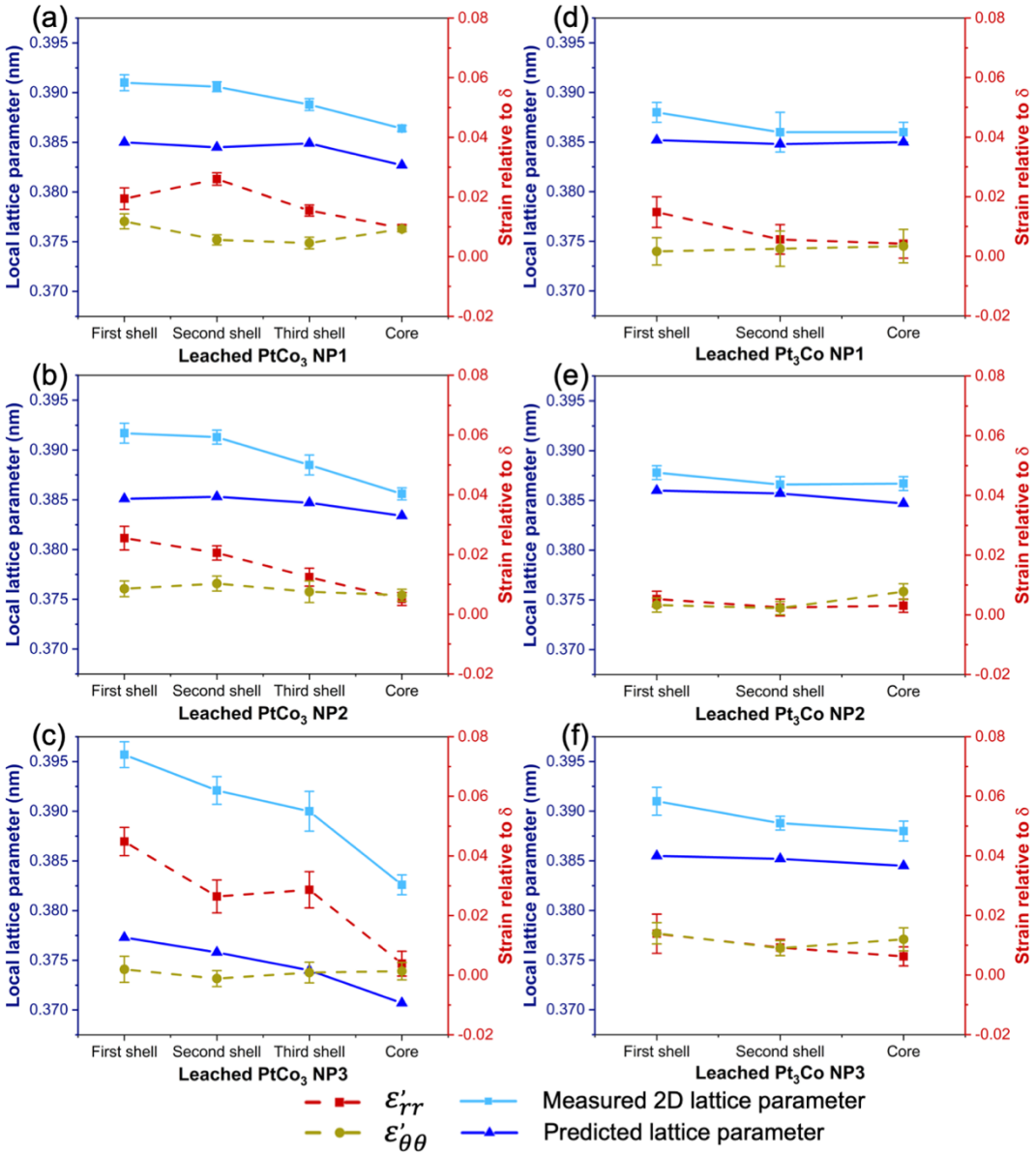

Figure 6.6 Polar strain, predicted and 2D local lattice parameters measurements for the unleached both $PtCo_3$ and Pt_3Co nanoparticle systems. The nanoparticles and corresponding shells are displayed and defined in Figure 6.5. Note that the calculated elastic polar strain is relative to the theoretical local lattice parameter predicted by Vegard's law. The predicted lattice parameters are calculated from the local composition using Vegard's law.

To investigate how the dealloying process influences the strain distribution within the Pt-Co nanoparticles, the measured lattice parameters were also compared to the predicted ones for the six leached nanoparticles, as shown in Figure 6.6. Here, due to the porosity and non-spherical shape of some dealloyed nanoparticles, the previous assumption ($\varepsilon_{\theta\theta} = \varepsilon_{\phi\phi}$) cannot always be applied to the determination of the 3D lattice parameter. For the unleached nanoparticles in Figure 6.4, the difference between the measured 2D and 3D lattice parameters is found to be small. Thus, the 2D local lattice parameters were used and compared between the different Pt-Co nanoparticle species in the following work. After the dealloying process, both the composition and measured lattice parameter distributions across the nanoparticles become more homogeneous. It appears that as the Co content decreases, the core-shell difference is narrowed. Particularly, in the leached Pt_3Co nanoparticles, the measured local lattice parameter is relatively constant between the outer shells and core. It reveals that the finite size (or the surface relaxation) of the nanoparticle does not introduce any additional strain to the surface. Additionally, the relative radial (ε'_{rr}) and circumferential strain ($\varepsilon'_{\theta\theta}$) were also measured and shown in Figure 6.6. The radial dilation strain within the leached nanoparticles has been significantly reduced, while the circumferential strain is approaching zero. It can be deduced that as the Co content decreases, the dilation strain becomes smaller.

6.6 High ensemble number analysis

Following the preceding quantification results, it has been found that the atom ratio of an individual nanoparticle does not always agree with the nominal loading during the synthesis, or the element ratio of the nanoparticle ensemble measured from the X-ray photoelectron spectroscopy (XPS) (Takahashi et al., 2016). Thus, knowing

composition, size and surface strain distributions among a large ensemble of the Pt-Co nanoparticles is crucial for the interpretation of the ensemble properties. However, the experimental simultaneous spectroscopic and HAADF data acquisitions on a single on-axis nanoparticle often requires several hours and sometimes days. It is not that meaningful to do simultaneous spectroscopic and HAADF imaging on every single one for hundreds of nanoparticles.

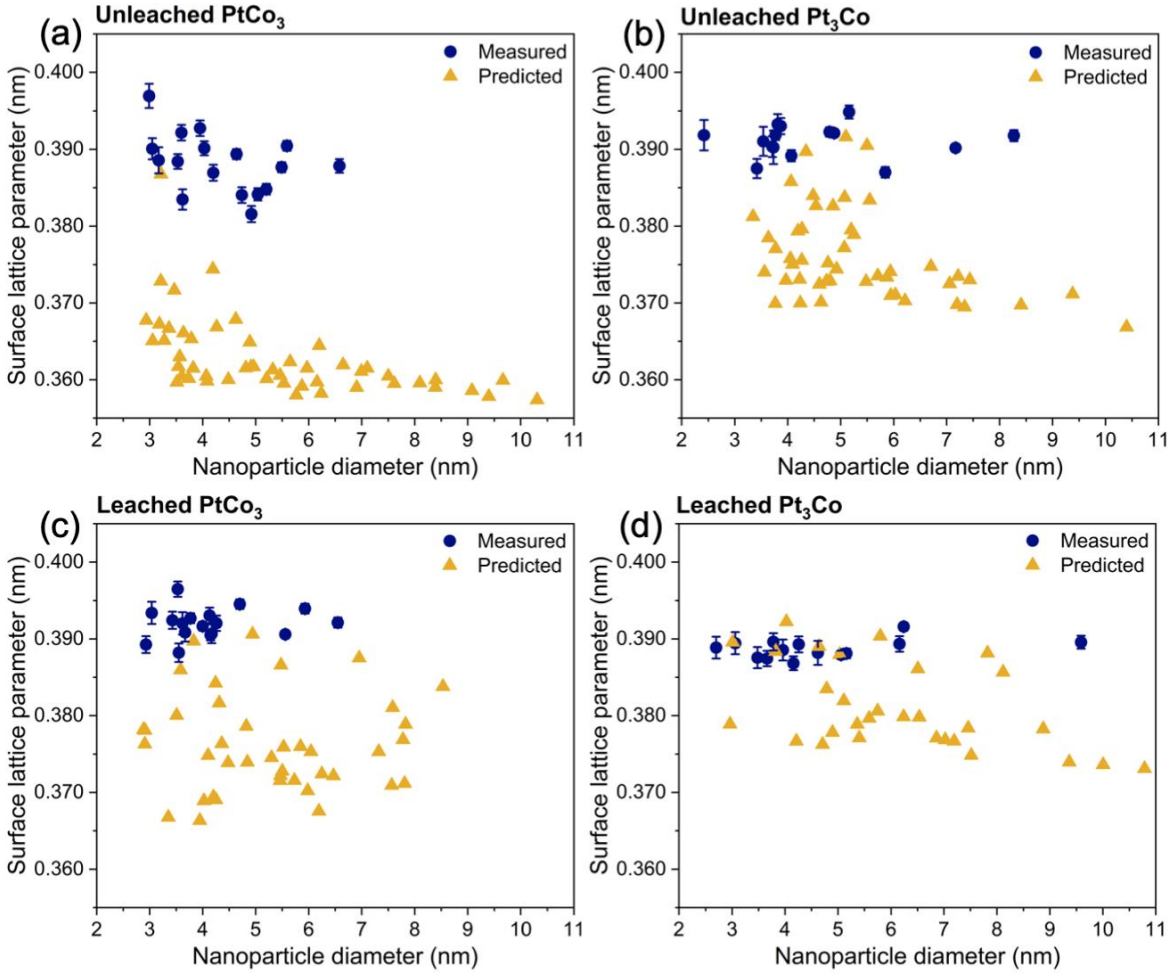

Figure 6.7 Comparison between the measured and predicted surface lattice parameters across a wider size range. The measured and predicted surface lattice parameters as a function of nanoparticle size for (a) the unleached $PtCo_3$, (b) the unleached Pt_3Co, (c) the leached $PtCo_3$ and (d) the leached Pt_3Co systems. Note that the predicted lattice parameters are calculated from the local composition using Vegard's law.

Herein, instead of simultaneous analyses, the composition and strain quantifications were separately performed on a large number of nanoparticles. 17, 15, 17 and 14 on-axis nanoparticles for the unleached $PtCo_3$ and Pt_3Co species, the leached $PtCo_3$ and

Pt_3Co species, respectively, were imaged at atomic resolution to measure the 2D local lattice parameters in the surface region. Here, the surface region is an outermost shell mask that covers the first three atomic layers of the nanoparticle in the HAADF image. The atomic layers are defined as rings of atomic columns, starting from the nanoparticle surface and moving in towards the centre. The measured surface lattice parameter in Figure 6.7 is the mean local lattice parameter with its standard error in the surface region of each on-axis nanoparticle. Also, ~50 off-axis nanoparticles overhanging over a vacuum region for each Pt-Co species were imaged for the composition analysis. The overall Pt fractional composition of each off-axis nanoparticle was quantified and plotted as a function of nanoparticle size, as shown in Figure 6.8. Regarding the unleached system, the highest overall Pt contents for the $PtCo_3$ and Pt_3Co nanoparticles are ~0.4 and ~0.8 at the nanoparticle size of ~3.5 nm, and decreases to ~0.1 and ~0.3, respectively, as nanoparticle size increases to 10 nm. This well-explains why the preceding quantified atom ratio of the nanoparticles does not match its nominal stoichiometry. Whereas, after dealloying process, the overall Pt contents for both the $PtCo_3$ and Pt_3Co nanoparticles are increased, and homogeneously distributed between 0.2 and 0.8, 0.4 and 1.0, respectively, over the size range.

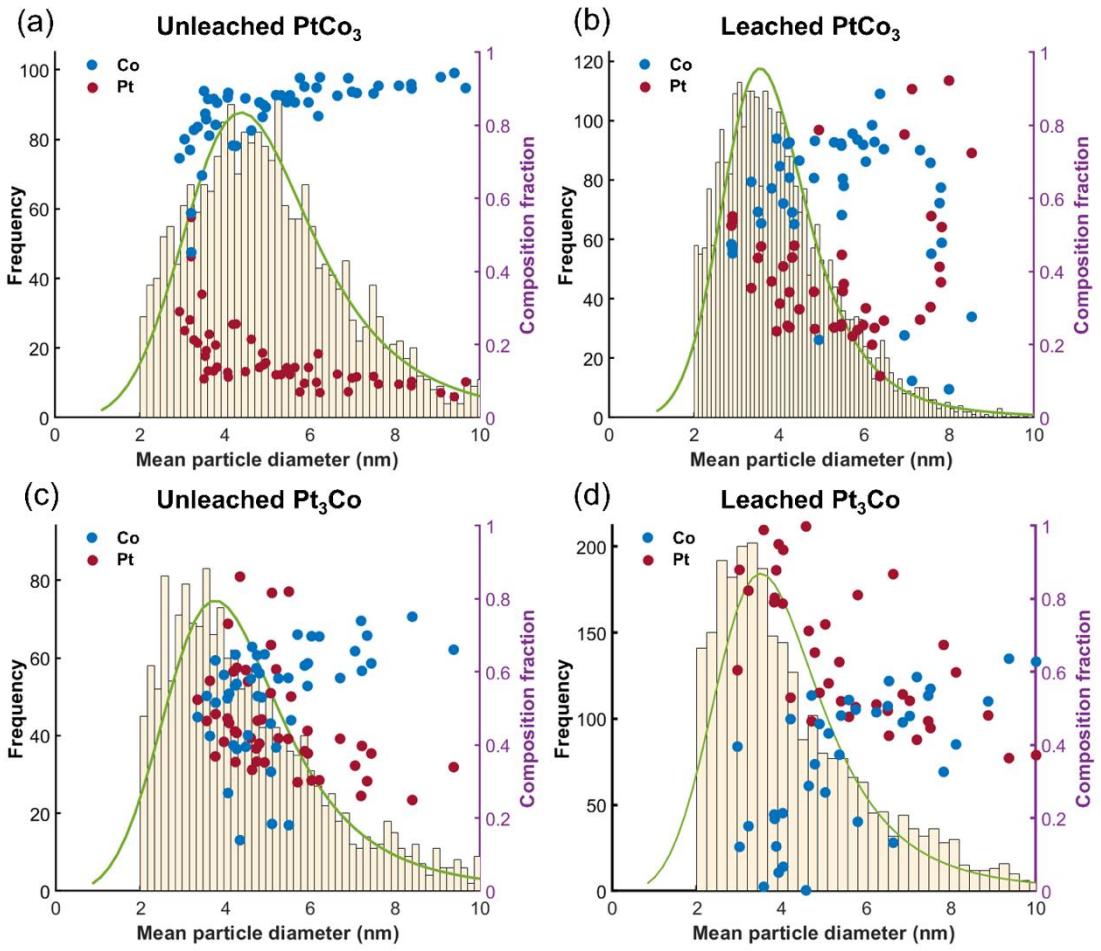

Figure 6.8 Nanoparticle size distribution histograms overlaid with overall fractional composition plots as a function of mean particle diameter for both, unleached and leached, $PtCo_3$ and Pt_3Co ensembles.

Additionally, the theoretical surface lattice parameters predicted from the Pt content in the surface region of these off-axis nanoparticles are compared to the measured ones in Figure 6.7. Remarkably, regardless of the nanoparticle composition, the surface region has an invariant local lattice parameter that is slightly smaller than that of pure Pt. The mean measured surface lattice parameters for the four nanoparticle batches are 0.388 ± 0.004 nm (unleached $PtCo_3$), 0.392 ± 0.002 nm (leached $PtCo_3$), 0.391 ± 0.002 nm (unleached Pt_3Co) and 0.389 ± 0.001 nm (leached Pt_3Co). The error presented here is the standard deviation of the mean, which demonstrates picometre-scale precision. Although a radial dilation strain is found to appear at the nanoparticle surface for the all four Pt-Co species, the surface dilation strain is reduced as the Co content decreases.

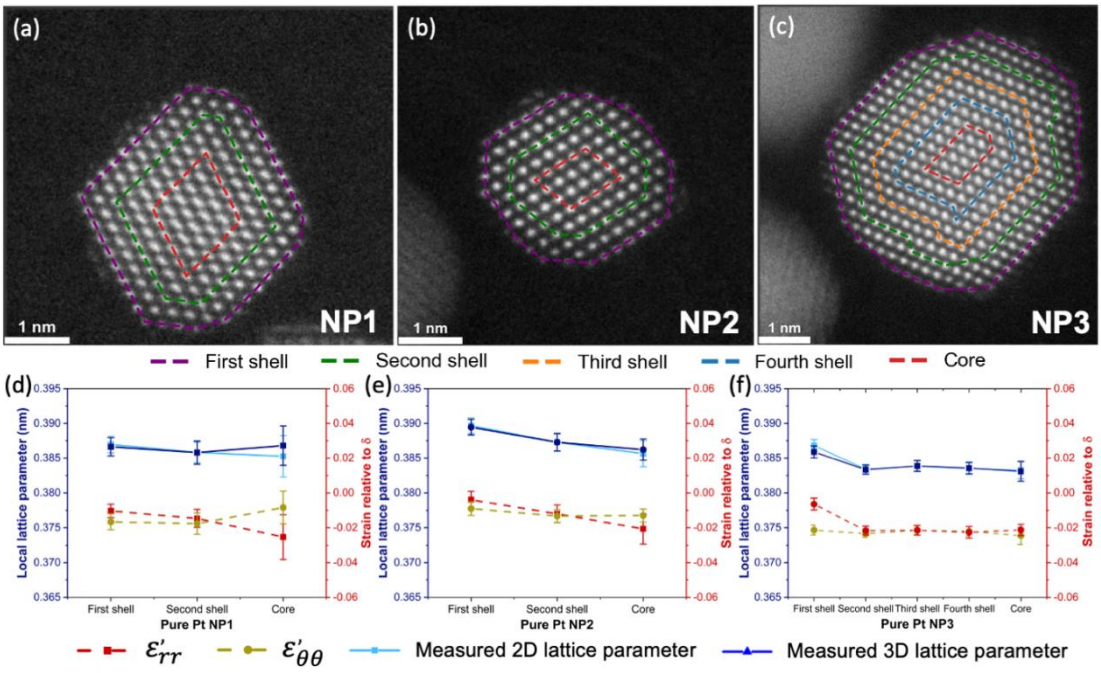

Figure 6.9 Strain analyses on on-axis pure Pt nanoparticles. (a-c) The atomic-resolution HAADF images of on-axis pure Pt nanoparticles. (d-f) Polar strain, 2D and 3D local lattice parameters measurements for the pure Pt nanoparticles. The nanoparticles and corresponding shells are displayed and defined in (a-c). The HAADF image in (c) comes from the previously published work (Aarons et al., 2017).

We further examined the strain behaviour of pure Pt nanoparticles, in Figure 6.9. Compressive strain is found to be uniformly distributed throughout the nanoparticles, where no difference between radial and circumferential strains is observed. Unlike the Pt-Co nanoparticles, the pure Pt nanoparticles do not exhibit a clear core-shell structure. The results can thus reveal that the introduction of Co brings dilation strain to the nanoparticles. The mechanism behind the Co-induced dilation strain is beyond the scope of this study, but is likely due to the oxidation of Co (Sode et al., 2019).

6.8 Conclusions

High-precision composition and strain quantification at atomic resolution have been simultaneously performed on both, alloyed and dealloyed, Pt_3Co and $PtCo_3$

nanoparticles. The composition analysis of the nanoparticles was achieved by atom counting using the spectroscopic signals (EDS and EELS), and has been shown to have high accuracy and reliability. The quantified atom counts were converted to the fractional composition, which is further used to predict the theoretical lattice parameter using Vegard's law. For strain mapping, the atomic site-specific local lattice parameter, radial and circumferential strains were measured and compared between the different Pt-Co species. As the results, in the unleached Pt-Co system, the Pt content of the nanoparticles decreases as the size increases. The alloyed Pt-Co core with the element ratio close to 1:1 of the nanoparticles appears to have an $L1_0$ type crystal structure. After the dealloying process, the Pt content for the two Pt-Co species increases and the composition is independent of the nanoparticle size. The nanoporosity was also observed in the leached $PtCo_3$ nanoparticles, which could contribute to the catalytic performance.

Despite the lattice parameter in the surface region of the nanoparticles being smaller than pure Pt, it is found that the lattice parameter is larger than that predicted by Vegard's law using the measured local composition. Indeed, no compressive elastic strain is observed, but a radial dilation strain relative to the Vegard predicted lattice parameter is observed at the surface. A smaller tensile circumferential strain is observed and tends to remain more constant throughout the individual nanoparticle. This finding is contrary to the prevailing conclusion which is that a compressive strain is imposed on the outer shell by the alloy core of the Pt-based bimetallic nanoparticles (Strasser et al., 2010). Because elastic compressive strain is not seen in any of the systems studied here, the shift in the d-band centre cannot be explained through a compressive strain-related broadening of the d-band, as previously suggested (Kitchin et al., 2004,

Stamenkovic et al., 2006). The results presented here suggest that the reduction in lattice parameter relative to pure Pt due to Co alloying combined with the radial dilation and the resultant high level of shear strain are the primary effects seen in the bimetallic nanoparticles.

Additionally, the $PtCo_3$ system has a larger dilation strain and a larger core-shell discrepancy compared to the Pt_3Co system, before and after the acid-leaching process. Also, the dealloying process significantly decreases the dilation strain and narrows the core-shell difference. It appears that the introduction of Co contributes to the formation of both the dilation strain and core-shell structure. Particularly, the core-shell structure is not observed in the leached Pt_3Co nanoparticles, where it can be deduced that the influence from the nanoparticle finite size does not add additional strain. Remarkably, the nanoparticle surface lattice parameter remains constant among the four Pt-Co species, and slightly smaller than the lattice parameter of pure bulk Pt. It indicates that the surface lattice parameter is insensitive to the local composition and finite size, but occurs through the local dilation radial strain. This work makes it possible to design the optimum ORR catalysts by tuning strain, composition, and structure of the Pt-based bimetallic nanoparticles.

6.9 References

Aarons, J., L. Jones, A. Varambhia, K. E. MacArthur, D. Ozkaya, M. Sarwar, C.-K. Skylaris and P. D. Nellist (2017). "Predicting the oxygen-binding properties of platinum nanoparticle ensembles by combining high-precision electron microscopy and density functional theory." *Nano Letters* 17(7): 4003-4012.

An, K. and G. A. Somorjai (2015). "Nanocatalysis I: synthesis of metal and bimetallic nanoparticles and porous oxides and their catalytic reaction studies." *Catalysis Letters* 145(1): 233-248.

Arblaster, J. (1997). "Crystallographic properties of platinum." *Platinum Metals Review* 41(1): 12-21.

Bligaard, T. and J. K. Nørskov (2007). "Ligand effects in heterogeneous catalysis and electrochemistry." *Electrochimica Acta* 52(18): 5512-5516.

Chattot, R., O. Le Bacq, V. Beermann, S. Kühl, J. Herranz, S. Henning, L. Kühn, T. Asset, L. Guétaz and G. Renou (2018). "Surface distortion as a unifying concept and descriptor in oxygen reduction reaction electrocatalysis." *Nature Materials* 17(9): 827-833.

Chen, S., M. Li, M. Gao, J. Jin, M. A. van Spronsen, M. B. Salmeron and P. Yang (2020). "High-performance Pt–Co nanoframes for fuel-cell electrocatalysis." *Nano Letters* 20(3): 1974-1979.

Cleve, T. V., S. Moniri, G. Belok, K. L. More and S. Linic (2017). "Nanoscale engineering of efficient oxygen reduction electrocatalysts by tailoring the local chemical environment of Pt surface Sites." *Acs Catalysis* 7(1): 17-24.

Ellaby, T., A. Varambhia, X. Luo, L. Briquet, M. Sarwar, D. Ozkaya, D. Thompsett, P. D. Nellist and C.-K. Skylaris (2020). "Strain effects in core–shell PtCo nanoparticles: a comparison of experimental observations and computational modelling." *Physical Chemistry Chemical Physics* 22(42): 24784-24795.

Ferrer, D., A. Torres-Castro, X. Gao, S. Sepulveda-Guzman, U. Ortiz-Mendez and M. Jose-Yacaman (2007). "Three-layer core/shell structure in Au− Pd bimetallic nanoparticles." *Nano Letters* 7(6): 1701-1705.

Fujita, T., P. Guan, K. McKenna, X. Lang, A. Hirata, L. Zhang, T. Tokunaga, S. Arai, Y. Yamamoto and N. Tanaka (2012). "Atomic origins of the high catalytic activity of nanoporous gold." *Nature Materials* 11(9): 775-780.

Gan, L., M. Heggen, R. O'Malley, B. Theobald and P. Strasser (2013). "Understanding and controlling nanoporosity formation for improving the stability of bimetallic fuel cell catalysts." *Nano Letters* 13(3): 1131-1138.

Gavartin, J., M. Sarwar, D. Papageorgopoulos, D. Gunn, S. Garcia, A. Perlov, A. Krzystala, D. L. Ormsby, D. Thompsett and G. Goldbeck-Wood (2009). "Exploring Fuel Cell Cathode Materials: A High Throughput Calculation Approach." *ECS Transactions* 25(1): 1335.

Goris, B., A. De Backer, S. Van Aert, S. Gómez-Graña, L. M. Liz-Marzán, G. Van Tendeloo and S. Bals (2013). "Three-dimensional elemental mapping at the atomic scale in bimetallic nanocrystals." *Nano letters* 13(9): 4236-4241.

Greeley, J., I. Stephens, A. Bondarenko, T. P. Johansson, H. A. Hansen, T. Jaramillo, J. Rossmeisl, I. Chorkendorff and J. K. Nørskov (2009). "Alloys of platinum and early transition metals as oxygen reduction electrocatalysts." *Nature Chemistry* 1(7): 552-556.

Jones, L. and P. D. Nellist (2013). "Identifying and correcting scan noise and drift in the scanning transmission electron microscope." *Microscopy and Microanalysis* 19(4): 1050.

Jones, L., A. Varambhia, R. Beanland, D. Kepaptsoglou, I. Griffiths, A. Ishizuka, F. Azough, R. Freer, K. Ishizuka and D. Cherns (2018). "Managing dose-, damage-and data-rates in multi-frame spectrum-imaging." *Microscopy* 67(suppl_1): i98-i113.

Jones, L., H. Yang, T. J. Pennycook, M. S. Marshall, S. Van Aert, N. D. Browning, M. R. Castell and P. D. Nellist (2015). "Smart Align—a new tool for robust non-rigid registration of scanning microscope data." *Advanced Structural and Chemical Imaging* 1(1): 1-16.

Khorshidi, A., J. Violet, J. Hashemi and A. A. Peterson (2018). "How strain can break the scaling relations of catalysis." *Nature Catalysis* 1(4): 263-268.

Kitchin, J. R., J. K. Nørskov, M. A. Barteau and J. Chen (2004). "Role of strain and ligand effects in the modification of the electronic and chemical properties of bimetallic surfaces." *Physical Review Letters* 93(15): 156801.

Kwon, J.-H., P. Lu, J. Hoffman, R. Yuan, A. Yoon, A. Bhattacharya and J.-M. Zuo (2016). "Elemental and lattice-parameter mapping of binary oxide superlattices of (LaNiO3) 4/(LaMnO3) 2 at atomic resolution." *Semiconductor Science and Technology* 32(1): 014002.

Li, J., S. Sharma, X. Liu, Y.-T. Pan, J. S. Spendelow, M. Chi, Y. Jia, P. Zhang, D. A. Cullen and Z. Xi (2019). "Hard-magnet L10-CoPt nanoparticles advance fuel cell catalysis." *Joule* 3(1): 124-135.

Liang, J., N. Li, Z. Zhao, L. Ma, X. Wang, S. Li, X. Liu, T. Wang, Y. Du and G. Lu (2019). "Tungsten-Doped L10-PtCo Ultrasmall Nanoparticles as a High-Performance Fuel Cell Cathode." *Angewandte Chemie International Edition* 58(43): 15471-15477.

Lima, F., J. De Castro, L. Santos and E. Ticianelli (2009). "Electrocatalysis of oxygen reduction on carbon-supported Pt–Co nanoparticles with low Pt content." *Journal of Power Sources* 190(2): 293-300.

Lima, F., W. Lizcano-Valbuena, E. Teixeira-Neto, F. Nart, E. Gonzalez and E. Ticianelli (2006). "Pt-Co/C nanoparticles as electrocatalysts for oxygen reduction in H2SO4 and H2SO4/CH3OH electrolytes." *Electrochimica Acta* 52(2): 385-393.

Luo, M. and S. Guo (2017). "Strain-controlled electrocatalysis on multimetallic nanomaterials." *Nature Reviews Materials* 2(11): 1-13.

MacArthur, K., T. Slater, S. Haigh, D. Ozkaya, P. Nellist and S. Lozano-Perez (2016). "Compositional quantification of PtCo acid-leached fuel cell catalysts using EDX partial cross sections." *Materials Science and Technology* 32(3): 248-253.

Mavrikakis, M., B. Hammer and J. K. Nørskov (1998). "Effect of strain on the reactivity of metal surfaces." *Physical Review Letters* 81(13): 2819.

Oezaslan, M. and P. Strasser (2011). "Activity of dealloyed PtCo3 and PtCu3 nanoparticle electrocatalyst for oxygen reduction reaction in polymer electrolyte membrane fuel cell." *Journal of Power Sources* 196(12): 5240-5249.

Pingel, T. N., M. Jørgensen, A. B. Yankovich, H. Grönbeck and E. Olsson (2018). "Influence of atomic site-specific strain on catalytic activity of supported nanoparticles." *Nature Communications* 9(1): 1-9.

Sadd, M. H. (2009). *Elasticity: theory, applications, and numerics*, Academic Press.

Saquib, M. and A. Halder (2018). "Dealloyed Pt3Co nanoparticles with higher geometric strain for superior hydrogen evolution reaction." *Journal of Solid State Chemistry* 262: 229-236.

Schulenburg, H., E. Muller, G. Khelashvili, T. Roser, H. Bonnemann, A. Wokaun and G. Scherer (2009). "Heat-treated PtCo3 nanoparticles as oxygen reduction catalysts." *The Journal of Physical Chemistry C* 113(10): 4069-4077.

Sode, J. O., R. J. Nicholls, P. D. Nellist, T. Tran and D. Ozkaya (2019). "Investigation of Cobalt Oxidation States in PtCo Nanoparticles Using STEM-EELS." Microscopy and Microanalysis 25(S2): 2148-2149.

Solliard, C. and M. Flueli (1985). "Surface stress and size effect on the lattice parameter in small particles of gold and platinum." *Surface Science* 156: 487-494.

Stamenkovic, V., B. S. Mun, K. J. Mayrhofer, P. N. Ross, N. M. Markovic, J. Rossmeisl, J. Greeley and J. K. Nørskov (2006). "Changing the activity of electrocatalysts for oxygen reduction by tuning the surface electronic structure." *Angewandte Chemie* 118(18): 2963-2967.

Stamenkovic, V. R., B. S. Mun, M. Arenz, K. J. Mayrhofer, C. A. Lucas, G. Wang, P. N. Ross and N. M. Markovic (2007). "Trends in electrocatalysis on extended and nanoscale Pt-bimetallic alloy surfaces." *Nature Materials* 6(3): 241-247.

Strasser, P., S. Koh, T. Anniyev, J. Greeley, K. More, C. Yu, Z. Liu, S. Kaya, D. Nordlund, H. Ogasawara, M. F. Toney and A. Nilsson (2010). "Lattice-strain control of the activity in dealloyed core–shell fuel cell catalysts." *Nature Chemistry* 2(6): 454-460.

Takahashi, S., N. Takahashi, N. Todoroki and T. Wadayama (2016). "Dealloying of nitrogen-introduced Pt–Co alloy nanoparticles: preferential core–shell formation with enhanced activity for oxygen reduction reaction." *ACS Omega* 1(6): 1247-1252.

Temmel, S. E., E. Fabbri, D. Pergolesi, T. Lippert and T. J. Schmidt (2016). "Investigating the role of strain toward the oxygen reduction activity on model thin film Pt catalysts." *ACS Catalysis* 6(11): 7566-7576.

Toda, T., H. Igarashi, H. Uchida and M. Watanabe (1999). "Enhancement of the electroreduction of oxygen on Pt alloys with Fe, Ni, and Co." *Journal of the Electrochemical Society* 146(10): 3750.

Varambhia, A., L. Jones, A. London, D. Ozkaya, P. D. Nellist and S. Lozano-Perez (2018). "Determining EDS and EELS partial cross-sections from multiple calibration standards to accurately quantify bi-metallic nanoparticles using STEM." *Micron* 113: 69-82.

Walsh, M. J., K. Yoshida, A. Kuwabara, M. L. Pay, P. L. Gai and E. D. Boyes (2012). "On the structural origin of the catalytic properties of inherently strained ultrasmall decahedral gold nanoparticles." *Nano Letters* 12(4): 2027-2031.

Wang, D., H. L. Xin, R. Hovden, H. Wang, Y. Yu, D. A. Muller, F. J. DiSalvo and H. D. Abruña (2013). "Structurally ordered intermetallic platinum–cobalt core–shell nanoparticles with enhanced activity and stability as oxygen reduction electrocatalysts." *Nature Materials* 12(1): 81-87.

Wang, J. X., H. Inada, L. Wu, Y. Zhu, Y. Choi, P. Liu, W.-P. Zhou and R. R. Adzic (2009). "Oxygen reduction on well-defined core− shell nanocatalysts: particle size,

facet, and Pt shell thickness effects." *Journal of the American Chemical Society* 131(47): 17298-17302.

Wu, J., P. Li, Y.-T. F. Pan, S. Warren, X. Yin and H. Yang (2012). "Surface lattice-engineered bimetallic nanoparticles and their catalytic properties." *Chemical Society Reviews* 41(24): 8066-8074.

Xiong, Y., Y. Yang, F. J. DiSalvo and H. D. Abruña (2020). "Synergistic Bimetallic Metallic Organic Framework-Derived Pt–Co Oxygen Reduction Electrocatalysts." *ACS Nano* 14(10): 13069-13080.

Zuo, J.-M., A. B. Shah, H. Kim, Y. Meng, W. Gao and J.-L. Rouviére (2014). "Lattice and strain analysis of atomic resolution Z-contrast images based on template matching." *Ultramicroscopy* 136: 50-60.

Chapter 7

Summary and outlook

7.1 Conclusions

The main aim of this thesis is to measure composition and strain variations in bimetallic Pt-Co catalyst nanoparticles using advanced electron microscopy. As discussed in Chapter 2, the Pt-Co nanoparticles are an excellent ORR catalyst candidate that is crucial to the performance of the H-PEMFC. The techniques used to investigate structure and composition of the nanoparticles were reviewed in Chapter 3.

Chapter 4 first highlighted the methodologies for strain analysis based on the transmission electron microscopy. The validity of the projection approximation was studied through STEM imaging simulations on the nanoparticle models. It was demonstrated that the difference between the measured 2D displacements and the projected actual radial 3D displacements is negligible, which indicates that interpreting the deformation behaviour of materials from the measured 2D strain maps is feasible. A technique for atomic site-specific deformation analysis on nanoparticles was then developed. The accuracy and precision for the displacement measurements in the proposed methodology are at the picometre level under the commonly-used experimental conditions. Next, various elastic deformation parameters that are defined on the discrete atomic columns instead of a continuum basis were reviewed and compared. The displacement vector which heavily relies on the reference grid is not effective for the local deformation analysis. The differential displacement vector and strain tensor are robust to the rigid-body shift but influenced by the rotation and scaling of the reference grid. Rotation of the reference grid could convert normal strain to shear

strain, and vice-versa. The principal strain only depends on the scaling of the reference grid, and can describe the local distortion direction. However, the local lattice parameter is an absolute value that is independent of the reference grid, as long as the image magnification is accurate, but fails in telling us the deformation direction. Therefore, simultaneous local lattice parameter and principal strain mapping enables us comprehensively understand the local deformation behaviour of materials. How the shift, rotation and scaling of the reference grid influence the strain tensor measurements was also investigated. It was shown that using the different reference grids only adds a series of uniform offsets to the strain variations.

Chapter 5 contains techniques for composition quantifications on nanoparticles using a broad range of STEM signals. Using ADF signals alone allows for atom counting on pure-element atomic columns, while spectroscopic signals (EDS and EELS) can provide atom counts for a specific element of multi-element materials. The ADF and spectroscopic signals can be unified by representing their intensities into scattering cross sections. In this chapter, the ADF, EDS and EELS spectrum images of an unleached $PtCo_3$ nanoparticle were simultaneously collected to quantify the composition variations from its surface to centre using the scattering cross section theory. As a result, estimates of Co atom counts using EDS and EELS signals are in excellent agreement, confirming the high accuracy of the spectroscopic quantifications. Also, a great consistency between ADF cross sections quantified from ADF and spectroscopic images has been achieved, validating that it is possible to directly compare and switch between different STEM signals seamlessly in terms of composition quantification.

In Chapter 6, simultaneous strain and composition quantifications at an atomic scale were performed within the on-axis individual nanoparticles for both unleached (alloyed) and leached (dealloyed), $PtCo_3$ and Pt_3Co systems. It was experimentally demonstrated that the $PtCo_3$ and unleached Pt_3Co nanoparticles have a larger lattice parameter and a higher proportion of Pt in the near-surface region, exhibiting a clear core-shell difference. However, such the core-shell structure is not observed in the leached Pt_3Co nanoparticles, where it can be deduced that the influence from the nanoparticle finite size does not cause any lattice expansion or contraction. The measured local lattice parameters were successfully related to local composition variations within each individual nanoparticle: the higher the Pt content is, the larger the local lattice parameter becomes. The ordered Pt-Co alloy core were also observed in the centre region of some nanoparticles.

Remarkably, the measured local lattice parameters are larger than the ones predicted by Vegard's law. Such the lattice expansion is mainly caused by the radial dilation strain that is commonly distributed throughout each nanoparticle. This result is contrary to the prevailing conclusion which is that the alloy core of the Pt-based bimetallic nanoparticle imposes a compressive strain on the near-surface region. Furthermore, the radial dilation strain is much larger than the circumferential dilation strain that remains constant and small throughout the individual nanoparticle. Accordingly, the radial strain is mainly responsible for the core-shell difference in the local lattice parameter of the nanoparticles. Another thing to note is that the $PtCo_3$ nanoparticles have a larger dilation strain and a larger core-shell discrepancy compared to the Pt_3Co counterparts, before and after the acid-leaching process. The dealloying process significantly decreases the dilation strain and narrows the core-shell difference. It appears that the

introduction of Co contributes to the formation of both the dilation strain and core-shell structure.

The surface lattice parameter of the nanoparticles which is believed to be highly associated with the catalytic activity was also measured. Regardless of the composition, the Pt-Co nanoparticles have an invariant surface lattice parameter, which is slightly smaller than the lattice parameter of the pure Pt bulk materials. It indicates that the surface lattice parameter is insensitive to the local composition and finite size, but depends on the local dilation strain. Further work will be incorporating these characterising results into the DFT modelling to design the optimum ORR catalysts by our collaborator. Our composition and strain quantifications can be routinely applied to other materials to study their physicochemical properties.

7.2 Future work

Three-dimensional strain mapping

In Chapter 4, the methodology for 2D strain mapping on atomic-resolution STEM images has been successfully developed. However, the actual specimen often has 3D deformation behaviour. Measuring the 3D strain tensor ($\varepsilon_{xx}, \varepsilon_{yy}, \varepsilon_{zz}, \varepsilon_{xy}, \varepsilon_{xz}$ and ε_{yz}) is crucial to relating the material structure to its physicochemical properties. 3D strain mapping cannot be directly performed on a 2D STEM image. Instead, a 3D model can be first reconstructed using the electron tomography or energy minimization methods. If necessary, the model can be relaxed under the different emulated experimental conditions such as annealing and tempering, by using DFT calculations. Then, the 3D strain measurements are performed on the model to investigate its deformation behaviour under a specific experimental condition. Different to the 2D strain analysis,

the 3D strain quantification makes use of 3D primitive unit cell, and the differential displacements ($\Delta\boldsymbol{u}_1, \Delta\boldsymbol{u}_2$ and $\Delta\boldsymbol{u}_3$) along three non-collinear basis vectors ($\boldsymbol{a}, \boldsymbol{b}$ and $\boldsymbol{c}$) need to be measured. *Eq. 4.5* can be accordingly rewritten as:

$$\begin{bmatrix} \varepsilon_{xx} & \varepsilon_{xy} & \varepsilon_{xz} \\ \varepsilon_{yx} & \varepsilon_{yy} & \varepsilon_{yz} \\ \varepsilon_{zx} & \varepsilon_{zy} & \varepsilon_{zz} \end{bmatrix} = \begin{bmatrix} \Delta u_{1x} & \Delta u_{2x} & \Delta u_{3x} \\ \Delta u_{1y} & \Delta u_{2y} & \Delta u_{3y} \\ \Delta u_{1z} & \Delta u_{2z} & \Delta u_{3z} \end{bmatrix} \begin{bmatrix} a_x & b_x & c_x \\ a_y & b_y & c_y \\ a_z & b_z & c_z \end{bmatrix}^{-1} \qquad \textit{Eq. 7.1}$$

The principal strain and local lattice parameter of each primitive unit cell can be derived from the calculated 3D strain tensor. The methodology for the 3D strain analysis would be particular valuable for investigating the anisotropy of the material properties at an atomic scale.

Three-dimensional bimetallic nanoparticle model reconstruction

Reconstructing a 3D model of pure-element nanoparticles from ADF STEM images has become a routine technique. As mentioned in Chapter 6, evaluating the number of atoms from the ADF image of the bimetallic nanoparticle is impossible, since the ADF signal alone is not sufficient in decoupling composition and thickness effects quantitatively. With the help of spectroscopic signals (EDS and EELS), atom counting has been successfully achieved on the Pt-Co nanoparticles. Unfortunately, in practice, atomic-resolution EDS and EELS imaging are mainly hampered by the poor counting statistics or the low SNR. However, using the cryo-transfer holder for the experiments could reduce the beam damage and therefore the acquisition time can be increased to collect more spectroscopic signals. Also, an alternative could be installing more EDS detectors to improve the collection efficiency.

Once atomic-resolution spectroscopic imaging is achieved, the number of atoms for different types (here, Pt and Co) in every atomic column can be obtained. However, a

full 3D inversion also requires the ordering of the atoms. To decouple atom ordering in each column, the electron channelling effect in the ADF image could be exploited using STEM simulations. For a binary atomic column have 3 Pt atoms and 2 Co atoms, there will be 10 different ordering configurations. The ADF scattering cross section varies with the ordering configuration because of the electron channelling. Thus, the ADF STEM simulation is performed for each ordering configuration to create a simulation library. By comparing the measured experimental ADF scattering cross section with the simulation library, the ordering information of each atomic column can be obtained. The z-height information of the atomic column can be obtained via electron tomography. The 3D model of the bimetallic nanoparticle is therefore reconstructed.

Co valence state of the Pt-Co nanoparticles

In chapter 2, it was demonstrated that the ORR catalytic activity of the Pt-Co nanoparticles heavily relies on the oxygen binding energy. The EELS spectrum not only can be used to quantify the number of atoms, but also provides the information about oxygen bonding. For the EELS spectrum of the Pt-Co nanoparticle, the O K edge and Pt $M_{4,5}$ edge are not resolvable, whereas the Co $L_{2,3}$ edge has a sharp fine structure and can be used to investigate oxygen bonding by calculating the ratio of L_2 and L_3 excitations. The ratio between the integrated L_2 and L_3 intensities gives an estimation of the Co valence state (or oxidation state). As the Pt-Co nanoparticle has a core-shell discrepancy in both composition and lattice parameter, knowing how the Co valence state changes from the nanoparticle surface to its centre would help understand the intrinsic mechanism of the catalytic activity.

Ptychographic atomic electron tomography

As mentioned before, atomic-resolution 3D reconstruction of the nanoparticle requires the z-height information of each atomic column, which is normally obtained by electron tomography. Conventional electron tomography involves ADF STEM imaging at multiple sample tilt orientations. The nanoparticle would experience a high electron dose, which could introduce serious beam damage to its morphology. However, electron ptychography has been widely used to image the beam-sensitive and light-element materials, and can be combined with electron tomography. This ptychographic tomography technique requires much fewer projections with much lower electron dose, which significantly avoids structure damage of the nanoparticle. In addition, performing ptychographic depth sectioning on a single 4D STEM dataset also gives the 3D information of materials. The ptychographic tomography would hopefully be a considerable benefit to the 3D reconstruction of the beam-sensitive materials.

In-situ electron microscopy

Methodologies for atomic-resolution composition and strain characterisations on the bimetallic Pt-Co nanoparticles have been successfully developed in this thesis. To better understand how the catalysts contribute to the ORR reaction, in-situ observation and characterisation are necessary. To emulate the PEMFC working environment, the bimetallic nanoparticles can be subjected to H_2 or O_2 gas at 80 ℃ in a DEN Solutions MEMS chip heating holder. The heating holder is inserted into the electron microscope, where the whole observation is conducted. Atomic-resolution ADF STEM imaging and spectroscopic imaging can be performed simultaneously on the same nanoparticle before and after exposure to gas. The analyses are subsequently conducted to investigate how the structure, strain and composition change during the reaction. The

in-situ experiments in the electron microscope would be particularly valuable for understanding the dynamics of chemical reactions.

Appendices

Appendix A

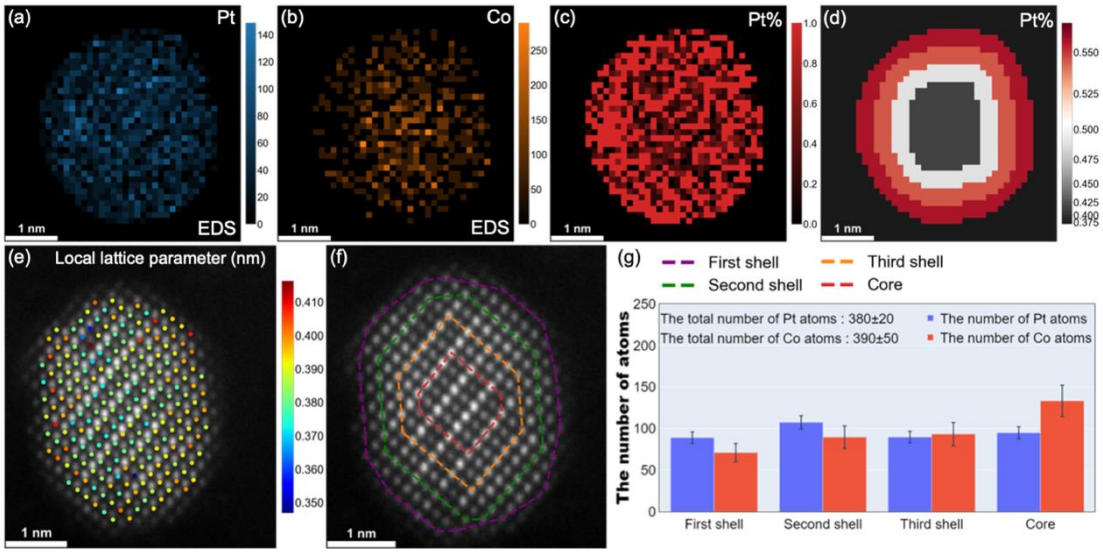

Figure S1 Simultaneous composition and strain quantifications of the unleached $PtCo_3$ NP1 using the HAADF and EDS signals. The nanoparticle areal density maps (atoms/nm^2) of (a) Pt from the EDS signals, (b) Co from the EDS signals. (c) A map of the fractional composition of Pt derived from (a) and (b). (d) The composition core-shell map of the nanoparticle. (e) The measured local lattice parameter map of the nanoparticle. (f) The HAADF image of the nanoparticle with the defined areas. (g) The number of Pt and Co atoms in the defined areas of the nanoparticle calculated using the EDS signals.

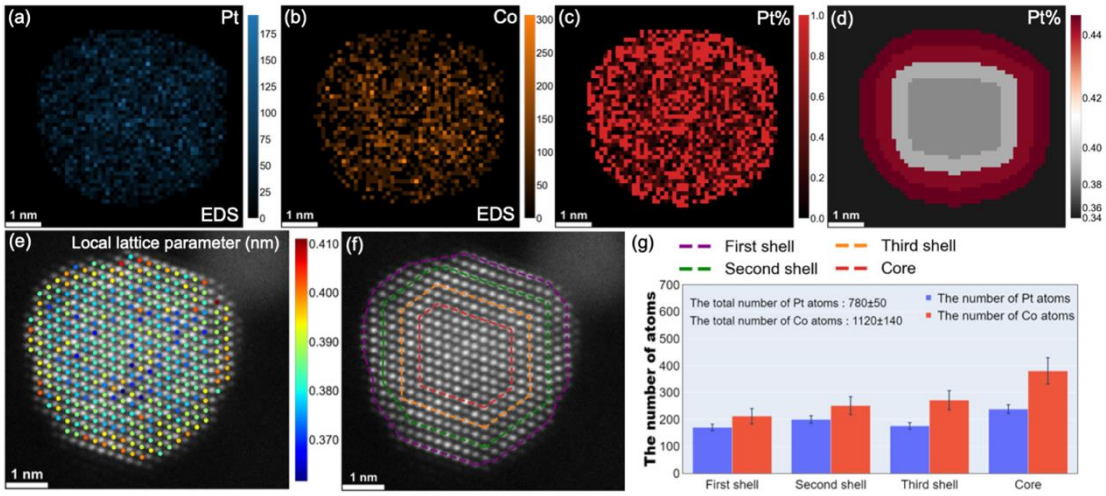

Figure S2 Simultaneous composition and strain quantifications of the unleached $PtCo_3$ NP2 using the HAADF and EDS signals. The nanoparticle areal density maps (atoms/nm^2) of (a) Pt from the EDS signals, (b) Co from the EDS signals. (c) A map of the fractional composition of Pt derived from (a) and (b). (d) The composition core-shell map of the nanoparticle. (e) The measured local lattice parameter map of the nanoparticle. (f) The HAADF image of the nanoparticle with the defined areas. (g) The number of Pt and Co atoms in the defined areas of the nanoparticle calculated using the EDS signals.

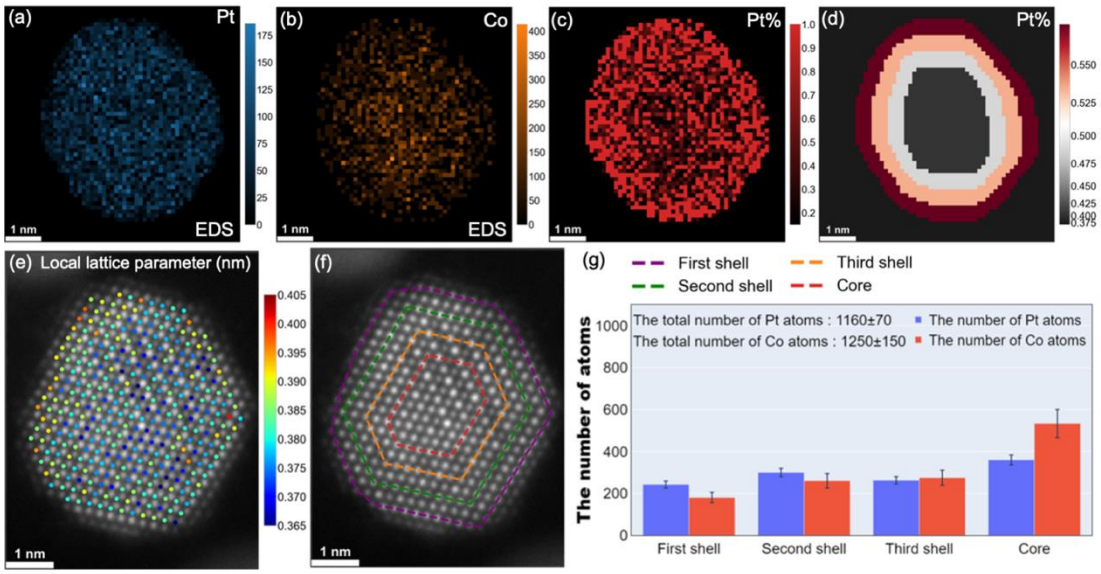

Figure S3 Simultaneous composition and strain quantifications of the unleached $PtCo_3$ NP3 using the HAADF and EDS signals. The nanoparticle areal density maps (atoms/nm^2) of (a) Pt from the EDS signals, (b) Co from the EDS signals. (c) A map of the fractional composition of Pt derived from (a) and (b). (d) The composition core-shell map of the nanoparticle. (e) The measured local lattice parameter map of the nanoparticle. (f) The HAADF image of the nanoparticle with the defined areas. (g) The number of Pt and Co atoms in the defined areas of the nanoparticle calculated using the EDS signals.

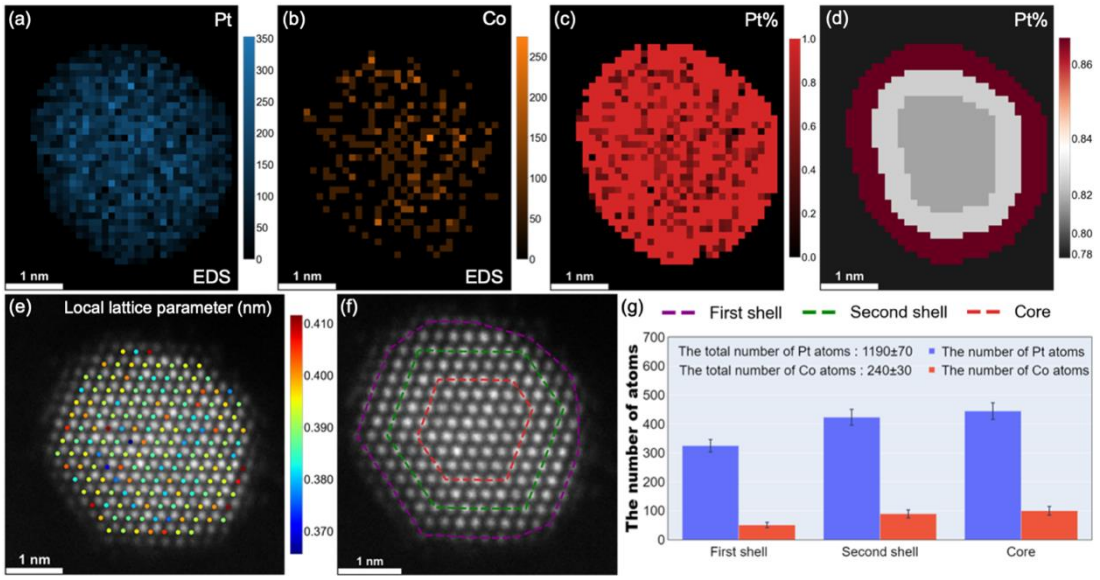

Figure S4 Simultaneous composition and strain quantifications of the unleached Pt_3Co NP1 using the HAADF and EDS signals. The nanoparticle areal density maps (atoms/nm^2) of (a) Pt from the EDS signals, (b) Co from the EDS signals. (c) A map of the fractional composition of Pt derived from (a) and (b). (d) The composition core-shell map of the nanoparticle. (e) The measured local lattice parameter map of the nanoparticle. (f) The HAADF image of the nanoparticle with the defined areas. (g) The number of Pt and Co atoms in the defined areas of the nanoparticle calculated using the EDS signals.

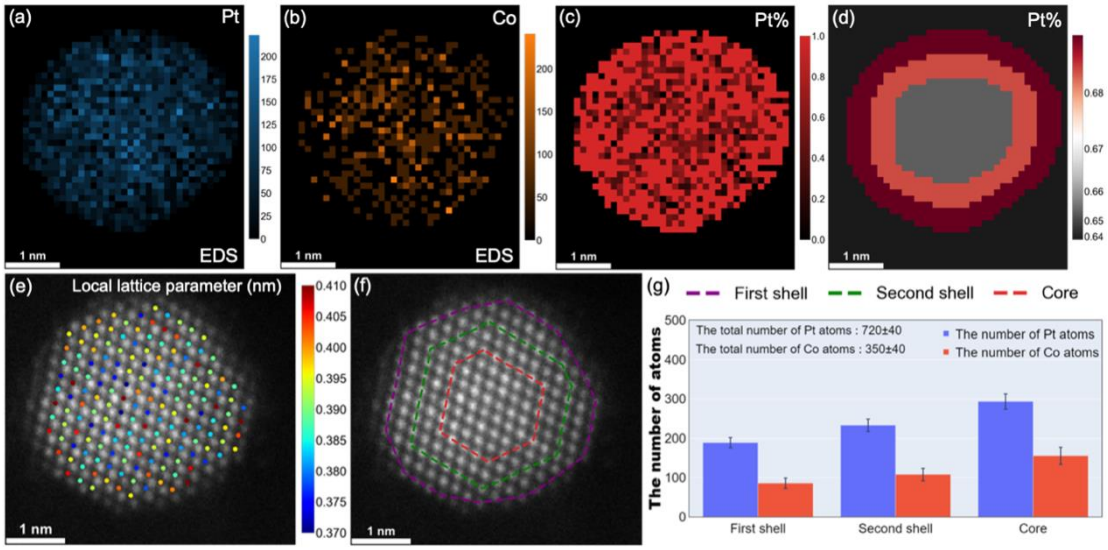

Figure S5 Simultaneous composition and strain quantifications of the unleached Pt_3Co NP2 using the HAADF and EDS signals. The nanoparticle areal density maps (atoms/nm^2) of (a) Pt from the EDS signals, (b) Co from the EDS signals. (c) A map of the fractional composition of Pt derived from (a) and (b). (d) The composition core-shell map of the nanoparticle. (e) The measured local lattice parameter map of the nanoparticle. (f) The HAADF image of the nanoparticle with the defined areas. (g) The number of Pt and Co atoms in the defined areas of the nanoparticle calculated using the EDS signals.

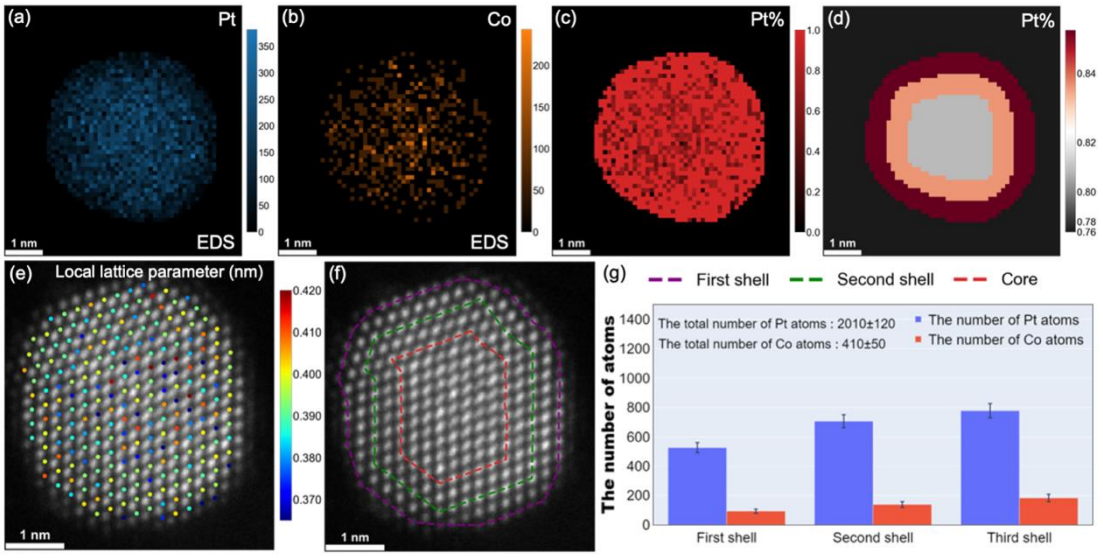

Figure S6 Simultaneous composition and strain quantifications of the unleached Pt_3Co NP3 using the HAADF and EDS signals. The nanoparticle areal density maps (atoms/nm^2) of (a) Pt from the EDS signals, (b) Co from the EDS signals. (c) A map of the fractional composition of Pt derived from (a) and (b). (d) The composition core-shell map of the nanoparticle. (e) The measured local lattice parameter map of the nanoparticle. (f) The HAADF image of the nanoparticle with the defined areas. (g) The number of Pt and Co atoms in the defined areas of the nanoparticle calculated using the EDS signals.

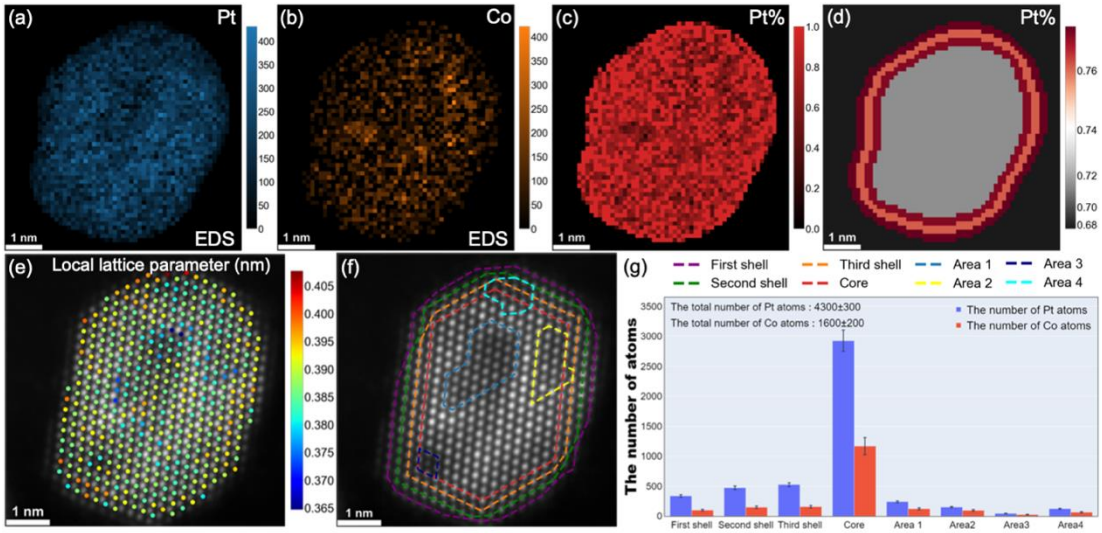

Figure S7 Simultaneous composition and strain quantifications of the leached $PtCo_3$ NP1 using the HAADF and EDS signals. The nanoparticle areal density maps (atoms/nm^2) of (a) Pt from the EDS signals, (b) Co from the EDS signals. (c) A map of the fractional composition of Pt derived from (a) and (b). (d) The composition core-shell map of the nanoparticle. (e) The measured local lattice parameter map of the nanoparticle. (f) The HAADF image of the nanoparticle with the defined areas. (g) The number of Pt and Co atoms in the defined areas of the nanoparticle calculated using the EDS signals.

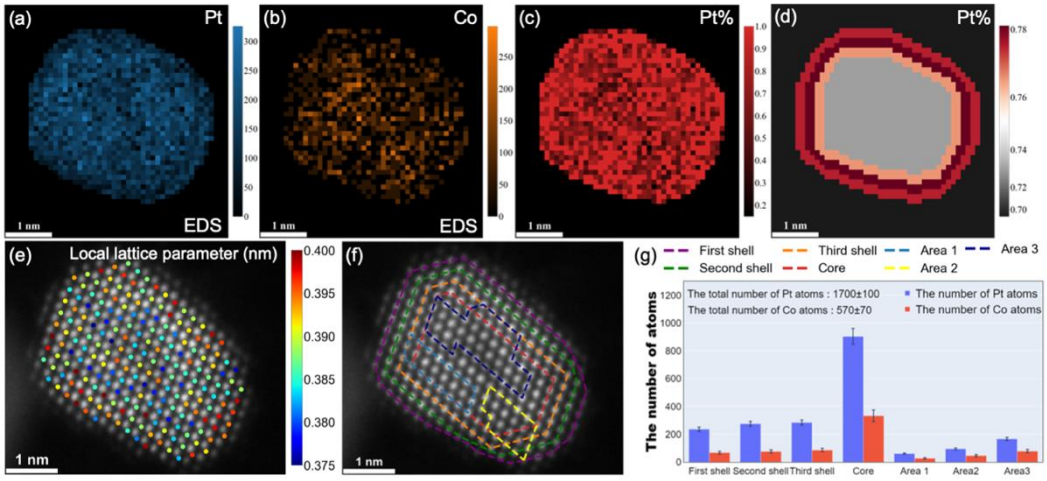

Figure S8 Simultaneous composition and strain quantifications of the leached $PtCo_3$ NP2 using the HAADF and EDS signals. The nanoparticle areal density maps (atoms/nm^2) of (a) Pt from the EDS signals, (b) Co from the EDS signals. (c) A map of the fractional composition of Pt derived from (a) and (b). (d) The composition core-shell map of the nanoparticle. (e) The measured local lattice parameter map of the nanoparticle. (f) The HAADF image of the nanoparticle with the defined areas. (g) The number of Pt and Co atoms in the defined areas of the nanoparticle calculated using the EDS signals.

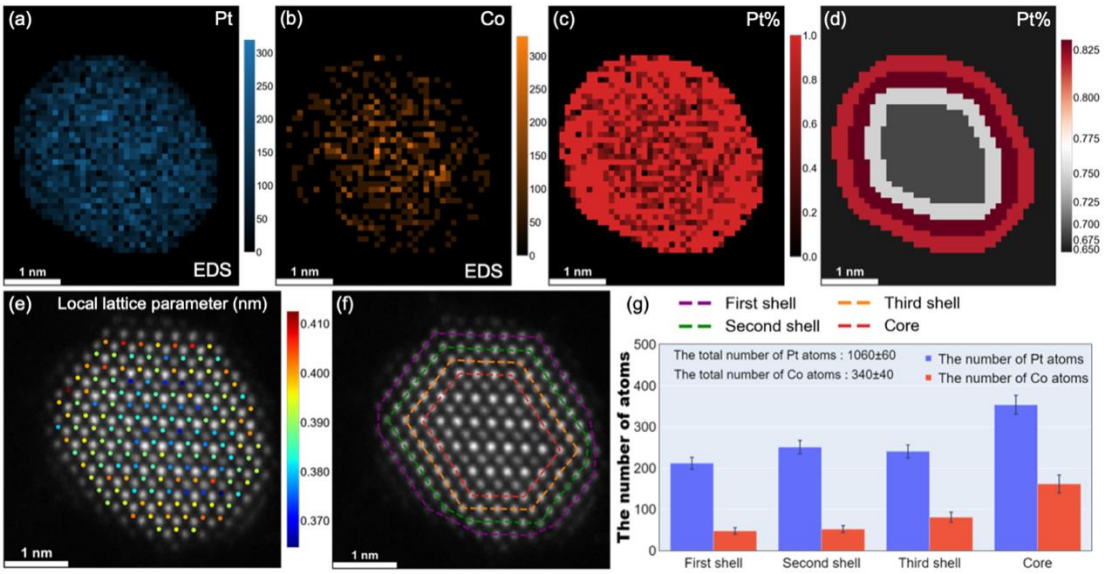

Figure S9 Simultaneous composition and strain quantifications of the leached $PtCo_3$ NP3 using the HAADF and EDS signals. The nanoparticle areal density maps (atoms/nm^2) of (a) Pt from the EDS signals, (b) Co from the EDS signals. (c) A map of the fractional composition of Pt derived from (a) and (b). (d) The composition core-shell map of the nanoparticle. (e) The measured local lattice parameter map of the nanoparticle. (f) The HAADF image of the nanoparticle with the defined areas. (g) The number of Pt and Co atoms in the defined areas of the nanoparticle calculated using the EDS signals.

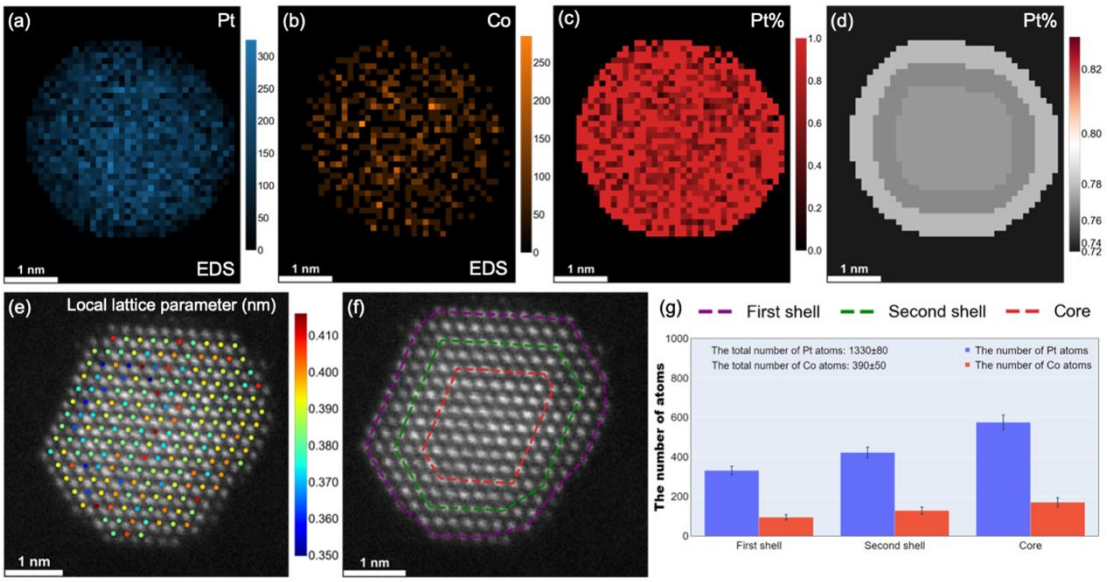

Figure S10 Simultaneous composition and strain quantifications of the leached Pt_3Co NP1 using the HAADF and EDS signals. The nanoparticle areal density maps (atoms/nm^2) of (a) Pt from the EDS signals, (b) Co from the EDS signals. (c) A map of the fractional composition of Pt derived from (a) and (b). (d) The composition core-shell map of the nanoparticle. (e) The measured local lattice parameter map of the nanoparticle. (f) The HAADF image of the nanoparticle with the defined areas. (g) The number of Pt and Co atoms in the defined areas of the nanoparticle calculated using the EDS signals.

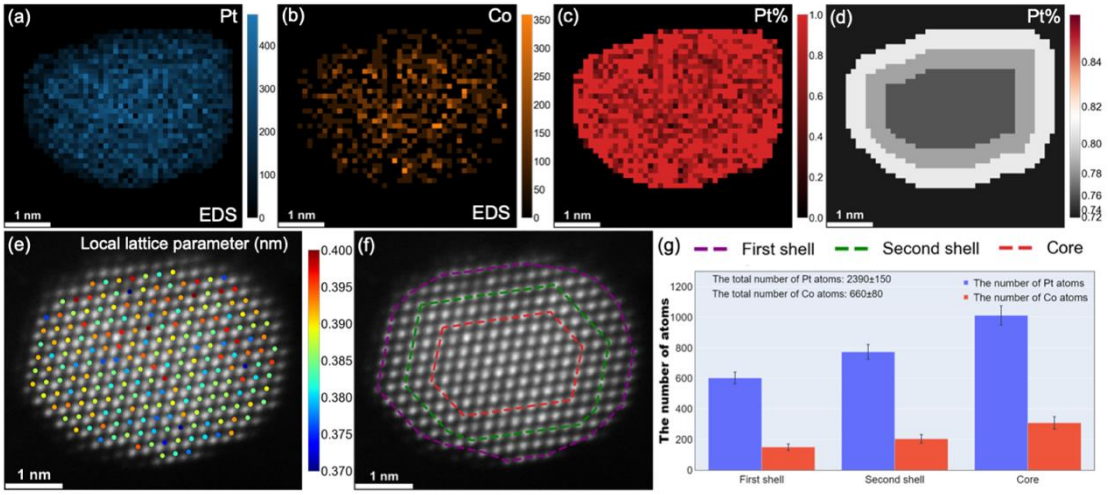

Figure S11 Simultaneous composition and strain quantifications of the leached Pt_3Co NP2 using the HAADF and EDS signals. The nanoparticle areal density maps (atoms/nm^2) of (a) Pt from the EDS signals, (b) Co from the EDS signals. (c) A map of the fractional composition of Pt derived from (a) and (b). (d) The composition core-shell map of the nanoparticle. (e) The measured local lattice parameter map of the nanoparticle. (f) The HAADF image of the nanoparticle with the defined areas. (g) The number of Pt and Co atoms in the defined areas of the nanoparticle calculated using the EDS signals.

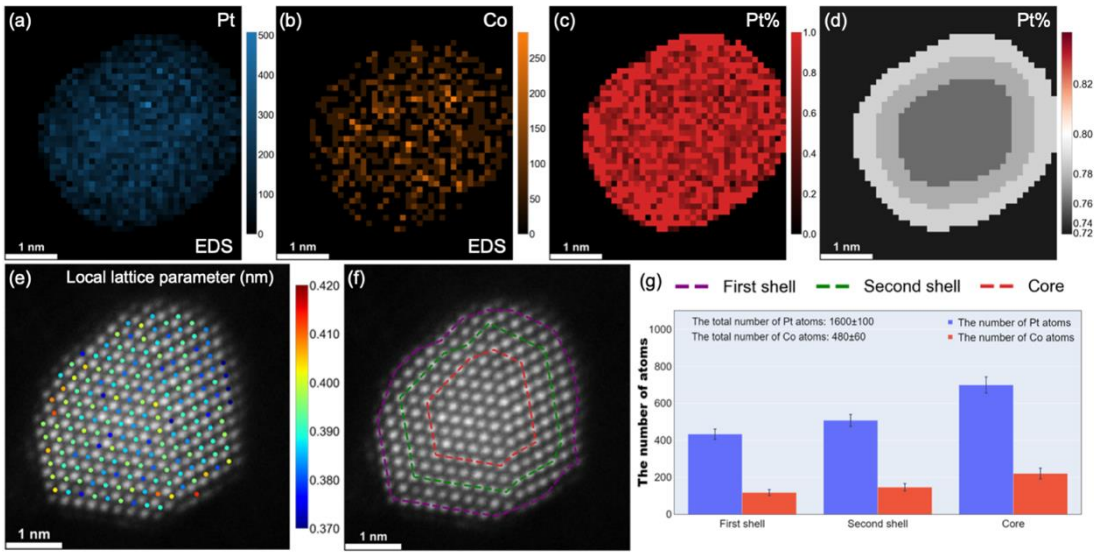

Figure S12 Simultaneous composition and strain quantifications of the leached Pt_3Co NP3 using the HAADF and EDS signals. The nanoparticle areal density maps (atoms/nm^2) of (a) Pt from the EDS signals, (b) Co from the EDS signals. (c) A map of the fractional composition of Pt derived from (a) and (b). (d) The composition core-shell map of the nanoparticle. (e) The measured local lattice parameter map of the nanoparticle. (f) The HAADF image of the nanoparticle with the defined areas. (g) The number of Pt and Co atoms in the defined areas of the nanoparticle calculated using the EDS signals.

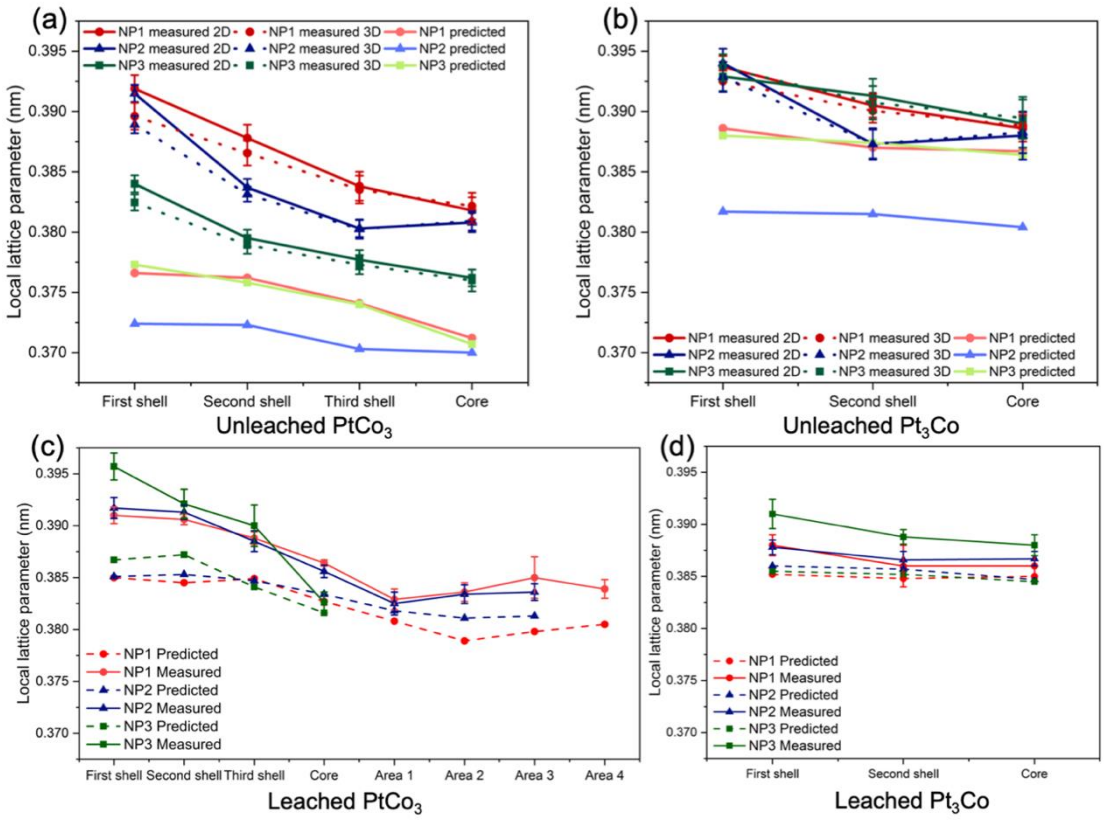

Figure S15 Comparison between measured and predicted local lattice parameter for the four Pt-Co nanoparticle species.

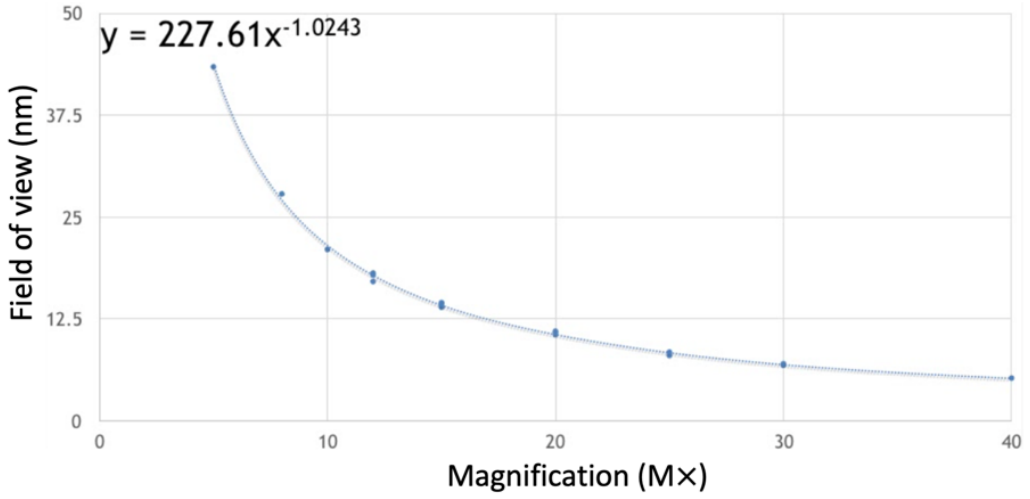

Figure S16 Magnification calibration for the JEOL ARM200F scanning transmission electron microscope

Appendix B

Glossary of terms

ADF – Annular Dark Field

BF – Bright Field

CBED – Convergent Beam Electron Diffraction

CCD – Charge Coupled Device

CTEM – Conventional Transmission Electron Microscopy

DF – Dark Field

DFEH – Dark Field Electron Holography

DFT – Density Functional Theory

EDS – Energy Dispersive X-ray Spectroscopy

EELS – Electron Energy Loss Spectroscopy

ELNES – Energy-Loss Near-Edge Structure

EXAFS - Extended X-Ray Absorption Fine Structure

GPA – Geometric Phase Analysis

HOLZ – Higher-Order Laue-Zone

HOR – Hydrogen Oxidation Reaction

IR – Infrared

MFSI – Multi Frame Spectrum Image

NBED – Nano Beam Electron Diffraction

ORR – Oxygen Reduction Reaction

PCA – Principal Component Analysis

PEMFC – Proton Exchange Membrane Fuel Cell

SAD – Selected Area Diffraction

SEM – Scanning Electron Microscope

SNR – Signal to Noise Ratio

STEM – Scanning Transmission Electron Microscope

TEM – Transmission Electron Microscope

UPD – Underpotential Deposition

UV-vis – Ultraviolet–visible

XRD – X-ray Diffraction

XPS – X-ray Photon Spectroscopy

ZLP – Zero Loss Peak